

# Sheffield Hallam University

*Numerical and experimental study of flow in a gas turbine chamber.*

DAUD, Harbi Ahmed.

Available from the Sheffield Hallam University Research Archive (SHURA) at:

<http://shura.shu.ac.uk/19535/>

## A Sheffield Hallam University thesis

This thesis is protected by copyright which belongs to the author.

The content must not be changed in any way or sold commercially in any format or medium without the formal permission of the author.

When referring to this work, full bibliographic details including the author, title, awarding institution and date of the thesis must be given.

Please visit <http://shura.shu.ac.uk/19535/> and <http://shura.shu.ac.uk/information.html> for further details about copyright and re-use permissions.

102 070 936 7



**REFERENCE**

ProQuest Number: 10694416

All rights reserved

INFORMATION TO ALL USERS

The quality of this reproduction is dependent upon the quality of the copy submitted.

In the unlikely event that the author did not send a complete manuscript and there are missing pages, these will be noted. Also, if material had to be removed, a note will indicate the deletion.



ProQuest 10694416

Published by ProQuest LLC (2017). Copyright of the Dissertation is held by the Author.

All rights reserved.

This work is protected against unauthorized copying under Title 17, United States Code  
Microform Edition © ProQuest LLC.

ProQuest LLC.  
789 East Eisenhower Parkway  
P.O. Box 1346  
Ann Arbor, MI 48106 – 1346

# **Numerical and Experimental study of Flow in a Gas Turbine Chamber**

Harbi Ahmed Daud

A thesis submitted in partial fulfilment of the requirements of  
Sheffield Hallam University  
for the degree of Doctor of Philosophy

July 2012

*By the grace of Allah the almighty, this thesis is dedicated to prophet Mohammed (peace and blessing be upon him), and to the loving memory of my father Ahmed Daud Salman*

## Abstract

This thesis examines the cooling performance and the flow on a gas turbine blade. Numerical and experimental methods are described and implemented to assess the influence of film cooling effectiveness. A modern gas turbine blade geometry has been used. The blade is considered as a solid body with the blade cross section from hub to shroud varying with a degree of skewness. Computational Fluid Dynamics (CFD) is employed to assess blade film cooling effectiveness via simulation of the effect of varying blowing ratios ( $BR=1, 1.5$  and  $2$ ), varying coolant fluid temperature ( $T_c=153$  K and  $T_c=287.5$  K), various angles of injection ( $35^\circ, 45^\circ$  and  $60^\circ$ ), increasing the number of cooling holes ( $32$  and  $42$ ) and increasing the cooling holes diameter ( $D=0.5$  mm and  $1$ mm). A full three-dimensional finite-volume method has been utilized in this study via the FLUENT 6.3 code with a  $k-\epsilon$  (RNG) turbulence model.

Results of the CFD models were carefully validated by studying aerodynamic flow and heat transfer in turbine blade film cooling performance. A two-dimensional channel and NACA 0012 airfoil were selected to investigate turbulence effects. The solution accuracy is assessed by carrying out a sensitivity analysis of mesh type and quality effects with enhancement wall treatment and standard wall function effects also addressed for turbulent boundary layers. In this study, four different turbulence models were utilized (S-A,  $k-\epsilon$ , (RNG), and (SST)  $k-\omega$ ). The computations were compared with available Direct Numerical Simulation (DNS) and experimental data. Good correlation was observed when using the RNG turbulence model in comparison with other turbulence models.

Film cooling effectiveness and heat transfer along a flat plate has been analyzed for four different plate materials, namely steel, carbon steel, copper and aluminum, with  $30^\circ$  angle of injection. The cooling holes arrangement was simulated for a hole diameter of  $D=1$  mm and different sections of the blade showing cooling effectiveness and heat transfer characteristic variation with increasing ( $BR = 0.5, 1$ ). Furthermore a symmetrical single hole at  $35^\circ$  angle of injection was studied both the solid and shell plate cases. Cooling effectiveness numerical results were compared with available experimental data and the effect of material thermal properties for the solid plate on cooling performance evaluated. Numerical modeling has clearly identified that there is no benefit in reducing the number of holes as this decreases film cooling effectiveness.

The experimental investigation showed the effect of increasing volumetric flow rate  $V^0=1000, 800$  and  $600$   $\text{cm}^3/\text{min}$ , as a term of the blowing ratio ( $BR$ ) and angle of injection ( $35^\circ, 45^\circ$  and  $60^\circ$ ) for a modern gas turbine blade specimen using Thermal Paint Technology (TPT) and a Thermal Wind Tunnel (TWT). Both methods confirmed that the blade specimen with angle of injection of  $45^\circ$ , blowing ratio of  $BR=2$  (which corresponds to  $1000\text{cm}^3/\text{min}$ ), cooling holes diameter  $D=1$ mm and  $42$  holes developed a better film cooling effectiveness compared with the  $35^\circ$  and  $60^\circ$  cases. In addition TPT is a sufficient and relatively easy method for evaluating temperature distributions in experimental studies.

## **Acknowledgments**

First, I would like to express my sincere gratitude and thanks to ALLAH for the guidance through this work and for all the blessings bestowed upon me. This study would not have been possible without the help of ALLAH.

I would also like to pay special thanks to my supervision team, primarily my director of study Dr. O. Anwar Bég for his continued support, patience and encouragement from 2008 to present, with all aspects of the work.

To my supervisor Dr Qinling Li I am grateful for her guidance and suggestions during this research. Dr Li always provided excellent advice in particular on the CFD simulations.

To my external research adviser, Dr Saud Ghani for his advice and efforts concerning the experimental work and for his excellent support and supervision of wind tunnel experiments in Qatar University in the summer of 2011.

I am truly and deeply indebted to Dr Bég, Dr Li and Dr Ghani and I wish to extend my sincere gratitude to them for giving me this opportunity to conduct research under their supervisions.

I would like to thanks the Government of Iraq, Ministry of higher Education for their generous financial support during my studies at Sheffield Hallam University.

I would like to thanks Sheffield Hallam University and in particular the Materials and Engineering Research Institute (MERI).

I am also grateful to the technical support provided by Mr. Brian Palmer, Mr. John Stanley, Mr. Steven Brandon, Mr. R. Wainwright and Mr. M. Jackson regarding the measurement of the gas turbine blade specimen coordinate points using the CMM machine, ordering experimental equipment and also CAD modeling stages of the present research.

I would like also to thank Qatar University and in particular the Mechanical and Industrial Engineering Department for their hospitality and for providing the opportunity to carry out experimental work in gas turbine film cooling under the supervision of Dr. Saud Ghani. I also wish to express my special gratitude to Mr. Yehia ElSaid for his support in setting up the thermal wind tunnel in the power generation lab. Without their help the experimental tests would not had been carried out fruitfully.

I would also like to thank [Wolverhampton University](#) and especially Dr. Mark Stanford for his assistance with the fabrication of blade turbine specimens used laser sintering technology.

I also wish to convey my deepest gratitude to my parents and my brothers and sisters for their great support during my study, especially my elder brother, Abdulwahab and Abdulhadi. I could not have achieved my academic goals without their encouragement. Finally, I reserve a very special thanks to my beloved sons, Mohammed and Mustafa, and apologize to them for not being able to spend more time with them during this study.

## Preface

The present work in this thesis was performed by PhD student, Harbi A. Daud, between October 2008 and January 2012 in the Materials Engineering and Research Institute (MERI), Sheffield Hallam University.

Numerical simulation of gas turbine flow is an important engineering problem which involves heat transfer, turbulence and film cooling technology in complex geometries. An important objective in the present study is to highlight the significance of validation of CFD simulations achieved with the commercial package FLUENT, with experimental tests, in order to accurately predict aerodynamic flow and heat transfer characteristics for a gas turbine blade.

As a result of this research, a number of journal and conference papers were published and no part of it has been submitted for award at any other College or University.

PhD candidate contributions:

1. *Poster presentation* for MERI Student seminar day in Sheffield Hallam University, 25<sup>th</sup> May 2009.
2. *Oral presentation* (20 minutes) for MERI Student seminar day in Sheffield Hallam University, 25<sup>th</sup> May 2010.
3. *Refereed Journal article*: Daud H. A., Li Q. , Bég O. A. and. AbdulGhani S. A. A. (20011A),, **Numerical investigations of wall-bounded turbulence**. Proc. IMechE Part C- J. Mechanical Engineering Science, 2011. **225**, p. 1163-1174.
4. *Refereed Conference article*: Daud H. A., Li Q. , Bég O. A. and. AbdulGhani S. A. A.(20011B), **Numerical simulation of blowing ratio effects on film cooling on a gas turbine blade**, Computational Methods and Experimental Measurements XV Conference. 2011: 31<sup>st</sup> May - 2<sup>nd</sup> June, New Forest, UK p. 279-292.
5. *Refereed Conference article*: Daud H. A., Li Q. , Bég O. A. and. AbdulGhani S. A. A.(2011C), **Numerical study of flat plate film cooling effectiveness with different material properties and hole arrangements**, 12<sup>th</sup> UK National Heat Transfer Conference, 30/31<sup>st</sup> August - 1<sup>st</sup> September 2011, University of Leeds, UK.
6. *Oral and poster presentation* of engineering sciences conference 1<sup>st</sup> & 2<sup>nd</sup> October 2011 held at University College London (UCL) under Iraqi cultural attaché guides.

(This achieved a 1<sup>st</sup> prize for Best Poster in Mechanical and Manufacture Engineering).

7. Daud H. A., Li Q., Bég O. A. and. AbdulGhani S. A. A., **Numerical Investigation of Film Cooling Effectiveness and Heat Transfer along a Flat Plate**, *Int. J. of Applied Mathematics and Mechanics (IJAMM)* 8(17) p.17-33 (2012).
8. *Refereed Journal article*: Harbi A. Daud, S A.A Abdul Ghani, O. Anwar Bég, Qinling Li and Mark Stanford, **Investigation of gas turbine film cooling using thermal paint technology**, *Experiments in Fluids*, January (2012). *Submitted (under review)*



## Table of Contents

<b>Abstract</b>	
<b>Acknowledgments</b>	
<b>Preface</b>	
<b>Declaration</b>	
<b>List of Figures</b>	
<b>List of Tables</b>	
<b>Nomenclature</b>	
<b>Abbreviations</b>	

<b>Chapter One</b>	<b>Introduction</b>	1
1.1	General introduction .....	2
1.2	International historical perspective of patents.....	3
1.2.1	British efforts.....	3
1.2.2	French efforts.....	4
1.2.3	German efforts.....	4
1.2.4	USA efforts.....	5
1.3	Gas turbine cooling method.....	7
1.3.1	Convection cooling method.....	7
1.3.2	Impingement cooling method.....	7
1.3.3	Film cooling method.....	8
1.3.4	Transpiration cooling method.....	9
1.4	Technology of cooling blades in a gas turbine.....	9
1.5	Aim of the research.....	11
1.6	Objective of the research.....	11
1.7	Motivation of the research.....	12
<b>Chapter Two</b>	<b>Literature Review</b>	15
2.1	Introduction.....	16
2.2	Fluid flow analysis .....	16
2.2.1	Wall bounded turbulence.....	17
2.2.2	Aerodynamics of gas turbines.....	19
2.3	Heat transfer and film cooling studies.....	22
2.3.1	Flat and curved plates.....	22
2.3.2	Gas turbine film cooling.....	27
2.4	Methodology.....	34
<b>Chapter Three</b>	<b>Introduction to Computational Fluid Dynamics (CFD) &amp; Numerical Equations</b>	37
3.1	Introduction.....	38
3.2	Mathematical model of the fluid flow.....	38
3.2.1	Navier –Stokes equation.....	38
3.3	Solution procedure.....	39
3.3.1	Finite volume method.....	40
3.3.2	Special discretization.....	41
3.4	Flow models	42
3.4.1	Reynolds average Navier –Stokes (RANS) equation...	43
3.4.2	k- $\epsilon$ Turbulent flow equation.....	44
3.4.3	Wall Treatment .....	46
•	Standard Wall Function approach (SWF).....	47
•	Enhancement Wall Treatment (EWT).....	47

3.5	CFD simulation procedure in FLUENT.....	48
3.6	FLUENT solver technologies.....	51
3.6.1	FLUENT solution algorithms.....	52
	• Segregated solver.....	52
	• Coupled solver.....	54
3.7	Summary.....	55
<b>Chapter Four</b>	<b><i>(Aerodynamic CFD Validation) Channel flow &amp; NACA 0012 Modeling &amp; Results</i></b>	56
4.1	Introduction.....	57
4.2	Benchmarking geometry, mesh and boundary condition	58
4.2.1	Turbulent channel flow.....	58
4.2.2	NACA0012 airfoil flow.....	59
4.3	Aerodynamic CFD validation results.....	60
4.3.1	Fully developed channel flow.....	60
4.3.2	NACA0012 airfoil turbulent flow.....	68
4.4	Summary.....	72
<b>Chapter Five</b>	<b><i>(Heat Transfer CFD Validation) Flat Plate Cooling Modeling &amp; Results</i></b>	74
5.1	Introduction.....	75
5.2	Film cooling for a flat plate case (solid and shell).....	75
5.2.1	Single film cooling hole.....	75
	• Geometry, mesh and boundary conditions.....	75
	• Validation of heat transfer CFD results.....	76
5.2.2	Two rows of film cooling holes .....	80
	• Geometry, mesh and boundary conditions.....	80
	• Validation of heat transfer CFD results.....	82
5.2.3	Film cooling holes arrangement.....	90
	• Geometry, mesh and boundary conditions.....	90
	• Validation of heat transfer CFD results.....	91
5.3	Summary.....	101
<b>Chapter Six</b>	<b><i>Blade Gas Turbine CFD Modeling &amp; Results</i></b>	102
6.1	Introduction.....	103
6.2	Essential independent turbine geometric parameters.....	103
6.3	Gas turbine blade and film cooling physical domain.....	107
6.4	Creating the computational domain.....	110
6.4.1	Blade meshing.....	112
6.4.2	Mesh independent solution.....	113
6.5	Boundary conditions.....	115
6.6	Selecting solver, equation and solution convergence....	117
6.7	Gas turbine results.....	119
6.7.1	Effect of blowing ratio.....	119
6.7.2	Effect of coolant temperature.....	128
6.7.3	Effect of injection angle.....	130
6.7.4	Effect of hole numbers.....	132
6.7.5	Effect of hole diameter.....	135

6.8	Pressure coefficient and velocity vector for 3-D skewed blade.....	137
6.9	Summary.....	140
<b>Chapter Seven</b>	<b><i>Experimental Modeling, Preparation &amp; Results</i></b>	143
7.1	Introduction.....	144
7.2	Gas turbine blade geometry.....	144
7.3	Gas turbine blade specimen manufacturing process.....	146
7.3.1	Laser sintering technology.....	146
7.3.2	Process of direct metal laser sintering (DMLS).....	147
7.3.3	Direct metal 20 description, application.....	148
7.4	Experimental equipments.....	149
7.4.1	K-type thermocouples.....	150
	• Thermocouple junction types.....	151
	• Grounded junction.....	151
	• Ungrounded junction.....	151
	• Exposed junctions.....	151
7.4.2	Pico USB TC-08 temperature data logger.....	152
7.4.3	Thermal paint temperature technology (TPTT).....	154
	• Types of thermal paint.....	155
	• Thermal paint temperature calibration.....	157
7.4.4	Air compressor.....	158
7.4.5	Gas turbine unit.....	158
7.4.6	Flow visualization and measurement system.....	159
	• Laser Doppler Anemometer (LDA).....	159
	• Air flow meter.....	160
7.5	Thermal wind tunnel design.....	161
7.5.1	Speed region classification.....	161
7.5.2	Tunnel geometry classification.....	161
7.5.3	Thermal wind tunnel (TWT) CFD optimization.....	162
7.5.4	Uniformity of test section air velocity.....	163
7.6	Preparation and Experimental test rig setup.....	163
7.7	Experimental test procedure.....	167
7.8	Accuracy of instrument and equipment.....	170
7.9	Experimental Results Analysis.....	171
7.9.1	Coolant fluid injected at 45 <sup>0</sup> degree.....	171
7.9.2	Coolant fluid injected at 60 <sup>0</sup> degree.....	178
7.9.3	Coolant fluid injected at 35 <sup>0</sup> degree.....	181
7.9.4	Thermal paint sensitivity for different angle of injection.....	183
7.10	Experimental and numerical validation .....	185
7.11	Summary.....	186
<b>Chapter nine</b>	<b><i>Conclusion and Recommendations</i></b>	188
8.1	Conclusions.....	189
8.2	Future Work.....	193
	<b><i>Reference</i></b>	194
<b>Appendix A</b>	Continuity equation, momentum equation and energy equation derivatives.....	211
<b>Appendix B</b>	Gas turbine geometric program (copied on CD)	

## List of Figure

Figure (1-1)	Components of gas turbine engine [Lu (2007)] .....	2
Figure (1-2)	Rolls Royce turbojet engine [Norman and Zimmerman (1948)].....	3
Figure (1-3)	Rolls Royce AVON Turbojet Engine, [Rolls Royce online (2008)].....	4
Figure (1-4)	Gas turbine thermodynamics [Brooks (2008)].....	5
Figure (1-5)	Theoretical variation of specific fuel consumption and specific thrust for a real engine with compressor pressure ratio and <i>TET</i> [Sargison (2001)].....	6
Figure (1-6)	Blade configurations for the convection cooling technique [Bathie (1995)].....	7
Figure (1-7)	General impingement cooling technique [Boyce (2002)].....	8
Figure (1-8)	Blade film-cooling [Bredberg (2002)].....	8
Figure (1-9)	Transpiration cooling method [Bathie (1995)].....	9
Figure (2-1)	Schematic of channel geometry.....	17
Figure (2-2)	Schematic representation of secondary flow and end-wall boundary layers [Kassim <i>et al.</i> (2007)].....	20
Figure (2-3)	Schematic of the solid plane plate with the heater-foil, the coolant injection, cooling holes, the main gas flow, and some relevant physical quantities [Vogel and Graf (2003)].....	22
Figure (2-4)	Research methodology and structure.....	36
Figure (3-1)	Cell center control volume for finite volume method A) structured mesh B) unstructured mesh.....	41
Figure (3-2)	Turbulent boundary layer universal velocity profile [Kravchenko <i>et al.</i> (1996)].....	47
Figure (3-3)	FLUENT simulation structure [FLUENT (2006B)].....	49
Figure (3-4)	Two dimensional and three dimensional cell type [FLUENT (2006A)].....	50
Figure (3-5)	Pressure based segregated algorithm [FLUENT(2006B)].....	53
Figure (3-6)	Coupled solver method [FLUENT(2006B)].....	54
Figure (4-1)	Fully developed turbulent channel flow for A) Triangular Mesh B) Quad Mesh [Daud <i>et al.</i> (2011A)].....	59
Figure (4-2)	NACA 0012 airfoil domain and Mesh [Daud <i>et al.</i> (2011A)].....	60
Figure (4-3)	Mean velocity profile: Mesh type effects for fully developed channel flow [Daud <i>et al.</i> (2011A)].....	61
Figure (4-4)	Mean velocity profile: Mesh type effects for fully developed channel flow [Daud <i>et al.</i> (2011A)].....	61
Figure (4-5)	Mean velocity profile: Mesh refinement effects for different number of cells compared with DNS of Moser <i>et al.</i> (1999) at $Re_\tau = 590$ [Daud <i>et al.</i> (2011A)].....	63
Figure (4-6)	Kinetic energy for different number of cells compared with DNS of Moser <i>et al.</i> (1999) at $Re_\tau = 590$ [Daud <i>et al.</i> (2011A)]...	63
Figure (4-7)	Mean velocity profiles: Effects of different turbulent model compared with DNS method Moser <i>et al.</i> (1999) at $Re_\tau = 590$ [Daud <i>et al.</i> 2011].....	65

Figure (4-8)	Mean velocity profiles: Mesh quality effects with and without boundary layer mesh (800, 820, 798, and 36 cells) [Daud <i>et al</i> (2011A)].....	65
Figure (4-9)	Mean velocity profiles: Effects of Reynolds number ( $Re_\tau= 590, 2320$ ) [Daud <i>et al.</i> (2011A)].....	67
Figure (4-10)	Velocity gradients: Effects of Reynolds number ( $Re_\tau= 590, 2320$ ) [Daud <i>et al.</i> (2011A)].....	68
Figure (4-11)	Static pressure distribution for the Reynolds numbers $Re= 4*10^5$ compared with Sagrado (2007). [Daud <i>et al.</i> (2011A)]..	69
Figure (4-12)	Mean velocity profiles at $X/C_x=0.55$ : different wall function effects (EWT and SWF). [Daud <i>et al.</i> (2011A)].....	69
Figure (4-13)	Mean velocity profiles at $X/C_x=0.55$ for $k-\epsilon$ , RNG, and $k-\omega$ turbulent models. [Daud <i>et al.</i> (2011A)].....	70
Figure (4-14)	Kinetic energy ( $K^+$ ) at $X/C_x=0.55$ for $k-\epsilon$ , RNG and SST $k-\omega$ turbulent models. [Daud <i>et al.</i> (2011A)].....	70
Figure (4-15)	Numerical velocity at $X/C_x=0.55$ for $k-\epsilon$ , RNG and SST $k-\omega$ turbulent models normalized with inlet velocity $U_\infty$ compared with Sagrado (2007). [Daud <i>et al.</i> (2011A)].....	71
Figure (4-16)	Numerical velocity at $X/C_x=0.96$ for $k-\epsilon$ , RNG and SST $k-\omega$ turbulence models normalized with inlet velocity, $U_\infty$ compared with Sagrado (2007). [Daud <i>et al.</i> (2011A)].....	72
Figure (5-1)	Geometry and computational model [Liu <i>et al.</i> 2008, Sinha <i>et al.</i> 1999].....	76
Figure (5-2)	Static temperature contour of the single hole at BR = 0.5 (a) the whole view, (b) zoom in [Daud <i>et al.</i> (2012) impressed in Chanada].....	78
Figure (5-3)	Local film cooling effectiveness for single hole at BR = 0.5; comparison with the numerical/experimental results of Liu <i>et al.</i> (2008) and Sinha (1999).....	78
Figure (5-4)	Geometry and arrangements of cooling holes along streamwise direction Yuen and Martinz-Botas (2005)].....	80
Figure (5-5)	Computational domain for mainstream, solid plate and coolant holes and mesh generation.....	81
Figure (5-6)	Film cooling effectiveness trajectory along the plate through the hole centerline at BR=0.5; A) Material thermal property effects; B) Solid and shell plate effects [Daud <i>et al.</i> (2012)].....	83
Figure (5-7)	Static temperature contour through the holes centerline at BR = 0.5 [Daud <i>et al.</i> (2012)] .....	84
Figure (5-8)	The effectiveness cooling distribution contour at different location for $X/D=0, 1, 3$ and 6 at BR = 0.5 [Daud <i>et al.</i> (2012)].....	85
Figure (5-9)	Effect of blowing ratio on the film cooling effectiveness distribution (BR = 0.5 and 1) [Daud <i>et al.</i> (2012)].....	86
Figure (5-10)	Streamwise velocity profiles at different location $X/D=0, 1, 3$ and 6 at BR= 0.5 and 1 [Daud <i>et al.</i> (2012)].....	87
Figure (5-11)	Mid of plate section velocity vector normalized by inlet velocity at BR = 0.5 and 1 [Daud <i>et al.</i> (2012)].....	87
Figure (5-12)	Local Nusselt number cooling distribution along the blade A)	

	Material thermal property effects, B) Blowing ratio effects. [Daud <i>et al.</i> (2012) impressed in Canada].....	89
Figure (5-13)	Geometry and arrangements of cooling holes along the streamwise direction [Yuen and Martinz-Botas (2005)].....	90
Figure (5-14)	The cooling effectiveness contour for the single row and double row of holes, P/D= 6 at BR = 0.5 with zooming section [Daud <i>et al.</i> (2011B)].....	92
Figure (5-15)	Spanwise distribution of local film cooling effectiveness at X/D=1, 3, 6 and 10 for the solid steel plate for single and double row at P/D= 6 with BR = 0.5[Daud <i>et al.</i> (2011B)].....	93
Figure (5-16)	Local film cooling effectiveness along streamwise compared with experimental [Yuen and Martinz-Botas (2005)] for P/D=6 at BR = 0.5 and 1[Daud <i>et al.</i> (2011B)].....	94
Figure (5-17)	The static temperature contour for coolant mainstream fluid, hot jet flow and steel plate at X/D=1 for BR=0.5 and 1[Daud <i>et al.</i> (2011B)].....	95
Figure (5-18)	Local film cooling effectiveness along streamwise compared with experimental Yuen and Martinz-Botas (2005) for P/D=3 at BR = 0.5 and 1 [Daud <i>et al.</i> (2011B)].....	96
Figure (5-19)	Film cooling effectiveness trajectory along the plate through the hole centerline for Solid and shell plate at BR=0.5. [Daud <i>et al.</i> (2011B)].....	97
Figure (5-20)	Film cooling effectiveness trajectory along the plate through the hole centerline; A) Material thermal property effects at BR=0.5; B) Effect of blowing increases from BR = 0.5 to 1. [Daud <i>et al.</i> (2011B)].....	97
Figure (5-21)	Local Nusselt number cooling distribution along the plate A) Material thermal property effects at BR=0.5; B) Effect of blowing increases from BR = 0.5 to 1. [Daud <i>et al.</i> (2011B)].	100
Figure (6-1)	The five key points and five surfaces function [Pritchard (1985)].....	104
Figure (6-2)	Leading edge and trailing edge tangency points [Pritchard (1985)].....	105
Figure (6-3)	Types of gas turbine blade geometry generated off Pritchard's program [Pritchard (1985)].....	107
Figure (6-4)	Series of rotating turbine blades.[Coulthard (2005)].....	108
Figure (6-5)	Actual blade model.....	109
Figure (6-6)	Computer Aided Measuring Machine (CMM).....	110
Figure (6-7)	Assembly of gas turbine blade geometric model.....	110
Figure (6-8)	Blade geometric model.....	111
Figure (6-9)	Holes geometric model.....	111
Figure (6-10)	Flow diagram of exploring process starts from CMM to FLUENT data results.....	112
Figure (6-11)	Local mesh of blade model as a solid body with cooling holes system[Daud <i>et al.</i> (2011C)].....	113
Figure (6-12)	Multi block technique at meshing whole flow simulation box with blade model and holes film cooling.....	113
Figure (6-13)	Mesh refinement solution strategy for temperature, pressure and velocity along the blade surface as gradient variables.....	115
Figure (6-14)	Boundary condition operations for blade, holes and simulation box volumes in GAMBIT.....	116

Figure (6-15)	Predicted counters temperatures of the blade model at different blowing ratio A) BR=1, B) BR=1.5, C) BR=2 [Daud <i>et al.</i> (2011C)].....	120
Figure (6-16)	Temperature and the Effectiveness cooling distributions difference in hub, mid and shroud area on the blade model by injecting coolant air at BR=2 [Daud <i>et al.</i> (2011C)].....	122
Figure (6-17)	Effects of blowing ratio (BR) on the blade effectiveness cooling- A) hub, B) mid and C) shroud [Daud <i>et al.</i> (2011C)]...	124
Figure (6-18)	Film cooling effectiveness contour at blowing ratio BR= 2 on the blade model [Daud <i>et al.</i> (2011C)].....	125
Figure (6-19)	Distributions of film cooling effectiveness at blowing ratio BR=1 at angle of injection 35 <sup>0</sup> : comparison between CFD results of Burdet <i>et al</i> (2007), the blade model calculation [Daud <i>et al.</i> (2011C)].....	125
Figure (6-20)	Predicted profile of Nusselt number (Nu) at midspan for BR=1, 1.5, 2 [Daud <i>et al.</i> (2011C)].....	126
Figure (6-21)	Nusselt number (Nu) counter on the blade model for BR=2 [Daud <i>et al.</i> (2011C)].....	127
Figure (6-22)	Effects of coolant fluid temperature on the film cooling effectiveness at BR=1, 1.5.....	129
Figure (6-23)	Effects of coolant fluid temperature on the temperature distribution BR=1.5 at 35 angle of injection.....	130
Figure (6-24)	Effects angle of injection at mid area with different (BR) on the blade effectiveness cooling.....	131
Figure (6-25)	Effects of injection angle on gas turbine temperature distribution at blowing ratio BR=1.....	132
Figure (6-26)	Cooling effectiveness trajectory at B R=1.5 for hub, mid and shroud area effected by number of holes.....	134
Figure (6-27)	Effects of holes number on gas turbine temperature distribution at blowing ratio BR=1.5 with angle of injection 45 <sup>0</sup> .....	135
Figure (6-28)	Cooling effectiveness trajectory at B R=2 for hub, mid and shroud area effected by holes diameter.....	136
Figure (6-29)	Effects of holes diameter on gas turbine temperature distribution at blowing ratio BR=2 with angle of injection 45 <sup>0</sup> ...	137
Figure (6-30)	Pressure coefficient distribution for gas turbine blade with 45 <sup>0</sup> angle of injection at BR <sup>0</sup> =2.....	138
Figure (6-31)	Velocity vector for gas turbine blade with 45 <sup>0</sup> angle of injection at BR <sup>0</sup> =2 for A) Hub B) Mid C) Shroud.....	139
Figure (7-1)	Gas turbine blade specimen model dimension and cooling holes position with projection side views.....	145
Figure (7-2)	EOSINT M 280 direct metal laser sintering machine [BMT, online].....	146
Figure (7-3)	A schematic diagram of the EOS machine [Custompartnet, online].....	147
Figure (7-4)	Gas turbine specimen fabricated in EOSINT M 250 X tended systems.....	149
Figure (7-5)	K-type thermocouples operation principle [Pico, online].....	150
Figure (7-6)	Thermocouple probe junction types, (A) grounded, (B) ungrounded and (C) exposed [Eutechinst, online].....	152

Figure (7-7)	K-type stainless steel thermocouple probe at 0.5 mm diameter with miniature plug.....	152
Figure (7-8)	Pico TC-08 data logger device.....	153
Figure (7-9)	Calibration process for cooper pipe with furnace and KN 5 coupon calibration.....	157
Figure (7-10)	Air compressor device.....	158
Figure (7-11)	Panel board for gas turbine unit.....	159
Figure (7-12)	Laser Doppler Anemometer (LDA) system principle [Dantec, online].....	160
Figure (7-13)	Rotameter airflow meter type.....	160
Figure (7-14)	Thermal wind turbine (TWT) designed in pro/Engineer Wildfire (CAE) package.....	162
Figure (7-15)	Pressure and velocity contour for additional parts of TWT.....	162
Figure (7-16)	Full Thermal wind Tunnel (TWT) manufactured design.....	163
Figure (7-17)	Preparation process steps to finalize TWT.....	164
Figure (7-18)	Thermocouples (K type) concealed in gas turbine blade.....	165
Figure (7-19)	Illustrates gas turbine blade coated by thermal paint (KN5) and thermal paint on vibrator machine.....	166
Figure (7-20)	Setup process of thermal wind tunnel, fixed gas turbine specimen in test section, inserting thermocouples, coolant air supplier and calibrates levels to be horizontal.....	167
Figure (7-21)	Schematic of film cooling test rig and data acquisition system...	167
Figure (7-22)	Experimental measurements of mainstream velocity at the inlet of test section utilizing by LDA.....	169
Figure (7-23)	Process of scaling thermal paint from blade specimen using Chloroform solvent and 30% of Nitric acid.....	169
Figure (7-24)	Percentage error bar for inlet and outlet test section temperature measurements point at thermocouple (1) against time.....	171
Figure (7-25)	Inlet and outlet test section temperature with five core blade temperature against time.....	172
Figure (7-26)	Effects of $V^0$ on film cooling effectiveness at A) measurement point (1) and B) measurement point (2).....	174
Figure (7-27)	Average of film cooling effectiveness for the last 30 <sup>th</sup> point of measured temperature for each location at holes angle of injection 45 <sup>0</sup> for A) $V^0=1000$ , $V^0=800$ and $V^0=600$ (cm <sup>3</sup> /min).....	176
Figure (7-28)	Blade surface temperature distribution patterns coloured by thermal paint with $V^0= 1000, 800, 600$ (cm <sup>3</sup> /min).....	178
Figure (7-29)	A) Transient temperature thermocouple measurements at $V^0=1000$ cm <sup>3</sup> /min, B) Temperature difference between pressure side and suction side.....	179
Figure (7-30)	A) Effect of varying BR on film cooling effectiveness against time for holes angle of injection 60 <sup>0</sup> B) Average film cooling effectiveness measurements along the blade at the mid region $V^0=1000$ cm <sup>3</sup> /min.....	181
Figure (7-31)	A) Transient temperature thermocouple measurements at $V^0=1000$ cm <sup>3</sup> /min, B) Temperature difference between pressure side and suction side.....	182
Figure (7-32)	Average film cooling effectiveness measurements along the blade for holes angle of injection 35 <sup>0</sup> at the mid region $V^0=1000$ cm <sup>3</sup> /min.....	183

Figure (7-33)	Blade surface temperature distribution patterns coloured by thermal paint for holes injection at $45^{\circ}$ , $35^{\circ}$ and $60^{\circ}$ at $V^0=1000(\text{cm}^3/\text{min})$ .....	184
Figure (7-34)	Temperature comparison between numerical and experimental data for holes angle of injection $45^{\circ}$ along the blade with A) $V^0=1000 (\text{cm}^3/\text{min})$ B) $V^0=800 (\text{cm}^3/\text{min})$ . ....	186

## List of Table

Table 3-1	GAMBIT face meshing element options [FLUENT(2006A)].....	50
Table 3-2	GAMBIT face meshing type options [FLUENT(2006A)].....	50
Table 4-1	The values of numerical and defined shear velocity at $Re_t=590$ .....	67
Table 4-2	The values of numerical and defined shear velocity at $Re_t=2320$ ...	67
Table 5-1	Comparison of CFD data, experimental data and previous numerical data at $X/D=3$ .....	79
Table 5-2	Comparison of CFD data, experimental data Sinha (1999) and previous numerical data Liu <i>et al.</i> (2008) at $X/D=6$ .....	79
Table 5-3	Solid plate material properties.....	81
Table 5-4	Solid plate material properties.....	91
Table 5-5	Nnumber of cells for each numerical simulation (single hole, two row of hole and holes arrangement) at solid and shell case with consuming time.....	101
Table 6-1	Application of boundary conditions.....	116
Table 6-2	Inlet hot gas and cooled air applied to FLUENT software.....	117
Table 6-3	The average film cooling effectiveness values at the mid area on pressure side gas turbine blade.....	141
Table 6-4	Computational time with number of cells for 3 D skewed gas turbine blade simulations at different angle of injection $35^0$ , $45^0$ and $60^0$ respectively.....	142
Table 7-1	Material property of direct metal 20[EOS (2004)].....	148
Table 7-2	Common thermocouple temperature ranges [Omega,online].....	151
Table 7-3	Lists the specification of the TC-08 data logger [Pico online].....	153
Table 7-4	Single change paints sorts [TPTT].....	156
Table 7-5	Multi-change paints sorts [TPTT].....	156
Table 7-6	Temperature and colour density for each color transition. [TPTT].	157
Table 7-7	Experimental test boundary conditions .....	170
Table 7-8	Percentage error of measurement equipment.....	170
Table 7-9	Average temperature values and difference .....	173
Table 7-10	Film cooling effectiveness values for each $V^0$ at the last 30 <sup>th</sup> point.....	176
Table 7-11	Average thermocouple temperature for all $V^0$ . and both sides.....	180
Table 7-12	Average thermocouple temperature difference for all $V^0$ . and both sides.....	182

## Nomenclature

$A$	Projected area of the cell
$BR$	Blowing ratio, $BR = \rho_c * V_c / \rho_\infty * V_\infty$
$CP$	Static pressure coefficient distribution, equation (4-7)
$C_p, (C_p)_s$	Specific heat the for the fluid flow, solid body
$C_x$	the blade axial chord (mm)
$C_y$	the blade width (mm)
$C_z$	the blade spanwise (mm)
$D$	Film hole diameter (mm)
$D_h$	Hydraulic diameter (mm) in equation (6-2)
$G_b$	general turbulence kinetic energy due to buoyancy
$G_k$	general turbulence kinetic energy due to the mean velocity gradients
$H$	channel width (m)
$k$	turbulence kinetic energy ( $m^2/s^2$ )
$K, K_s$	thermal conductivity for fluid flow, solid body (W/m-K)
$K^+$	dimensionless turbulent kinetic energy based on $u_\tau$ , equation (4-2)
$K_{Local}$	local kinetic energy, $K_{Local} = \frac{1}{y^+ \Delta y^+} \int u^+ dy^+$
$L$	length of the film hole or length of channel flow (mm)
$L$	mixing length is presumed known in turbulent viscosity
$l$	length scale (m)
$l_\epsilon$	mixing length for EWT based on turbulent rate of dissipation (m)
$l_\mu$	mixing length for EWT based on laminar viscosity (m)
$\dot{m}$	Mass flow rate (kg/sec)
$N_u$	Nusselt number
$P$	Pressure ( $N/m^2$ )
$P_{01}$	inlet total pressure. ( $N/m^2$ )
$P_s$	static pressure on the surface ( $N/m^2$ )
$P_{s2}$	outlet static pressure ( $N/m^2$ )
$Pr, Pr_t$	laminar and turbulent Prandtl number
$q^{\bullet}$	heat flux ( $W/m^2$ )
$Re$	free stream Reynolds number
$(Re_\tau)$	friction Reynolds numbers based on $u_\tau$ , $Re_\tau = (\rho * u_\tau * H) / \mu$
$R_{ij}$	Boussinesq relationship equation (3-10)
$S_{ij}$	stress tensor.(1/sec)
$T$	temperature (K)
$\Delta T$	temperature difference
$T_c$	injection film cooling temperature (K)
$T_w$	local wall temperature (K)

$T_\infty$	mainstream temperature(K)
Tu	turbulent intensity, equation (6-1)
$u_i$	averaged velocity components (m/sec)
$u^+$	dimensionless mean velocity based in the wall unit, $u^+ = u/u_\tau$
$u_\tau$	friction velocity, $u_\tau = \sqrt{\tau_w / \rho}$ (m/sec)
$V_\infty$	mainstream velocity (m/sec)
$V_c$	coolant velocity (m/sec)
X,Y,Z	Spatial coordinates (mm)
$y^+$	dimensionless distance from the wall to nearest grid cell( $y^+ = \rho u_\tau y / \mu$ )
$\rho_c, \rho_\infty$	Coolant fluid and mainstream density, (kg/m <sup>3</sup> )
$\frac{\partial}{\partial x_j} (-\rho \overline{u'_i u'_j})$	Reynolds stress (closure).
$\partial P / \partial x$	Pressure gradient
$\partial / \partial x_i$	represents the variation of parameters in X, Y and Z
$\varepsilon$	Turbulent rate of dissipation
$\mu, \mu_t$	dynamic viscosity, turbulence (or eddy) viscosity (kg/m.sec)
$\delta_{ij}$	Kronecker delta function (equal to one if $i = j$ , else zero)
$\tau_w$	wall shear stress (kg/m.sec <sup>2</sup> )
$\theta$	velocity scale (m/sec)
$\eta$	film cooling effectiveness

## Abbreviations

AoA	Angle of Attack
<i>B.C</i>	Boundary Condition
<i>B.L</i>	Boundary Layer
CFD	Computational Fluid Dynamics
CHT	Conjugate Heat Transfer
CMM	Computer Aided Measuring Machine
DES	Detached Eddy Simulation
DNS	Direct Numerical Simulation
EWT	Enhancement Wall Treatment
FVM	Finite-Volume Method
IGES	Initial Graphics Exchange Specification
IR	Infrared Thermography Method
LCT	Liquid Crystal Technique
LDA	Laser Doppler Anemometer
LDV	Laser Doppler Velocimetry
LES	Large-eddy Simulation
MRF	Micro-Riblet Film
MTU	<u>Germany's leading aircraft engine manufacturer</u>
MUSCL	Monotone Upwind Scheme for Conservation Laws
PDE	Partial Differential Equations
PIV	Particle Image Velocimetry
PS	Pressure side
PSP	Pressure Sensitive Paint
RANS	Reynolds Averaged Navier-Stokes
RNG	Re-Normalization Group RNG Model
RP	Rapid prototyping
RSM	Reynolds Stress turbulence Model
S-A	Spalart- Allmars Turbulence Models
SFC	Specific Fuel Consumption
SIMPLE	Semi-Implicit Method for Pressure Linked Equation
SS	Suction side
SST	Shear Stress Transport
ST	Specific Thrust
SWF	Standard Wall Function
TET	Turbine Entry Temperature
TLV	Two Layer Velocity Scale Model
TLVA	Anisotropic Two Layer turbulence model and DNS Based Model
TLVA- $P_r$	Anisotropic two layer turbulence model and DNS based Model of $P_r$ in the boundary layer
TPTT	Thermal Paint Temperature Technology
TWT	Thermal Wind Tunnel
VKI	Von Karman Institute, Belgium

## 1.1 General introduction

A Gas Turbine (GT) is a device used for converting thermal energy into mechanical energy in the form of reaction of the runner, under high pressure and then discharging the gas in the desired direction [Norman and Zimmerman (1948)].

As shown in Figure (1-1), a typical gas turbine engine comprises of three main components, namely the compressor, combustor and turbine [Nasir (2008)].

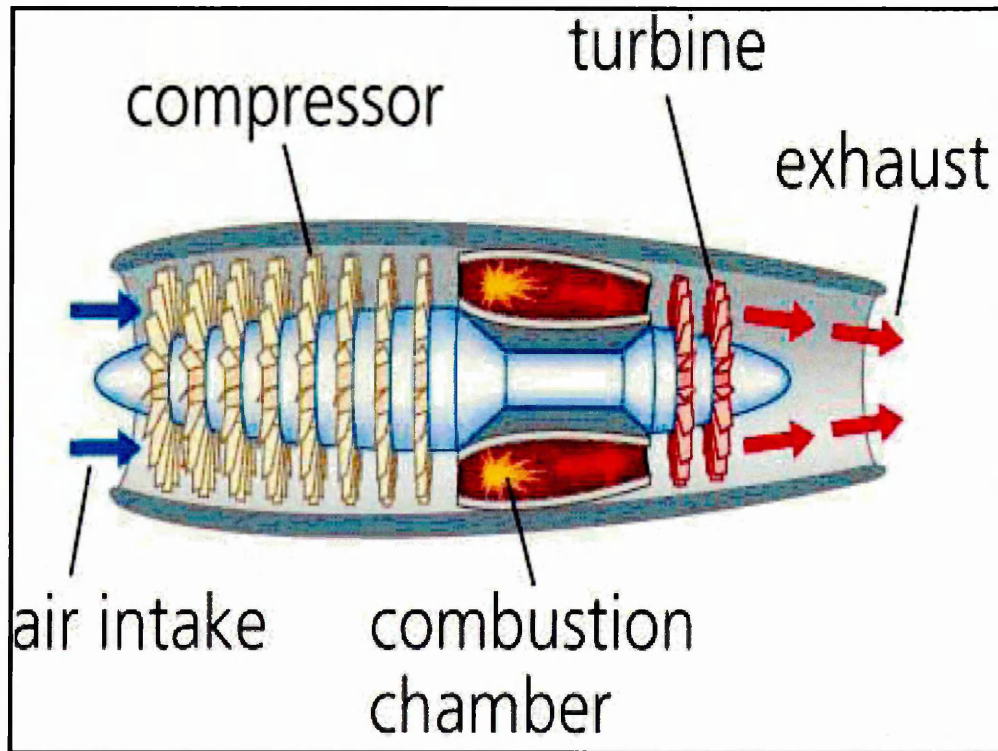


Figure (1-1) Components of gas turbine engine [Lu (2007)]

Gas turbines has been developed for a number of applications; including, electrical power generation, aircraft propulsion, industrial gas turbine engines, naval vessels propulsion and trains.

Considerable effort has been devoted to patent gas turbine engines, following the first design of a gas turbine in 1791 by John Barber. Gas turbine engineers have endeavored to improve the performance of turbines via refining their understanding of aerodynamic flow, thermal cooling effect and heat transfer in the passages of blades, using theoretical and experimental studies in two dimensions or three dimensions. For example, in 1914 impulse turbine was built experimentally in Switzerland with 1000 horsepower through

increased number of explosion chamber [Oberg and Jones (1917)]. The objective has been to enhance the overall efficiency, reduce the consumption of fuel and increase thrust in the aircraft engine. So, a brief historical review will be made of gas turbine innovations and designs

## 1.2 International historical perspective of patents

### 1.2.1 British efforts

In England, gas turbines were constructed and tested to power airplanes by two research groups. The first group, led by Frank Whittle, concentrated on the turbojet using the centrifugal flow compressor. The second group, led by Griffith at Liverpool, worked on testing and constructing the axial flow compressor. Whittle's group achieved the first patent in 1930; however this project was not accepted by the Air Force Ministry and private companies since it was deemed to be a long term research project and adequate funding was not available. However, in summer 1939 the Air Force Ministry signed a contract for the power jet. In 1936, the Griffith group in England began work with the Royal Aircraft Establishment on constructing and testing axial flow compressors. Through a series of research efforts, the UK completed the first airplane flight powered by the gas turbine in 1941, [Bathie (1995)]. Figure (2-1) illustrates the first turbo jet engine.

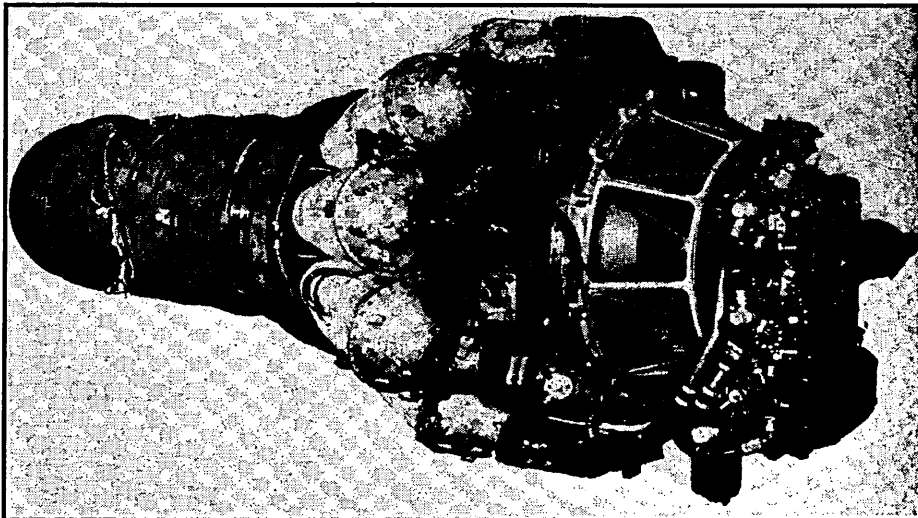


Figure (1-2) Rolls Royce turbojet engine [Norman and Zimmerman (1948)].

Since that time, competition between many companies has continued. For example Rolls-Royce and Pratt and Whitney (USA) produced several gas turbines to increase performance. Figure (1-3) shows the Avon turbojet engine, developed by Rolls- Royce.

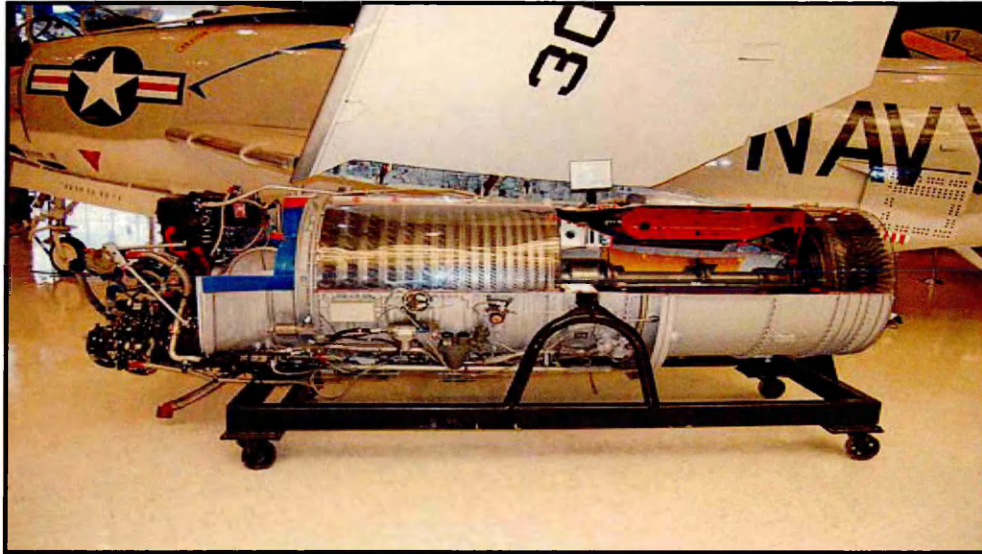


Figure (1-3) Rolls Royce AVON turbojet engine, [Rolls Royce, (2008)]

### 1.2.2 French efforts

Bresson idea was to drive pressurized air in a combustion chamber by using a fan. The air was mixed with the fuel gas and then combusted. Additional air was used to cool the combustion products before delivery to the turbine blades [Giampaolo (2006)].

### 1.2.3 German efforts

Hans von Ohain developed the gas turbine for propulsion and patented the turbojet engine with a centrifugal compressor before 1935. The first successful flight engine (after redesigning the combustion chamber) took place in 1938; using the He S-3b engine. August 27th 1939 marked the first turbojet powered flight. The second line of development during this period was achieved by Junkers Airplane Company; these efforts focused on an axial turbojet 004; Bramo was working on a more advanced axial turbojet [Bathie (1995)]. However, the competition between the Germans and the British in this field produced great progress in the performance of turbojets.

### 1.2.4 USA efforts

Historically, the National Advisory Committee for Aeronautics (NACA) used the work of S. Campini from 1930 onwards. They designed a ducted axial fan motorized by the reciprocating engine. The efficiency of turbines and the compressor was not well developed at this time. However, in 1939 Brown Boveri built the first commercial gas turbine power plant for generating power (4000 kW). In the United States in 1940, the 2500- hp turboprop engine was developed for the US Army and US Navy. Since this time, the USA has led developments in the design and building of many gas turbines, many of which are reported in the ASME Journal of Gas Turbines and Power Journal [Bathie (1995)].

However, these efforts are aims to increase the thrust, overall efficiency and reduce the fuel consumption, as much as possible, by increasing the turbine inlet temperature. (Combustor exit temperature) as illustrated in Figure (1-4).

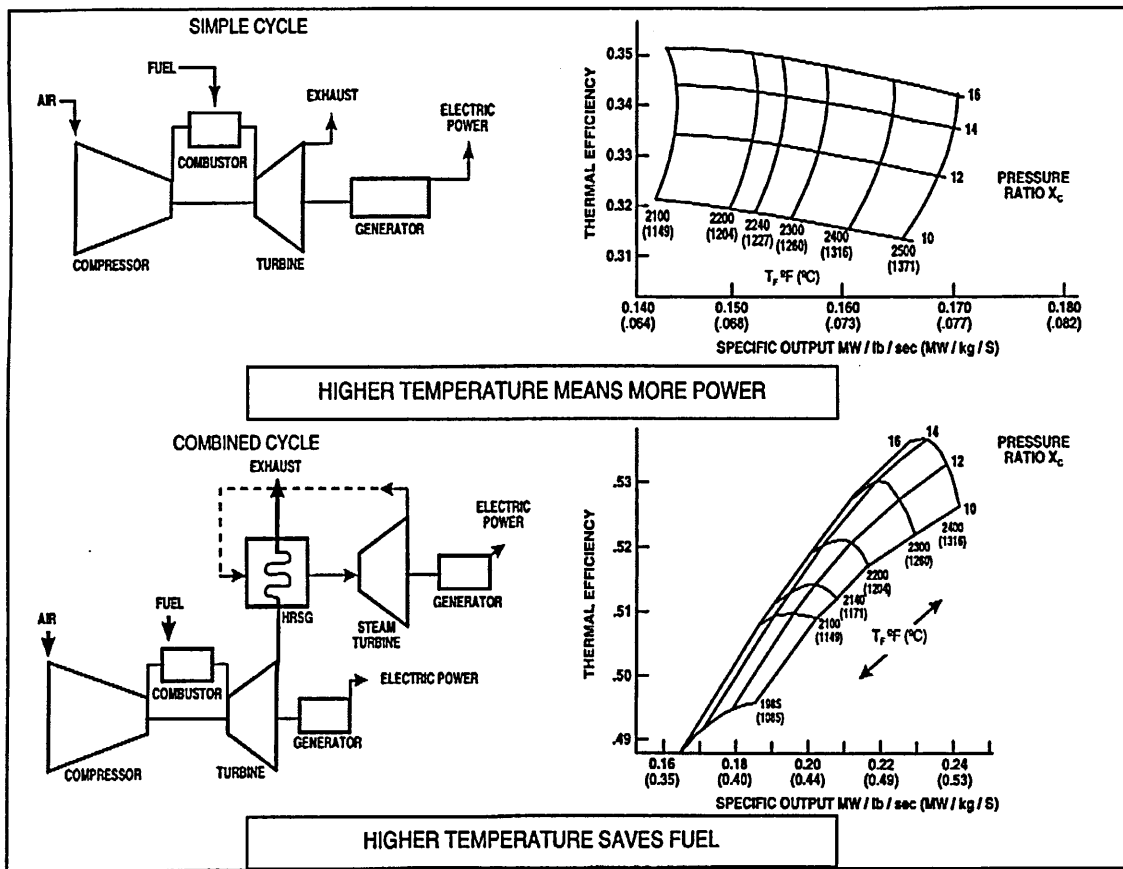


Figure (1-4) Gas turbine thermodynamics [Brooks (2008)].

Most of the previous research published documented that with an increase in the inlet temperature of the turbine, the thermal efficiency is also enhanced. Figure (1-5) which is based on the thermodynamics of the gas turbine cycle, illustrates the variation of

Specific Fuel Consumption (SFC) and furthermore Specific Thrust (ST) with Turbine Entry Temperature (TET) and compressor pressure ratio. The increase in the TET at a constant pressure ratio through a change in fuel/air ratio causes an increase in the specific work output, or specific thrust. However, this variation does not change the overall efficiency of the engine. Additionally, increasing the compressor pressure ratio (which has the effect of increasing TET at constant fuel/air ratio), causes an increase in efficiency or reduction in SFC, as result of which in any real gas turbine cycle, there is an optimum pressure ratio for SFC and specific thrust, at a particular TET [Sargison (2001)].

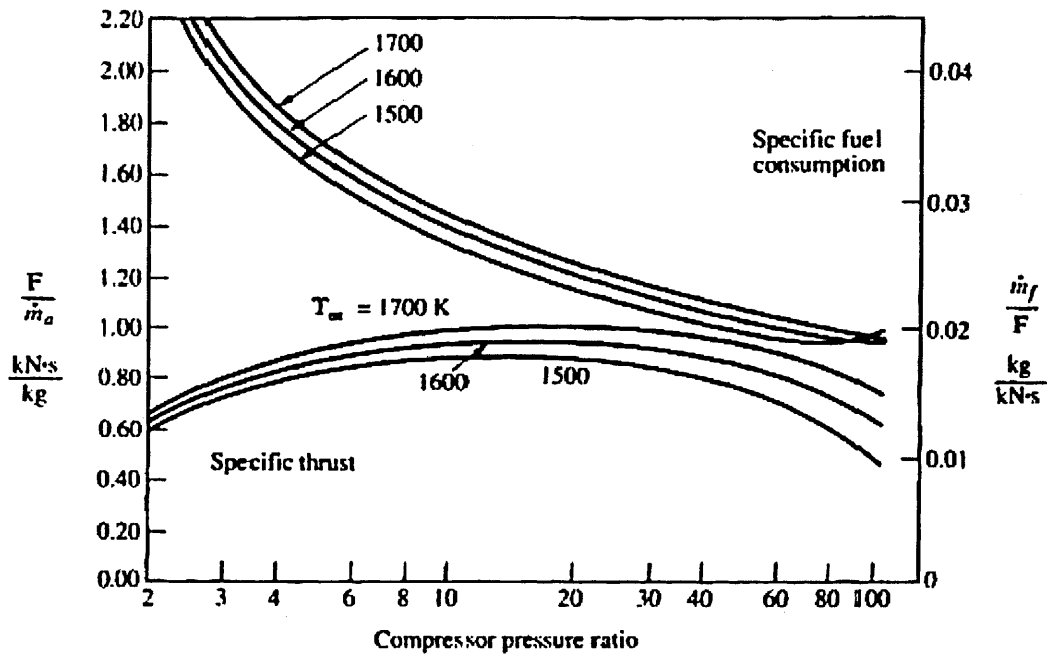


Figure (1-5) Theoretical variation of specific fuel consumption and specific thrust for a real engine with compressor pressure ratio and  $TET$  [Sargison (2001)]

Unfortunately, higher temperatures have negative effects on the integrity of high pressure turbine components and materials comprising the turbine blades [Kassim *et al.* (2007)]. Designers of gas turbines have resolved the problem of blade surface degradation and rapid failure from high inlet temperatures by using blade cooling technology. In this dissertation, numerical and experimental methods are used to examine the flow in a high-pressure gas turbine chamber in order to investigate blade film cooling.

There are four methods utilizing air as the coolant fluid for gas turbine blade cooling, which are discussed in turn, below:

## 1.3 Gas turbine cooling method

### 1.3.1 Convection Cooling Method

In this method, the coolant (air) flows outward from the base of the turbine blade to the end through internal passages within the blade [Bathie (1995)]. Figure (1-6) illustrates several passageways for the convection cooling technique. The quantity of cooling air and the size of internal passages are the greatest limitation on the cooling effectiveness of the convection method. Therefore, high velocity and internal surface areas are essential for the coolant air. An additional major disadvantage of convection cooling is that no cooling air passes through the thin trailing edge of the blade [EL-Sayed (2008)].

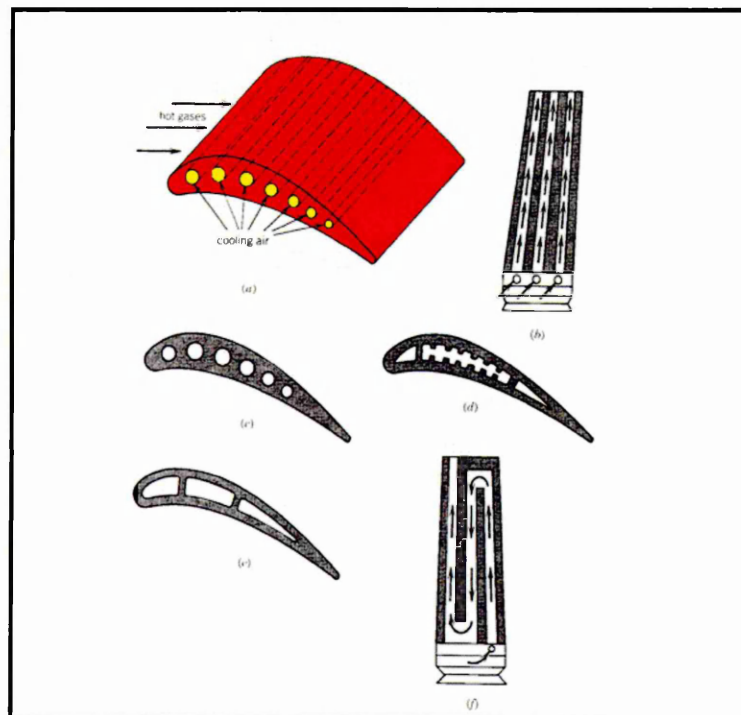


Figure (1-6) Blade configurations for the convection cooling technique [Bathie (1995)].

### 1.3.2 Impingement Cooling Method

Figure (1-7) illustrates the mechanism of the modified impingement cooling method, which is a form of convection cooling. In this method, the cooling air is blown in a radial pattern through a single centre core of the blade and then is turned normal to the radial direction through a series of holes by high velocity air jets. The blade section restricts the effectiveness of this method, so that coolant air impinges on the inside of the blade [Boyce (2002)].

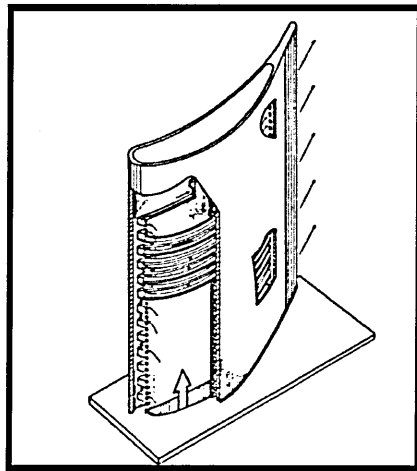


Figure (1-7) General impingement cooling technique [Boyce (2002)].

### 1.3.3 Film Cooling Method

As illustrated in Figure (1-8), the film cooling method is as an external cooling technique. It involves injection of a secondary fluid from the inside of the blade into the boundary layer of the primary hot gas through a number of holes [Peng (2007)].

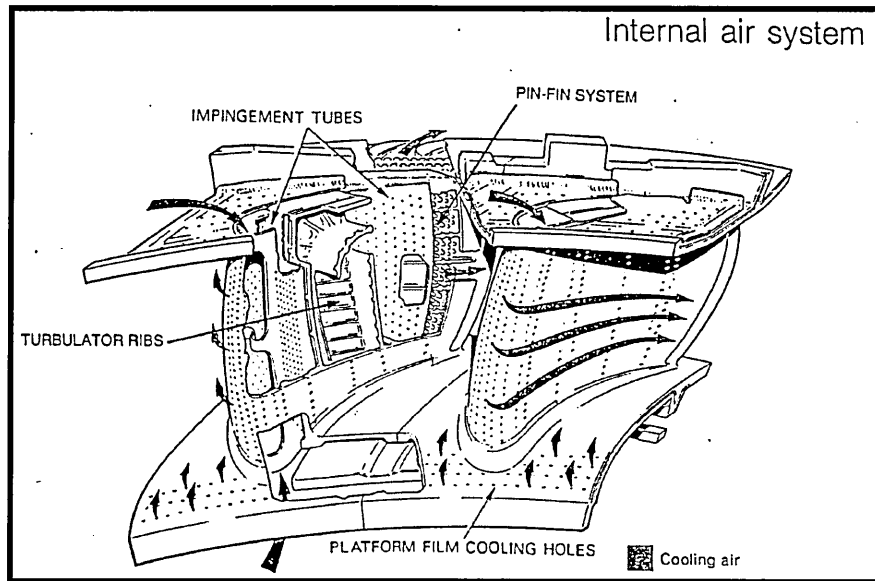


Figure (1-8) Blade film-cooling [Bredberg (2002)].

Cool air provides an effective method of protecting the gas turbine blade surface (pressure side and suction side) from the hot gases and maintains a lower blade material temperature to minimize degradation and melting effects [Bathie (1995)]. The injection of coolant air into the boundary layer reduces some of the advantages of using higher turbine inlet temperatures. If the velocity of injected air is too high, the coolant air will

penetrate the incoming flow, counter-acting the purpose of film cooling, as turbine losses will occur. However, film cooling is a more effective method than standard convection, or impingement cooling, since it does provide a protective layer along the surface of the blade.

### 1.3.4 Transpiration Cooling Method

As shown in Figure (1-9), the coolant air is blown (injected) through a porous blade surface to achieve full blade film cooling. The transpiration cooling method is effective at very high turbine inlet temperature as the pores cover the entire blade with coolant air [Boyce (2002)].

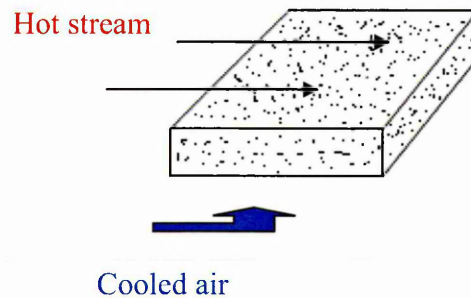
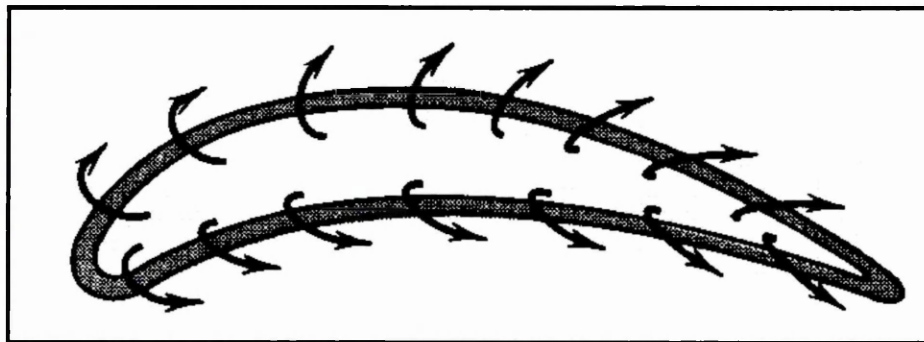


Figure (1-9) Transpiration cooling method [Bathie (1995)].

## 1.4 Technology of cooling blades in a gas turbine

The durability of gas turbine engines is strongly dependent on the component temperatures. Film cooling blade technology is instrumental in designing turbines to reduce component temperature. New technologies of cooling turbines are developing to maximize protection from high temperature especially for turbine airfoils and endwalls.

The phenomenon of jet-in crossflow (coolant fluid) which is a characteristics of film cooling, results in mixing in shear layer which reduces the surface temperature of the blade i.e. enhance the film cooling effectiveness [Bogard and Thole (2006)]. Hence, characterization of the gas flow and heat transfer through a modern turbine are important engineering considerations, as they which represent very complex flow fields and high turbulence levels. In the first stage of turbine blade design, it is crucial to reduce the over-heating effect on the blade surface. A disadvantage of this technique is a source of loss in the overall power output since coolant fluid has to be extracted from the compressor. Approximately 20-25% of compressed air bleeds to the cooling system [Ekkad *et al.* (2006)]. Despite this, the benefits in reduced SFC and increased specific power output which follow from an increase in permissible TET (combined with an increase in compressor pressure ratio) are still substantial when the additional losses introduced by the cooling system are taken into account [Sargison (2001)]. Therefore, optimum cooling technology can be influenced by the following parameters:

- A). Selection of a method to protect gas turbine elements from thermal overheating by using an air efficient cooling system which may be either internal cooling (convection cooling system or impingement cooling system) or external cooling (film cooling system or transpiration cooling system)[EL-Sayed (2008)].
- B). Selection of a suitable coolant fluid (water or air).
- C). The degree of cooling air (characterized by mass flux ratio which is simulated by a Blowing Ratio (BR).

$$BR = \rho_c * V_c / \rho_\infty * V_\infty$$

Where

$\rho_c$  is a coolant fluid density, (kg/m<sup>3</sup>)

$V_c$  is a coolant velocity (m/sec)

$\rho_\infty$  is a mainstream density, (kg/m<sup>3</sup>)

$V_\infty$  is a mainstream velocity (m/sec)

- D). The injection angle (lateral injection, stream-wise inclined and span-wise).
- E). The discharge geometry (number of holes, diameter of the holes and row of holes).

As mentioned in previous paragraph, many of cooling methods were employed in gas turbine. Therefore, this research have been used film cooling method as a way of protection from incoming hot gas in addition to select the air as a coolant fluid to increase blade life time by reducing blade surface degradation. Hence, the aim of this

research will be concerned with performance of gas turbine through study aerodynamic and heat transfer numerically and experimentally. Different parameters i.e. effects blowing ratio, cooling temperature, angle of injection, number of holes and holes diameter are mainly interest with the optimum performance of gas turbine blade.

## **1.5 Aim of the research**

This research is mainly concerned with the performance of gas turbines. Numerical and experimental methods are used to examine the flow in a gas turbine chamber in order to investigate blade film cooling. Aerodynamic flow and heat transfer rates are computed using numerical and experimental methods. The optimization process examines film cooling blade design (blowing ratio, angle of injection). Moreover, channel flow, NACA 0012 airfoil and flat plate were used to investigate the performance of FLUENT code solver through explain the restrictions in fundamental turbulent flow simulations and mesh generation. The research will calculate pressure drop, Nusselt number and cooling effectiveness at three key locations and show effect of cross section area variation in gas turbine blade on film cooling performance, namely the hub, mid and shroud.

## **1.6 Objectives of the research**

To aim of this research is to investigate the film cooling performance in a realistic 3-D skewed gas turbine blade model using the Fluent 6.3 CFD software. This begins with understanding flow structures and the validating the commercial code by selecting two different benchmarks, namely fully-developed channel flow as a simple geometry and the NACA 0012 airfoil as a more complex case, involving a curved boundary. Next, the research examines the performance of jet cross-flow on a simple flat plate geometry via studying different parameter effects (blowing ratio, angle of injection, material properties etc) in order to further establish confidence in the CFD code, which is fundamental for subsequent numerical simulation of a real 3-D gas turbine blade. Fluent simulations of a 3-D skewed blade are then conducted and verified

experimentally with a Thermal Wind Tunnel (TWT). Therefore, the main objectives of the present thesis are:

1. Validation of numerical calculations inside channel flow and above a NACA 0012 airfoil using FLUENT code with available numerical and experimental published data.
2. Verification of the amount of heat transfer and film cooling for a flat plate surface simulated as a solid and shell. The simultaneous calculation of conduction and convection is called Conjugate Heat Transfer (CHT). The conjugate approach involves time-consuming computation as the number of grid points increase as both fluid and solid domain have to be taken into consideration [Kane and Yavuzkurt (2009)]
3. Identification of useful parameters to satisfy high film cooling effectiveness on gas turbine blades with FLUENT simulation. This involves:
  - A) Generation of a Cartesian-coordinate based geometric model of a gas turbine blade geometry at the three main areas (hub, mid and shroud), using the pre-processor (generating the meshing using GAMBIT tool). A size function tool will be used to control the model meshes by creating a regular size of mesh intervals for edges, elements, faces and volumes [FLUENT (2006A)].
  - B) Application of the FLUENT Computational Fluid Dynamics (CFD) software to simulate fluid flow and heat transfer in the turbine geometry.
4. Validation of numerical results using published data and previous related work
5. Conducting experiments on fabricated blade test sections and analyzing experimental results to validate numerical results.

## **1.7 Motivation of the research**

Turbulent flows are fundamental to aerospace and mechanical engineering. Wall-bounded turbulent flows are in particular important in gas turbine applications. Therefore, numerical investigations of wall-bounded turbulence have been examined robustly in this thesis, using the Fluent 6.3 CFD software. To establish confidence in the software, and prior to simulating actual gas turbine flows, we perform an extensive validation. First a simple two-dimensional fully-developed channel flow has been examined which is a popular benchmark employed in validating computational codes. Next we build on this validation by considering a more complex case involving a

curved boundary, namely the NACA 0012 airfoil, in order to explore aspects relevant to gas turbine geometries which can then be validated with experimental data. Having established confidence in the computational code, we next examine the first case of gas turbine simulation, namely flat plate film cooling with different hole arrangements and consider blowing ratio and other effects, validating the new computations with experimental results from the literature. The next stage is then to simulate the film cooling performance in a realistic 3-D skewed gas turbine blade model, and to conduct experiments for this configuration. Consequently, the motivations of this research are:

**Firstly**, to assess restrictions of the **FLUENT** code solver in fundamental (and therefore more advanced) turbulent flow simulations. The aim is to investigate the relative accuracy of three different turbulence models ( $k-\epsilon$ , RNG, SST  $k-\omega$ ) in the numerical analysis. Furthermore, this thesis will explore the strong influence of mesh refinement and mesh type near the wall and outer layer turbulence structures on the flow characteristics for the two test cases of turbulent channel flow and turbulent NACA 0012 airfoil flow.

**Secondly**, numerical predictions of film cooling effectiveness, heat transfer, temperature distribution for a flat transpiring plate, will be investigated, by focusing on:

- The mainstream (hot gas) and coolant system (cooled fluid) with differences in temperature, pressure and chemical composition for the hot gas and cooled air.
- Solid plate thermal properties which will be simulated by choosing the type of manufacturing blade material for example, steel, carbon steel (**SAE4140**), aluminum, copper, and carbon steel shell plate into the FLUENT software property specification pre-processor.

**Finally**, this study is utilizing a complex geometry for a 3-D skewed solid blade to numerically investigate film cooling effectiveness, heat transfer, temperature distribution and the effect of coolant fluid property in the hub, mid and shroud area. In addition, experimental wind tunnel blade cooling tests are conducted. Therefore, this study will present the following aspects:

- Using different cross section blade geometry (from hub to shroud) with angle of twist.

- Addressing solid body thermal properties which will be simulated by utilizing the type of blade material for example. carbon steel (SAE4140) in the FLUENT software property specification pre-processor.
- Including aerodynamic flow and heat transfer computations. Modern gas turbine constitutes a very complex flow field with high turbulence levels. Therefore film cooling is applied in this work near the leading edge of the blade. This is additionally complicated due to the resulting interference between the main flow and injected coolant.

## 2.1 Introduction

As mentioned in chapter one, the historical efforts in design and development have been aimed to increase thrust and thermal efficiency by increasing inlet temperature of gas turbines and employing efficient methods (e.g. cooling method) to protect gas turbine component by reducing blade surface degradation.

In order to accomplish the numerical and experimental study of flow in a gas turbine successfully this chapter will review gas turbine innovations, designs and recent research through a series of investigations. A discussion of the computations performed with the FLUENT code for *wall-bounded turbulent flows in a two-dimensional channel* and *boundary layer flow along a NACA airfoil* are presented which are popular benchmarks in computational fluid dynamics (CFD). Simulations of the amount of heat transfer along a flat plate using film cooling holes is a simplified model of relevance to the more geometrically complex case of jet-crossflow in 3-D skewed gas turbine blade model. Most of previous studies have concentrated on numerical and experimental analysis, namely, film cooling holes configurations and heat transfer from flat and curved plates. Fundamentally, heat transfer to turbine blades involves steady heat transfer based on mean-flow conditions, as well as unsteady heat transfer due to fluctuations in the mean flow [Nix (2003)]. For film cooling in gas turbine blades there is the additional complexity of flow around the blade (jet-cross-flow). Again, the objective of the cooling design is focused on computing the heat load to extend component life, to minimize coolant air and optimize the performance of gas turbine blades.

## 2.2 Fluid flow analysis

To provide fundamental foundation for the later work presented in this thesis, namely flat plate film cooling simulation and 3-D skewed blade film cooling, detailed numerical calculations of wall-bounded turbulent flows conducted with the FLUENT CFD code is shown. The computational studies have a number of objectives. They ensure that the mesh density near the wall region is correctly specified so that the best possible refinement is attained. They also serve to compare the relative performance of different

turbulence models (for example. k-epsilon, K-omega), thereby demonstrating the best models for implementation in terms of accuracy and compilation times.

### 2.2.1 Wall bounded turbulence

Channel flow was selected as one of the two fundamental flow regions studied to aid in numerical simulations discussed in later chapters. This flow region is common in many branches of mechanical engineering including power generation, propulsion, materials processing, rocket chamber flows. The characteristics of flow inside channels are strongly related to the wall effects and the Reynolds number. A number of excellent studies examined such flows both numerically and experimentally. Figure (2-1) illustrates a schematic of the channel geometry studied.

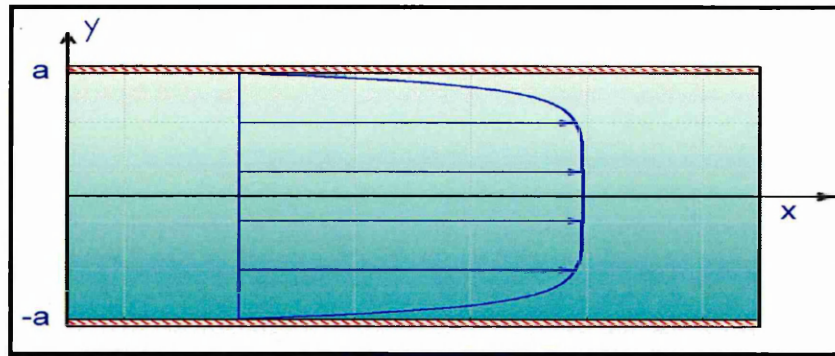


Figure (2-1) Schematic of channel geometry.

Iwamoto *et al.*(2005) presented a fully-developed turbulence channel flow study utilizing Direct Numerical Simulation (DNS) at  $Re_\tau = 2320$ , using 16 billions node points and showing that mean velocity profile results compared with earlier studies for  $Re_\tau = 650$  and  $150$ , respectively. However, this study indicated that at  $100 < y^+ < 600$ , the velocity profile in this region does not follow the logarithmic law, in addition to near wall turbulence depends on both fine-scale structure and large-scale structure ( $y^+$  is a non-dimensional distance similar to local Reynolds number, often used in CFD to describe the coarseness or fineness of a mesh for a particular flow). It is the ratio between the turbulent and laminar influences in a cell [Salim and Cheah (2009)]. This study showed that the trajectory of  $K_{Local}$  (local kinetic energy) gradually declines with increasing friction Reynolds number ( $Re_\tau$ ).

$K_{Local}$  (local kinetic energy) which should equal the von Karman constant) is defined [Iwamoto *et al.*(2005)] as follows:

$$K_{\text{Local}} = \frac{1}{y^+ \kappa^2 \delta^+} / \alpha y^+ \quad (2-1)$$

Moser *et al.* (1999) conducted a DNS turbulent channel flow study, with  $Re_\tau$  (friction Reynolds number varied from 180, 390 to 590). The results suggested that the  $Re_\tau = 590$  flow simulation was at sufficiently large Reynolds number to be free of the most obvious low-Reynolds number effects. The authors obtained excellent correlation of results for the mean velocity profile up to  $y^+ \sim 200$  with the logarithmic law, for friction Reynolds number values of 590 and 390; however they identified deviation for  $Re_\tau = 180$  due to low Reynolds number effect.

Kim *et al.* (1987) performed a fully spectral DNS study for 3D incompressible turbulent channel flow at low Reynolds number ( $Re$ ) at the channel center at 3300 and the friction Reynolds number  $Re_\tau=180$ , with grid  $192*129*160$  in the x, y, z directions. The first grid point away from the wall is  $y^+ = 0.05$ . Turbulence statistics were computed and compared with the experimental data. Special attention was given to the turbulence behavior near-wall.

Daud *et al.* (2011A) investigated numerically the effects on turbulence for two important flow regions-*fully developed channel flow* and *flow past a NACA 0012 airfoil*, using commercial software - FLUENT 6.3. The solution accuracy was explored via a sensitivity study of mesh type and quality effects, employing different element types for example, quadrilateral and triangular. This work elucidated the effects of Enhancement Wall Treatment (EWT) and Standard Wall Function (SWF) on the turbulent boundary layer. Furthermore, four different turbulence models were utilized in this study, namely, S-A, k- $\epsilon$ , RNG and SSTk- $\omega$ . The numerical solutions were compared with available DNS results by Moser *et al.* (1999) and experimental data by Sagrado (2007). Good correlation was achieved. In addition, the statistical turbulence results related to the RNG turbulence model were shown to yield much closer correlation with DNS and experimental data. The effect of Reynolds number ( $Re_\tau = 590$  and  $Re_\tau = 2320$ ) were studied for the channel flow region and the near wall resolution examined in detail by controlling in the  $y^+$  value.

Lee and Jang (2005) experimentally investigated the control of flow structures in the wake behind a NACA 0012 aerofoil via a V shaped Micro-Riblet Film (MRF). The

measurements were performed for the Reynolds number ranged from  $1.03 \times 10^4$  to  $5.14 \times 10^4$ . However, the drag force on the MRF, which covered the airfoil, was about 6.6% lower than that on the smooth airfoil at Reynolds number  $Re = 1.54 \times 10^4$ . At high Reynolds number  $Re = 4.62 \times 10^4$ , the drag force increased by 9.8% for MRF. The Particle Image Velocimetry (PIV) technique and ensemble averaged was utilized to measure the distributions of turbulence intensity and turbulent kinetic energy including the mean velocity through 500 instant velocity fields behind the airfoil, in addition to a smoke wire flow visualization technique. The results for the case of *drag reduction* ( $Re = 1.54 \times 10^4$ ) had a shorter vortex formation region and higher vertical velocity component, compared with smooth airfoil. Conversely, for the *increased drag case* ( $Re = 4.62 \times 10^4$ ), the presence of MRF grooves on the airfoil were observed to increase the vertical velocity component and decrease the height of the large-scale streamwise vortices which interacted strongly. Thus, indicating an increase in the Reynolds shear stress and turbulent kinetic energy leading to higher drag force on airfoil.

Sagrado (2007) performed experiments in which pressure fluctuations and velocity field were measured in the tripped and untripped turbulent boundary layer on a NACA 0012 airfoil surface. In this study, attention was focused on the trailing edge zone. Different Reynolds numbers ( $Re$ ) and angles of attack ( $\alpha$ ) were examined, specifically  $Re = (4, 2) \times 10^5$  and  $\alpha = 0^\circ, 12.6^\circ, 16^\circ$  degrees respectively. In addition, the study included low and moderate Reynolds number studies for untripped boundary layers and high Reynolds numbers for the tripped boundary layer case, which can also play an important role in validation of Large Eddy Simulation (LES) and DNS models.

### 2.2.2 Aerodynamics of gas turbines

This section briefly reviews previous aerodynamic flow studies of the gas turbine blades. Actually, the flows in turbomachines have both *steady* and *unsteady* components. Since the first stage of the stator in high pressure turbine is possibly steady flow, then the upstream blades effects down stream blades primarily due to the wakes which they shed [Howell (1999), Howell et al.(2001)]. Other stages also exhibit complex flow field phenomena. The unsteadiness of the flow field is a result of relative motion of the rows of blades, wake passing and shock waves from blade row interactions and freestream turbulence generated in the combustor [Nix (2003)]. Figure

(2-2) shows illustrates the secondary flow and end-wall boundary layers in gas turbine flows.

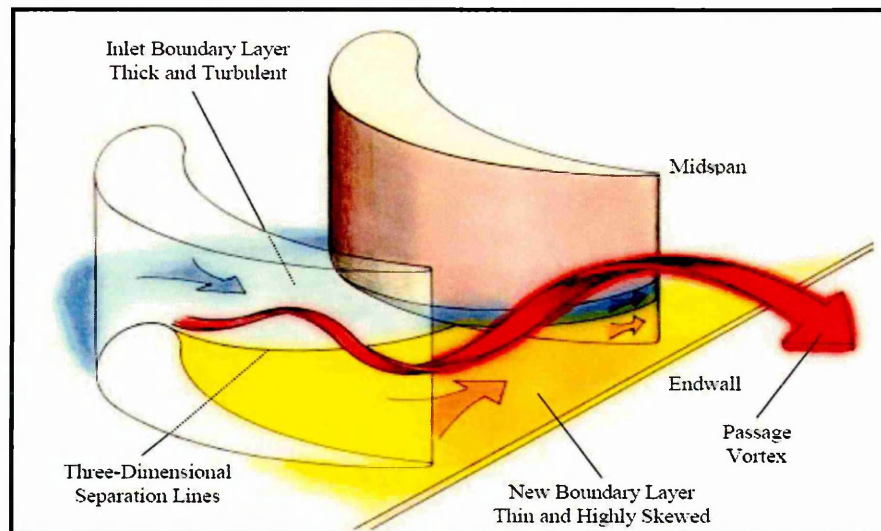


Figure (2-2) Schematic representation of secondary flow and end-wall boundary layers [Kassim *et al.* (2007)]

Djouimaa *et al.* (2007) studied two-dimensional flow for the blade-to-blade transonic gas turbine, using an irregular structured grid and the FLUENT 6.0 software with a Reynolds Averaged Navier-Stokes (RANS) model. The characteristics of the flow were compared with experimental tests and included reflecting and non-reflecting boundary conditions. Different turbulence models ( $k-\epsilon$ , RNG  $k-\epsilon$ , Realizable  $k-\epsilon$ , SST  $k-\omega$ ) were also examined to compute the pressure distribution around the blades, with the inlet Reynolds numbers  $(0.5-1.0) \cdot 10^6$  and exit Mach numbers (1.0–1.3). The RNG model was employed in particular to show the effects of inlet turbulence intensities, exit Mach number and inlet Reynolds numbers.

Ames *et al.* (2006) calculated details of total pressure losses; turning angle and secondary velocities at three Reynolds numbers,  $Re = 0.5 \cdot 10^6$ ,  $1 \cdot 10^6$  and  $2 \cdot 10^6$ . Pressure losses, omega and secondary velocity flow were presented at 1/4 axial chord from vane 3 trailing edge based on exit  $Re = 1 \cdot 10^6$  for both low and high turbulence conditions. A mock aero-derivative combustor was used to generate the high turbulence condition and a five-hole cone probe employed to measure secondary flow velocity. Evidently, the high turbulence produced a broader wake than the low turbulence case. However, total pressure losses at high turbulence were about 0.02 greater than at low turbulence, due to the state of suction at the surface of the blade. Losses decreased

moderately with increasing Reynolds number. The exit measurements also elucidated further the end-wall heat transfer distributions, the secondary flows in the passage and the losses.

Mei and Guha (2005) developed numerical simulations for turbine cascade and compressible transonic flow, using a self-adaptive, unstructured mesh. The Euler and Navier-Stokes equations were applied in the numerical program. Turbulence was simulated with an algebraic Baldwin-Lomax turbulence model, and the two-equation turbulent model ( $k-\omega$  model) with high order accuracy through applied MUSCL approach. The Gauss-Seidel algorithm was used to solve the linear equations for each time iteration. Good correlation was obtained between the numerical and experimental results.

Michelassi *et al.* (1998) investigated boundary layer and wake flow in a transonic turbine rotor cascade, numerically and experimentally. Measurements included pressure and total pressure profiles for the blade in addition to isentropic Mach number. Computations were performed by FAST 3DC and FLOW3D solvers with different turbulence models ( $k-\omega$  and two layer model TLK) and three different transition models. The results provided a realistic description of the flow field allowing the calculation of pressure distribution and shock boundary layer interaction induced by small flow separation on the suction side which is generated due to transitions models. The experiments also indicated the presence of trailing edge vortices.

Chmotine *et al.* (1997) used the 2-dimensional Euler equations to model high pressure turbine flow in an aircraft engine. This study was based on the large-particle method, which is a numerical method for the stator and rotor blade; the unsteady effect was represented for the rotor blades moving along the fixed grid and the pressure and absolute total temperature were calculated on the rotor blade surface.

Numerous published works have studied the 2-D and 3-D turbulent channel flow and often utilize DNS since this is the most accurate numerical method, although it is very expensive computationally. Therefore Fluent 6.3 software is used to simulate turbulent channel flow to demonstrate the effects of mesh refinement, mesh type and also to examine different turbulent model accuracies. This establishes basic confidence in the Fluent software. Furthermore the more geometrically complex case of flow over a curved boundary (NACA 0012 airfoil) is then simulated, as this case is more relevant to

actual gas turbine geometries, and the Fluent computations are compared with available experimental data from Cambridge University.

## 2.3 Heat transfer and film cooling studies

### 2.3.1 Flat and curved plates

Figure (2-3) shows cooling region for a solid plane plate with the heater-foil, the coolant injection, cooling holes, the main gas flow, and relevant physical quantities. Many important studies of “film cooling” have been conducted.

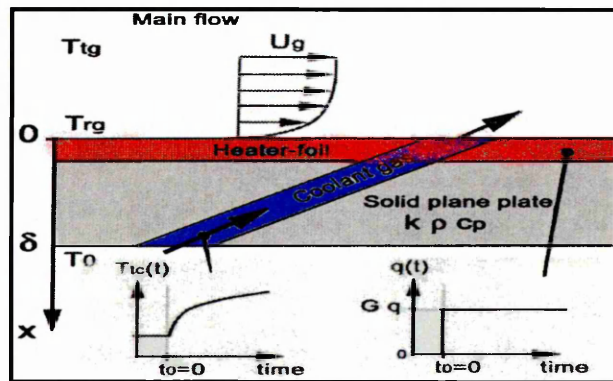


Figure (2-3); Schematic of the solid plane plate with the heater-foil, the coolant injection, cooling holes, the main gas flow, and some relevant physical quantities [Vogel and Graf (2003)]

Daud *et al.* (2011B) A 3-D finite-volume method has been employed with a (RNG) turbulence model to investigate the film cooling effectiveness and heat transfer along a flat plate for four different plate material properties (steel, carbon steel, copper and aluminum) with  $30^\circ$  angle of injection and different holes arrangements. Single and double rows of holes with pitch-to-diameter ratio ( $P/D = 3$  and  $6$ ) with a hole diameter of  $D = 10$  mm have been considered. The numerical results illustrate the cooling effectiveness and heat transfer characteristic variation with increasing injection Blowing Ratio (BR) which ranges from 0.5 to 1 for different sections. In terms of the film cooling performance, high BR does not enhance cooling effectiveness at all locations of the plate with injection. The study highlighted the importance of validation in Computational Fluid Dynamics (CFD) heat transfer simulations and the necessity for sustaining a high degree of accuracy with industrial CFD software. The numerical results have been compared with available experimental data and previous numerical

results by Yuen and Martinez-Botas (2005) and good correlation has been achieved. The effects of material thermal properties for the solid plate have been elucidated, in addition to variation concepts between the shell plate and the solid plate, on the film cooling effectiveness.

Nemdili *et al.* (2011) investigated the influence of film cooling holes imperfection on flat plate numerically with a symmetrical single perpendicular hole exhibiting jet flow. Numerical calculations were performed with the Reynolds Average Navier Stokes and an energy equation using the finite volume method to predict hydrodynamic flow and thermal effects. In addition, turbulence closure was achieved via the standard wall function  $k - \varepsilon$  model. The simulation process was executed with the CFX 10 software package and the computational domain modeled as a structured mesh. Four imperfection hole cases were studied with 0%, 23.44%, 43.75% and 60.94% obstruction. Good agreement was obtained between numerical computations and the experimental results of Jovanovic *et al.* (2006). However, cooling effectiveness value was found to decrease quickly when the obstruction is higher than 50% and occurred close to holes exit implying that thermal protection for the blade was profoundly reduced.

Ghorab (2010) presented schemes of louver and hybrid film cooling performance over a flat plate experimentally using the Thermochromic Liquid Crystal Technique (TLC). The louver scheme (proposed in Canada) involves the film hole design allowing coolant fluid to pass through a bend and to encroach plate material (impingement effects) and then exit to the outer surface. This study aimed to evaluate the film cooling effectiveness and heat transfer at blowing ratios of 0.5, 1 and 1.5. In addition, a hybrid scheme was deployed to analyze the flow pattern at different blowing ratios. It was shown that the hybrid film hole allows the coolant fluid to be directed to the secondary flow in the horizontal direction and reduces the jet liftoff at different blowing ratios. Both louver and hybrid scheme provides high local film cooling and reduction in net heat flux compared with previous work. Moreover, enhancement in the film cooling of holes is obtained further along the spanwise direction.

Takeishi *et al.* (2010) measured cooling effectiveness on a flat wall with the effects of swirling coolant flow using circular and other shaped holes with the aid of a low speed wind tunnel. Pressure Sensitive Paint (PSP) and Particle Image Velocimetry (PIV)

techniques were also employed to obtain the measurements for two blowing ratios (1, 2) with four swirling motions of the coolant. The results showed that the cooling effectiveness is strongly enhanced due to swirling effects due to the interaction between coolant film jets, mainstream and swirling motion (coolant fluid is deflected in the pitch direction in the case of circular film holes). Shaped film cooling was also improved. However, the optimum combination involved the shaped holes geometry and swirl number (speed of rotation). Overall, it was demonstrated that the film cooling effectiveness downstream was 50% higher than for the non-swirl case.

Tao *et al.* (2009) measured the coefficient of heat transfer for flat blade film cooling in stationary and rotating conditions. The rotational speed was varied from 0 or 800 rpm and the blowing ratio varied from 0.4 to 2 with density ratio 1.02 and 1.53 utilized for air and carbon dioxide (CO<sub>2</sub>). Film cooling was simulated by a single hole with angle of injection of 35 degrees angle along the streamwise direction with 4 mm diameter holes. The surface temperature of the flat blade was measured using the TLC technique. The results indicated that the heat transfer coefficient trajectory on the pressure side decreased compared with the stationary case and was enhanced only for  $x/D < 1.0$  for the suction side. Actually, in the rotating case the film trajectory on the suction side was deviated due to Coriolis and centrifugal force contrast with the pressure side. With injected air as the coolant fluid the heat transfer coefficient was also reduced for both surfaces. Finally, the density ratio was shown to have substantial effects on the heat transfer distributions along the streamwise direction for the rotating condition case.

Hung *et al.* (2009) studied 3-D cooling effectiveness and heat transfer over concave and convex plates using a TLC technique. The performance of film cooling was investigated with one row of injection holes (angle of injection 35°) for various blowing ratios (BR = 0.5, 1, 1.5 and 2). The *concave* model results showed that with increasing blowing ratio, the heat transfer coefficient and film cooling effectiveness increased. The *convex* model surface results demonstrated that the compound angle (0°, 45° and 90°) increases both heat transfer and film cooling effectiveness at moderate and high blowing ratios.

Liu *et al.* (2008) studied and improved the accuracy of spanwise cooling effectiveness distributions for single film cooling holes. The study showed the effect of turbulent Prandtl numbers on the flow field outside the near-wall regions. The realizable k- $\epsilon$  model with one equation model was employed. The results showed that turbulent

Prandtl number exerts a strong influence on the computation- a reduction in turbulent Prandtl number *increases* film cooling effectiveness. Under high blowing ratios, the cooling effectiveness of the entire spanwise region on the plate was enhanced due to a reduced turbulent Prandtl number. However, the results also showed that with small blowing ratio and low Prandtl number, the effectiveness falls in the center region whereas there is an improved cooling effectiveness of the lateral region off the centerline (some discrepancy still exists in the area relatively far from the centerline). Good agreement was obtained between the computed and experimental results by Sinha *et al.* (1999) with the two layer  $k-\varepsilon$  turbulence model TLVA- $P_r$  (TLVA- $P_r$  is the combination of anisotropic two layer turbulence model and DNS based model of  $P_r$  in the boundary layer, [Lakehal (2002)]) turbulent model achieving the best results in the computed cases.

Guangchao *et al.* (2008) measured experimentally the film cooling effectiveness, heat transfer ratio and heat load for three holes designs - fanned, cylindrical and the 3- in-1 hole system. In this study, Carbon dioxide was employed as a coolant fluid with momentum flux ratios of 1, 2 and 4. With increased momentum ratio in the cylindrical holes, the cooling effectiveness was enhanced with an increase in heat transfer coefficient; in addition for the 3-in-1 holes case, there were lower heat transfer and cooling effectiveness values with an increase in momentum flux ratio. The best hole design was shown to be the *fanned hole system* since it supplies high cooling effectiveness with low heat transfer coefficients. In contrast to this, the cylindrical holes generated inefficient cooling.

Renze *et al.* (2008) utilized Large Eddy Simulation (LES) to investigate numerically the effects of the velocity and density ratio on gas turbine film cooling effectiveness. The coolant fluid was effused through an inclined single pipe inclined at 30 degrees to the turbulent boundary layer at a Reynolds number  $Re = 400,000$  along a flat plate ( $CO_2$  was injected into the air). LES simulation was shown to successfully capture the jet cross flow physics of this system. LES was also shown in [Renze *et al.* (2008)] to be an efficient method for low subsonic flow based on an implicit dual time stepping scheme at a low Mach number. Good agreement was achieved between the numerical results and the experimental data retrieved from Particle Image Velocimetry (PIV) measurements. Furthermore, the velocity ratio was also determined for the recirculation region and inclination of the shear layers.

Tao *et al.* (2008) used a liquid crystal technique to experimentally demonstrate the cooling effects of a single film hole over a rotating flat blade. Carbon dioxide (CO<sub>2</sub>) and air coolant fluid was injected at 30° angle (laid-back hole). Coolant fluid is injected in the downstream region and five different rotating speeds ( $\Omega = 0, 300, 500, 800$  and  $1000$  r/min) were selected. Overall, the results showed that film cooling effects on the suction side are less than the pressure side due to rotation effects. On the other hand, with an increase in rotation speed when  $\Omega > 500-600$  r/min, the cooling effectiveness on the pressure side improved initially and then subsequently fell.

Yuen and Martinz-Botas (2005), Yuen and Martinz-Botas (2003) studied experimentally the cooling effectiveness on a flat steel plate. The film cooling was simulated by 30, 60 and 90 degrees angles of injection with cylindrical hole geometries possessing constant length (aspect ratio was taken as  $L / D = 4$ ). The operating Reynolds number was 8563 based on free stream velocity and hole diameter for all three injection angles. The blowing ratio was varied between 0.33 and 2 for the experimental studies and the results compared favorably with published studies.

Jia *et al.* (2005) investigated a slot jet into a crossflow numerically and experimentally with Laser Doppler Velocimetry (LDV). Numerical simulations were conducted with the time-averaged Navier-Stokes equations and with the SST  $k-\omega$ , V2F  $k-\epsilon$  and stress- $\omega$  turbulence models. Comparisons were made between computations using the Reynolds stress turbulence model and LDV experiments for three jet angles 30, 60 and 90 degrees with blowing ratios of 2 to 9. The results showed that the recirculation bubble vanished when the angle of injection was lower than 30 degrees; in addition, the recirculation and cooling effectiveness were shown to be greatly affected by the blowing ratio.

Sinha *et al.* (1999) studied experimentally film cooling effectiveness using a single row of holes across a flat plate. The density of the coolant fluid across the freestream varied from 1.2 to 2. Surface temperatures were measured using a surface thermocouple arrangement with free conduction error along the jet centerline and across lateral location. By independently varying density ratio, mass flux ratio velocity ratio and momentum ratio, the cooling effectiveness was determined experimentally. The results showed that at low blowing rates the cooling jets remaining attached to the wall; conversely with high blowing rates the detachment and reattachment of coolant was

found to become important. Increases in momentum flux ratio and decreases in density ratio were found to reduce the spreading of the film cooling jet, leading to a *reduction* in cooling effectiveness.

Kadja and Bergeles (1997) discussed numerical computations of blade turbine cooling via injection of a fluid into the main stream flow. The numerical flow model involved a two-dimensional single slot along the flat surface. Typically, the local film cooling effectiveness was shown in this study to increase with increasing blowing ratio and the Nusselt number was found to decrease near the slot.

Saumweber *et al.* (2003) investigated experimentally the effects of free stream turbulence on film cooling performance. Three types of holes geometry were tested; cylindrical, fan shaped (expanded in lateral direction) and laidback hole (expanded in lateral and streamwise direction). Three holes at 5 mm diameter separations were arranged as one row with inclination angle of  $30^{\circ}$  and an operating condition of Mach number ( $Ma = 0.3$ ) varied in terms of freestream turbulence intensity. Furthermore, blowing ratio ranged between 0.5 and 2.5 with a density ratio of 1.7. The experimental results showed that with cylindrical holes, film cooling effectiveness reduced with increased free turbulence flow at low blowing ratio. However, there was a small increase at high blowing ratio. Negative effects were obtained for shaped holes at increased free turbulence even with high blowing ratio. It was also found that the heat transfer coefficient ratio increased with high turbulence flow.

### **2.3.2 Gas turbine film cooling**

Considerable research has also been conducted in the area of gas turbine film cooling. Some selected studies are reviewed as follows.

Carullo *et al.* (2011) examined effect of freestream turbulence, turbulence length scale and exit Reynolds number on aerodynamic and surface heat transfer distribution of a turbine blade in a transonic cascade. Three turbulence levels (2%, 12% and 14%), in addition to length scale (0.02, 0.26 and 0.41) normalized by blade pitches were generated by passive turbulence grids at the inlet cascade. Thin film gauges were used to predict the amount of heat transfer at the mid span for both side pressure and suction surface by platinum sensor through recording a change in resistance with temperature

(as one arm of a Wheatstone bridge). Actual tests were performed at exit Mach number 0.55, 0.78 and 1.03 which correspond with exit Reynolds number  $6 \cdot 10^5$ ,  $8 \cdot 10^5$  and  $11 \cdot 10^5$  respectively. However, experimental results showed that the amount of heat transfer was enhanced on both pressure and suction sides at high freestream turbulence, compared with the low turbulence case. Consistently, the greatest heat transfer occurred at the leading edge and decreased as the flow proceeded down. An increase in exit Reynolds number as well Mach number, raised the heat transfer level and induced earlier boundary layer transition (at nominal conditions to exit Mach 0.78 the average heat augmentations of 23% and 35%).

Gao *et al.* (2008) measured film cooling effectiveness experimentally using the Pressure Sensitive Paint (PSP) technique. The inlet and outlet cascade Mach numbers were set as 0.27 and 0.44, respectively. The coolant fluid was injected either in two rows of holes on the suction side or in four rows of holes on the pressure side with blowing ratios varied from 0.4 to 1.5. The results showed that with blowing ratio of 0.6 and 0.9, the cooling effectiveness attains the highest value directly downstream of holes and with high blowing ratio covers the widest blade surface. Film cooling on the pressure side is lower than the suction side except for the region affected by secondary vortices.

Burdet and Abhari (2007) and Burdet *et al.* (2007) simulated computationally improved hole arrangements for the film cooling in turbine blade using three-dimensional CFD model. A Reynolds Averages Navier-Stokes equations (RANS) simulation was compared with experimental data to predict transonic film flow, cooling effectiveness and Nusselt number around the blade. This study highlighted the macro-flow structure for the interacting coolant jet process, especially near the hole region, at different hole rows on the pressure side of the blade. The drawback of this study was that experimental Nusselt number data was not available for all the blade surfaces.

Lu *et al.* (2007) used the transient infrared thermography technique to measure film cooling effectiveness on a blunt body with semi-cylinder leading edge and flat after-body, modeled as turbine blade test case. Three rows of holes were arranged as showerhead holes; the first row of holes was located on the stagnation line and the other two rows of holes were located at  $15^\circ$  on the either side of the stagnation line, in addition to angles of  $0^\circ$ ,  $30^\circ$ ,  $45^\circ$  in the transverse direction. The fanned holes shape configuration was also investigated for injection angles of  $30^\circ$  and  $45^\circ$ . The fanned

shaped holes geometry supplied the highest film cooling, greatly in excess of the transverse and baseline holes. Heat transfer coefficient was slightly enhanced with the spanwise angle. All measurements were obtained at mainstream Reynolds number of 19500 based on the cylindrical leading edge diameter.

Yuan *et al.* (2007) predicted numerical and experimental three dimensional flow fields (velocity) and cooling effectiveness for stationary, rotor turbine cascade. Three discrete holes of 2 mm diameter were located on suction and pressure sides. The FINE<sup>TM</sup>/Turbo CFD software was used using the  $k - \varepsilon$  turbulence model and experimental analyses were carried out using Laser Doppler Velocimetry (LDV). The pressure side was influenced by cooling effectiveness more significantly than the suction side for rotor blade compared with stationary blade.

Ahn *et al.* (2007) Measured showerhead film cooling effectiveness distribution on a gas turbine by using Pressure Sensitive Paint (PSP) technique. The influence of the rotational speed on the film cooling trace was investigated at three rotational speeds. The Reynolds number was prescribed as  $2 \cdot 10^5$  and the total to exit pressure ratio was 1.12. However, the results showed that the cooling effectiveness was depressed by the rotational speed and conversely increased with increasing in blowing ratio.

Kassim *et al.* (2007) studied thermal effects in turbine blade film cooling on the flow over a blade surface, using a three dimensional incompressible flow model of the film cooling effectiveness, and simulating the interaction between the jet and the cross main stream flow. The NACA 0021 airfoil was modeled and tested experimentally to study the jet flow penetration and flow configuration (the effect of jet angle and velocity ratio on the penetration area). Good agreement was obtained between the experimental and computational results for the different angles of attack.

Gord (2007) calculated heat transfer coefficients over a rotor surface in a pre-swirl rotating disc system, to simulate cooling of gas turbines by the impingement cooling technique. A three dimensional steady, incompressible turbulent flow model was used and the results were compared with published experimental results. The static, total pressure coefficient and heat transfer coefficients were shown to be in good agreement. However, for total heat transfer ( $h$ ), the correlation between computation and measurements was less accurate.

Azzi and Jubran (2004) investigated film cooling of blade turbine system with the three dimensional finite volume method and multi block technique. The numerical domain included the plenum of film cooling and curved blade surface and was conducted using a k- $\epsilon$  turbulence model. However, Two Layer Velocity (TLV) scale model and TLVA (DNS-based anisotropic extension) models were used. Nevertheless, the results did not show any improvement in the prediction of the lateral average film cooling effectiveness compared with the wall function strategy. The experimental results were also obtained by varying the injection angles ( $25^{\circ}$ ,  $30^{\circ}$ ,  $35^{\circ}$  and  $60^{\circ}$ ). The case of  $25^{\circ}$  angle of injection was found to provide the best film cooling effectiveness. The TLV model is a trade off between wall function and low Re model by considering the viscosity region near the wall by one equation model and outer flow solved with standard wall function. In TLVA model Lakehal *et al.* (2001) and Azzi and Lakehal (2002) have been proposed extended viscose sub-layer through multiplying eddy viscosity by a factor based on fluctuation value ( $\overline{u'}$ ) correlates with sets of boundary layer and channel flow DNS data [Lakehal (2002)].

Forest *et al.* (2004) applied the heat transfer design code (HTDC) with a series of experimental measurements on a scale model gas turbine blade. A computational method was used to simulate transonic gas turbine flow to obtain aerodynamic and thermal performance, with a mix of hot gas and relatively cool air injected via holes in the turbine blade. Transpiration cooling was achieved by adding holes to the optimum shape.

Thorpe *et al.* (2004) studied heat transfer and static pressure distributions over the tip casing wall for a high pressure transonic axial turbine flow. Time-mean heat transfer and time-mean static pressures were recorded in a series of experiments. For a nozzle guide vane with exit flow conditions of Mach number (0.93) and Reynolds number ( $2.7 \cdot 10^6$ ), all variables such as, static pressure, heat transfer rate, adiabatic wall temperature and Nusselt number, were quantified. The results showed that the heat flux falls by a factor of 6 (from 120 to 20 kW/m<sup>2</sup>) and also the Nusselt number falls by 36% between the rotor inlet plane and 80% rotor axial chord. The time mean pressure plots revealed the same circumferential variations with a large pressure gradient in the axial direction.

Heidmann *et al.* (2003) used Boundary Element Method (BEM) to solve and predict the conjugate heat transfer effects on a realistic film cooling for a variety of blade materials. The NASA Glenn-HT multiblock heat transfer code was utilized to solve fluid convection, while solid conduction model based on BEM. (No volumetric grid is required inside the solid- only the surface grid is needed since a surface grid is readily available from the fluid side of the problem). This method eliminates one of the most time-consuming elements of the computation for complex geometry. Two conjugate solutions were presented for high thermal conductivity Inconel nickel based alloy and low thermal conductivity as a Silicon nitride ceramic vane case compared with an adiabatic wall. Numerical results showed that the conjugate case had a lower outer wall temperature due to thermal conduction from the outer wall to the plenum. Stagnation point temperature was reduced as thermal conductivity increased. However, some locations of increased temperature were seen in the higher thermal conductivity for Inconel vane case on the pressure side. Furthermore, three-dimensional heat conduction in the solid allows for conduction heat transfer from the outer to the inner wall along the vane wall.

Martini *et al.* (2003) presented numerical and experimental results for film cooling effectiveness through a cutback trailing edge surface. The numerical calculation was performed on an MTU (Germany's leading aircraft engine manufacturer) aero engine using FLUENT code 6.0 with mesh generation Gambit 2.0. Experimental work was conducted at Karlsruhe University, Germany. The film cooling effectiveness was studied for three blowing ratios (0.5, 0.8 and 1.1) and also a slot discharge coefficient for the double-in-line rib. Numerical results show deviations in film cooling effectiveness at trailing edge compared with experimental data.

Ou and Rivir (2001A), Ou and Rivir (2001B) performed experimental studies using a liquid crystal technique to obtain film cooling and heat transfer coefficients on the blade leading edge with three rows of holes. The 1<sup>st</sup>, 2<sup>nd</sup> and 3<sup>rd</sup> film holes injected at 0<sup>o</sup>, ±21.5<sup>o</sup> respectively and the holes diameter  $d = 76$  mm with pitch to diameter ratio is 7.86. The blowing ratio was utilized  $BR = 1, 1.5, 2$  and 2.5 with two free stream turbulence level,  $Tu = 1\%$  and 20% for  $Re = 30000$  and 60000. However, the discharge coefficient measurements of the film cooling holes at the stagnation row were varied between 0.62-0.69 and 0.39-0.54 in addition to 0.54-0.59 and 0.47-0.52 for 21.5<sup>o</sup> rows.

The results showed the effect of increased turbulence intensity for  $Re=30000$  was to reduce the cooling effectiveness between the rows about 61% to 20% for all BR. While, at  $Re=60000$  an increase in film cooling effectiveness was obtained for  $BR = 1, 2$  and  $2.5$  with high free turbulence. The effect of increasing blowing ratio provides highest film cooling also increased Frössling number and the best blowing ratio was obtained at  $BR=2$ . Moreover, the cooling effectiveness improved for all blowing ratios as the Reynolds number increased for 20% higher turbulence case and the major effects were obtained at  $BR=1$  with 55% when  $Re$  was increased from 30000 to 60000.

Lakehal *et al.* (2001) calculated three dimensional flow and heat transfer in film cooling for a symmetrical turbine blade, using a three dimensional finite volume method. The experimental work was carried out in an open subsonic wind tunnel by Haslinger and Hennecke (1997) in Germany. Film cooling utilized a set of holes arranged at the leading edge as one row on each side (pressure side and suction side). Computations of the flow field, temperature and film cooling effectiveness were performed for various blowing ratios ( $M=0.3, 0.5, \text{ and } 0.9$ ) and lateral injection angles of ( $0^\circ, 45^\circ$ ) were used. The standard wall function turbulence model ( $k-\varepsilon$ ) was used with a two layer model. The calculation of film cooling effectiveness contours with the measurements showed reasonably good agreement.

Theodoridis, *et al.* (2001) utilized the FAST 3D CFD code to develop incompressible fully implicit three dimensional finite volume simulations to investigate the injection of coolant air at the leading edge of a high pressure turbine blade. The computation results for different blowing ratios ( $M= 0.0, 0.7, 1.1$ ) were compared with experimental data including isentropic Mach number, velocity and pressure field. The turbulence model ( $k-\varepsilon$ ) with wall function identified major features of the flow field. Such as, secondary flow vortices (injected air) especially on the suction side.

Ekkad and Han (2000) measured turbine blade convective heat transfer using transient liquid crystal thermography technique. The process involved coating the blade test surface with liquid crystals to quantify Nusselt number and the cooling effectiveness. This technique was employed for a complex gas turbine geometry and the results included heat transfer with jet impingement, internal cooling, channel flow with ribs, flat plate film cooling, and gas turbine film cooling.

Garg and Abhari (1997) computed the Nusselt number for film cooling on a rotating blade using three dimensional Navier-Stokes equations simulations. The transonic rotor blade contained 93 cooling films, with five rows along the span. The computation was based on an explicit finite volume code with an algebraic turbulence model. More than 2.5 million grid points were employed to calculate the flow. The computed heat transfer with the film cooling near the hub on the suction surface and the experimental measurement of heat flux were compared. However, the results generated on the pressure surface were poor.

Garg and Gaugler (1997) studied the effect of coolant temperature and mass flow on turbine blade cooling effectiveness. A Von Karman Institute, Belgium (VKI) rotor blade turbine was selected in this study with six rows of cooling holes, namely three of rows indicated on shower head. The results show that with high coolant temperature that the effectiveness was better than with lower coolant temperature for mass flow ratio 5%. In addition, through increased coolant mass flow ratio, the cooling effectiveness was enhanced on the suction side, while on the pressure side it decreased for constant coolant temperature. Generally, the cooling effectiveness was lower for higher coolant temperature due to the effects of air compressibility.

Heidmann (1995) calculated the effect of an upstream blade wake causing unsteadiness on the performance of the film cooling on the downstream axial turbine blade. Aerodynamics and heat transfer were studied using a showerhead film cooling arrangement (typical of the modern gas turbine engine) with a steady three-dimensional viscous turbulent numerical simulation, to determine upstream swirl and stagnation pressure. The computations obtained good results for predicting the span-average film effectiveness.

Numerical and experimental method studies of heat transfer for flat plate using film cooling holes, have been reviewed. The prediction of convective and conduction heat transfer will be achieved using Fluent 6.3 CFD code to examine film effectiveness performance. Validation between computational results and available experimental data will be considered by showing the differences between *solid* and *shell plate* case which correspond to conjugate heat transfer (CHT) and non-conjugate (non-CHT), respectively. Furthermore the effects of plate material property and blowing ratio (BR) will be demonstrated. The literature review has highlighted that the vast majority of existing studies use a simple blade geometry and shell surface case. To extend this, and

also to build on these flat plate film cooling simulations, a *complex gas turbine blade geometry* will then be used in this study, to assess optimum performance of film cooling in CHT for a 3-D skewed blade by examining in detail the effects of variation in sections area (Hub, mid and shroud) on film cooling performance. Both Fluent numerical simulations and also experimental testing of the 3-D skewed model will be conducted.

## 2.4 Methodology

After reviewing the previous published studies, the majority of studies communicated thus far, have focused on 2-D or 3-D aerodynamic flow and heat transfer on a simple blade geometry, flat or curved plate, NACA 0012 aerofoil, symmetrical turbine blade and simple cross section blade from hub to tip. Consequently, the methodology and the logical thread structure in this research are represented in Figure (2-4). The complexity of the present Thesis gradually increases. It commences with basic channel flow, then progresses to NACA0012 simulation (2-D curved geometry) and thereafter to a flat plate heat transfer case and finally to the most complex scenario, a 3-D skewed gas turbine blade. For the first three cases purely numerical simulations are conducted. For the last case (3-D skewed blade), since this is the most realistic and representative of actual gas turbine blades, both computational and experimental methods are used to study the performance of blade film cooling.

The first stage of the study focuses on the flow structure inside channels and flow over NACA 0012 airfoil. This aspect of the work is included to explain the restrictions of the FLUENT code 6.3 solver by examining the influence of mesh refinement and mesh type on the wall, employing three different turbulence models ( $k$ - $\epsilon$ , RNG, SST  $k$ - $\omega$ ) and studying Reynolds number effects with detailed comparison with previous Direct Numerical Simulation (DNS) data and experimental data.

The second stage of this study will concentrate on heat transfer and flow over a flat plate surface by exploring the effects of blowing ratio and blade material property on flow characteristics. Numerical results will be compared with available experimental data.

The third stage of this dissertation will analyze film cooling effectiveness on a gas turbine blade by studying the effects of blowing ratio, cooling temperature, angle of

injection, number of holes and holes diameter. This step will evaluate thermal performance of the film cooling parameters on a gas turbine blade in order to attain optimum film cooling design. Boundary conditions will also be examined in detail.

The fourth and final stage of this dissertation is the experimental study. Three turbine blades models have been fabricated with film cooling holes injected at angles of  $35^{\circ}$ ,  $45^{\circ}$  and  $60^{\circ}$ . The specimens are then experimentally assessed in the wind tunnel test section. Experimental results will be obtained from the thermal test section as a temperature reading for each mode.

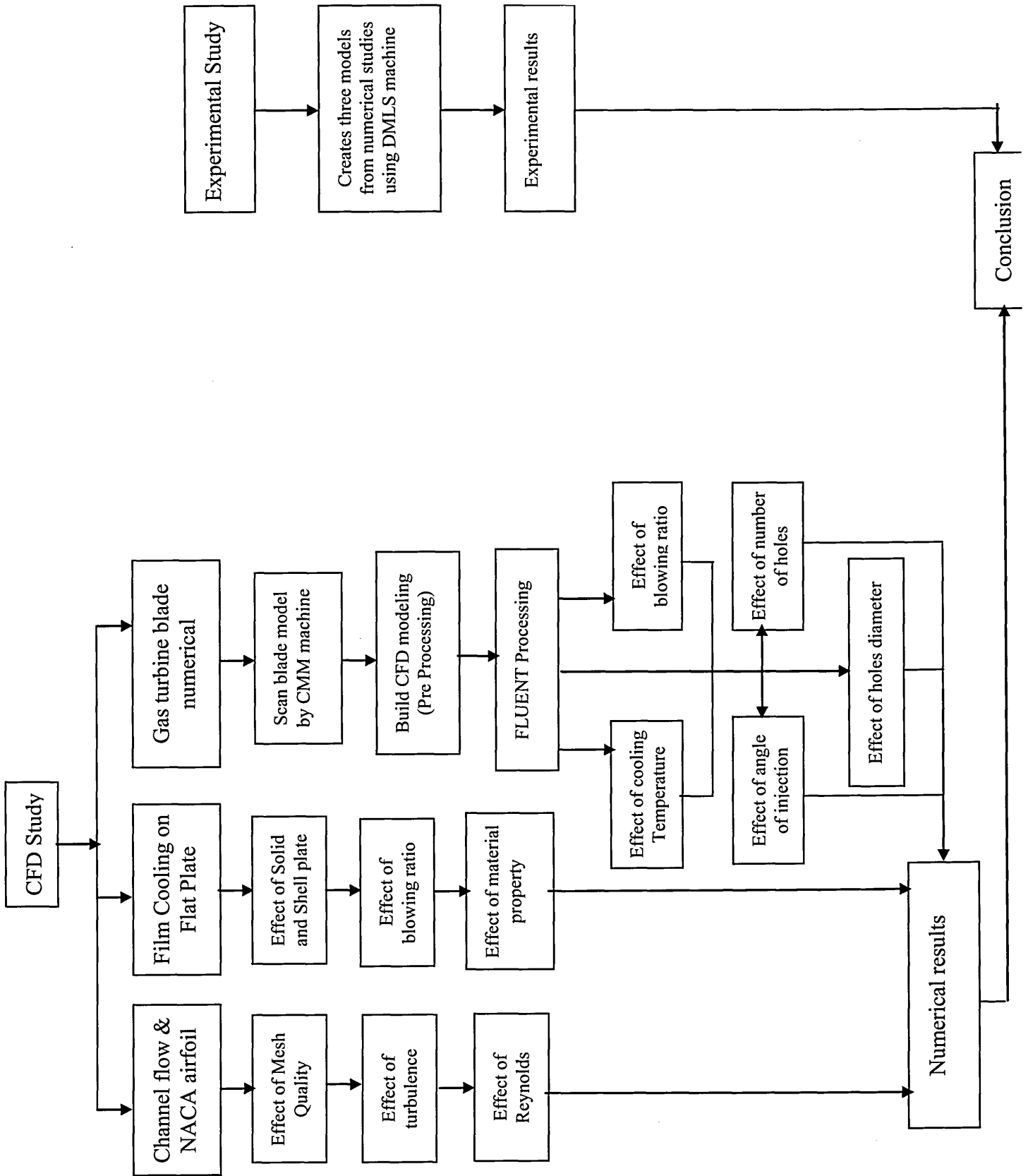


Figure (2-4) Research methodology and structure

## *Chapter Three*

# *Introduction to Computational Fluid Dynamics (CFD) & Numerical Equations*

## 3.1 Introduction

Computational Fluid Dynamics (CFD) is a technique employed to simulate internal and external aerodynamic flow, heat transfer, chemical reaction, mass transfer, mechanical movement and phase change related with body structure change. This is achieved by solving mathematical equations which govern the given process using a numerical algorithm on a computer with appropriate boundary conditions.

CFD simulation is a powerful mechanism for predicting fluid dynamics phenomena and, when used correctly, provides accurate results with detailed and informative computer-generated output (visualization of flow fields). However, CFD must be used judiciously since incorrect application can lead to quantitative errors which largely result from insufficient information, improper boundary condition specification, and inadequate resolution of meshes [Celik (1993)].

Therefore, knowledge of flow characteristic performances and the full capabilities of a CFD code are instrumental in obtaining, such things as an optimum blade shape in gas turbine flows, before any experimental work or design is undertaken.

In this chapter, a mathematical model of fluid flow has been described and the numerical analysis equations which are employed to accomplish a complete simulation of the gas turbine flow dynamics and heat transfer are introduced. In addition, this chapter elucidates the Fluent CFD code structure methodology.

## 3.2 Mathematical model of the fluid flow

### 3.2.1 Navier–Stokes equations

The numerical simulation of the physical flow and heat transfer is considered in CFD, based on fundamental governing equations which describe the behavior of a continuum fluid. Therefore, the governing equations for fluid motion can be derived from the first law of thermodynamics and Newton's second law. The Navier–Stokes equations (N-S) for three- dimensional, unsteady, viscous flow (in general form), take the form:

Continuity

$$\frac{\partial \rho}{\partial t} + \frac{\partial}{\partial x_i}(\rho u_i) = 0 \quad (3-1)$$

Momentum equation

$$\frac{\partial}{\partial t}(\rho u_i) + \frac{\partial}{\partial x_j}(\rho u_i u_j) = -\frac{\partial P}{\partial x_i} + \frac{\partial}{\partial x_j} \left[ \mu \left( \frac{\partial u_i}{\partial x_j} + \frac{\partial u_j}{\partial x_i} - \frac{2}{3} \delta_{ij} \frac{\partial u_k}{\partial x_k} \right) \right] \quad (3-2)$$

The energy equation can be presented as:

$$\frac{\partial E}{\partial t} + u_j \frac{\partial E}{\partial x_j} = \frac{q^*}{\rho} + \frac{1}{\rho} \frac{\partial}{\partial x_j} \left( k \frac{\partial T}{\partial x_j} \right) \quad (3-3)$$

where  $u_i$  are the instantaneous velocity components,  $\rho$  is the fluid density,  $P$  is the pressure,  $\mu$  is the dynamic viscosity,  $\delta_{ij}$  is the Kronecker delta function (equal to one if  $i = j$ , else zero),  $\partial/\partial x_i$  represents the variation of parameters in  $X$ ,  $Y$  and  $Z$  coordinates,  $T$  is the temperature,  $q^*$  is the heat flux,  $K$  is thermal conductivity,  $C_p$  is the specific heat and  $E = C_p T$  [Bradshaw *et al.*(1981)]. (The derivations of continuity, momentum and energy equation are presented in Appendix (A)). [Anderson (1995)], Anderson *et al.* (1984)].

In this study, the energy equation for a 3-D solid plate has been used to identify conjugate heat transfer in a Cartesian coordinate system with temperature  $T$  as the dependent variable, in the following form:

$$(\rho C_p)_s \frac{\partial T}{\partial t} + (\rho C_p)_s \frac{\partial u_i T}{\partial x_i} = \frac{\partial}{\partial x_i} (K_s) \frac{\partial T}{\partial x_i} + q^* \quad (3-4)$$

Some assumptions have been applied in this research and these include steady state conditions, absence of volumetric heat sources, a stationary solid body and position-independent thermal conductivity.

### 3.3 Solution procedure

Very few flows exist for which an analytical solution to the Navier-Stokes and energy equations are possible. [Bredberg (2002)]. Consequently, numerical techniques for CFD

codes have been developed in order to solve the governing equations as set of partial differential equations. Numerical methods approximate the partial differential equations by forming a set of algebraic equations for the variables involved at the discrete grid points. This process of transforming variables is termed *discretization*. There are number of numerical methods which can be used to produce the equation which must be solved. Fluent solvers are based on Finite Volume Method (FVM).

### 3.3.1 Finite volume method

The Finite Volume Method (FVM) is one of the most versatile discretization techniques used in CFD. This approach is popular owing to its ability for accommodating not only *structured* meshes but also unstructured meshes for handling arbitrary geometrical shapes. Based on the control volume formulation of analytical fluid dynamics, the first step in the FVM is to divide the domain into a number of control volumes (cells) and at the centroid of each of the control volumes, the variable values are calculated. Figure (3-1) shows application of finite volume method based on cell center for structured and unstructured meshes [Tu *et al.* (2008)]. This numerical method consists of a number of steps:

- Formal integration of the governing equation of the liquid flow over all the (finite) control volumes of the solution domain.
- Discretization, including the substitution of a variety of finite difference type approximation for the term in the integrated equation representing flow processes such as convection, diffusion and sources. This converts integral equation into a system of algebraic equations.
- Solution of the algebraic equation by iterative method.[Palmer *et al.* (2008)]

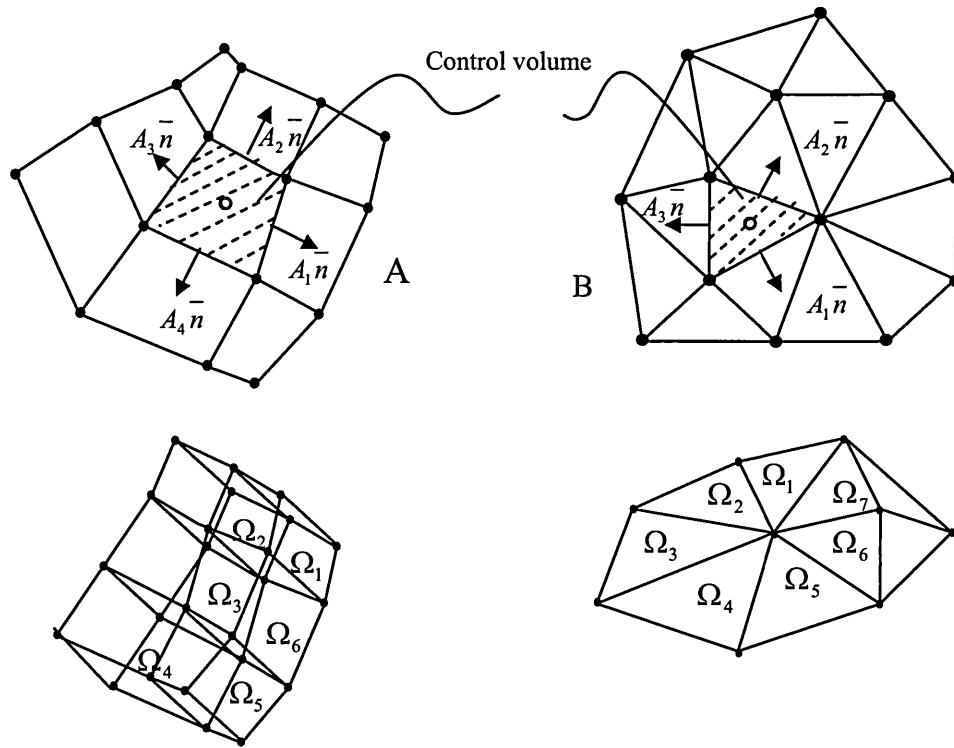


Figure (3-1) Cell center control volume for finite volume method  
 A) structured mesh B) unstructured mesh

### 3.3.2 Spatial discretization

With numerical methods, there is a difference between the *exact* solution and *numerical representation* of the solution in *space* and time. This dissimilarity in the solution is termed the *discretization error* which is associated with spatial and time discretization (difference between exact solution and numerical solution). In the Fluent 6.3 CFD software there are some different schemes which can be applied to *reduce* these errors. For example, the *second order upwind scheme*, which has been used in this study, demonstrates improved solution accuracy compared with the first order scheme. Essentially, the second order upwind scheme is applied with triangular/tetrahedral meshes; the solution convergence may therefore be slower. [Peyret (2000), Papadakis and Bergeles (1995), Tu *et al.* (2008)]. In this study, the second order upwind scheme is selected to achieve improved accuracy via the following equation[FLUENT (2006B)]:

$$\phi_f = \phi + \nabla\phi \cdot \vec{r} \quad (3-5)$$

where  $\phi_f$  is the face value of the cell centered and  $\nabla\phi$  is the gradient in the upstream cell and,  $\vec{r}$  is the displacement vector from the upstream to the cell centroid.

The gradient  $\nabla\phi$  of a given variable  $\phi$  is used to discretize the convection and diffusion terms in the flow equations. All the gradients are computed in Fluent 6.3 according to Green-Gauss Cell-Based methods. Consequently, the discrete form to compute the gradient of the scalar  $\phi$  at the cell center via the following equation:

$$(\nabla\phi) = \frac{1}{\Omega} \sum_f^N \overline{\phi_f} \overline{A_f} \quad (3-6)$$

By default, the face value  $\overline{\phi_f}$  is calculated from the average values at the neighboring cell centers using the following relationship:

$$\overline{\phi_f} = \frac{\phi_{f_i} + \phi_{f_{i+1}}}{2} \quad (3-7)$$

where  $\phi_{f_i}$  and  $\phi_{f_{i+1}}$  are the neighboring cell center values

### 3.4 Flow models

Turbulence is a natural phenomenon in fluids which occurs when velocity gradients are high, resulting in significant disturbance in flow domain. Turbulent flows invariably come in contact with boundaries and are always characterized by three dimensional, random fluctuations. Turbulence requires a substantial modification of the laminar Navier-Stokes equations resulting in even more complex non-linear Partial Differential Equations (PDE). The successful solution of turbulent flow problems drastically depends on how accurately these new terms can be modeled in terms of the other flow variables. There are basically four approaches to handle these additional terms:

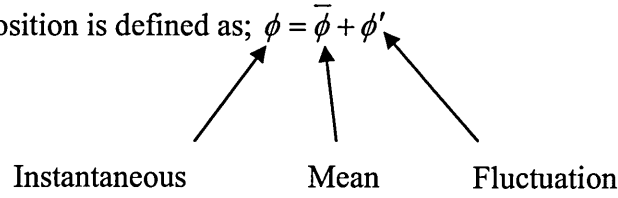
1. Direct Numerical Simulation (DNS)
2. Large Eddy Simulation (LES)
3. Detached Eddy Simulation (DES)
4. Reynolds Averaged Navier Stokes (RANS)

The Reynolds Averaged Navier-Stokes (RANS) equations are the most popular approach implemented in CFD calculations for realistic engineering problems which can be applied to perform numerical approximations. [Lucas (2005), Chung (2002)].

### 3.4.1 Reynolds Averaged Navier Stokes (RANS) equation

The methodology is based on the decomposition of the flow variables into a mean and a fluctuating part. Hence, the governing N-S equations (3-1 -3-3) can be solved for the mean values, which is the most relevant for engineering applications. Time averaging of mass and momentum equation for either incompressible or lower compressible flows can then be performed [Blazek (2005)].

Since Reynolds decomposition is defined as;  $\phi = \bar{\phi} + \phi'$



Therefore:

$$\frac{\partial \bar{\rho}}{\partial t} + \frac{\partial}{\partial x_i} (\overline{\rho u_i}) = 0 \quad (3-8)$$

$$\frac{\partial}{\partial t} (\overline{\rho u_i}) + \frac{\partial}{\partial x_j} (\overline{\rho u_i u_j}) = -\frac{\partial \bar{P}}{\partial x_i} + \frac{\partial}{\partial x_j} \left[ \mu \left( \frac{\partial \bar{u}_i}{\partial x_j} + \frac{\partial \bar{u}_j}{\partial x_i} - \frac{2}{3} \delta_{ij} \frac{\partial \bar{u}_i}{\partial x_i} \right) \right] + \frac{\partial}{\partial x_j} (-\overline{\rho u'_i u'_j}) \quad (3-9)$$

where  $\frac{\partial}{\partial x_j} (-\overline{\rho u'_i u'_j})$  is the Reynolds stress (closure).

Transition between the Navier-Stokes (laminar) and Reynolds equations (turbulent) displays additional terms known as *closure terms*, which are due to turbulent fluctuating motion (where the prime and above-bar indicates the turbulence fluctuation and Reynolds averaging). It is necessary to produce a robust relation between the Reynolds stresses and the quantities of the mean motion [Schlichting and Gersten (2003)]. Some consideration is required to move from the eddy viscosity method to the Reynolds stress closures. Two assumptions are necessary.

First, the flow is assumed to be *not far* from equilibrium so that convection and diffusion are small compared to production and dissipation. Secondly, Reynolds number is high [Bradshaw *et al.* (1981)]. The following relationship is commonly employed:

$$\text{Boussinesq relationship: } R_{ij} = -\overline{u_i' u_j'} = 2 \frac{\mu_t}{\rho} S_{ij} \quad (3-10)$$

where  $S_{ij} = \frac{1}{2} \left( \frac{\partial u_i}{\partial x_j} + \frac{\partial u_j}{\partial x_i} \right)$  is the stress tensor.

The level of closure models can be:

- *Zero equation* (mean motion is unaffected by turbulence intensity and length scale,  $L$  is mixing length which is presumed known).

$$\mu_t = \rho L^2 \sqrt{2 S_{ij} S_{ij}}$$

- *One equation model* is assumed directly proportional to kinetic energy ( $k$  model) or turbulence viscosity (Spalart – Allmaras model).
- *The two-equation model* is less restrictive, both kinetic energy ( $k$ ) and dissipation  $\varepsilon$  or kinetic energy ( $k$ ) and vorticity  $\omega$  are represented by transport equations ( $k-\varepsilon, k-\omega$  models). [Eghlimi *et al.* (1997)] supposed and applied two models for ReNormalization Group (RNG) turbulence to predict turbulent gas particles flow in Eulerian formulation.
- *Full Reynolds stress closures.*

Therefore, the RANS equation model includes all of the flow eddies. The objective in RANS turbulence modeling is to represent the unknown Reynolds stress (closure) in terms of the known (mean flow).

### 3.4.2 $k-\varepsilon$ Turbulent flow equation

Launder and Spalding proposed the two-equation turbulence model, which includes kinetic energy ( $k$ ) of the fluctuating motion and kinematic rate of dissipation ( $\varepsilon$ ) [Patankar (1980)]. Clearly, CFD transport equations also allow additional phenomena to be simulated, for example, non-reacting gas mixtures, which are introduced as a jet in a crossflow at a different density as described by Renze *et al.* (2008). Consequently, the  $k-\varepsilon$  equation is the *command turbulence model* and widely employed in engineering simulations and this requires specification of the initial boundary conditions. These involve algebraic approximations for turbulence kinetic energy ( $k$ ) and its rate of dissipation ( $\varepsilon$ ) via a semi-empirical model. The ( $k-\varepsilon$ )

turbulence model has been applied to incompressible flow and is widely used in FLUENT, for which the initial boundary conditions need to be supplied. The turbulence kinetic energy ( $k$ ) and its rate of dissipation ( $\varepsilon$ ) are a *semi-empirical* model; hence these equations can be written as:

$$\frac{\partial}{\partial t}(\rho k) + \frac{\partial}{\partial t}(\rho k u_i) = \frac{\partial}{\partial x_j} \left[ \left( \mu + \frac{\mu_t}{\sigma_k} \right) \frac{\partial k}{\partial x_j} \right] + G_k + G_b - \rho \varepsilon - Y_M + S_K \quad (3-11)$$

$$\frac{\partial}{\partial t}(\rho \varepsilon) + \frac{\partial}{\partial x_i}(\rho \varepsilon u_i) = \frac{\partial}{\partial x_j} \left[ \left( \mu + \frac{\mu_t}{\sigma_\varepsilon} \right) \frac{\partial \varepsilon}{\partial x_j} \right] + C_{1\varepsilon} \frac{\varepsilon}{k} (G_k + C_{3\varepsilon} G_b) - C_{2\varepsilon} \rho \frac{\varepsilon^2}{k} + S_\varepsilon \quad (3-12)$$

where

$G_k$  is the general turbulence kinetic energy due to the mean velocity gradients

$G_b$  is the general turbulence kinetic energy due to buoyancy

$Y_M$  is the contribution of the fluctuating dilation in compressible turbulence to the overall dissipation rate.

Turbulent kinetic energy ( $k$ ) is used as form of velocity scale ( $\theta$ ) and the dissipation rate ( $\varepsilon$ ) as length scale ( $l$ ).

Noting that:  $\theta = k^{(0.5)}$  and  $l = \frac{k^{(\frac{3}{2})}}{\varepsilon}$

$\mu_t$  : is the turbulence (or eddy) viscosity,  $\mu_t = C_\mu \rho \theta l = \rho C_\mu \frac{k^2}{\varepsilon}$

$C_{1\varepsilon} = 1.42$

$C_{2\varepsilon} = 1.68$

$C_\mu = 0.085$

$\sigma_k = 0.7194$

$\sigma_\varepsilon = 0.7194$

In this thesis, computations were completed in **FLUENT 6.3** via a series of steps, including grid checking, model solver definition (segregate implicit CFD technique) selection and turbulence simulation with the standard RNG( $k-\varepsilon$ ) model. The ReNormalization Group RNG model suggested by Yakhot *et al.* (1992). RNG model is employed in this study to renormalize the Navier–Stokes equations, to account for the effects of *smaller* scales of motion. Basically, the RNG turbulence model is derived

from instantaneous Navier–Stokes equations using the mathematical technique known as RNG theory. The RNG model includes modification terms for the rate of dissipation ( $\epsilon$ ) with scale expansion for Reynolds stress to improve the accuracy for rapidly strained flow and provides an effective turbulent viscosity for low Reynolds number effects. The RNG model is a powerful methodology in modern turbulence studies and has been used by Zhang and Orszag (1998) to simulate high Reynolds number pipe flow. In addition to, Lakehal (2002) has elucidated that there is little advantage to using different viscosity data for Reynolds Stress turbulence Model (RSM) as compared with the eddy viscosity model. Recently, wall bounded turbulence was investigated numerically by Daud *et al.* (2011A) with different turbulence models (Spalart–Allmars,  $k-\epsilon$ , Re-Normalization Group (RNG), and Shear Stress Transport (SST)  $k-\omega$ ) and compared with DNS and experimental data. The RNG numerical results in particular, achieved good correlation.

### 3.4.3 Wall Treatment

The amount of heat transfer is strongly linked to the flow structure near the solid wall associated with the boundary layer and also to the turbulence model effects. Consequently, the flow structure near the wall region can be divided principally into three layers. Firstly, the *interior layer (viscous layer)* is almost laminar and the viscosity plays a dominant role in momentum (and heat transfer). Secondly the *intermediate region (buffer layer)* is affected by the viscosity layer and the turbulent layer. Finally the *outer layer (turbulent layer)* is fully turbulent and here turbulence exerts a major role. Figure (3-2) shows turbulent boundary layer universal velocity profile.

Since the viscous sub layers are not resolved in most practical calculations with the  $k-\epsilon$  model, numerical accuracy is sufficiently achieved through refining the boundary layer mesh near the wall at the sub-layer region. In this work, two kinds of wall treatments have been employed, namely *Standard Wall Function (SWF)* and *Enhanced Wall Treatment (EWT)*.

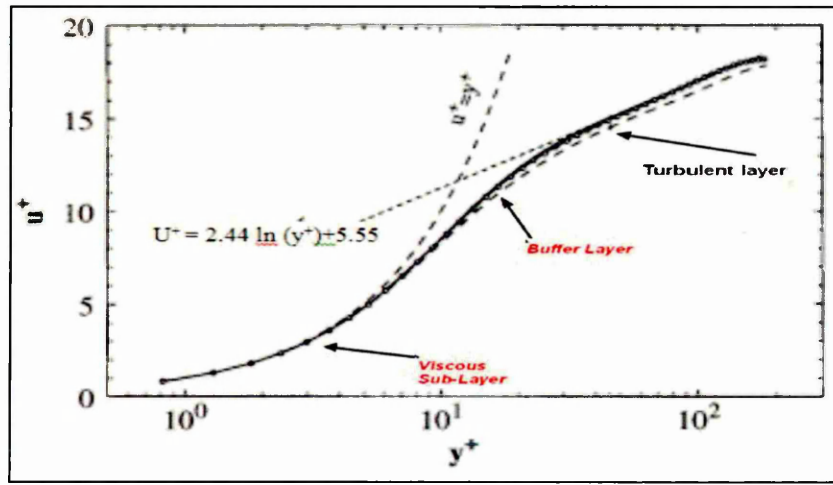


Figure (3-2) Turbulent boundary layer universal velocity profile [Kravchenko *et al.* (1996)]

- **Standard Wall Function approach (SWF)**

In this approach, there is no ability to compute the flow within the viscous and buffer region of the boundary layer where the molecular diffusion is significant. Fully turbulent effects are placed next to the wall grid points. In 1972, Launder and Spalding proposed a semi-empirical formulation to describe field variable profiles in full turbulence [Launder and Spalding (1972)]. However, the simple boundary conditions for wall shear are replaced with the wall-function. Hence, wall shear in the cell adjacent to the wall is calculated using equation:

$$\tau_w = \frac{C_\mu^{(1/4)} k^{(1/2)} \rho u}{\frac{1}{0.42} \ln\left(\frac{9.793 \rho y C_\mu^{(1/4)} k^{(1/2)}}{\mu}\right)} \quad (3-13)$$

The  $k$ - $\epsilon$  model with SWF is normally suggested for high Reynolds number simulations, where the viscosity-affected region (viscous sublayer and buffer layer) is not resolved. Instead, wall functions are used to bridge the wall and the fully turbulent region.

- **Enhanced Wall Treatment (EWT)**

EWT involves near-the-wall modeling and combines the two-layer model and enhancement wall function. Therefore, the two layer model approach uses a *wall-distance based Reynolds number* ( $Re_y = \rho u y / \mu$ ) and divides the simulation domain into a *viscosity-affected region* (typically  $Re_y < 200$ ) and a *fully turbulent region*

( $Re_y > 200$ ) [Wolfstein (1969), Chan and Patel (1988)]. Both turbulent viscosity and dissipation rate are determined from modified formulas:

$$\begin{aligned}\mu_\tau &= \rho C_\mu \sqrt{k} l_\mu \\ \varepsilon &= \frac{k^{(3/2)}}{l_\varepsilon}\end{aligned}\tag{3-14}$$

Where the two mixing lengths are defined by:

$$\begin{aligned}l_\varepsilon &= C_l y [1 - \exp(-\frac{Re_y}{A_\varepsilon})] \\ l_\mu &= C_l y [1 - \exp(-\frac{Re_y}{A_\mu})]\end{aligned}\tag{3-15}$$

$$\text{With } A_\mu = 70, \quad C_l = k C_\mu^{(-3/4)}, \quad A_\varepsilon = 2C_l$$

The enhancement wall function is employed in all flow domains near the wall. Namely, at the Laminar sublayer, buffer layer and turbulent layer.

However, the fully turbulent law will be modified and is extended to account for other effects such as pressure gradients or variable properties. The velocity profile in this case is represented where  $3 < y^+ < 10$  (buffer layer). [Kader (1993)]

### 3.5 CFD simulation procedure in FLUENT

Three main CFD simulation procedure steps are summarized in Figure (3-3). Namely, the pre-processor, solver and postprocessor, appear as coloured arrows on the flowchart (left hand side) to assist in understanding the technique followed. The Pre-processor step commences with an attempt to create CAD wire frame geometry for the fluid flow physical domain. GAMBIT is used to build the model geometry. There is an additional feature to import Initial Graphics Exchange Specification files (IGES). This feature facilitates importing the geometry wire frame constructed using other CAD packages. Once the physical domain geometry is represented in the GAMBIT editor as a wire frame, a *surface generation* procedure is employed to construct the solid surface or skin using the wire frame geometry or so called body skeleton. Subsequently, GAMBIT performs stitching of the solid surface into integrated volume sub-blocks.

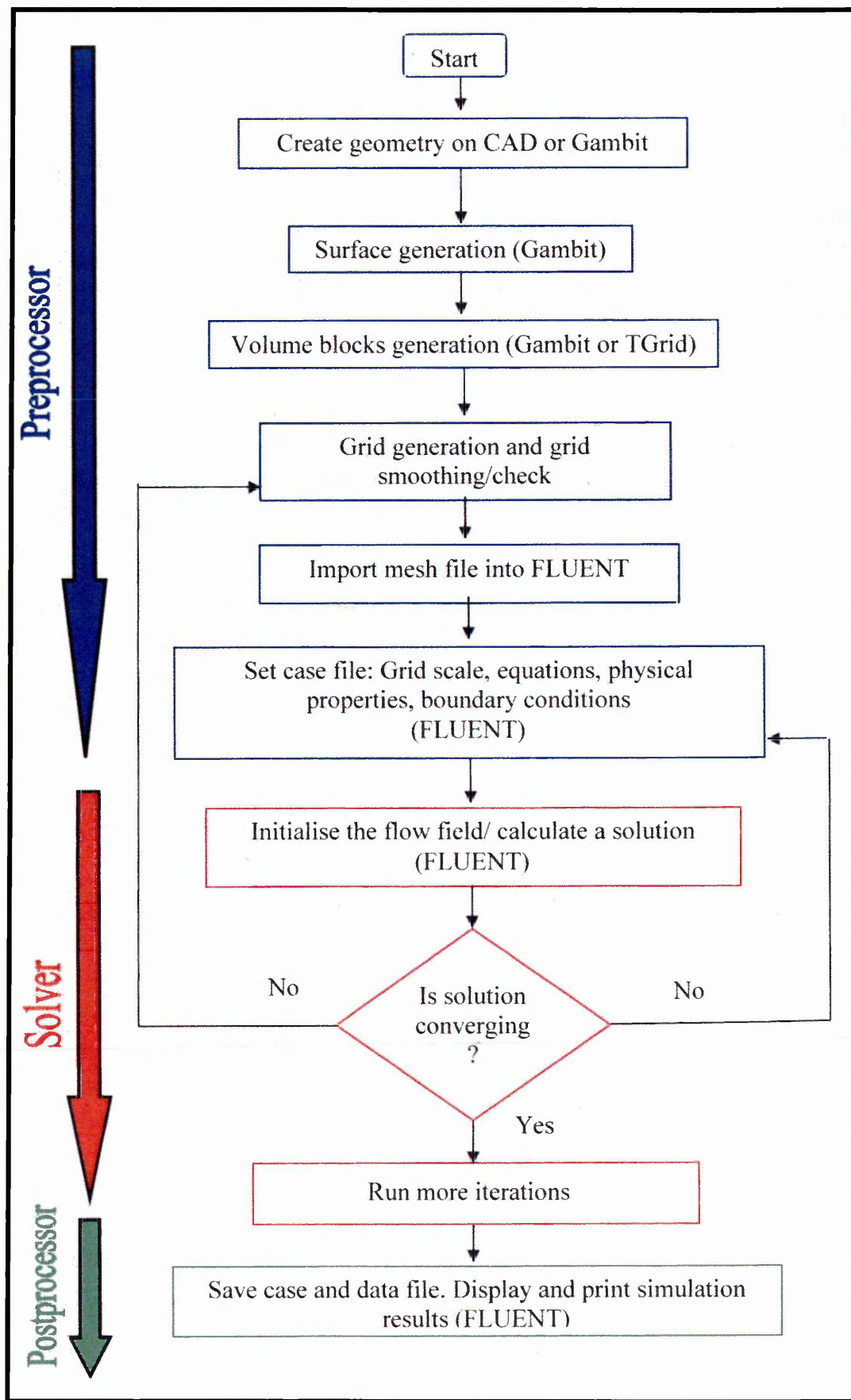


Figure (3-3) FLUENT simulation structure [FLUENT (2006B)].

However, GAMBIT allows users to select different varieties of mesh elements for grid generation. Table (3-1) and Table (3-2) lists the options available for surface mesh generation in GAMBIT. In order to complete solid volume meshing in the GAMBIT software, there are option elements used to constitute in two dimensions (2D) or three dimensions (3D) as shown in Figure (3-4). These include tetrahedral, hexahedral and also element type options such as TGrid or Cooper.

**Table (3-1): GAMBIT face meshing element options [FLUENT (2006A)]**

Option	Description
Quad	Specifies that the mesh includes only quadrilateral mesh element
Tri	Specifies that the mesh includes only triangular mesh element
Quad/Tri	Specifies that the mesh is composed primarily of quadrilateral mesh elements but includes triangular corner elements at user specified location.

**Table (3-2): GAMBIT face meshing type options [FLUENT (2006A)]**

Option	Description
Map	Creates a regular, structured grid of mesh elements.
Submap	Divides an unmappable face into mappable regions and creates structures grids of mesh elements in each region.
Pave	Creates an unstructured grid of mesh elements.
Tri Primitive	Divides a three- sided face into three quadrilateral regions and creates a mapped mesh in each region.
Wedge Primitive	Creates triangular elements at the tip of wedge shaped face and creates a radial mesh outward from the tip.

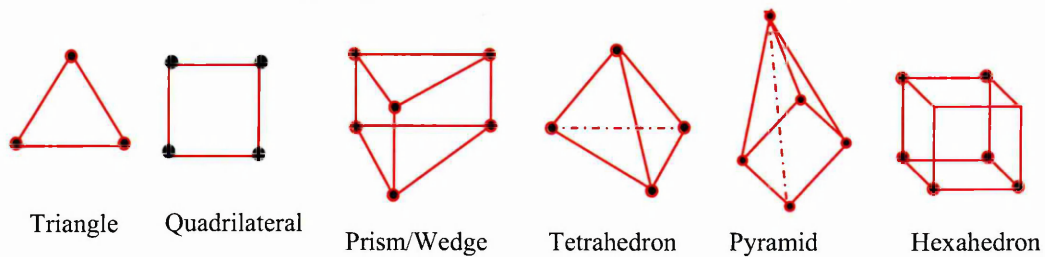


Figure (3-4) Two dimensional and three dimensional cell type [FLUENT (2006A)]

The process of grid generation strongly depends on a number of factors including the numerical calculation procedure, degree of geometry complexity, computational domain and computer power. Consequently, *unstructured* meshes can be successfully used for unstructured volumes (complex shapes) while structured meshes are utilized for uniform volume shapes. Once the volumes have been meshed, the flexibility of GAMBIT allows the checking of mesh quality (skewness degree). The best meshing is achieved when the skewness degree is less than 0.85. If the mesh skewness is between 0.85 and 1, this corresponds to a high level of skewness within the geometry.

Appropriate physical boundary conditions can be defined and employed consecutively in the GAMBIT and FLUENT software for the required surface, walls, fluid properties and flow domain to perform numerical simulation. Therefore, after acquiring a converged solution (the solution convergence strategy will be demonstrated in chapter six), the FLUENT editor offers presenting numerical results as velocity vector plots, counter plots and XY plots. Numerical solution and set up can be saved as *case* and *data* files for further calculations or refinement.

### 3.6 FLUENT solver technologies

There are two approaches which may be used in any CFD code for simulating fluid flow and heat transfer. Firstly, the **pressure-based approach** which traditionally has been used for incompressible and *mildly* compressible flow as well as laminar and turbulent flows [Djavareshkian and Reza-Zadeh( 2006)], provides a high resolution scheme in calculating interference density values to enhance the shock capturing property. This study utilized the **Semi-Implicit Method for Pressure Linked Equation (SIMPLE)** algorithm to solve velocity-pressure coupling with a segregated implicit technique.

Secondly, the **density-based approach** has been designed for high speed compressible flow with an existing two formulation methodology- implicit and explicit. In contrast to this approach, the pressure-based approach uses only an implicit formulation.

Both formulations are alternate methodologies for linearizing the coupled equations. The implicit technique is used for steady flow and provides faster runs but requires much more memory and there is only one set of unknown variable in all the mesh cells at any one time.

### 3.6.1 FLUENT solution algorithms

There are two strategic steps used in the FLUENT software for solver algorithm methods. These are the *segregated* solver and the *coupled* solver. In this thesis, the segregated solver has been used.

#### Segregated solver

Segregated solution method is a very common solver. It is widely implemented in numerous industrial flow applications. This type of solver is a *non-linear* solver. Consequently, several iterations of the solution loop must be performed before a converged solution is attained. The solution steps for the segregated solver are illustrated in Figure (3-5) and are as follows:

1. Fluid properties are updated based on the current solution. If the calculation has just commenced, the fluid properties will be updated from the initialized solution.
2. The  $u, v$  and  $w$  momentum equations are each solved using the current value for pressure and face mass fluxes, in order to update the velocity field.
3. Solve the pressure correction equation using obtained velocity and mass flux.
4. Correct face mass flux such that continuity is satisfied and the pressure and the velocity field using pressure correction are obtained from step 3.
5. Suitable equations for scalars such as turbulence and energy are solved using the previous update for the other variations.
6. A check for convergence of the equation set is made [FLUENT(2006B)].

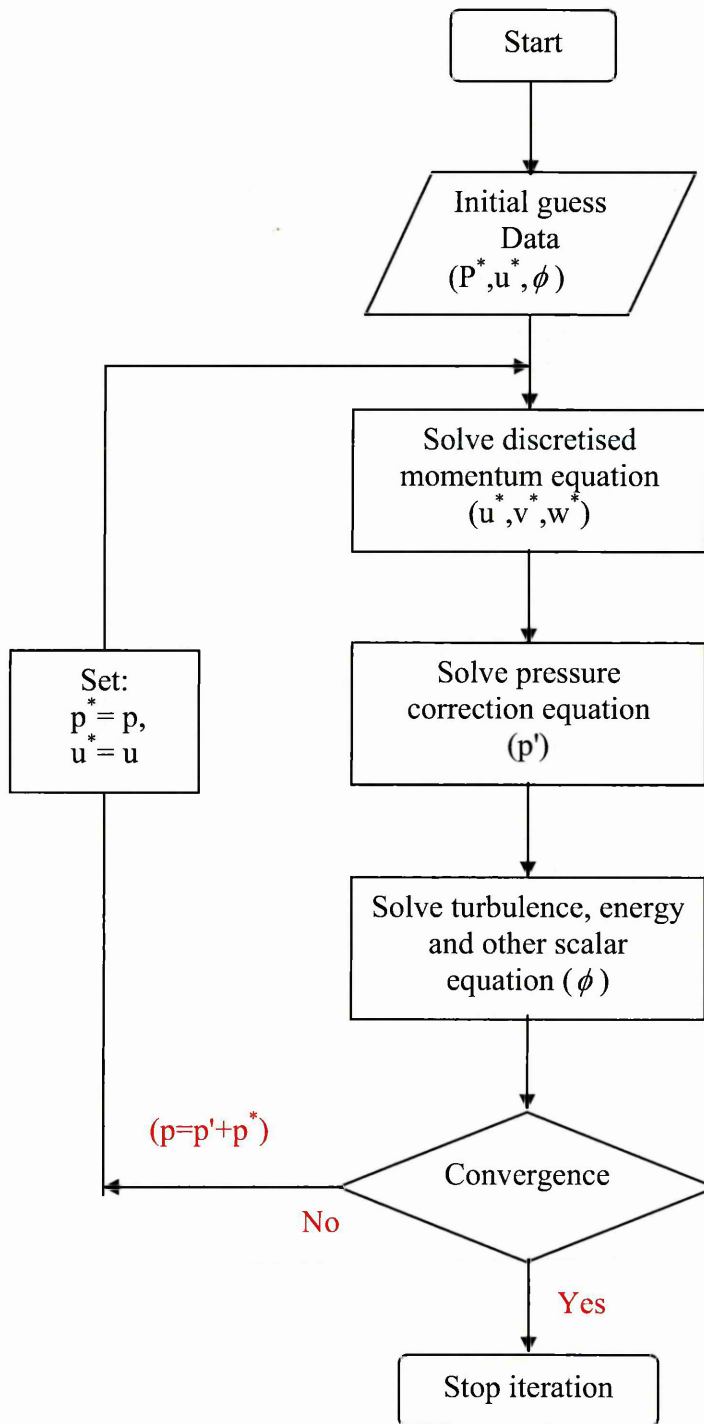


Figure (3-5) Pressure based segregated algorithm [FLUENT(2006B)].

## Coupled solver

The difference between the segregated solver and the coupled solver is that conservation equations are solved sequentially in the former and not in the latter. The details of the coupled solver method are illustrated in Figure (3-6) below and listed as follows:

1. Fluid properties are updated, based on the current solution. If the calculation has just begun, the fluid properties will be updated from the initialized solution.
2. The continuity, momentum, energy and species equations are solved simultaneously.
3. Where appropriate, equation for scalars such as turbulence and energy are solved using the previous updated values of the other variables
4. A check for convergence of equation set in made [FLUENT(2006B)].

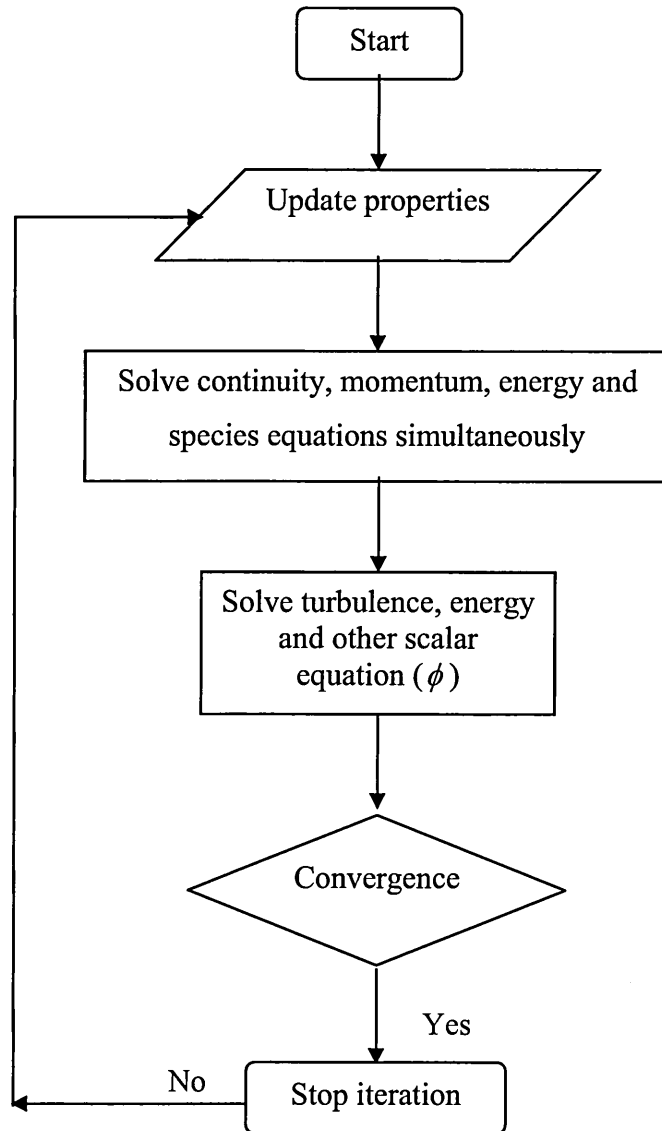


Figure (3-6) Coupled solver method [FLUENT(2006B)].

### 3.7 Summary

This chapter briefly reviewed the theory of CFD simulation. Namely, pre-processing, processing equations (continuity equation, momentum equation, energy equation and turbulence equation) and post-processing. In this thesis, the finite volume method has been employed based on the **FLUENT 6.3** solver. The appropriate partial differential conservation equations are discretized to describe and evaluate the flow surrounding each cell in the computational domain. The **SIMPLE** algorithm is employed to solve velocity-pressure coupling with a segregated implicit technique. Moreover, a second order upwind scheme has been deployed to increase accuracy of the numerical solution.

## *Chapter Four*

*(Aerodynamic CFD Validation) Channel  
flow & NACA 0012 Modeling & Results*

## 4.1 Introduction

In the present study, Computational Fluid Dynamics (CFD) is utilized as a tool-to simulate gas turbine aerodynamics and heat transfer. It provides many useful numerical algorithms suitable for solving flows under various operating boundary conditions and in many geometrically complex regions [Djavareshkian and Reza-zadeh (2006)]. Intrinsic to robust CFD simulations, is the need to understand how to optimize the solver through the selected mesh type, mesh quality (standard wall function and enhanced wall treatment), different state-of-the-art turbulence models, Reynolds number, comparison (benchmarking) with other numerical methodologies for example. DNS (the most accurate/expensive method) and also with experimental results. In this research, three different benchmarks are used to assess the relative performance and numerical calculation accuracy of the FLUENT's solver and various turbulence models which can be used to accomplish refined prediction of aerodynamic flow and heat transfer characteristics for a gas turbine blade.

In this chapter, two-dimensional fully developed channel flow and turbulent flow around a NACA0012 airfoil model is presented. The FLUENT simulation results of the NACA0012 airfoil provide indication of the accuracy of the approach adopted in this thesis since they demonstrate strong verification and validation of the FLUENT results with previous studies. Consequently, topics covered in this chapter include the following;

1. Benchmarking Geometry, Mesh and Boundary Conditions.
  - a. Turbulent Channel Flow.
  - b. NACA 0012 Airfoil Flow.
2. CFD Validation Results
  - a. Fully developed Channel Flow Results
  - b. NACA0012 Aerofoil Turbulent Flow Results

## 4.2 Benchmarking geometry, mesh and boundary condition

### 4.2.1 Turbulent channel flow

Figure (4-1) illustrates the two-dimensional turbulent flow model in a channel of length,  $L=1$  m, and width,  $2H=2$  m. Fully developed channel flow can be satisfied numerically through specifying boundary conditions for the channel as *no slip* at the top and bottom walls and *periodic boundaries* for the inlet and outlet flows. The meshing process for the turbulent channel flow is performed using structured and unstructured hybrid (Quad+Tri) meshes. The mesh refinement been conducted in the near wall regions with 800 (coarse), 1800 (medium) and 13300 (fine) cells, respectively, to assess grid independence, capture the flow field characteristics (gas dynamic in channel flow) and permit an accurate evaluation of the shear stress near the wall.

Fully developed turbulent channel flow with constant cross sectional area, is achieved when the velocity profile becomes independent of the streamwise coordinate at some distance from the inlet.

In the numerical simulations, in order to achieve fully developed turbulent channel flow, periodic boundary conditions have been employed. This has been performed in FLUENT by using the "link option" between the inlet and outlet edges via a specified reference vertex. The velocity components exhibits a periodic behavior, in the streamwise direction. For a 2D flow, that is  $u(x,y)=u(x+L, y)$  and  $v(x,y)=v(x+L, y)$ .

The physical properties of the incoming fluid in turbulent channel flow are defined as follows: density ( $\rho$ ) is  $1 \text{ kg/m}^3$  and dynamic viscosity ( $\mu$ ) =  $0.0017 \text{ kg/ms}$ , the flow at the channel is set as periodic at both of the inlet and outlet. A no-slip wall boundary condition is applied at the channel walls. In addition, the initial boundary condition details for friction Reynolds number,  $Re_\tau=590$  are defined as follows; pressure gradient ( $\partial P/\partial x$ ) =  $1 \text{ Pa/m}$  and velocity ( $u$ ) =  $1 \text{ m/s}$ . The data and boundary conditions are used in the FLUENT 6.3 code. All these boundary conditions have been extracted from Moser et al. [Moser *et al.* (1999)].

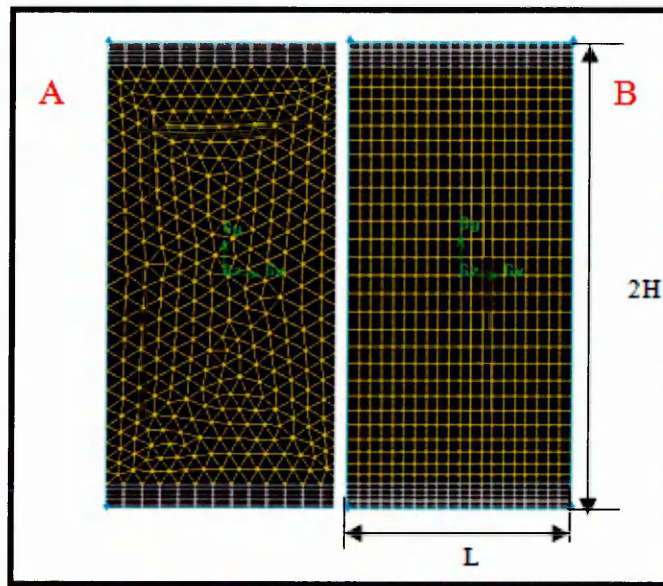


Figure (4-1) Fully developed turbulent channel flow for A) Triangular Mesh B) Quad Mesh [Daud *et al.* (2011A)]

#### 4.2.2 NACA0012 airfoil flow

As illustrated in Figure (4-2), the second scenario considered is the two-dimensional turbulent flow around a NACA0012 airfoil model. The axial chord length,  $C_x$  is 0.3 m, where ( $C_x$ ) represents the blade axial chord and the blade width  $C_y$  is 0.036 m. In addition, the simulation flow box dimensions is taken as (10, 2.34)  $C_x$ . Triangular mesh type are utilized to investigate turbulent flow. Approximately 497,822 cells (elements) were generated in addition to a boundary layer mesh constructed to confine flow around the airfoil. The NACA 0012 airfoil is surrounded by air flow with an axial chord-based Reynolds number (in terms of  $C_x$ ) of  $4 \times 10^5$ . The air properties are density ( $\rho = 1.225 \text{ kg/m}^3$ ) and viscosity ( $\mu = 1.7894 \times 10^{-5} \text{ kg/ms}$ ). The boundary condition for the inlet velocity is  $u = 20 \text{ m/s}$  and at a static pressure is prescribed at the outlet. The physical domain of the turbulent flow around a NACA 0012 airfoil is therefore defined as a computational domain via efficient mesh generation. The number of cells have been selected influenced by two factors: firstly, a Boundary Layer (B.L.) mesh for the upper and lower airfoil wall to capture the flow dynamic structure when  $y^+ \sim 12$ , and secondly, far away from the wall, via an unstructured mesh type (Triangular) to evaluate the flow accurately in this region.

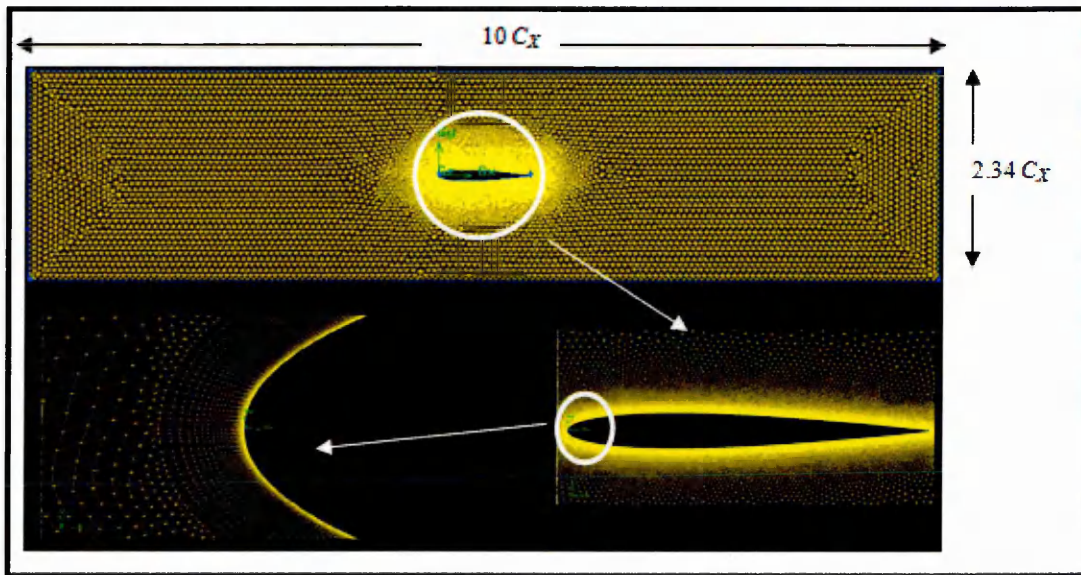


Figure (4-2) NACA 0012 airfoil domain and Mesh. [Daud *et al.* (2011A)]

### 4.3 Aerodynamic CFD validation results

#### 4.3.1 Fully developed channel flow.

The study of the fully developed turbulent channel flow main purpose is to understand the structure of gas dynamic near the wall by plotting mean dimensionless velocity profiles in the wall unit  $u^+ = u/u_\tau$  (based on wall shear velocity) via  $y^+$  ( $y^+ = \rho u_\tau y/\mu$ ). The effects of mesh type for fully developed channel flow are illustrated in Figure (4-3) (quadrilateral and triangular type) and the number of cells are 800 and 820 respectively. Figure (4-1) shows the mesh type besides quality with identical quadrilateral mesh density used near walls. For turbulent wall-bounded flow, the dominated flow phenomena just happen in the near wall region. Thus, with the above mesh strategy, the trajectory curves of  $u^+$  for the quadrilateral and triangular mesh for the fully developed turbulent channel flow seem similar. This phenomena is also observed through plotted kinetic energy  $K^+$  in Figure (4-4). This is a very important feature for commercial CFD software, such as FLUENT, which has the ability to extend simulations into more complicated geometries by just controlling the near wall mesh quality.

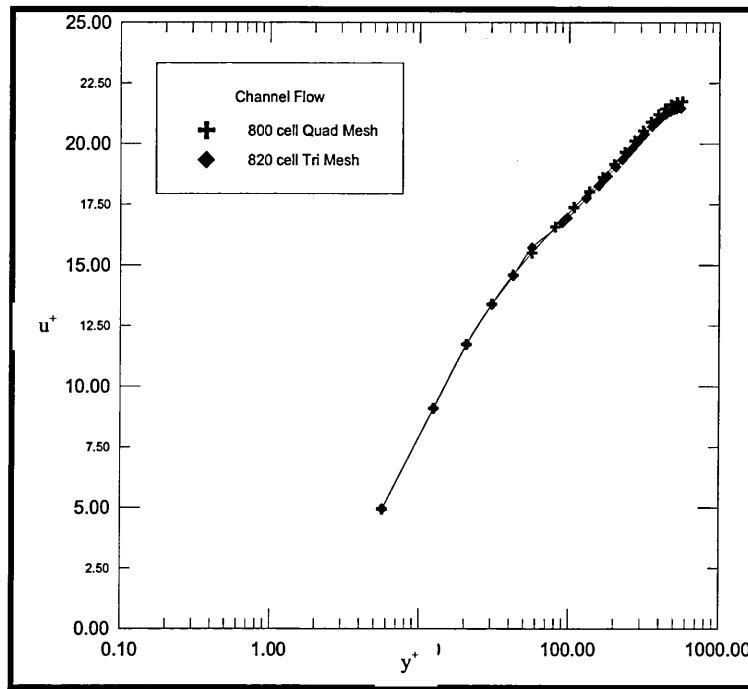


Figure (4-3) Mean velocity profile: Mesh type effects for fully developed channel flow [Daud *et al.* (2011A)]

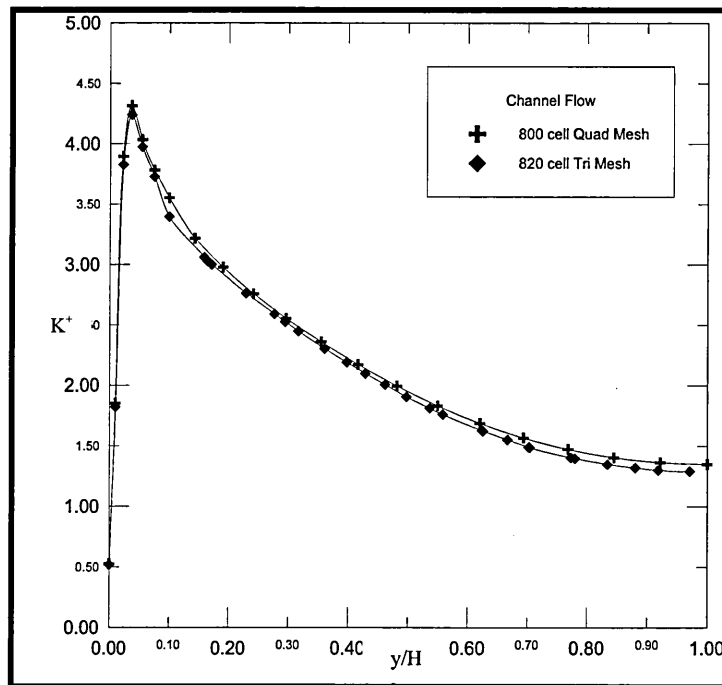


Figure (4-4) Mean velocity profile: Mesh type effects for fully developed channel flow [Daud *et al.* (2011A)]

Figure (4-5) shows the effect of grid refinement with an increased number of cells compared with DNS solution of Moser *et al.* (1999). The first grid point away from the wall for 800 and 1800 cells is located at  $y^+ = 6$  and 2. In addition, by increasing the number of cells to 13300, the accuracy is improved to coincide with the DNS data as

demonstrated by superposition of the trajectory curves. In fact, within the sub layer region especially,  $y^+ < 3$ , both DNS and the present CFD calculation follow a linear law of the wall. The numerical solution was considered valid with the  $k$ - $\epsilon$  model (with 1800 and 13300 cells) employing Enhancement Wall Treatment (EWT).

A key objective in optimized CFD is to check that the best grid refinement has been employed to achieve a good solution. Figure (4-5) illustrates the turbulent channel flow mean velocity profile in the wall unit ( $u^+ \sim y^+$ ) and compared with log law in addition to DNS data. All the numerical solutions in Figure (4-5) use the wall enhancement  $k$ - $\epsilon$  turbulence mode. The numerical solution at the sub-layer region is presented at  $y^+ < 10$  which is in good agreement with log law, the latter being computed from the equation:

$$U^+ = 2.44 \ln(y^+) + 5.55 \quad (4-1)$$

The boundary layer mesh near the wall must be adequately refined to increase the accuracy of the results at this area. Beyond  $y^+ = 10$ , the flow structure appears to deviate from the log law which is certainly attributable to the effects of turbulent flow. Figure (4-6) demonstrates the distribution of  $K^+$  for the channel flow and good agreement has been obtained between the numerical simulation and DNS solutions of Moser et al. (1999), especially at the peak location at  $y/H = 0.037$ . It is interesting to notice that the coarse mesh (800 cell) gives better agreement with DNS solution at  $y/H > 0.1$ . Consequently, the difference can be due to the limitation of turbulence model. The  $k^+$  can be calculated from:

$$K^+ = k/(u_\tau)^2 \quad (4-2)$$

where  $k$  is the kinetic energy,  $u_\tau$  is the wall shear velocity.

Considerable effort is devoted to clarify which turbulence model yields a better solution for wall-bounded turbulence.

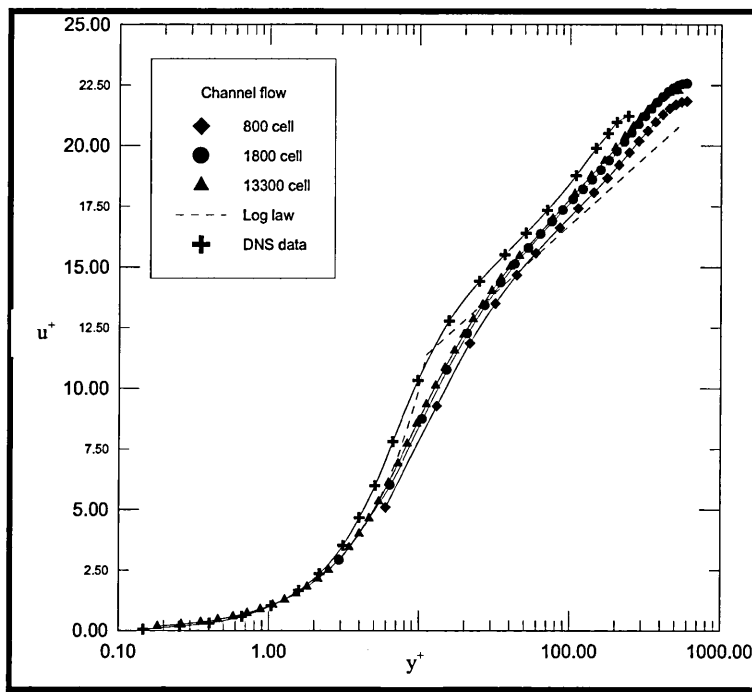


Figure (4-5) Mean velocity profile: Mesh refinement effects for different number of cells compared with DNS of Moser *et al.* (1999) at  $Re_\tau = 590$  [Daud *et al.* (2011A)]

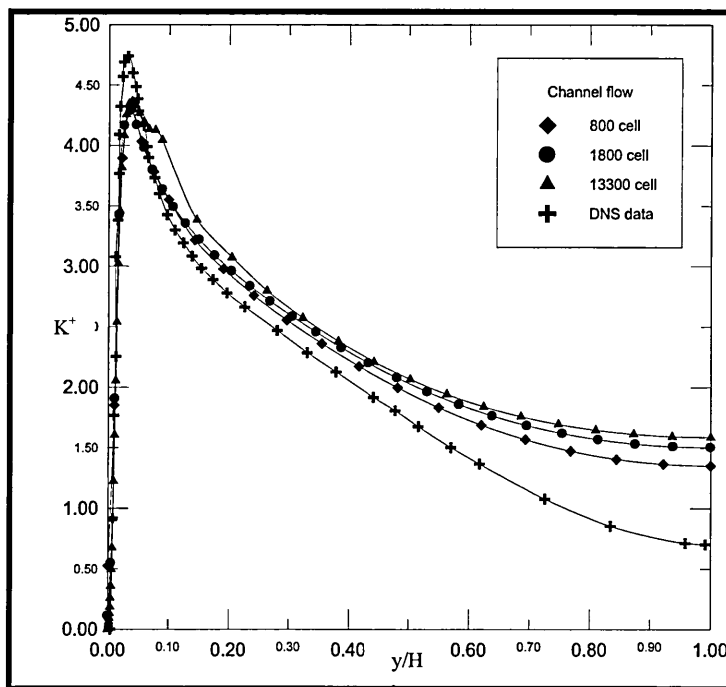


Figure (4-6) Kinetic energy for different number of cells compared with DNS of Moser *et al.* (1999) at  $Re_\tau = 590$  [Daud *et al.* (2011A)]

For the case of turbulent channel flow, Figure (4-7) illustrates the numerical solutions (13300 cell) for the mean velocity profile  $u^+$  vs.  $y^+$  for different turbulence models, compared with the DNS solutions of Moser *et al.* (1999). The RNG and k- $\epsilon$  turbulence models exhibit better correlation with the DNS solutions, compared with *SST K- $\omega$*  and *S-A* (Spalart-Allmars) turbulence models.

The accuracy of numerical calculation mainly depends on the *quality* of the mesh and the *number* of cells. The velocity profile is affected by these features. Figure (4-8) shows mesh quality effects with and without Boundary Layer (B.L.) mesh features. The first point of the gas dynamic velocity profile for 800, 820 has been located at  $y^+ = 6$  absolutely due to the B.L. mesh near the wall and the quantity of cells. The coarse mesh was also generated for fully turbulent channel flow and the first grid point away from wall is  $y^+ = 30, 70$  for 798 and 36 cells respectively. As mentioned in the FLUENT 6.3 User Manual (2006B), the Standard Wall Function (SWF) profile requires that the first node nearest the wall should be within the range of  $50 < y^+ < 200$ . Since the gradient in Fig 3-2 alters at  $y^+ \sim 12$  in the viscous sub-layer- it is vital therefore to define the first node to capture this change. Hence in the present simulations in order to get a reasonable result, the first grid point away from wall should be  $y^+ \sim 12$ . It is important layer to defined B L. since the viscosity and turbulent effects are appears in this region see section 3.4.3. From Figure (4-8), the shape of the velocity profile corresponding to the coarse mesh for 798 cells is nearly the same as the fine mesh; but the velocity profile for 36 cells is not completely accurate, due to the poor resolution and the effect of neglecting the B.L mesh. (the velocity profiles is shifted to the left with increasing number of cells).

The numerical solution has been obtained for turbulent channel flow at  $Re_\tau=2320$  (friction Reynolds number), where this parameter is defined by.

$$Re_\tau = (\rho * u_\tau * H) / \mu \quad (4-3)$$

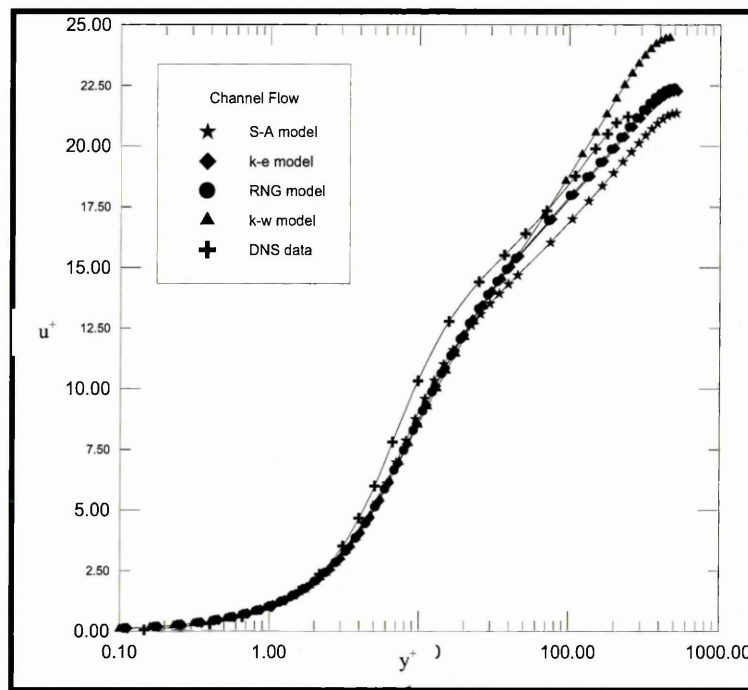


Figure (4-7) Mean velocity profiles: Effects of different turbulent model compared with DNS method Moser *et al.* (1999), at  $Re_{\tau} = 590$  [Daud *et al.* (2011A)]

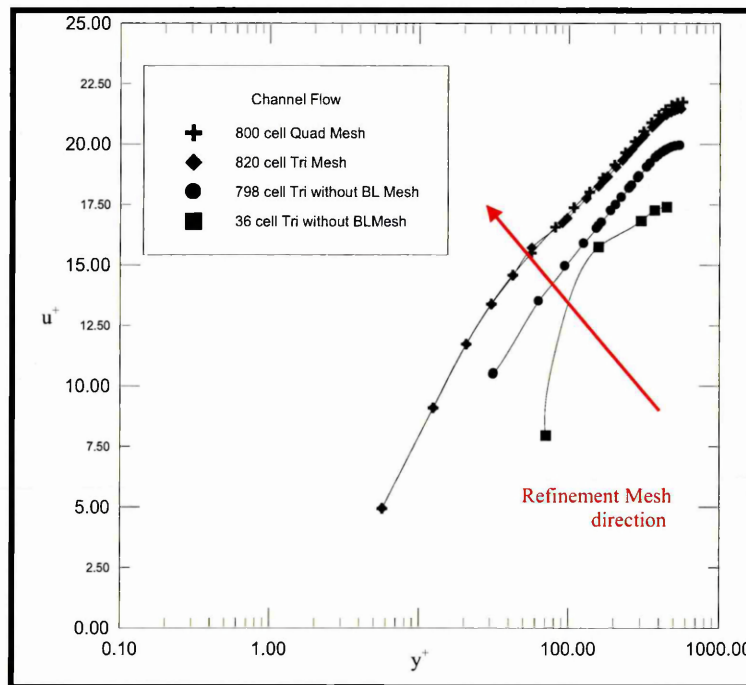


Figure (4-8) Mean velocity profiles: Mesh quality effects with and without boundary layer mesh (800, 820, 798, and 36 cells) [Daud *et al.* (2011A)]

Figure (4-9) shows the mean velocity profiles of the channel flow at  $Re_{\tau}=590, 2320$  conducted using the RNG turbulence model. It is evident that the deviation of the velocity for high Reynolds number at  $Re_{\tau}=2320$  and low Reynolds number at  $Re_{\tau}=590$  appears beyond  $y^+ = 200$  which is again caused by the intensity of the turbulent motion

and the Reynolds number effect. The velocity gradient in a turbulent channel flow has been demonstrated in Figure (4-10) for  $Re_{\tau}=590, 2320$ . The correlations between the friction of the Reynolds number and also the velocity gradient near the wall can be derived from the equation (4-3). Consequently, the final formula will be:

$$Re_{\tau} = (\rho^*(du/dy)_w / \mu)^{(1/2)} \quad (4-4)$$

However, the maximum value of velocity gradients represents maximum value of friction Reynolds number near the wall due to the velocity gradient (shear force), fluid property ( $\mu$ ) and type of wall (no slipping). The defined value of  $u_{\tau, D}$  was computed from the friction Reynolds number (590 or 2300 in this research) in equation (4-3). The CFD wall shear stress,  $\tau_w = \mu(du/dy)_w$ , has been calculated numerically in the FLUENT code, and so the converged CFD friction velocity can be calculated from equation (4-5)

$$u_{\tau} = \sqrt{\tau_w / \rho} \quad (4-5)$$

The percentage error is calculated from equation (4-6)

$$\text{Error \%} = \text{abs}(u_{\tau} - u_{\tau, D}) / u_{\tau, D} \quad (4-6)$$

The  $u_{\tau, D}$  value is the focus for the CFD simulations and Tables 4-1, 4-2 shows percentage error of the shear velocity between the numerical calculation with definition value to realize  $Re_{\tau}=590, 2320$  for different mesh number and turbulent model. The maximum error is 1.5453%, 0.1851% respectively. Thus, the numerical calculations of a fully developed channel flow are being achieved as the error is negligible when the first grid point is nearly at  $y^+ \sim 12$ .

**Table 4-1: The values of numerical and defined shear velocity at  $Re_\tau=590$**

$Re_\tau=590$	800 cell	1800 cell	13300 cell			
	RNG	RNG	S-A	k- $\epsilon$	RNG	k- $\omega$
$u_\tau$ Calculation	1.0116	1.017	1.0165	1.0185	1.0140	1.0034
$u_\tau$ definition	1.003	1.003	1.003	1.003	1.003	1.003
Error %	0.8574	1.3958	1.3459	1.5453	1.0967	0.0398
$y^+$	6	2	0.17			

**Table 4-2: The values of numerical and defined shear velocity at  $Re_\tau=2320$**

$Re_\tau=2320$	13300 cell RNG
$u_\tau$ Calculation	3.9513
$u_\tau$ definition	3.944
Error %	0.1851
$y^+$	0.17

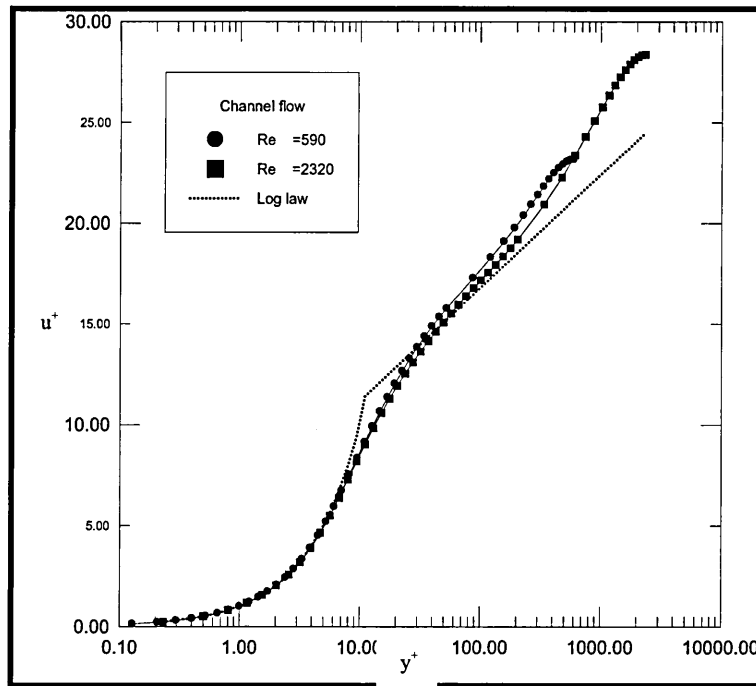


Figure (4-9) Mean velocity profiles: Effects of Reynolds number ( $Re_\tau= 590, 2320$ ) [Daud *et al.* (2011A)]

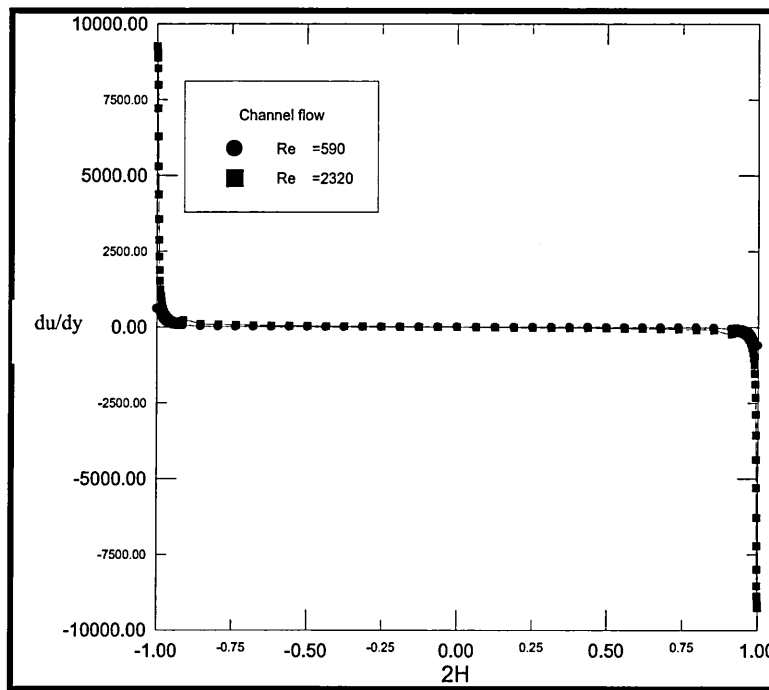


Figure (4-10) Velocity gradients: Effects of Reynolds number ( $Re_t=590, 2320$ ) [Daud *et al.* (2011A)]

#### 4.3.2 NACA0012 airfoil turbulent flow

The second part of this study concerns flow around the NACA 0012 aerofoil using different turbulence models ( $k-\epsilon$ , RNG, SST  $k-\omega$ ). Figure (4-11) illustrates the static pressure coefficient distribution  $CP$  for  $Re = 4 \times 10^5$ , which is related to static pressure and can be defined as equation (4-7)

$$CP = (P_{01} - P_S)/(P_{01} - P_{S2}) \quad (4-7)$$

Where  $P_{01}$  is the inlet total pressure,  $P_S$  is the static pressure on the surface of the airfoil, and  $P_{S2}$  is the outlet static pressure. The symmetric airfoil is orientated at  $0^\circ$  Angle of Attack (AoA) and the pressure distribution for upper and lower surface will be the same. Evidently,  $CP$  distributions for  $k-\epsilon$ , RNG, and  $k-\omega$  turbulent models show similar trajectories and good agreement with the experimental results of Sagrado (2007). The mean velocity profile of the NACA 0012 aerofoil has been plotted in Figure (4-12) for the  $k-\epsilon$  model with SWF and EWT features. The data of the mean velocity in Figure (4-12) corresponds to the logarithmic velocity law. Hence, the EWT velocity coincides much more closer with the log law and yields more accurate results compared to the SWF profile. Three different turbulence models ( $k-\epsilon$  RNG, SST $k-\omega$ ) have been tested to capture BL characteristics in the flow near the wall.

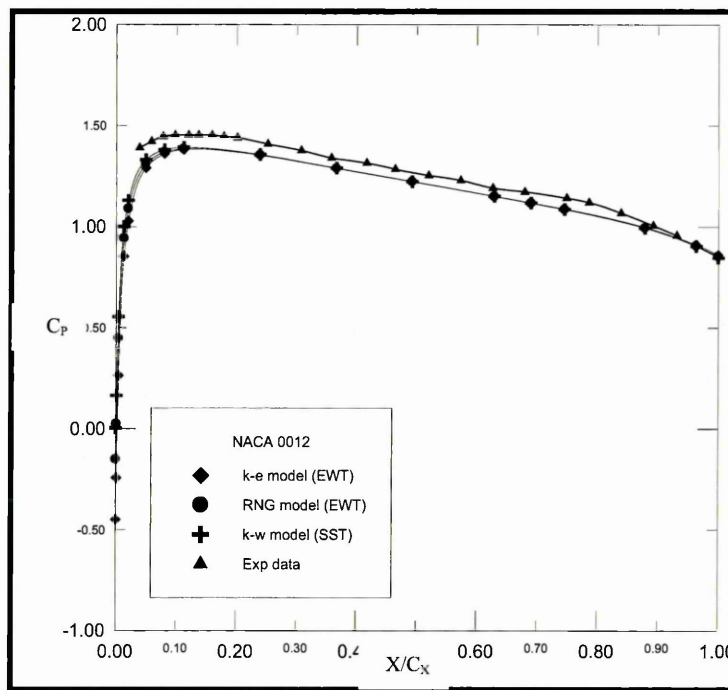


Figure (4-11) Static pressure distribution for the Reynolds numbers  $Re=4 \cdot 10^5$  compared with Sagrado (2007). [Daud *et al.* (2011A)]

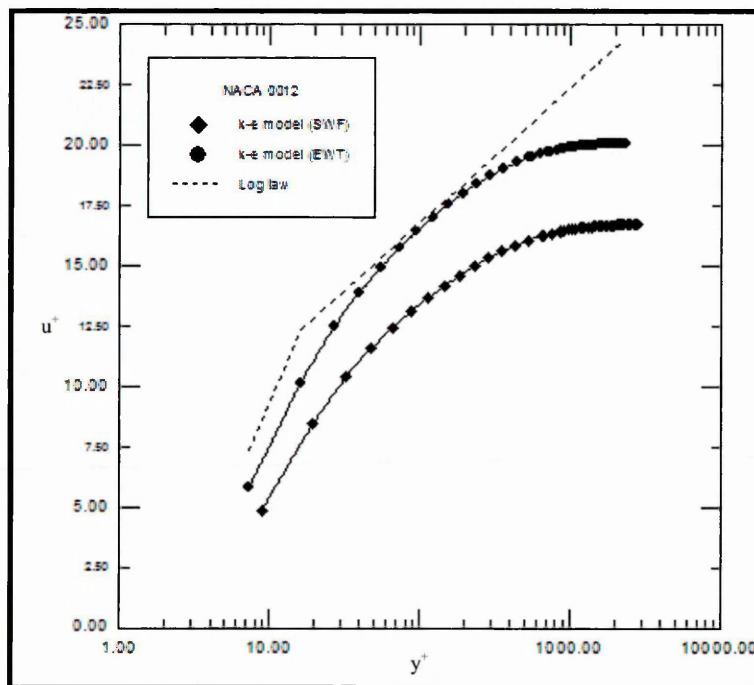


Figure (4-12) Mean velocity profiles at  $X/C_x=0.55$ : different wall function effects (EWT and SWF). [Daud *et al.* (2011A)].

Figure (4-13) emphasizes that the RNG model gives the best prediction based on the velocity profile (gas dynamic) in logarithmic law, compared to the  $k-\epsilon$  and SST  $k-\omega$  turbulence models. The kinetic energy calculated for each of these three turbulence models is depicted in Figure (4-14). Unfortunately, there is no available experimental

data to compare with. Due to the good correlations between the mean velocity using the RNG turbulence model and the logarithmic law in Figure (4-13), the best  $K^+$  plots in Figure (4-14) are those yielded by the RNG turbulence model.

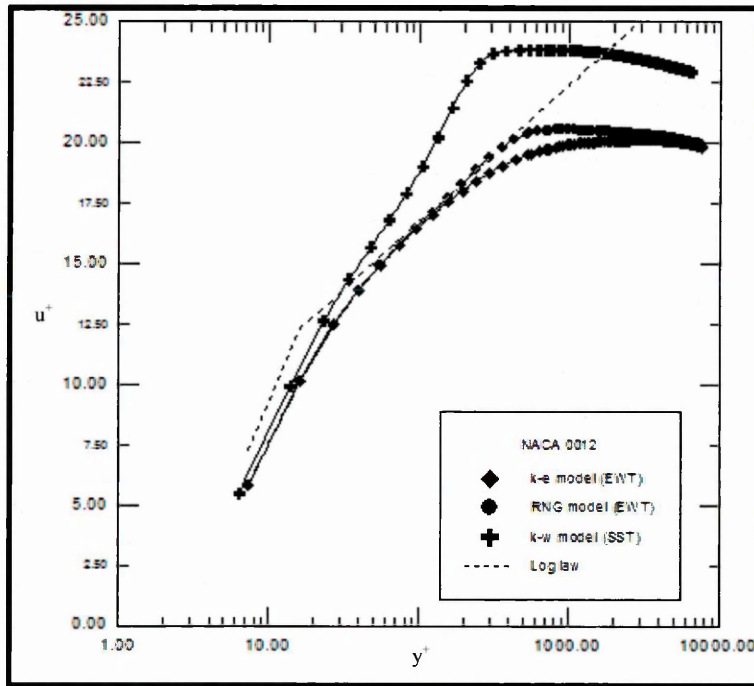


Figure (4-13) Mean velocity profiles at  $X/C_x=0.55$  for  $k-\epsilon$ , RNG, and  $k-\omega$  turbulent models. [Daud *et al.* (2011A)]

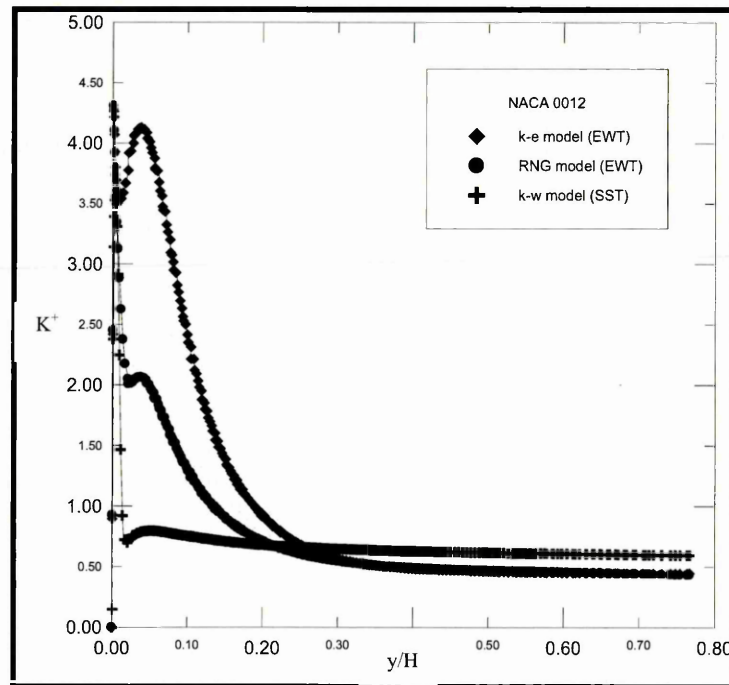


Figure (4-14) Kinetic energy ( $K^+$ ) at  $X/C_x=0.55$  for  $k-\epsilon$ , RNG and SST  $k-\omega$  turbulent models. [Daud *et al.* (2011A)]

Figures (4-15) and (4-16) provide velocity profiles for three turbulent models normalized to the inlet velocity ( $U_\infty$ ) and is compared with experimental results obtained by Sagrado (2007) at  $X/C_X = 0.55$  and  $X/C_X = 0.96$ , respectively. Generally, the solution near to the wall for all turbulence models seems consistent with the experimental data. Nevertheless, the RNG turbulence model is the best overall model as demonstrated by the closest correlation obtained with this model and other published work. The RNG turbulence model therefore holds potential in more advanced turbulence simulations.

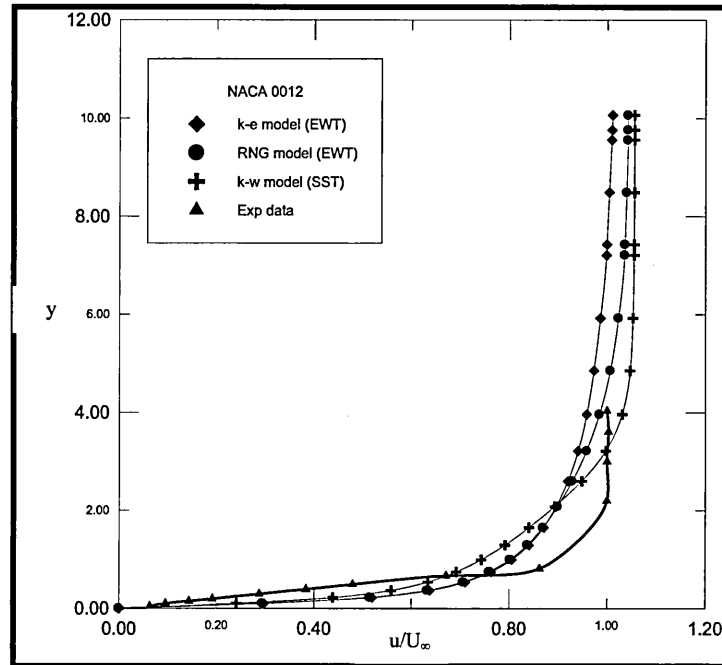


Figure (4-15) Numerical velocity at  $X/C_X=0.55$  for  $k-\epsilon$ , RNG and SST  $k-\omega$  turbulent models normalized with inlet velocity  $U_\infty$  compared with Sagrado (2007). [Daud *et al.* (2011A)]

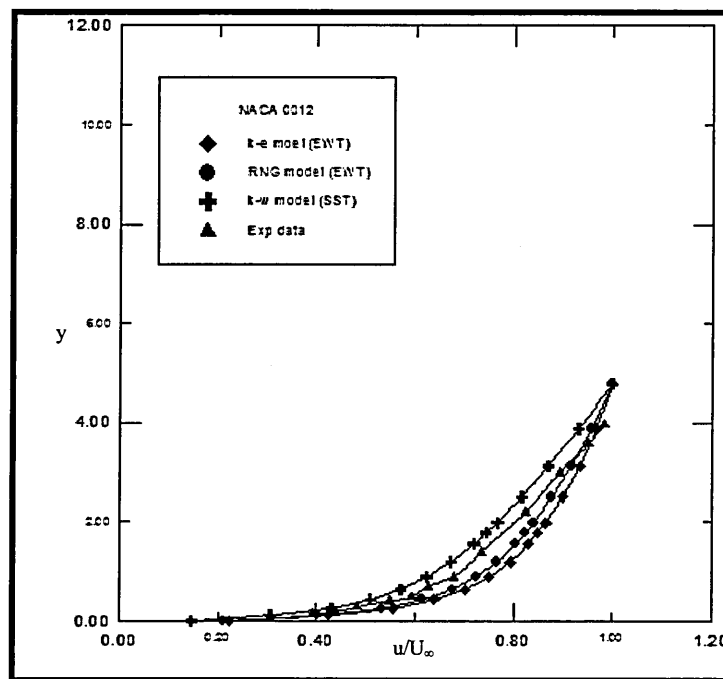


Figure (4-16) Numerical velocity at  $X/C_x=0.96$  for  $k-\epsilon$ , RNG and SST  $k-\omega$  turbulence models normalized with inlet velocity,  $U_\infty$  compared with Sagrado (2007). [Daud *et al.* (2011A)]

#### 4.4 Summary

This chapter has described benchmark modeling of turbulent channel flow and a NACA airfoil as a basis for aerodynamic CFD validation. The various processes intrinsic to *pre-processing* (mesh generation) and also solution strategies (*processing*) have been discussed. Different turbulence models were described for flow phenomena in full developed channel flow (RNG and  $k-\epsilon$  turbulence models exhibit better correlation with the DNS solutions, compared with *SST  $K-\omega$*  and *S-A* (Spalart-Allmars) turbulence models). Consequently, CFD simulation results have been compared and validated against experimental and numerical analysis results of the gas dynamic velocity of benchmark turbulent channel flow, NACA airfoil with DNS solution and experimental results. Furthermore, the boundary conditions required for the solution of the flow region have been presented in this chapter.

The motivation of this chapter is to establish confidence in the Fluent 6.3 CFD software, prior to simulating actual 3-D skewed gas turbine flows. Therefore an extensive validation has been performed for a simple geometry and a more complex *curved* boundary (NACA0012 airofoil) by benchmarking simulations with previous published

DNS studies (the most accurate/expensive method) and also with experimental results. In addition, an objective has been to capture and understand the flow field characteristics and permit an accurate evaluation of the shear stress near the wall in order to subsequently explore gas flows and film cooling for the 3-D skewed gas turbine blade dynamic, which is relevant to real gas turbine geometries. This study investigated the relative accuracy of four different turbulence models ((S-A,  $k$ - $\epsilon$ , *RNG*, *SST*  $k$ - $\omega$ ) in the numerical analysis. Finally, the influence of mesh refinement and mesh type was explored on the wall and outer layer turbulence structures for the two test cases of turbulent channel flow and turbulent NACA 0012 airfoil flow.

## *Chapter Five*

### *(Heat Transfer CFD Validation) Flat Plate Cooling Modeling & Results*

## 5.1 Introduction

Two flat plate simulations have been conducted in this chapter. There are the solid case which corresponds to CHT (conjugate heat transfer) and the shell case which corresponds to non-CHT (non-conjugate heat transfer). These are extended later to 3-D skewed blade case for more realistic gas turbine film cooling geometry. The latter are much less common than the flat plate models which deal with injection of a coolant fluid. In addition, the simulation studies of surface heat transfer of full film cooling for real *rotating* turbine blades are also rare [Lakehal (2002)]. The flat plate considered in this chapter and the presented FLUENT simulations provide a verification platform to the accuracy of the approach adopted in this thesis. The motivation of this study is examined the effects of increasing jet-crossflow value ( $BR=0.5$  and  $1$ ) on velocity flow structure above the flat plate with different hole arrangements. In addition to predict the amount of heat transfer through studying the effects of material property inform of the film cooling effectiveness for CHT plate (solid) and non-CHT plate (shell) by validate numerical simulation results and available published data. Consequently, topics covered in this chapter include;

1. Film Cooling for a Flat Plate case (Solid and shell)
  - a. Single Film Cooling Hole
    - Geometry, Mesh and Boundary conditions
    - Validation of Heat Transfer CFD Results
  - b. Two Rows of Film Cooling Holes.
    - Geometry, Mesh and Boundary conditions
    - Validation of Heat Transfer CFD Results
  - c. Film Cooling Holes Arrangement.
    - Geometry, Mesh and Boundary conditions
    - Validation of Heat Transfer CFD Results

## 5.2 Film cooling for a flat plate case (solid and shell).

### 5.2.1 Single film cooling hole

- Geometry, mesh and boundary conditions

Figure (5-1) illustrates the symmetrical computation domain for the single film hole model studied and also modified in the present chapter. This structural model was considered experimentally by Sinha *et al.* (1999) where the incoming hot gas

temperature is  $T_x = 300$  K and is cooled down from  $T_c = 150$  K to 250K at density ratio 2 to 1.2 respectively. [Liu *et al.* (2008)] also studied the same model implementing a special numerical code. The centerline of the hole and plate creates a symmetrical hole and plate wall respectively. However, the hole diameter is 12.7 mm and the length-to-diameter L/D is 1.75. The coolant fluid is injected at an angle of  $35^\circ$ .

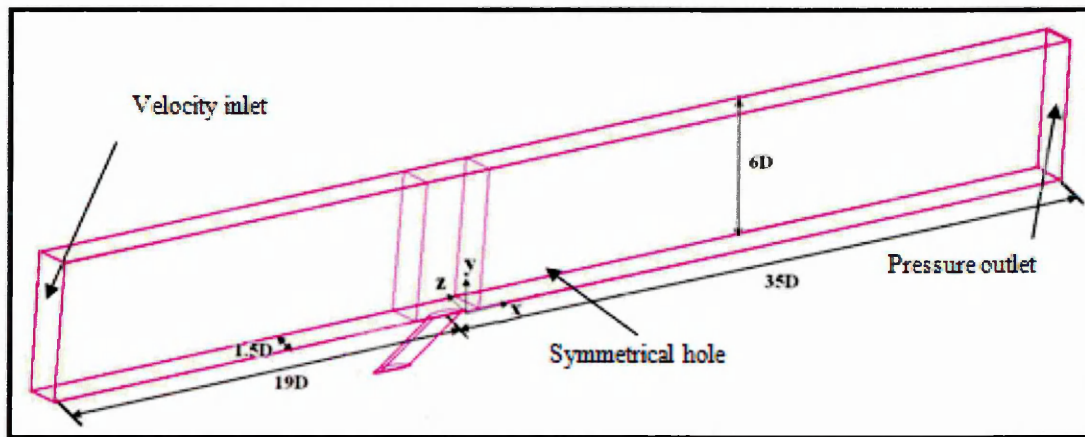


Figure (5-1) Geometry and computational model [Liu *et al.* (2008), Sinha *et al.* (1999)]

The meshing for the film cooling geometry is achieved via the multi-block method which employing structured meshes for the hot mainstream with the **FLUENT Wall Boundary Layer (WBL)** mesh option. [Daud *et al.* (2011A)] suggested in a CFD study for wall-bounded turbulence, that the first grid point away from the wall should be located at  $y^+ \sim 12$ , when employing the RNG turbulence model with Enhanced Wall Treatment (EWT). Therefore, unstructured meshing is employed for the coolant film hole via selection of an appropriate size function mesh tool option for the edges, faces and volume. In this simulation, a high quality mesh for the hot gas, coolant fluid and plate domain has been generated for the volumes in excess of 6 million cells (elements).

- **Validation of heat transfer CFD results**

The static temperature contour for the single hole at BR = 0.5 is depicted in Figure (5-2). Inspection of this plot shows that the downstream temperature is gradually increased after the hole. This is most probably attributed to the mixing process between the hot mainstream flow and the injected coolant air and the temperature along the hole is maintained at 153 K until the cross-flow region, which is clearly shown in the enlarged visualization. Local film cooling effectiveness ( $\eta$ ) is analyzed in this study paper as a

function of mainstream temperature ( $T_{\infty}$ ), wall temperature ( $T_w$ ) and the coolant ( $T_c$ ) using the following relationship:

$$\eta = \frac{(T_{\infty} - T_w)}{(T_{\infty} - T_c)} \quad (5-1)$$

The cooling effectiveness factor is dimensionless and is used to interpret the temperature decay distribution in the reversed direction. Consequently, one of the goals is to discuss the similarities and differences between the results of full Conjugate Heat Transfer (CHT) as solid plate case and non-CHT calculations as shell plate case through compare them with available experimental data.

Figure (5-3) depicts the spanwise (XZ) distribution of local film cooling for the solid plate with thermal conductivity of  $k = 0.027$  W/m.K at  $B R = 0.5$ , with a comparison between computations obtained in this study and the earlier numerical/experimental results of Liu *et al.* (2008) and Sinha (1999) respectively. Good correlation is obtained between the present Fluent results and the computational calculations of Liu *et al.* (2008) and also Sinha (1999) at  $X/D=1, 3, 6$  and  $10$ , The interpretation of the small deviation among the Fluent numerical results and previous numerical and experimental results is due to firstly the method of fixing temperature sensors on the plate in experimental studies. Secondly, the value of the turbulent Prandtl number in the Fluent code is constant ( $Pr_t=0.85$ ) using the RNG turbulence model. (Thermal conductivity for the solid and shell plate was taken from Sinha (1999)). These two effects will be further subsequently addressed in this research. A particular objective in the present study is to highlight the importance of validation of the CFD results and sustaining a high degree of accuracy with other numerical code and experimental data, aspects which are often largely ignored in many modern aerodynamics simulations with commercial CFD programmers. A second key objective of this study is to elucidate the effect of the material thermal properties of the solid plate on the film cooling.

Where; X is measurement points in downstream direction

Z is measurement points in spanwise direction

D is holes diameter

However, the percentage error is calculated from

$$\text{Error \%} = \text{abs}(\eta_{\text{exp}} - \eta_{\text{CFD}}) / \eta_{\text{exp}} \quad (5-2)$$

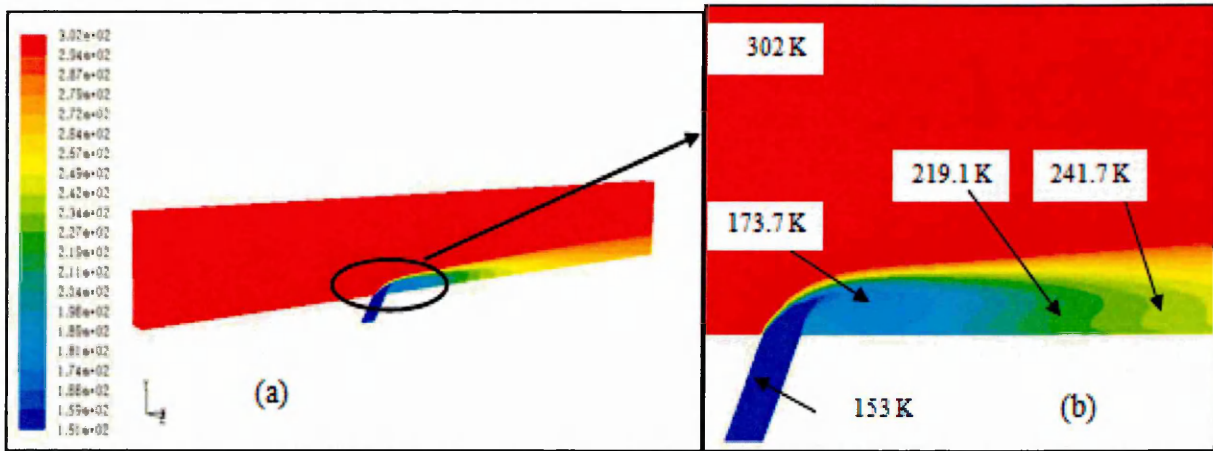


Figure (5-2) Static temperature contour of the single hole at BR = 0.5 (a) the whole view, (b) zoom in [Daud *et al.* (2012)]

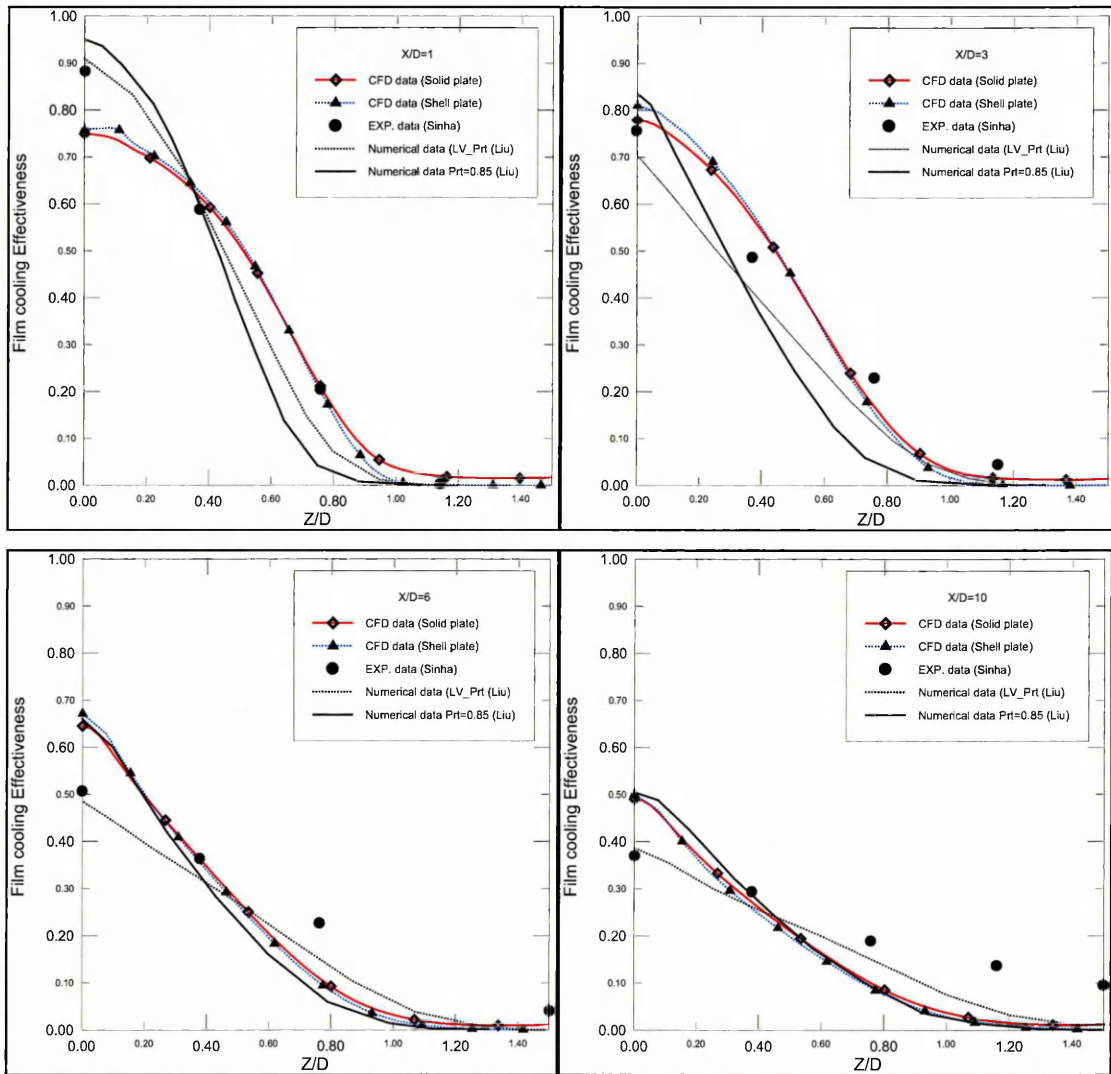


Figure (5-3) Local film cooling effectiveness for single hole at BR = 0.5; comparison with the numerical/experimental results of Liu *et al.* (2008) and Sinha (1999).

In this study, Tables 5-1 and 5-2 show numerical accuracy as a percentage error for present and previous CFD studies in ref [Liu *et al.*], contrast with four selected points in ref [Sinha] (experimental data). The film cooling effectiveness is focus for CFD simulations (solid plate), experimental and previous numerical studies tabled at  $X/D=3$  and 6. However, the minimum percentage error is obtained at  $X/D=3$  between the present study with experimental data compared with the numerical result in ref [Liu *et al.*].

Furthermore, percentage error of film cooling effectiveness at  $X/D=6$  is simplified in Table 5-2. Thus, CFD simulation error located between two previous numerical errors in ref [Liu *et al.*]. The numerical calculations of cooling effectiveness for solid plate are sufficiently accurate since this error is negligible.

The second key objective of this chapter is to elucidate the effect of material thermal properties of the solid plate on the film cooling.

**Table 5-1: Comparison of CFD data, experimental data and previous numerical data at  $X/D=3$**

Current CFD 1	Exp 2	LV_Pr <sub>t</sub> (Liu <i>et al.</i> (2008)) 3	Pr <sub>t</sub> =0.85(Liu <i>et al.</i> (2008)) 4	Error %		
				1&2	2&3	2&4
0.7789	0.7560	0.7014	0.8360	03.03	07.22	10.58
0.5154	0.4860	0.4413	0.3780	06.04	09.19	22.22
0.2034	0.2290	0.1792	0.2433	11.14	21.71	06.26
0.0163	0.0450	0.0016	0.0016	63.25	96.41	96.46

**Table 5-2: Comparison of CFD data, experimental data Sinha (1999) and previous numerical data Liu *et al.* (2008) at  $X/D=6$**

Current CFD 1	Exp 2	LV_Pr <sub>t</sub> (Liu <i>et al.</i> (2008)) 3	Pr <sub>t</sub> =0.85(Liu <i>et al.</i> (2008)) 4	Error %		
				1&2	2&3	2&4
0.6445	0.5060	0.4830	0.6606	27.44	004.55	30.56
0.3465	0.3629	0.3407	0.3350	04.53	006.14	07.70
0.1467	0.2259	0.1700	0.1303	35.08	024.76	42.34
0.0134	0.0402	0.0000	0.0012	66.70	100.00	96.93

## 5.2.2 Two rows of film cooling holes

- Geometry, mesh and boundary conditions

Figure (5-4) illustrates the geometry and arrangements of the cooling holes. This structural model for the holes was studied experimentally [Yuen and Martinz-Botas (2005)] and the specification of the holes in accordance with these studies is represented by a hole diameter of 10 mm, 9 holes in each row and a  $30^\circ$  angle of injection.

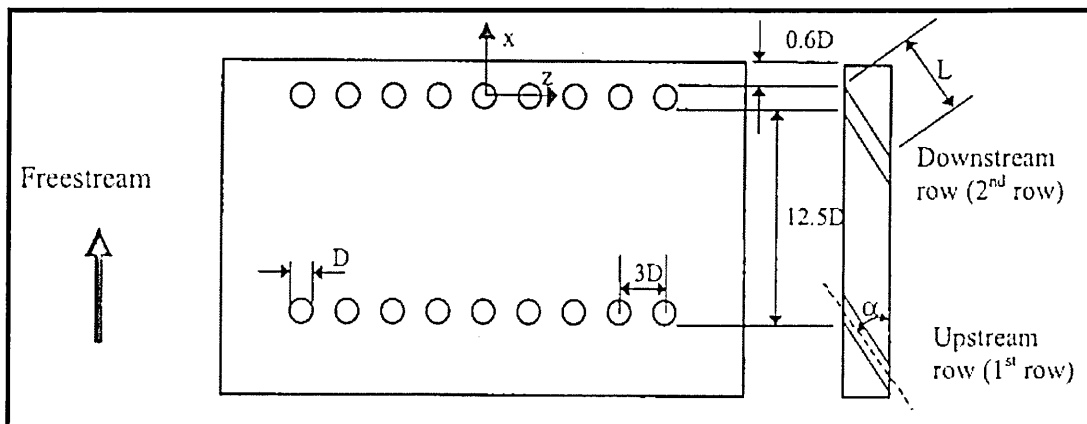


Figure (5-4) Geometry and arrangements of cooling holes along streamwise direction [Yuen and Martinz-Botas (2005)]

As depicted in Figure (5-5), the computational domain is defined in three parts: the *mainstream domain* (1271mm long \* 100 mm height \* 280 mm), the *solid plate* which is (1197 mm long \* 20 mm height \* 280 mm) and the *holes geometry*. The multi-block method technique is employed for meshing the geometry by means of structured meshes for the mainstream with the FLUENT (WBL). Unstructured meshing is employed for the film hole via selection of an appropriate size function meshing tool option for the edges, faces and volume. As mentioned in chapter three, airflow simulations depend on a good predictions of near wall turbulence and the numerical accuracy may also be increased through refining the boundary layer mesh near the wall at the sub-layer region by means of modifying the dimensionless distance from the wall to the nearest grid cell ( $y^+$ ).

However, to ensure high mesh quality of the mainstream domain, film holes domain and the solid plate, the value of  $y^+$  parameter is selected to be in the range of  $4 < y^+ < 12$ . The solid plate domain geometry is created as an unstructured mesh near the holes and structured mesh-as a result of the meshing process. Effectively, the final mesh generated for the three volumes contains in excess of 8 million cells (elements) and the mesh near the plate wall is sufficiently refined ( $y^+ \sim 4$ ) to increase the numerical accuracy.

The initial Boundary Condition (B.C) for film cooling on the flat plate surface geometry (benchmark case) has been extracted from [Liu *et al.* (2008)]. Subsequently, the (B.C) details are inserted in the Fluent code-the inlet main velocity is prescribed as 20 m/sec. The Reynolds number used in this study is based on the holes diameter and takes the value of  $Re= 15928.1$  for the single film cooling hole case and 12541.8 for the two row of holes case. The mass flux (blowing) ratio value for the plenum is taken as  $BR = 0.5$ . In addition, the ratio of the hot gas temperature to the cooled air temperature was specified as  $T_x/T_c = 1.97$  where; ( $T_c$ ) is the coolant temperature and ( $T_x$ ) designates the incoming hot gas temperature ( $T_x = 302$  K). In the numerical simulation the outlet flow was defined as a static pressure.

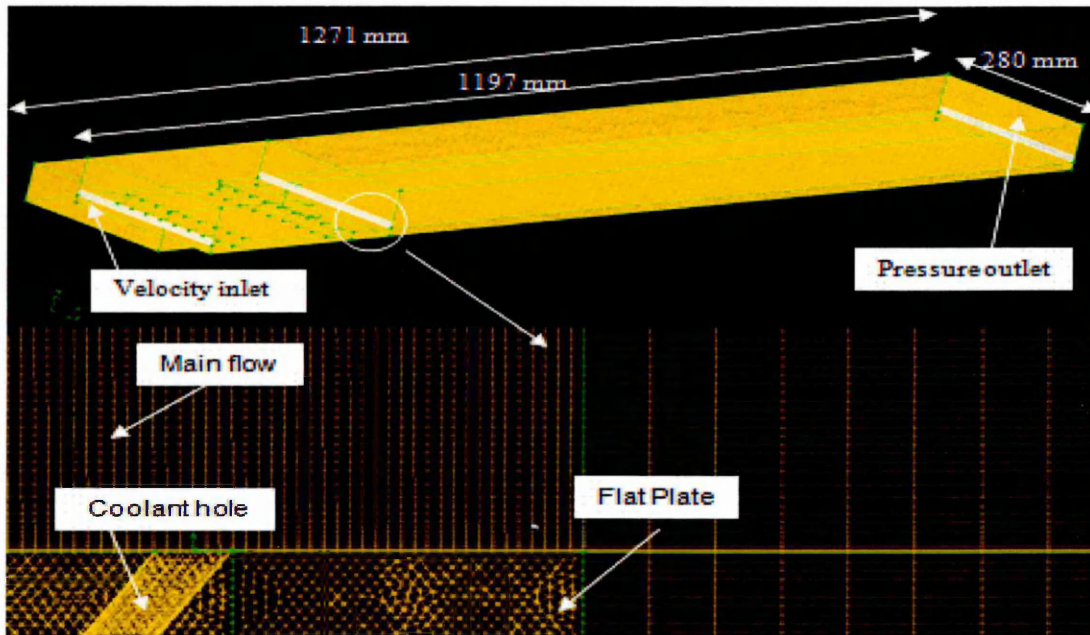


Figure (5-5) Computational domain for mainstream, solid plate and coolant holes and mesh generation.

**Table 5-3: Solid plate material properties**

Material type	Density ( $\rho$ ) kg/m <sup>3</sup>	Thermal conductivity (K <sub>s</sub> ) W/m-K	specific heat (C <sub>p</sub> ) J/kg-K
Carbon steel	8030	42.7	473
Copper	8978	387.6	381
Aluminum	2719	202.4	871

The computational domain and B.C. have been inserted and represented in Fluent 6.3 CFD software as experimental test section which is extracted from Yuen and Martinz – Botas(2005) and show in Figure (5-5). A segregated solution strategy is favored, with pressure and velocity coupled using the Semi Implicit Method for Pressure Linked Equation (**SIMPLE**) algorithm. The scheme is applied to benchmark cases using a variety of quadrilateral, hexahedral, triangular tetrahedral, and hybrid meshes with shown satisfactorily performance [Mathur and Murthy, (1997)]. Consequently, all simulations were executed until the solution convergence factor of  $1 \times 10^{-7}$  was satisfied in the energy equation. The solution has been controlled by selecting **SIMPLE** algorithm to solve velocity-pressure coupling with an implicit procedure, such that more than 2000 iterations are sustained to convergence (solution stability). The solid plate material properties are provided in Table 5-3; for carbon steel, copper and aluminum and are inserted into the Fluent code.

- **Validation of heat transfer CFD results**

Figure (5-6A) illustrates the cooling effectiveness trajectory at the mid-plate through the hole centerline along the plate with a different thermal property. Some materials absorb the heat from the mainstream hot gas flow in a slow rate and also reject the heat slowly. As shown in Table 5-3, three materials with different thermal properties have been assessed in this study. Clearly, the plate with carbon steel material has the highest cooling effectiveness compared with the plate fabricated from copper or aluminum materials. Consequently, carbon steel would appear to be the best material for gas turbine blades, owing to the low thermal conductivity and the maximum cooling effectiveness.

Numerous previous studies have simulated film cooling for a flat plate or curved plate as a shell wall and ignored the plate as a solid body. However, the present study explains the difference between the shell plate and the solid plate, as documented in (Figure 5-6B). Zero cooling effectiveness at  $X/D < -13.5$  when the plate is defined as shell carbon steel and suddenly increases due to the 1<sup>st</sup> row of holes (in holes space) and gradually drop between the 1<sup>st</sup> and 2<sup>nd</sup> row of holes. Evidently, the maximum cooling efficiency after the 2<sup>nd</sup> row at  $X/D=0.57$  on the plate is  $\eta=0.918$  and then steadily drops to 0.135 at the end of the shell plate. Where X is the measurement points in downstream direction and D is the holes diameter

The cooling is greatly correlated with mass of the plate and thermal properties of the plate materials- in Figure (5-6B) at  $X/D > -19.1$  the efficiency,  $\eta$  is considerably

increased since the coolant fluid at the 1<sup>st</sup> row of holes will absorb the heat from the plate through the holes walls due to convection cooling (internal cooling). The cooling effectiveness in the distance between the 1<sup>st</sup> and 2<sup>nd</sup> row will be enhanced. This is attributed to internal and external cooling compared with the shell plate model. The film cooling drops to approximately 69% at  $X/D=0.57$  on the plate when the plate is defined as a solid compared with a shell plate due to the nature and ability of solid material to act as a heat sink by collecting the heat from the hot air or rejecting it to the cold air.

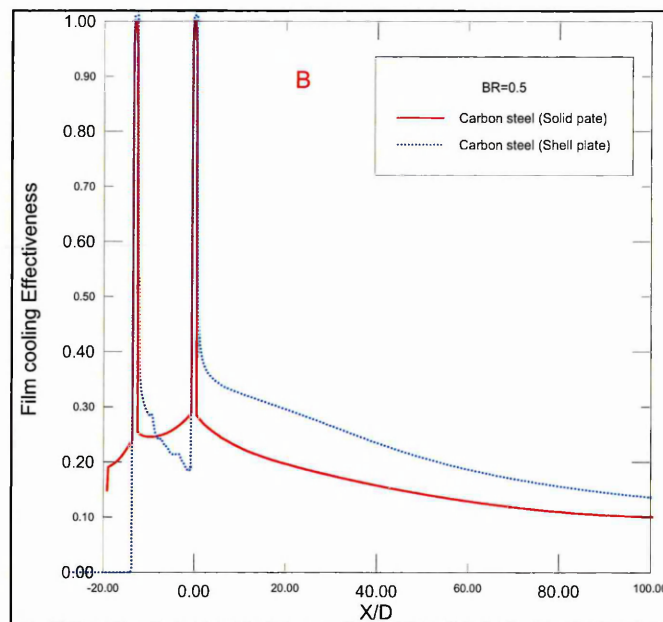
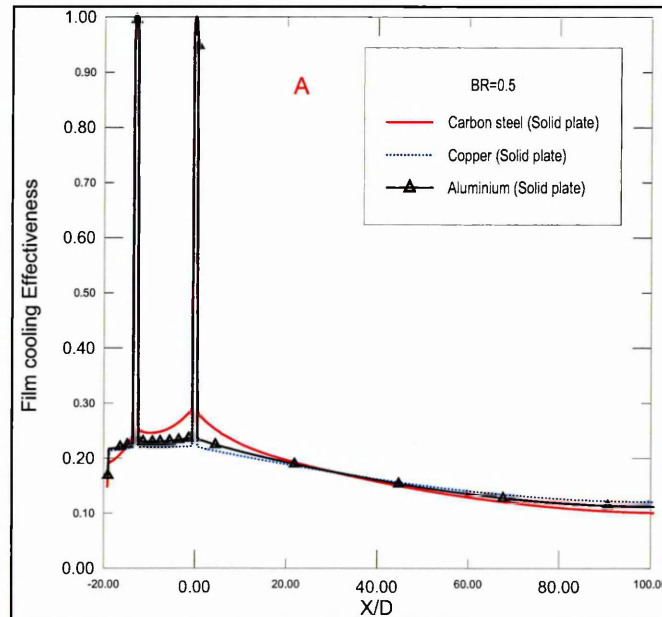


Figure (5-6) Film cooling effectiveness trajectory along the plate through the hole centerline at  $BR=0.5$ ; A) Material thermal property effects; B) Solid and shell plate effects. [Daud *et al.* (2012)]

Figure (5-7) illustrates the static temperature contour for hot mainstream flow, coolant fluid and carbon steel plate through the holes centerline. The cooling effectiveness distribution contour sections for the hot, cold downstream path and carbon steel plate at  $X/D=0, 1, 3$  and  $6$  are presented in Figure (5-8) at  $BR=0.5$ . Therefore, the horizontal axis represented as flat plate spanwise direction ( $Z$ ) and vertical axis represented as flat plate and main flow height ( $Y$ ). The effect of coolant fluid is gradually reduced in downstream direction on both the main flow and solid plate through redacting in film cooling effectiveness values from one section to another above the plate due to mixing process between coolant fluid and main hot gas.

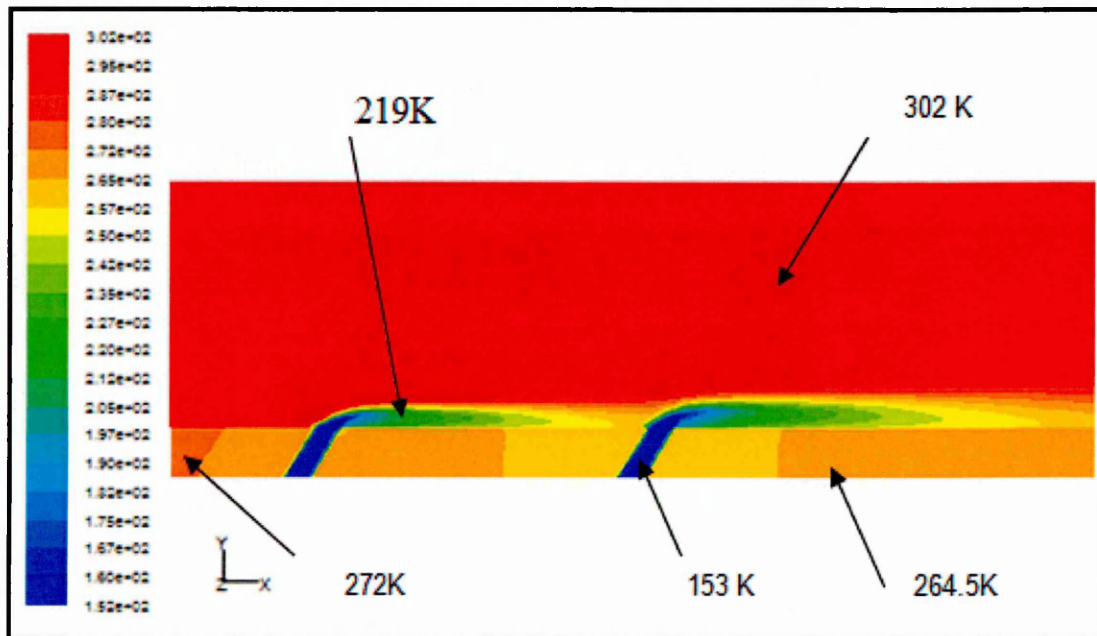


Figure (5-7) Static temperature contour through the holes centerline at  $BR = 0.5$ .  
 [Daud *et al.* (2012)]

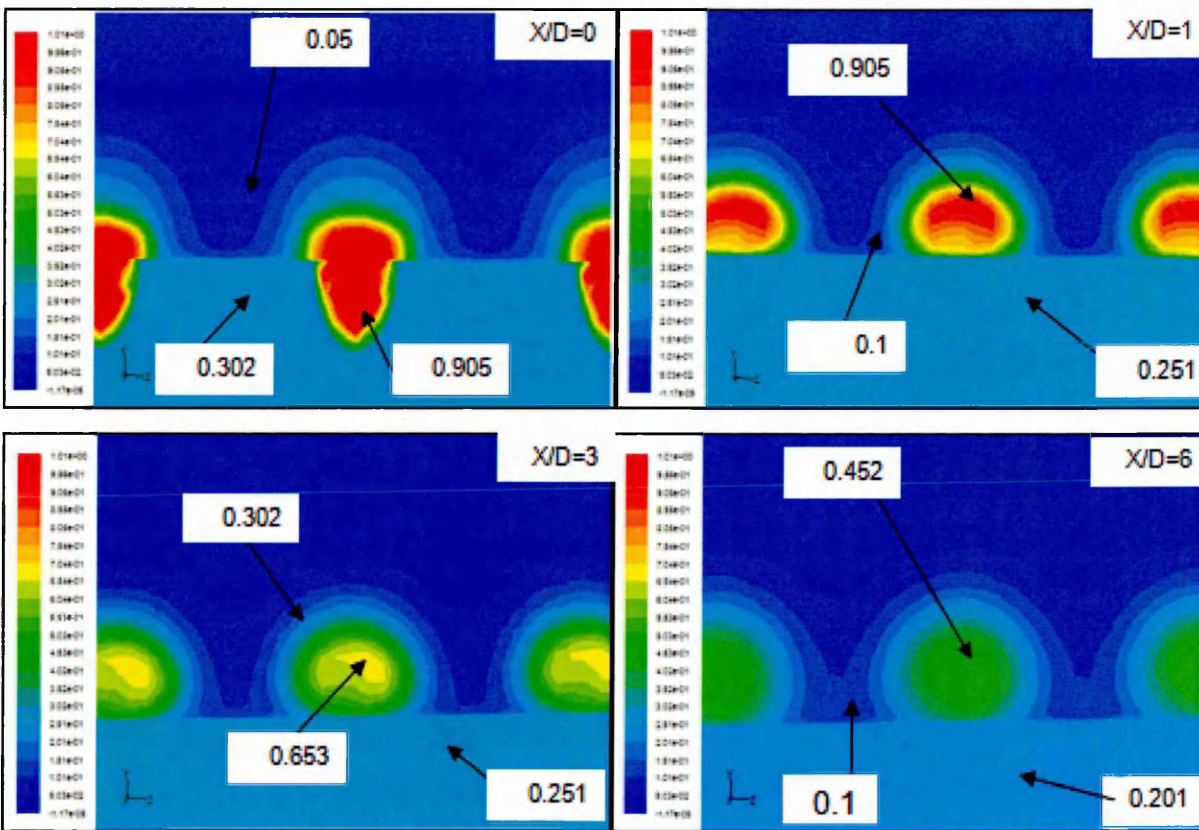


Figure (5-8) The effectiveness cooling distribution contour at different location for  $X/D=0, 1, 3$  and  $6$  at  $BR = 0.5$ . [Daud *et al.* (2012)]

The effects of blowing ratio ( $BR$ ) on the distribution of wall temperature ( $T_w$ ) by injecting coolant fluid into main hot gas are also studied. Blowing ratio ( $BR$ ) is calculated by equation (5-3):

$$BR = \frac{\rho_c * V_c}{\rho_x * V_x} \quad (5-3)$$

After selecting carbon steel as the most suitable material compared with copper and aluminum to achieve better cooling effectiveness, Figure (5-9) shows the effect of increasing the blowing ratio from  $BR=0.5$  to  $1$  with the carbon steel plate through the trajectory of film cooling effectiveness. The effect of increasing  $BR$  from  $0.5$  to  $1$  follows this trend:

- Firstly, a small rise in  $\eta$  occurs before the 1<sup>st</sup> row of holes at  $-13.5 > X/D > -19.1$  due to convection cooling and the coolant fluid absorbing the heat from the plate through the holes.

- Secondly, at  $X/D < 23.8$  to  $X/D =$  zero and between the 1<sup>st</sup> and 2<sup>nd</sup> row of holes the cooling ( $\eta$ ) will drop due to an increase in penetration of coolant fluid to the hot mainstream flow (injected coolant fluid will be away from the wall plate). At  $X/D > 23.8$  the carbon steel plate cooling effectiveness at the wall will be more steady and no drop will arise as a consequence of the mixing process between the hot and cold air. (High BR will enhance rear plate cooling effectiveness).

The boundary layer mesh near the plate wall must be sufficiently refined to increase the accuracy of the sub-layer region so a value of  $y^+ \sim 4$  is utilized in this study. Figure (5-10) demonstrates the gas dynamic velocity profiles normalized by the inlet velocity at different locations for BR = 0.5 and 1. The effect of increasing BR is depicted in the velocity trajectory during a shift in the velocity profile to the right in the downstream and upward direction owing to interference between freestream and coolant fluid generating in that recirculation region (vortices ring). An enhancement in BR causes increasing recirculation flow intensity with reversed flow after the holes. Figure (5-11) presents the recirculation of gas dynamic position (coloured by velocity vectors normalized by inlet velocity  $V_\infty = 20$  m/sec) at the mid plate region through the hole. [Jia *et al.* (2005)], demonstrated that if the mass flux of coolant fluid is reduced the recirculation of the jet inflow will become much smaller. Certainly, recirculation of the jet inflow is a wake zone and the size of recirculation depends on cross to the jet flow ratio and the existence of recirculation phenomena correlated with jet angle.

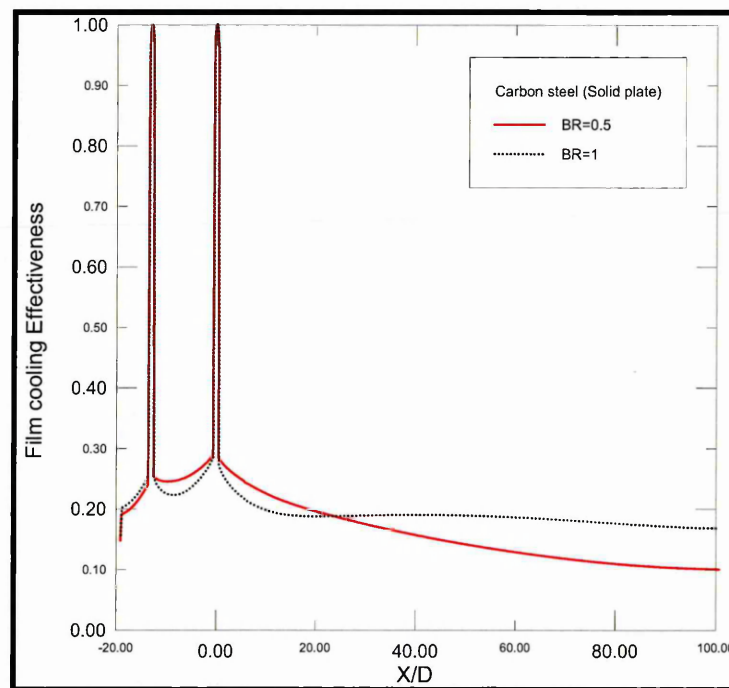


Figure (5-9) Effect of blowing ratio on the film cooling effectiveness distribution (BR = 0.5 and 1). [Daud *et al.* (2012)].

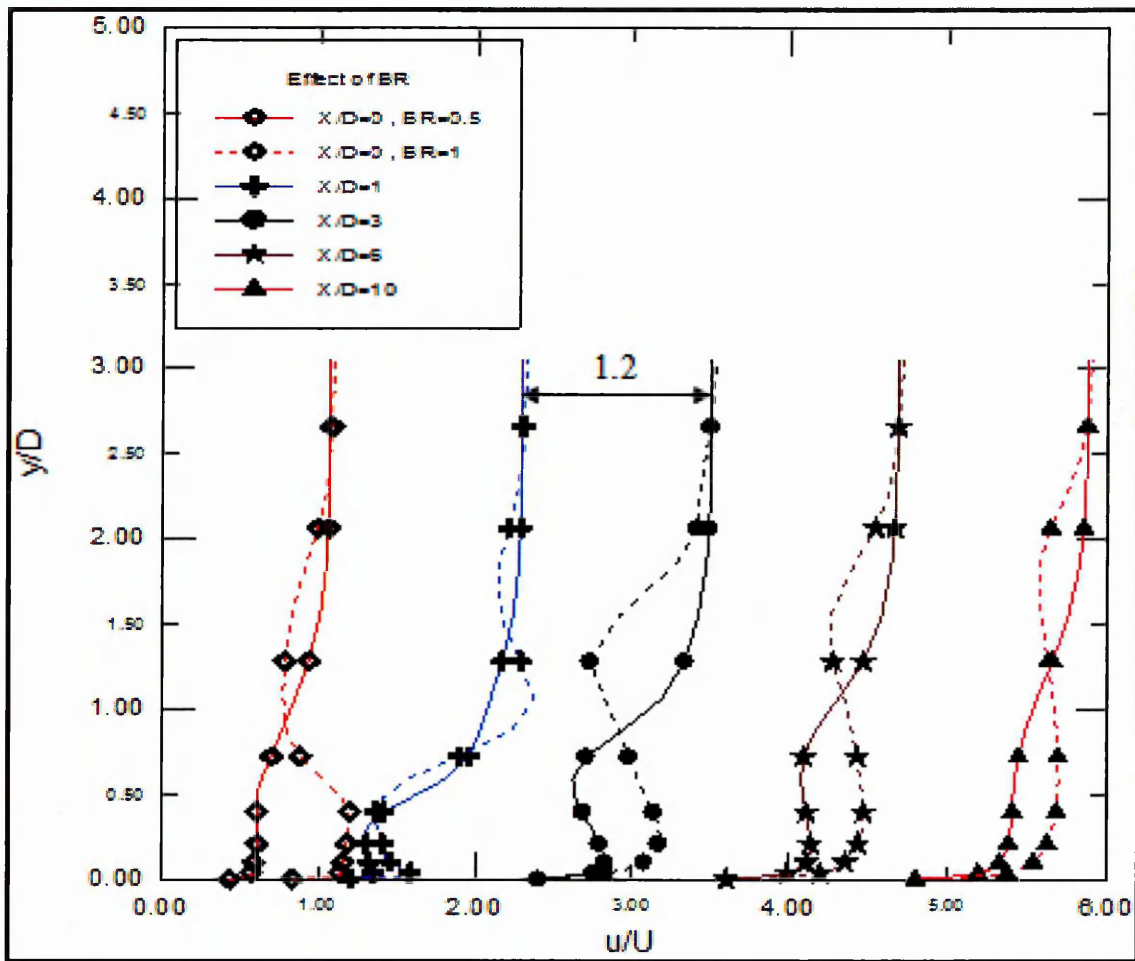


Figure (5-10) Streamwise velocity profiles at different location  $X/D=0, 1, 3$  and  $6$  at  $BR=0.5$  and  $1$ . [Daud *et al.* (2012)]

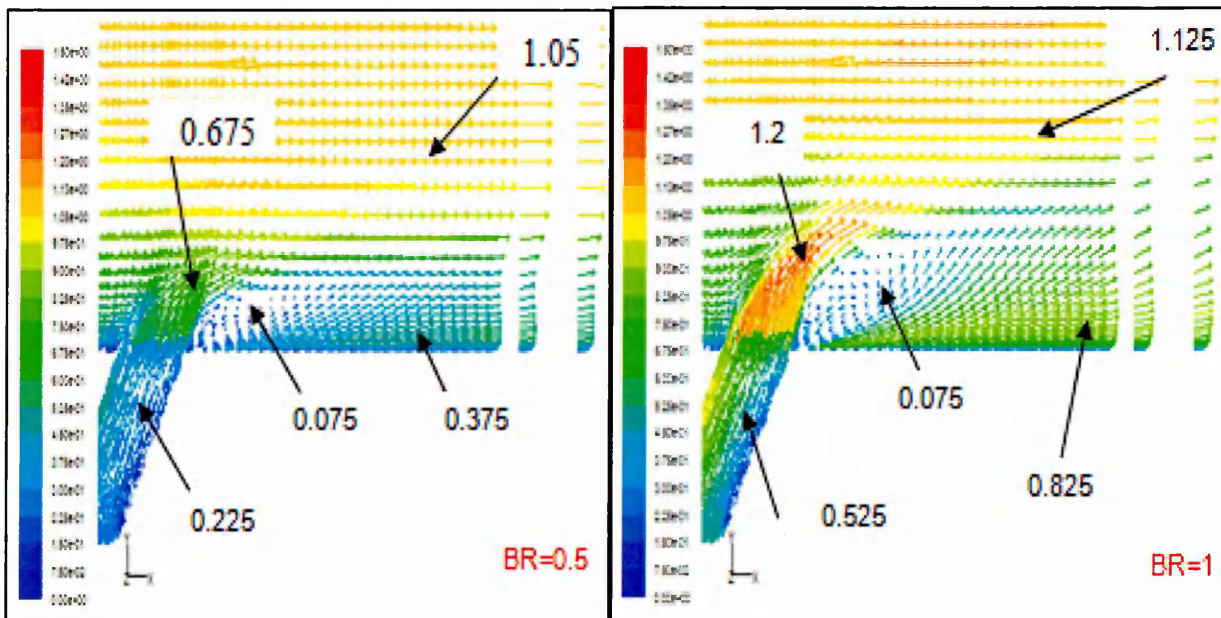


Figure (5-11) Mid of plate section velocity vector normalized by inlet velocity at  $BR=0.5$  and  $1$ . [Daud *et al.* (2012)]

Prediction of heat transfer from the hot gas towards the flat plate can be achieved via the Nusselt number ( $N_u$ ) based on the axial position (X) and this is defined as equation (5-4):

$$N_u = (q \cdot X) / K(T_\infty - T_w) \quad (5-4)$$

where,  $q$  is the blade wall heat transfer rate and all other terms are as defined earlier.

Figure (5-12A) illustrates the local Nusselt number at the mid of plate section. Normally, the shape of the Nusselt number profile can be delineated into three zones. Firstly, Nusselt number distribution begins with a high value due to heat transfer to the plate (plate absorbs heat). Secondly, the trajectory near the holes region commences to a strong descent as a result of cooling effect (heat rejection). Finally, the Nusselt number curve suddenly jumps after the holes position owing to the secondary flow and turbulent flow effects. Hence, at the end of plate the trajectory tends to approximately zero due to a thermal equilibrium being achieved at this location between the plate and the hot air.

The heat load trajectory for three different flat plate materials (carbon steel, copper and aluminum) for BR=0.5 looks analogous at  $X/D < 20$ . However, when  $X/D > 20$  the  $N_u$  path is shifted upward due to material thermal property effects so, carbon steel provides lower Nusselt number value compared with copper and aluminum as shown in Figure (5-12A). Clearly, for  $X/D < 0$ , the Nusselt number curve is reversed; the Nusselt number after the 1<sup>st</sup> and 2<sup>nd</sup> row of holes will be maximized at  $N_u \sim 1500$  and decrease to zero, respectively. (In reality the  $N_u$  value near the holes should be the lowest but the negative sign for X will reverse it to a maximum value).

The effect of BR on the Nusselt number distribution is shown in Figure (5-12B). The profile shape of  $N_u$  after the 1<sup>st</sup> row of holes starts changing and suddenly decreases due to increasing coolant fluid mass flux ratio and turbulence effects. Essentially, the heat transfer trajectory at  $38 > X/D > 0$  for BR=0.5 is lower than BR=1 shows a higher film cooling effectiveness at BR=0.5. The cooling process explains why with high BR the coolant fluid will penetrate the hot gas layer – the hot gas will be displaced further away from the row of holes and cool air will cover the walls after  $X/D=38$ . This will provide more protection with low Nusselt number at the sections away from the holes.

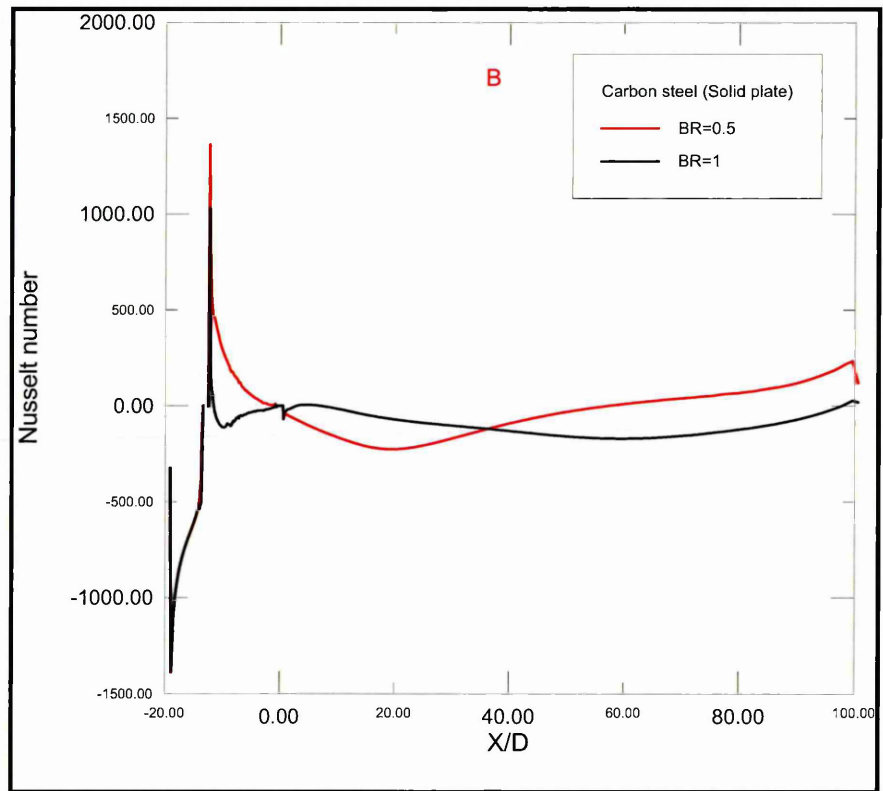
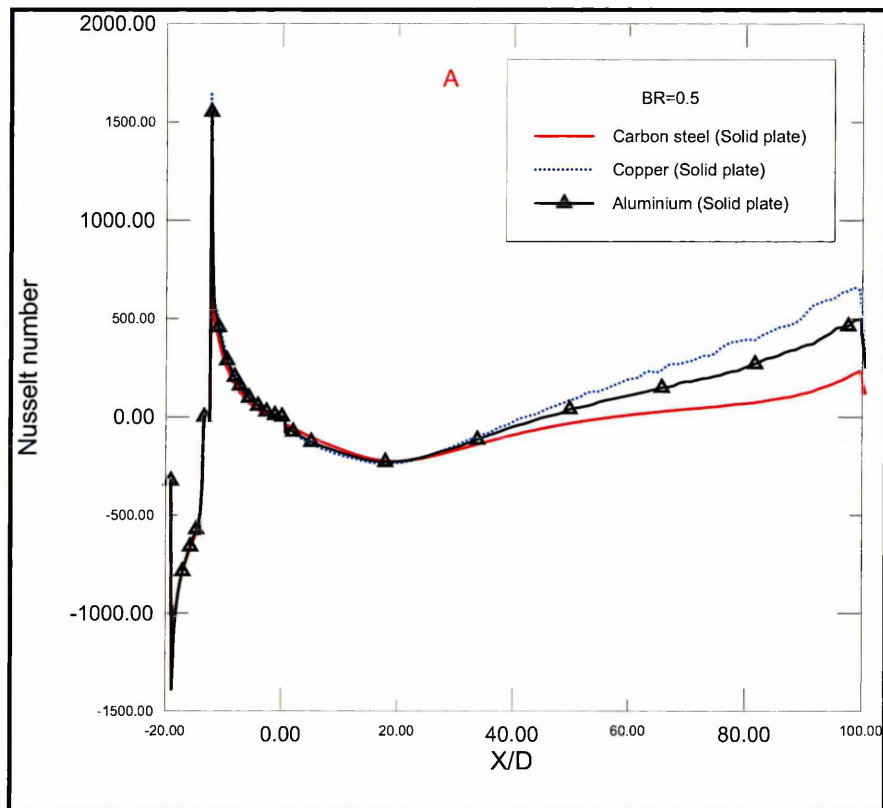


Figure (5-12) Local Nusselt number cooling distribution along the blade  
 A) Material thermal property effects, B) Blowing ratio effects. [Daud *et al.* (2012)]

### 5.2.3 Film cooling holes arrangement

- Geometry, mesh and boundary conditions

Film cooling holes arrangements structural model is demonstrated in Figure (5-13). Hence, experimentally measurements test case was done by Yuen and Martinz-Botas (2005) and the specification of the holes in accordance with these studies is represented in previous section 5.2.2.

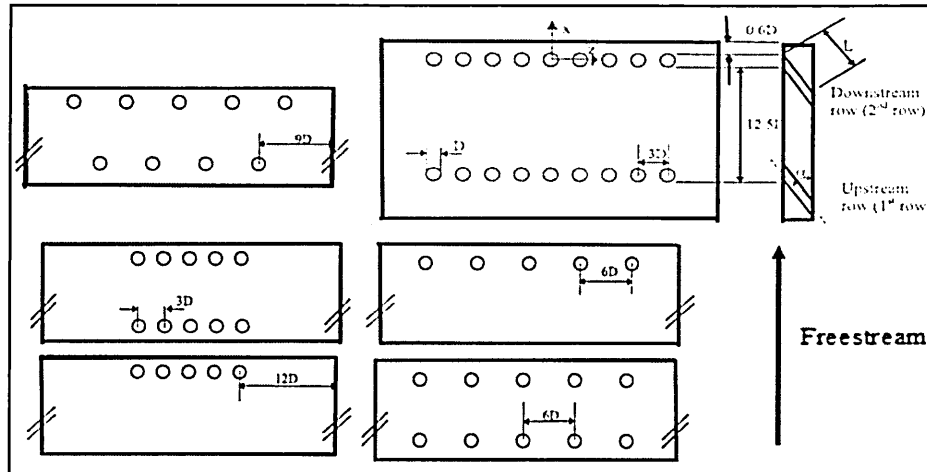


Figure (5-13) Geometry and arrangements of cooling holes along the streamwise direction [Yuen and Martinz-Botas (2005)]

The initial Boundary Condition (B.C) details are inserted in the code-the inlet main velocity is prescribed at 13 m/sec and the mass flux (blowing) ratio value for the plenum has been taken as  $BR = 0.5$  and  $1$ . In this simulation, the jet gas flow through the film holes into a main flow is defined as hot gas. Therefore, the ratio of the mainstream temperature to the injection temperature was specified as  $(T_{\infty}/T_i = 0.936)$  where;  $(T_i)$  is the injection temperature and  $(T_{\infty})$  designates the incoming gas temperature ( $T_{\infty} = 293K$ ). In the numerical simulation, the outlet flow was defined as a static pressure. All boundary conditions were extracted from Yuen and Martinz-Botas (2005). The Reynolds number (Re) in terms of the main flow and the hole diameter is taken as 8791.

Mesh generation and the computational domain have been described in the previous section. Moreover, the solid plate material properties are provided in Table 5-4; for steel, carbon steel, copper and aluminum.

**Table 5-4: Solid plate material properties**

Material type	Density ( $\rho$ ) kg/m <sup>3</sup>	Thermal conductivity (k) W/m-K	Specific heat (C <sub>P</sub> ) J/kg-K
Steel	8030	16.27	502.48
Carbon steel	8030	42.7	473
Copper	8978	387.6	381
Aluminum	2719	202.4	871

- **Validation of heat transfer CFD results**

The cooling effectiveness contour for the single row and double row of holes at  $BR = 0.5$  is illustrated in Figure (5-14). It is evident that the downstream cooling effectiveness is gradually decreased after the hole. Certainly, this is due to the *mixing process* between the hot mainstream flow and the injecting coolant air; Film cooling effectiveness along the centerline of the hole is maintained at one while effectiveness gradually descends near the hole edge and hole exit (clearly shown in the enlarged visualization) owing to heat transfer from the solid plate to the film holes. The amount of heat transfer from the flat plate to the holes steadily increases with increasing number of holes and holes rows, achieving flat plate effectiveness. The areas of film cooling effectiveness are extended and enhanced by extending a single row to double rows of holes hence about 19.9% and 25.4% improvement was obtained in solid blade- see Figure (5-14).

The cooling effectiveness factor is dimensionless and is used to interpret the temperature decay distribution in the reversed direction. Figure (5-15) shows the spanwise distribution of local film cooling effectiveness at  $X/D=1, 3, 6$  and  $10$  for the solid steel plate with  $BR = 0.5$ . The maximum value of the cooling effectiveness is located near the holes and gradually decays in the downstream direction. Definitely, double row effectiveness is superior to single row due to the number of holes (which encourages jet mass flow in the crossflow).

Figure (5-16) shows computational centerline film cooling trajectory along a solid and shell steel plate compared with the experimental results of Yuen and Martinz-Botas (2005) at blowing ratios of  $BR=0.5$  and  $1$ , for the case of single and double rows with  $5$

holes and  $P/D=6$ . In the case of a single row of holes, the results show good correlation between the Fluent numerical results for the steel shell and experimental data at  $X/D < 15$  in contrast with steel solid plate at  $BR=0.5$ . Experimental values for  $X/D > 15$  fluctuate between the solid and shell plate for both single and double row at  $BR=0.5$ . A good agreement is attained between the CFD results for the steel shell plate and experimental data at  $BR=1$  for single and double rows of holes in comparison with steel solid plate CFD results. The deviation among the Fluent numerical results and experimental data is attributed firstly to the method of fixing temperature sensors on the plate in experimental studies. Secondly, in their experiments, Yuen and Martinez-Botas (2005) used a sheet of steel plate, this was inserted between the solid and shell plate and this sheet thickness has not been defined in their article. An objective in the present study is to highlight the importance of validation of CFD simulations against experimental results, aspects which are often ignored in many modern aerodynamics simulations by CFD engineers. A second key objective of this chapter is to elucidate the effect of material thermal properties of the solid plate on the film cooling.

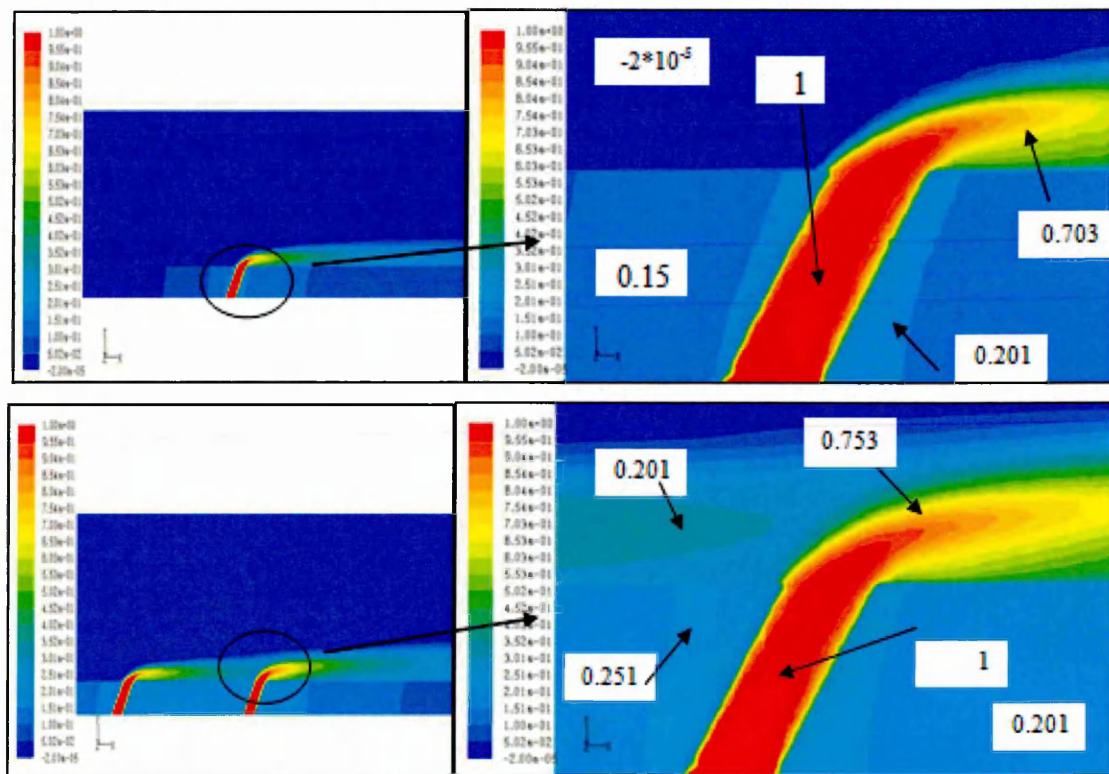


Figure (5-14) The cooling effectiveness contour for the single row and double row of holes,  $P/D=6$  at  $BR = 0.5$  with zooming section [Daud *et al.* (2011B)].

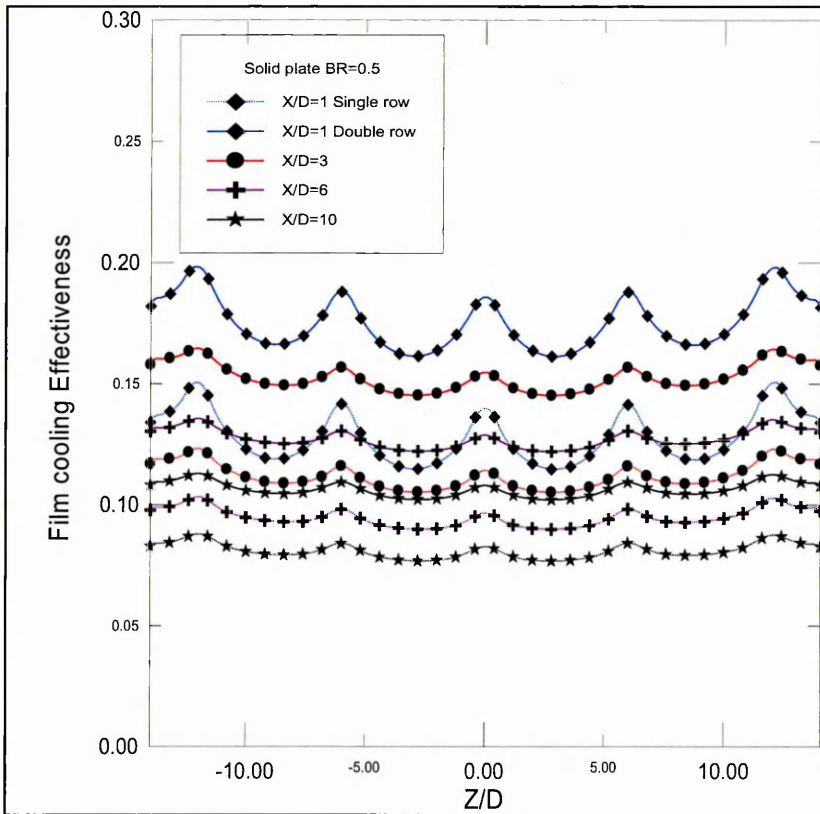


Figure (5-15) Spanwise distribution of local film cooling effectiveness at  $X/D=1, 3, 6$  and  $10$  for the solid steel plate for single and double row at  $P/D=6$  with  $BR = 0.5$ [Daud *et al.* (2011B)].

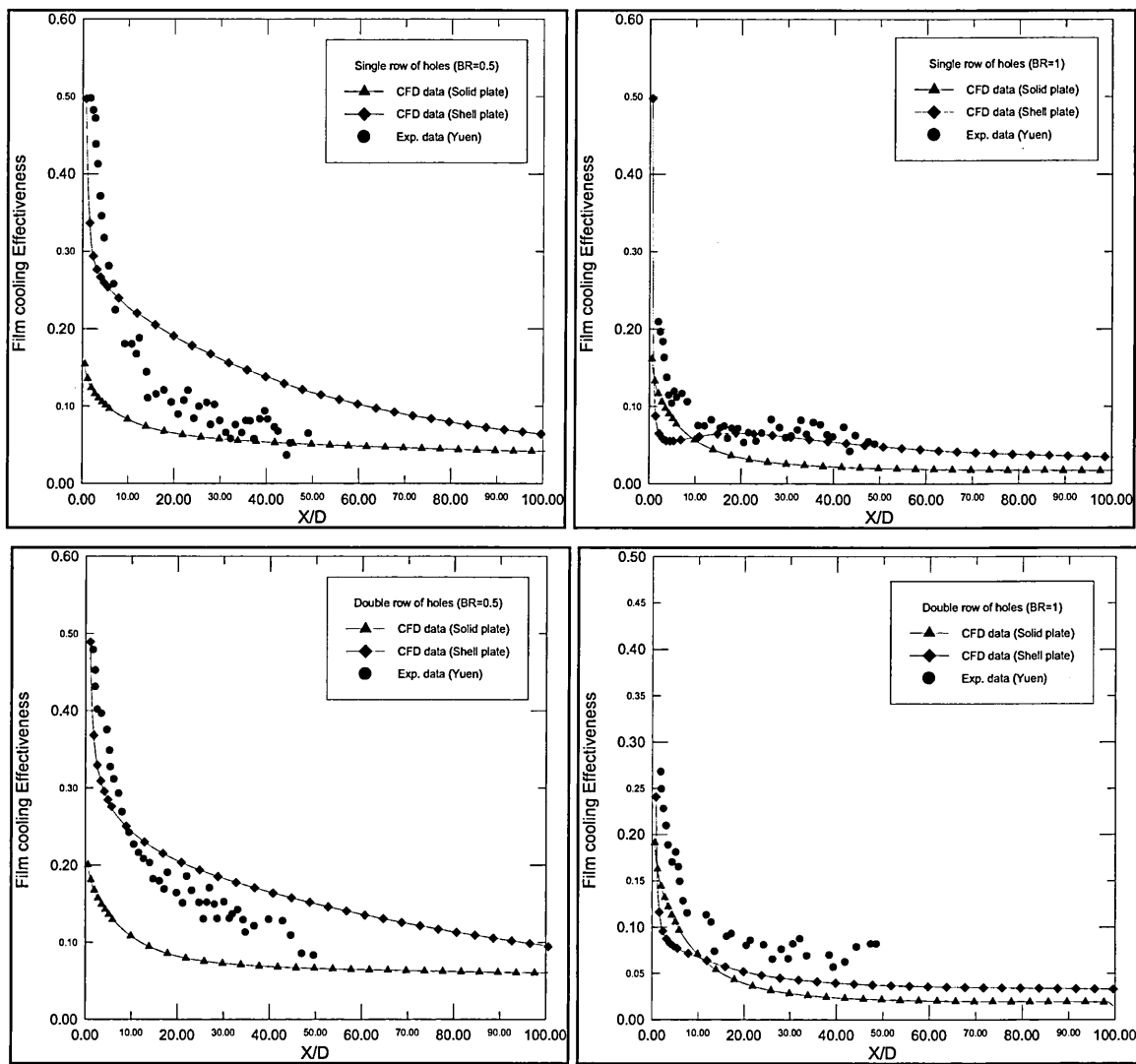


Figure (5-16) Local film cooling effectiveness along streamwise compared with experimental Yuen and Martinz-Botas (2005) for  $P/D=6$  at  $BR = 0.5$  and  $1$  [Daud *et al* (2011B)].

The static temperature contours for coolant mainstream fluid hot jet flow through the holes and steel plate is illustrated in Figure (5-17) for  $BR=0.5$  and  $1$  at double row of holes when  $P/D=3$ , at  $X/D=1$ . The technique of injecting hot gas through the holes was also employed by Yuen and Martinz-Botas (2005). The penetration process increases with increasing  $BR$  from  $0.5$  to  $1$ ; this is clearly observed in the altitude of hot jet flow above the steel plate into the crossflow. In addition, the solid steel plate temperature plummets due to a reduction in the amount of heat transfer from the injection of hot gas to the plate as depicted in Figure (5-17). (The hot gas layer will be pushed away from the steel plate surface with increasing blowing ratio). Therefore, caution must be observed in indiscriminately increasing  $BR$ , since the detachment of the film cooling boundary layer is not desired. About  $1$  degree of temperature was reduced in the solid

plate near to the holes that mean there is no achievement in film cooling when increasing the BR value from 0.5 to 1. Regarding Yuen's published work, hot air was injected into holes and the main flow was kept with lower temperature.

Numerical solid and shell plate film cooling effectiveness curves are shown in Figure (5-18) and are compared with previous experimental work carried out by Yuen and Martinz-Botas (2005) at BR = 0.5 and 1. The arrangement of holes is presented as P/D=3 for a single row and double row of holes. Consequently, the results confirm good correlation between the numerical results for the *steel shell* and experimental results, especially at X/D<10 at BR=0.5. There is small deviation in experimental results between the solid and shell plate due to the thickness of the experimental sheet. The results also agree well at X/D>12 for BR=1 in contrast with steel *solid* plate.

For the double row holes cases, the curves shown in Figure (5-18) exhibit good correlation with experimental results, especially at BR = 0.5 for the shell plate, compared with solid plate. Furthermore, numerical data for the shell plate converges closer to experimental results compared with solid plate results at BR=1.

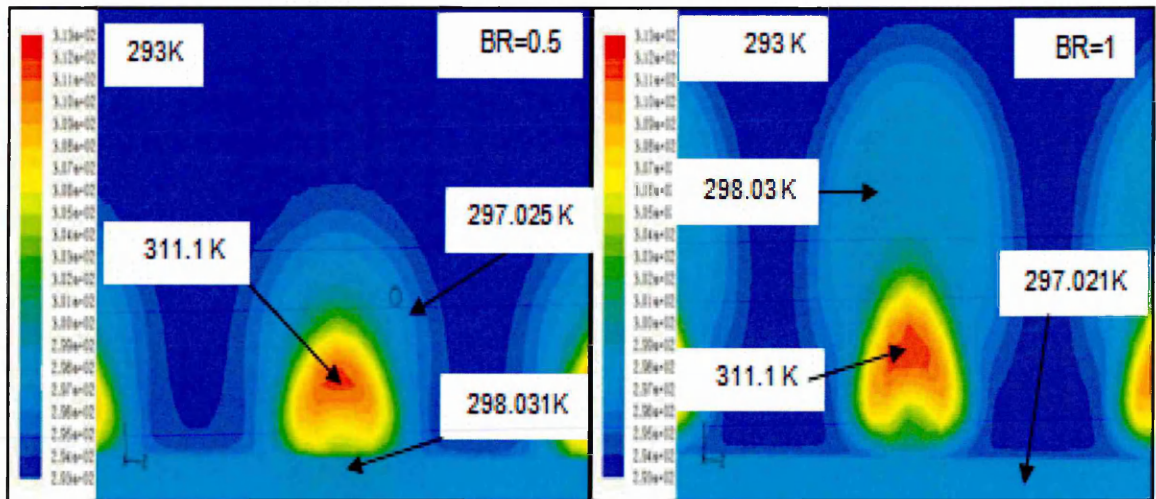


Figure (5-17) The static temperature contour for coolant mainstream fluid, hot jet flow and steel plate at X/D=1 for BR=0.5 and 1 for double row of holes when P/D=3[Daud *et al.* (2011B)].

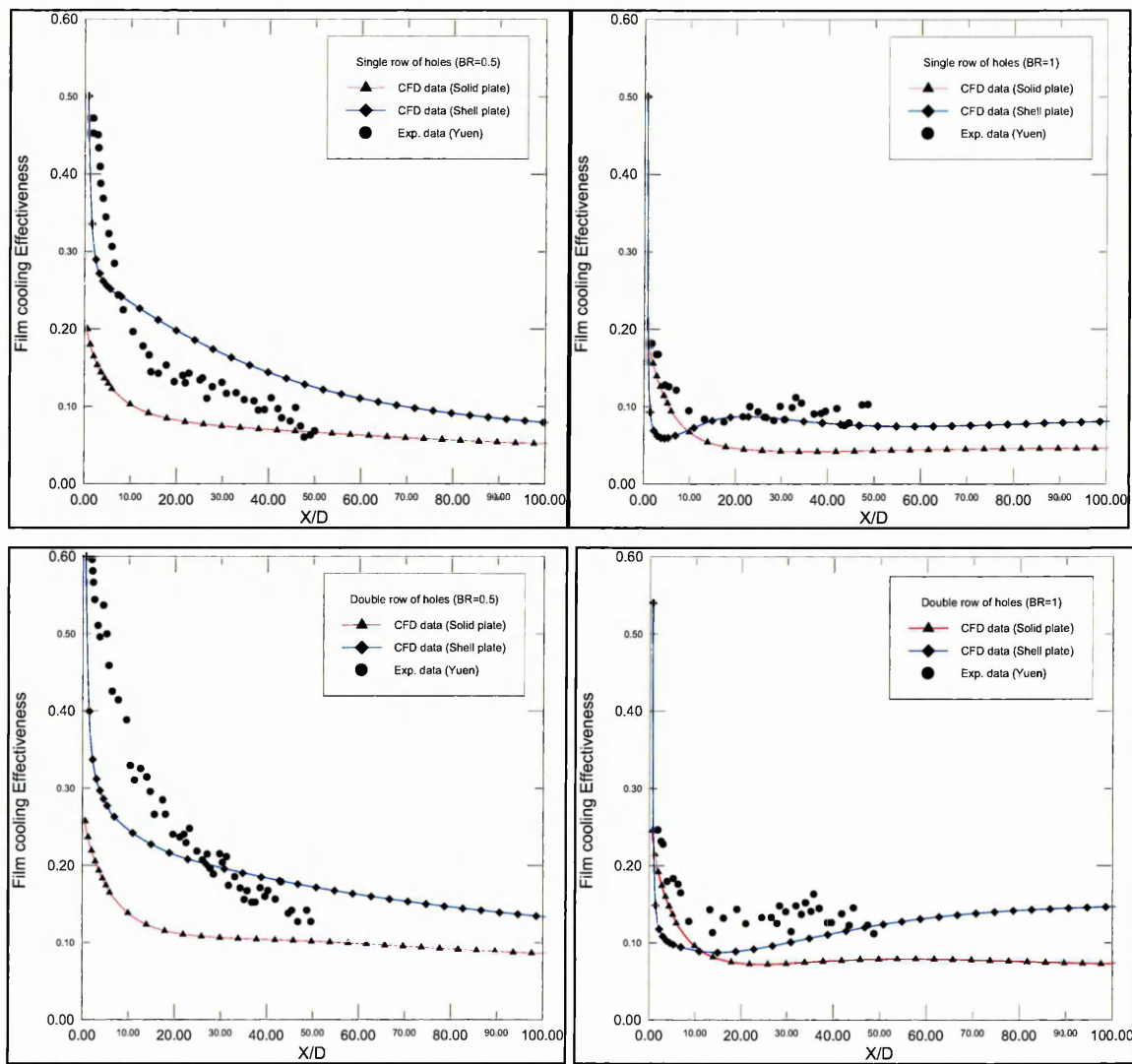


Figure (5-18) Local film cooling effectiveness along streamwise compared with experimental Yuen and Martinz-Botas (2005) for  $P/D=3$  at  $BR = 0.5$  and  $1$  [Daud *et al.* (2011B)].

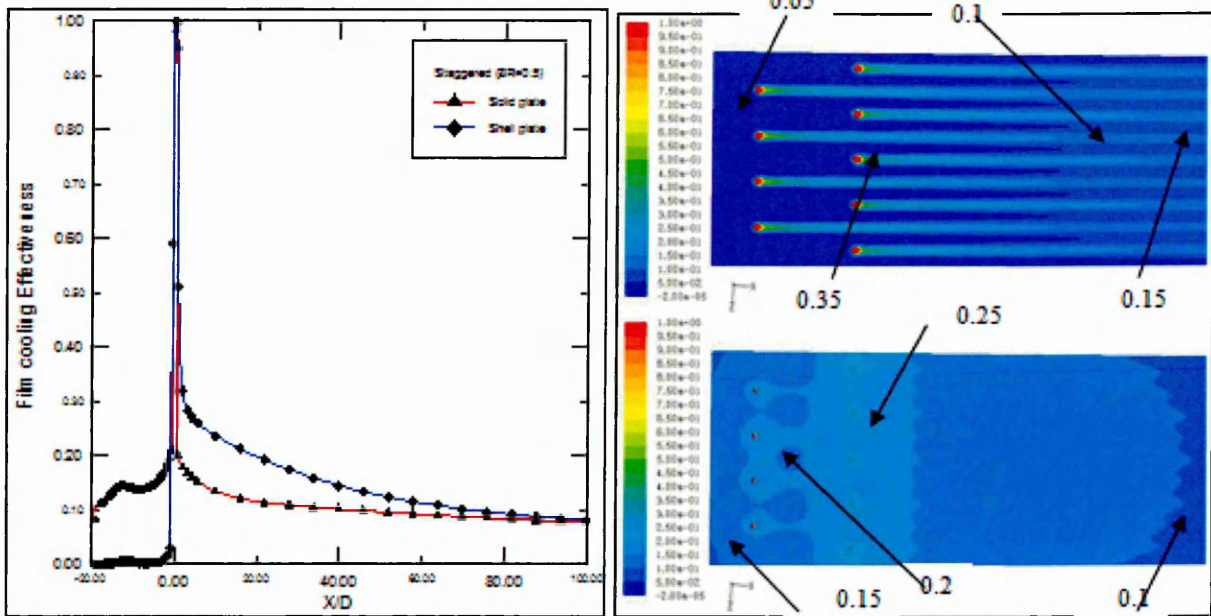


Figure (5-19) Film cooling effectiveness trajectory along the plate through the hole centerline for solid and shell plate at BR=0.5. [Daud *et al.* (2011B)].

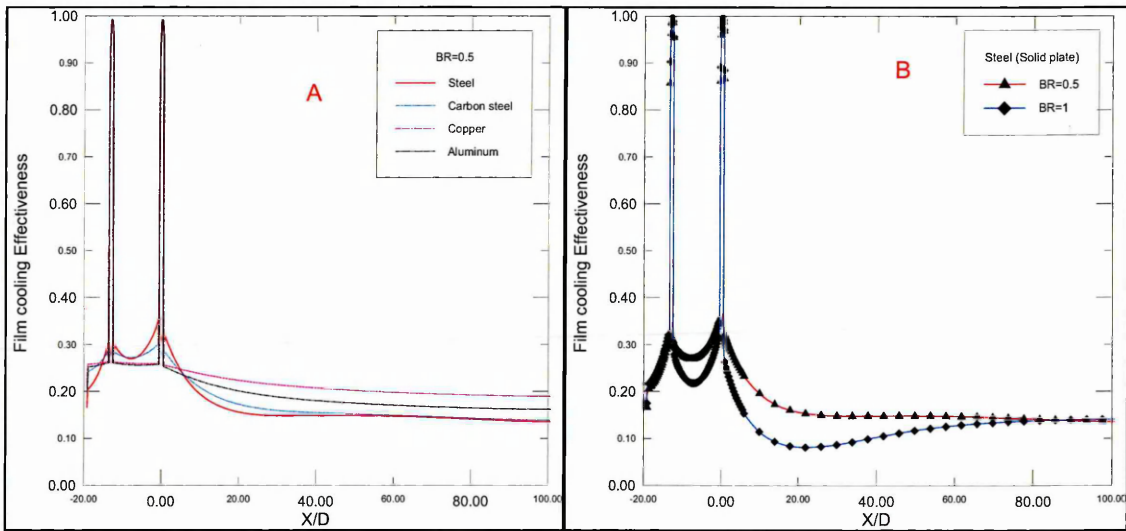


Figure (5-20) Film cooling effectiveness trajectory along the plate through the hole centerline; A) Material thermal property effects at BR=0.5; B) Effect of blowing increases from BR = 0.5 to 1. [Daud *et al.* (2011B)].

Numerous previous studies have simulated film cooling for a *flat plate* or *curved plate* as a *shell wall* and have therefore ignored the modelling of the plate as a *solid* body. However, the present study explains the difference between the shell plate and the solid plate in terms of the staggered holes arrangement, as documented in Figure (5-19). Zero cooling effectiveness is observed at  $X/D < 0$  when the plate is defined as *shell steel* and very small increase is observed at the 1<sup>st</sup> row due to the staggered geometry (see Figure (5-13)). Above the 2<sup>nd</sup> row of holes, the cooling effectiveness suddenly increases. Evidently, the maximum cooling efficiency after the 2<sup>nd</sup> row at  $X/D=0.577$  on the plate is  $\eta = 0.899$  and then steadily drops to less than 0.1 at the end of shell plate. Film effectiveness contours for staggered geometry shows variation between solid and shall plat regulation so, about 66.7% in film cooling value is enhanced near the 1<sup>st</sup> row of holes with expanded protection area.

The effectiveness is greatly related to the mass of the plate and to the thermal properties of the plate materials. In Figure (5-19), at  $X/D > -19.1$  the efficiency,  $\eta$  is considerably increased since the coolant fluid at the 1<sup>st</sup> row of holes will absorb the heat from the plate through the holes walls to the injected fluid due to convection cooling (internal cooling). In the space between the 1<sup>st</sup> and 2<sup>nd</sup> row of holes, the cooling effectiveness will be enhanced and this is attributable to internal and external cooling compared with the shell plate model. The film cooling drops to approximately 76.6% at  $X/D=0.577$  on the plate when the plate is defined as a *solid* compared with the *shell* plate model, due to the nature and ability of solid material to act as a heat sink through absorb the heat from the hot air or reject it to the cold air. Cooling effectiveness colour contours are also presented for the steel plate as both a shell and a solid. The difference is strong in the coolant path after the holes. In the shell case, the jet flow temperature will be constant along the hole until the onset of mixing with the mainstream flow. The solid plate calculation is more realistic in simulating blade life characteristics, as elaborated by Kane and Yavuzkurt (2009). Overall, conjugates heat transfer simulations achieve better predictions of heat transfer and correlate more closely with experimental works. Burd and Simon (2000) as well as Garg (2002) studied film-cooling holes effects and internal cooling channels with ribs and bleed holes to improve the heat transfer. The study demonstrated film cooling performance sensitivity to the hole length and coolant delivery plenum geometry. Computationally, the boundary layer mesh near the plate wall must be *sufficiently refined* to increase the accuracy of the sub-layer region so a value of  $y^+ \sim 4$  is utilized in this study.

Figure (5-20A) illustrates the cooling effectiveness trajectory at the mid-plate for double rows of holes with a setup of 9 holes per row. Clearly, the plate with *steel material* has the highest cooling effectiveness near the holes compared with the plate fabricated from carbon steel, copper or aluminum materials. Generally, the material of the lowest thermal conductivity is the best material for gas turbine blade film cooling. This result agrees with Heidmann *et al.* (2003) which shown that some locations of increased temperature arise with the higher thermal conductivity for Inconel vane case on the pressure side of the blade. Figure (5-20B) shows the effect of increasing the blowing ratio from  $BR=0.5$  to 1 with the steel plate through the trajectory of film cooling effectiveness. The effect of increasing BR from 0.5 to 1 as follows:

Firstly, a small rise in  $\eta$  occurs with increasing BR before the 1<sup>st</sup> row of holes at  $-13.5 > X/D > -19.1$  due to the speed of convection cooling through the holes absorbing heat from the plate.

Secondly, after the 1<sup>st</sup> row of holes the cooling ( $\eta$ ) will drop due to an increase in penetration of the coolant fluid to the mainstream flow (injected coolant fluid will be away from the wall plate). Jia *et al.* (2005) identified that if the mass flux of coolant fluid is reduced, the recirculation of the jet inflow will become much smaller. Certainly, recirculation of the jet inflow is a wake zone and the size of recirculation depends on the cross-to-jet flow ratio and the existence of recirculation phenomena are correlated with the jet angle.

Figure (5-21A) illustrates the heat load trajectory for four different flat plate materials (steel, carbon steel, copper and aluminum) for  $BR=0.5$  the along mid of plate section in form of the Nusselt number. Normally, the shape of the Nusselt number profile can be divided into three zones. Firstly, the plate region before the 1<sup>st</sup> row of holes, where the Nusselt number distribution is of a high value due to the heat transfer to the plate (plate acts as a heat sink) and gradually drops before the 1<sup>st</sup> row and drops down due to the film holes. Secondly, the plate region near and between 1<sup>st</sup> and 2<sup>nd</sup> row of holes. Here, the values of the Nusselt number decreases after the 1<sup>st</sup> row due to the effects of secondary flow (micro-structure) generated from the mixing process and Nusselt trajectory begins a increase (solid plate absorbing heat) up to the 2<sup>nd</sup> row of holes. Above the 2<sup>nd</sup> row the Nusselt number will also decrease due to the presence of injection holes. The first and second parts are reversed due to the negative value of  $X/D$  ( $< 0$ ) - see Eq; (5-4) and also at  $X/D < 5$  for all material types (in reality the  $N_v$  value near the holes should be the lowest but the negative sign for X will reverse it to a

maximum value). The Nusselt number above the 1<sup>st</sup> and 2<sup>nd</sup> row of holes will be maximized at  $N_u \sim 600$  and decrease to zero, respectively. Finally, the third plate region after the 2<sup>nd</sup> row of holes – here the Nusselt number curves varies in value due to the solid plate thermal conductivity. When  $X/D > 5$  the  $N_u$  path is shifted upward due to the material thermal property effects. In addition, the  $N_u$  curve is considerably reduced at  $X/D \sim 38$  to reaching  $N_u = -250$  and the heat transfer trajectory at  $X/D > 38$  gradually increases until the end of plate for  $BR=0.5$  since the effects of the coolant fluid have been diminished.

Effects of increasing  $BR$  from 0.5 to 1 are evidently observed on the Nusselt number in Figure (5-21B). However, dissimilarity in curves is observed between the 1<sup>st</sup> and 2<sup>nd</sup> row and after the 2<sup>nd</sup> row of holes along the plate area. After the 1<sup>st</sup> to 2<sup>nd</sup> row, the curve seems reversed due to the high mass flow rate for  $BR=1$  in contrast with  $BR=0.5$  at the same position. The Nusselt number curve after 2<sup>nd</sup> row slightly stabilizes and drops down, and is thereafter gradually increased after  $X/D > 20$  which is higher than Nusselt number curve at  $BR=0.5$ . Hence, this confirms that there is no advantage in increasing  $BR$  beyond the values studied. The film holes achieve a high film cooling effectiveness and low Nusselt number. Lower  $BR$  will provide more protection to the blade structure with low a Nusselt number along the plate.

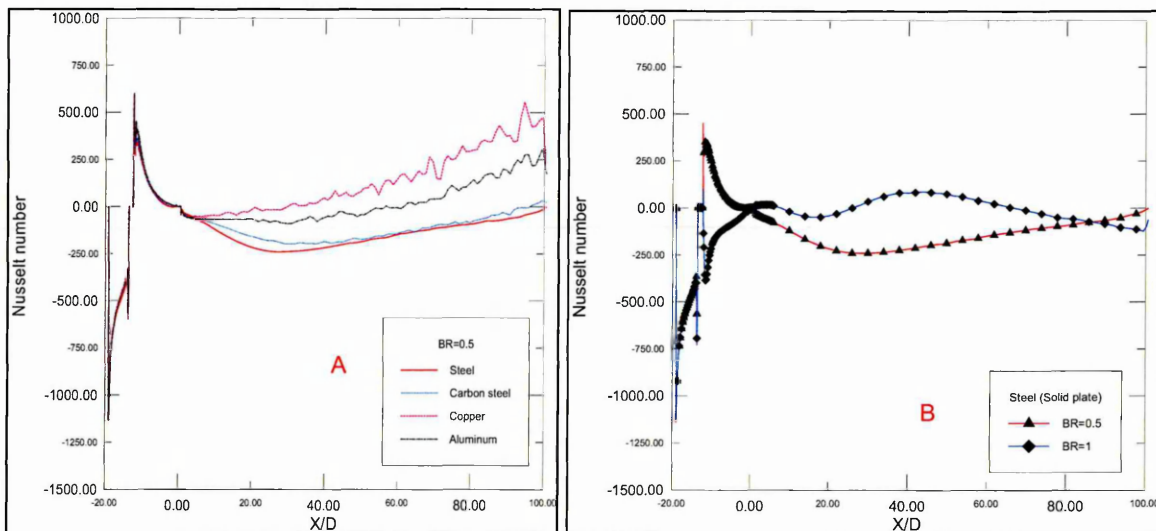


Figure (5-21) Local Nusselt number cooling distribution along the plate A) Material thermal property effects at  $BR=0.5$ ; B) Effect of blowing increases from  $BR = 0.5$  to 1. [Daud *et al.* (2011B)].

### 5.3 Summary

Heat transfer benchmark modeling (flat plate film cooling) are described in this chapter. Aspects of the solid body and shell body are also examined through *pre-processing* (mesh generation) and also solution strategies (*processing*). Computational simulation results were compared with available experimental published results. In addition, a detailed description is given to quantify the percentage error for single film cooling hole and one and two row of cooling holes. All boundary conditions for solution of the flow region is presented in this chapter.

The investigation presented in this chapter focused on 2-D or 3-D aerodynamic flow and heat transfer for flat or curved plates. Consequently, the motivation of this study is to achieve robust Fluent 6.3 CFD numerical prediction of film cooling effectiveness (jet-crossflow), heat transfer, and temperature distribution for a flat plate by focusing on the *mainstream (hot gas)* and *coolant system* (cooled fluid) with differences in BR value, temperature and pressure due to Boundary Conditions (B.C.). Different solid plate thermal properties, for example. Steel, carbon steel (SAE4140), aluminum, copper, and steel shell plates are examined to highlight the effect of the shell and the solid plate on the cooling effectiveness. Table 5-5 shows number cells for each numerical simulation (single hole, two rows of hole and holes arrangement) at solid and shell case with consuming time. Simultaneous calculation of conduction and convection is termed a *conjugate heat transfer* problem, where heat conduction in the solid region is closely coupled with convection heat transfer in an adjacent fluid region is also addressed.

**Table 5-5 Number of cells for each numerical simulation (single hole, two row of hole and holes arrangement) at solid and shell case with consuming time**

Case	Number of cell		Computational time
Single film cooling holes	Solid	6288322	144 hours
	shell	5064295	96 hours
Two row of holes	Solid	8027588	168 hours
	shell	6121305	120 hours
Film cooling holes arrangement	Solid	8027588	168 hours
	shell	6121305	120 hours

## *Chapter Six*

# *Blade Gas Turbine CFD Modeling & Results*

## 6.1 Introduction

Convective heat transfer is an aspect related to the active cooling method to achieve high blade cooling performance in modern gas turbine [Kim *et al.* (1995)]. Both, Kim *et al.* (1995) and Kim and Metzger (1995) measured heat transfer and film effectiveness in the tip region of blades due to the presence of earlier damage through exposed to hot gases in gap. Consequently, various combinations of clearance gap heights, Reynolds number and blowing ratio with different injection geometries in addition to the radius of curvature of the pressure side corner was presented. The experimental results using a transient thermal liquid crystal technique shows that the film cooling performance drastically depends on the shape of the coolant supply holes and the injection locations for a given tip geometry. Hence, competent film cooling holes scheme are required to prevent degradation in exposed turbine blades from incoming high temperature main flow [Ameri (2001)]. The design of film cooling holes system demand some detailed knowledge to attain optimum film cooling performance through investigating the effects of blowing ratio, cooling temperature, angle of injection, number of holes and holes diameter. In relation to blade turbine geometry parameters. Consequently, this chapter addresses the following topics;

3. Essential independent turbine geometry parameters
4. Gas turbine physical domain.
5. Creating the computational domain.
  - a. Blade meshing
  - b. Mesh independent solution
6. Defining boundary conditions
7. Selection of the solver, equation and solution convergence.
8. Gas turbine results

## 6.2 Essential independent turbine geometric parameters

Designers of gas turbines aim to achieve improved blade performance through refining aerodynamics, minimizing total pressure loss and enhancing the amount of heat transfer by *increasing film cooling effectiveness*. This study identified-eleven different geometric

parameters are necessary and adequate to model an axial turbine blade using circular arcs, cubic polynomials. These eleven parameters include, airfoil radius, axial and tangential chords, inlet blade and wedge angles, exit blade angle, Leading Edge (LE) and Trailing Edge (TE) radii, unguided turning, number of blades and throat area [Pritchard (1985)].

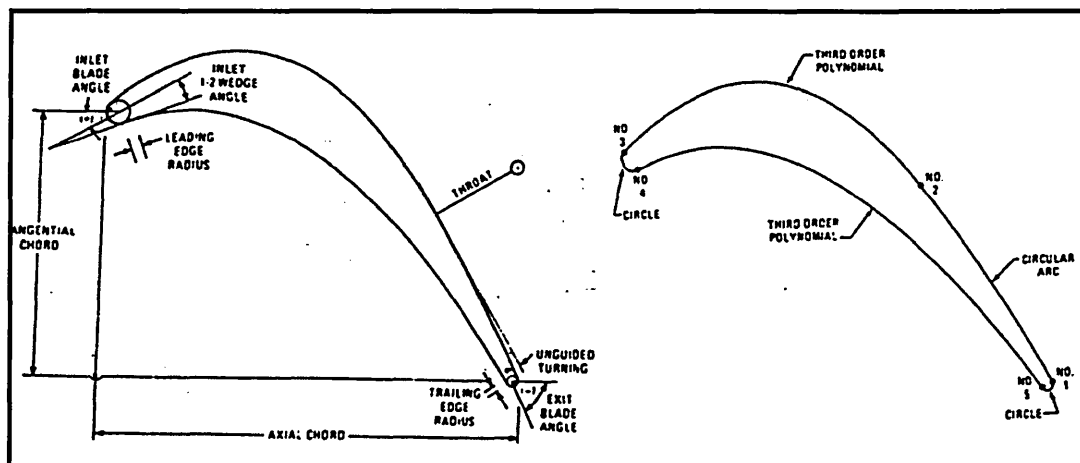


Figure (6-1) The five key points and five surfaces function [Pritchard(1985)].

Figure (6-1) elucidates five key steps necessary to describe any geometry of turbine blade airfoil (hub, mid and shroud). These five key points on the airfoil surface result from:

1. Locating the leading and trailing edge circles in space.
2. Finding the suction and pressure surface tangency points.
3. Setting the throat.

Usually, these five key steps are computed off the eleven independent parameters using the following equations:

### Step No. 1

Suction surface trailing edge tangency point can be found from:-

$$\beta_1 = \beta_{out} - \epsilon_{out}$$

$$x_1 = C_x - R_{TE} * (1 + \sin \beta_1)$$

$$y_1 = R_{TE} * \cos \beta_1$$

Where,

$\beta_1$  is blade angle at point 1 see Figure (6-1),  $\beta_{out}$  is exit blade angle

$\varepsilon_{out}$  is half wedge angle ,  $C_X$  is axial chord

$R_{TE}$  is radius of trailing edge circle ,  $x_1, y_1$  is coordinates point

### Step No. 2

Suction surface throat point

$$\beta_2 = \beta_{out} - \varepsilon_{out} + \zeta$$

$$x_2 = C_X - R_{TE} + (0 + R_{TE}) * \sin \beta_2$$

$$y_2 = (2\pi R / N_B) - (0 + R_{TR}) * \cos \beta_2$$

Where,

$\beta_2$  is blade angle at point 2,  $\zeta$  is unguided turning angle

0 is throat  $R$  is airfoil radius

$N_B$  is number of blades

The former equations were extracted from Figure (6-2) shown below

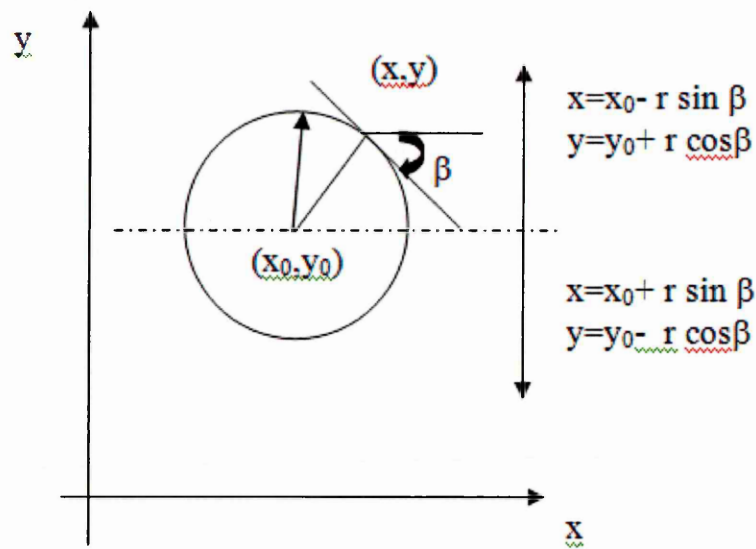


Figure (6-2) Leading edge and trailing edge tangency points [Pritchard (1985)].

### Step No. 3

Suction surface leading edge tangency point

$$\beta_3 = \beta_{in} + \varepsilon_{in}$$

$$x_3 = R_{LE} * (1 - \sin \beta_3)$$

$$y_3 = C_Y + R_{LE} * \cos \beta_3$$

Where

$\beta_3$  is blade angle at point 3,       $\beta_{in}$  is inlet blade angle

$R_{LE}$  is radius of leading edge ,       $C_Y$  is tangential chord

#### Step No. 4

Pressure surface leading edge tangency point

$$\beta_4 = \beta_{in} - \varepsilon_{in}$$

$$x_4 = R_{LE} * (1 + \sin \beta_4)$$

$$y_4 = C_Y - R_{LE} * \cos \beta_4$$

Where

$\beta_4$  is blade angle at point 4,

#### Step No. 5

Pressure surface trailing edge tangency point, referring to Figure (6-2)

$$\beta_5 = \beta_{out} + \varepsilon_{out}$$

$$x_5 = C_X - R_{TE} * (1 - \sin \beta_5)$$

$$y_5 = -R_{TE} * \cos \beta_5$$

Where

$\beta_5$  is blade angle at point 5,

It should be noted that the exit half-wedge angle is a dependent variable that must be iterated to remove the suction surface throat point discontinuity. A first starting value of the exit half-wedge angle is one-half the unguided turning. In addition, all the angles and parameters described before can be shown in Figure (6-1). From the above equations, a FORTRAN program was coded by Pritchard [Pritchard (1985)] and is open to public use. The details of the turbine blade geometry selected are given in Appendix (B).

Figure (6-3) shows how a variety of gas turbine blade geometries can be generated off this program

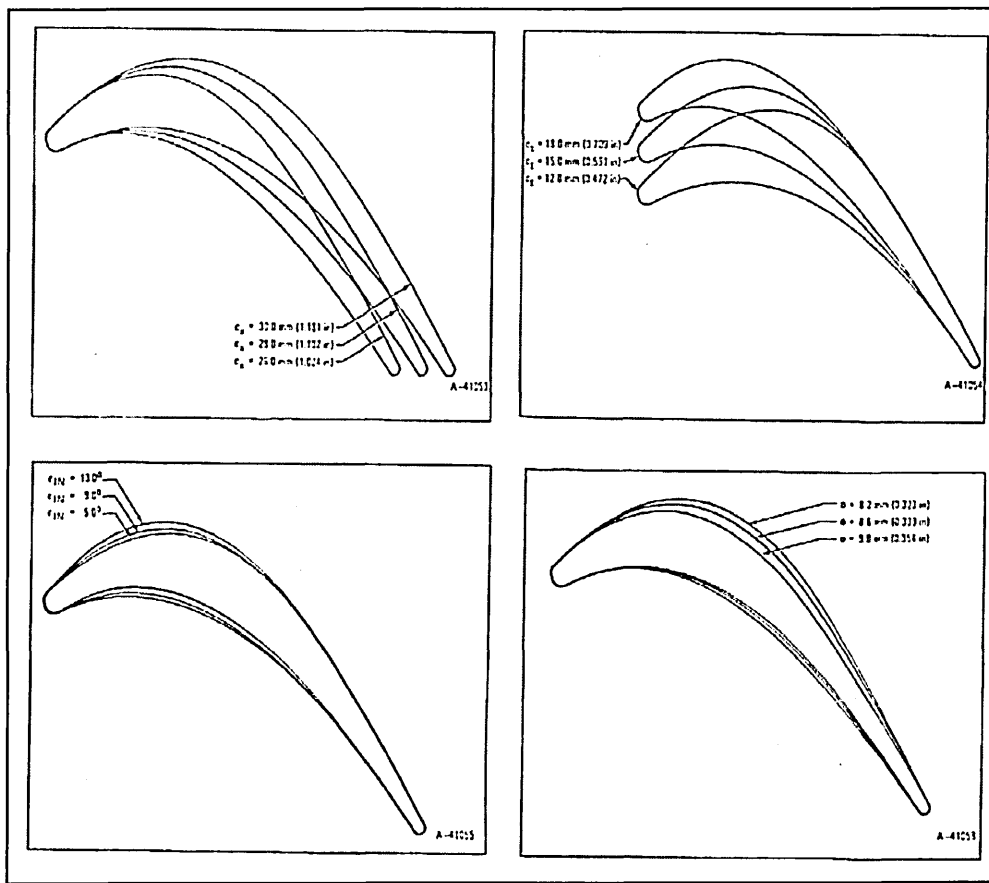


Figure (6-3) Types of gas turbine blade geometry generated off Pritchard's program [Pritchard (1985)]

### 6.3 Gas turbine blade and film cooling physical domain

As depicted in Figure (6-4), any turbine must contain a number of blades arranged on the shaft. It would be complicated inefficient, expensive and time consuming if the numerical simulation was carried out on the whole gas turbines due to very complex flow phenomena characterized by high turbulence levels. Hence, the complications would include the high period time of simulation, very complex meshing and needed computing power. As a result of these complications, the vast majority of researchers focus on a single blade model [Burdet and Abhari(2007), Burdet *et al.*(2007) and Lakehal *et al.* (2001)] and this is the approach adopted in the present thesis. Therefore, simple boundary conditions have been utilized in order to validate the CFD simulations results against available published data which also adopt simple boundary conditions e.g. Sagrado (2007), Liu et al. (2008), Yuen and Martinz-Botas (2005), Burdet and

Abhari(2007), Burdet *et al.*(2007) for single NACA airfoil, flat plate film cooling case and single blade model . These results are gave a strong foundation and confidence for the final 3-D skewed blade simulations.



Figure (6-4) Series of rotating turbine blades. [Coulthard(2005)]

As mentioned in the previous chapter (section 3.5), the first step in pre-processing is to describe the physical domain. Initially, the blade geometric model in this research is created based on the actual blade geometry shown in Figure (6-5) using Computer Aided Measuring Machine (CMM).

As illustrated in Figure (6-6), the CMM machine is a manual or motor-driven system used to extract a citizen coordinated system for any complicated parts and to improve the accuracy, reproducibility of individual measurements. In addition to reducing the time required to inspect record, analyze, and document parts measurements. The measurement process starts when the probe is passed over a part feature to find its displacements. Through creating three measurement axis points based on reference measuring point. Hence, the measured points are transmitted to a central processing unit for comparison to programmed specifications. [The free Library, (1989)]

A Cartesian coordinate( $x, y, z$ ) geometric model was created by measuring the actual blade using a CMM. This machine records coordinates ( $x, y$  and  $z$ ) for each cross section from the hub to tip as a data file: dot 'Act.'. The number of points per section (these sections represent the number of blades) depends on the increment of the CMM indicator machine and may be controlled by the user. The output CMM data file compiles points for the blade curve (per section). Then the measured sections are described, smoothed and assembled in the pro/Engineer Wildfire (CAE) package to create the blade's solid volume. In addition, the main lateral holes volume is also

created, as illustrated in Figures (6-7). The blade model has the following specifications: a maximum length  $C_x = 52 \text{ mm}$  with a maximum width  $C_y = 27.3 \text{ mm}$  and spanwise  $C_z = 114.5 \text{ mm}$  a lateral hole diameter of 4 mm, with an inclined angle of  $9.13^\circ$  along the span. Clearly, the one lateral hole volumes are designed in CAE package to integrate a number of film cooling holes with injection angles of  $35^\circ$ ,  $45^\circ$  and  $60^\circ$ .

The applications of film cooling holes provides the first and best line of defense via creating a blanket of coolant fluid over the gas turbine blade surface. After reviewing the seminal previous published studies in this topic, such as (Lakehal *et.al* (2001), Burdet *et al.*(2007)), the best suggestions for angles of injection were found to be when cold air is injected cold air is injected at 35, 45 and 60 degrees, respectively. Lower angles and higher angles outside this range have been found to produce inefficient cooling in many studies in the literature. Therefore, the three angles of injection of 35, 45 and 60 degrees have been found to show a very good range of feasible film cooling in both numerical and experimental aspects of the Thesis and constitute the optimal range for accomplishing blade protection.

In this study, the lateral hole is located near the leading edge of the gas turbine blade model. Therefore, the blade contains 42 coolant holes on both sides (pressure and suction side) with a hole diameter of  $D=1 \text{ mm}$ , with a lateral spacing of pitch equal to  $5*D$ . After creating the blade and lateral holes volume the next step is to export the volumes as a file dot 'Stp.'

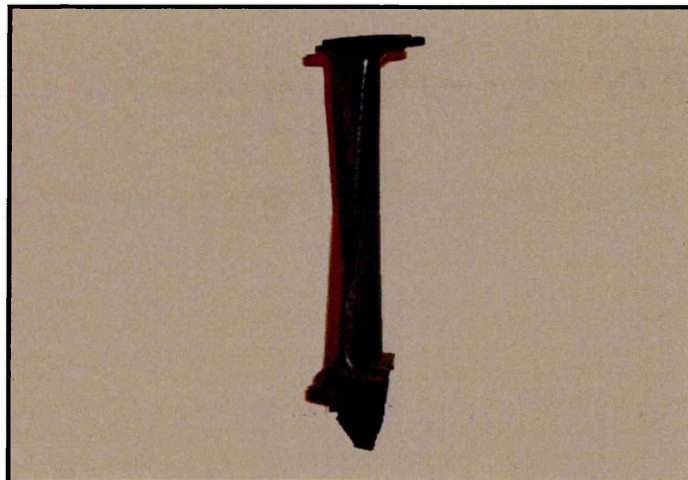


Figure (6-5) Actual blade model



Figure (6-6) Computer Aided Measuring Machine (CMM)

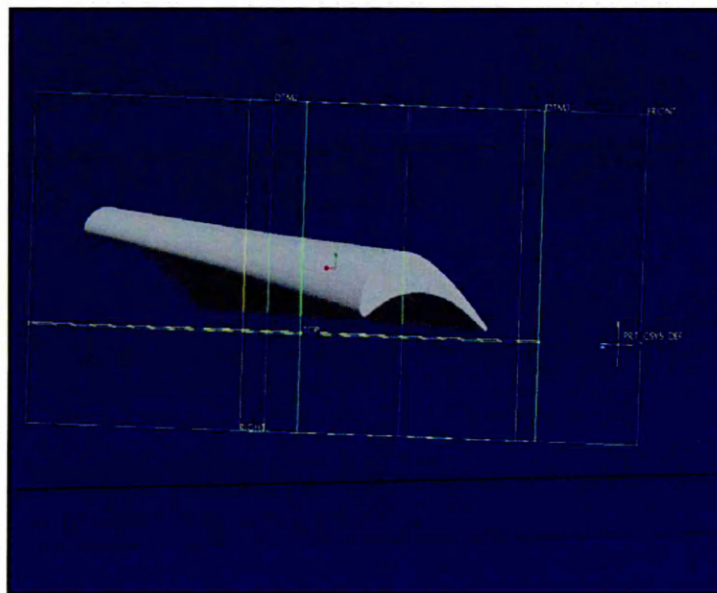


Figure (6-7) Assembly of gas turbine blade geometric model

## 6.4 Creating the computational domain

Accurate conversion of the geometry physical domain into the computational domain is a fundamental step in any CFD simulation. Mesh generation is the approximation of the object continuous surfaces into the continuous computational domain volume. As described earlier, the GAMBIT software tool is used to perform the mesh generation of the flow domain. The first step in the GAMBIT software involves importing the gas turbine blade and lateral cooling hole volumes file as a dot 'Stp' file, as displayed in

Figure (6-8), (6-9) respectively. Whole flow diagram of exploring process starts from CMM to FLUENT data results is demonstrated in Figure (6-10).

In addition, the flow simulation box is created and represented in dimensions (4.81\*2.11\*3.85) C<sub>x</sub> such that three volumes have been combined together. The flow simulation box, the turbine blade model and the film cooling holes (this process of splitting is used to generate three volumes attached together) and the dimensions for all domains were achieved in mm

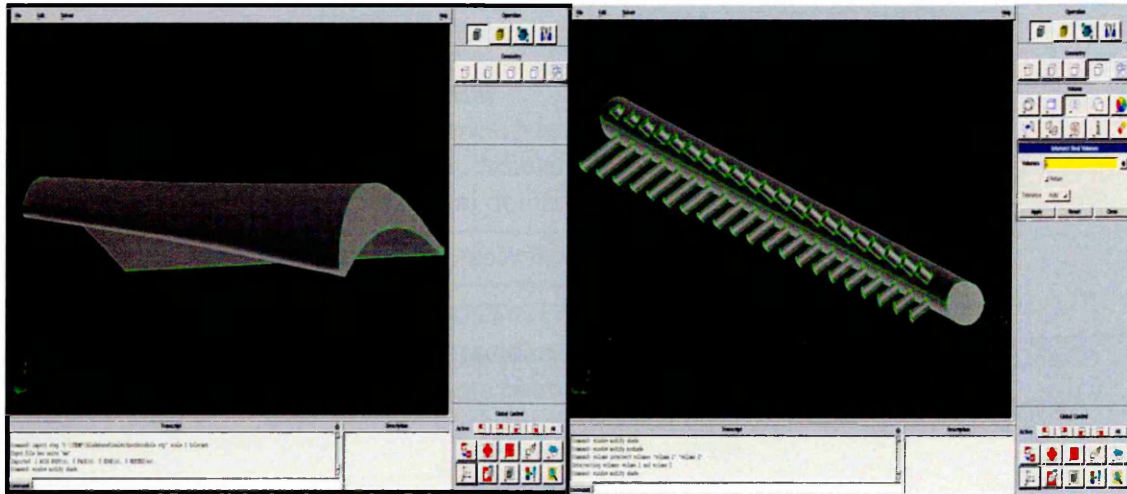


Figure (6-8) Blade geometric model

Figure (6-9) Holes geometric model

blade model as a solid body with cooling holes system and multi block technique meshing of the whole flow simulation box with the blade model and holes film cooling volumes respectively.

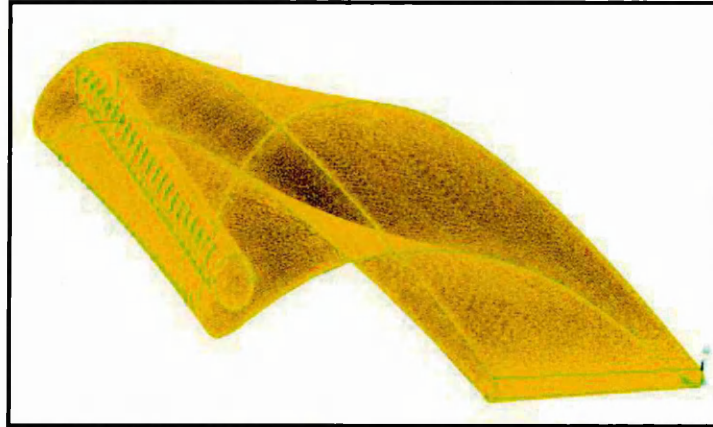


Figure (6-11) Local mesh of blade model as a solid body with cooling holes system [Daud *et al.* (2011C)]

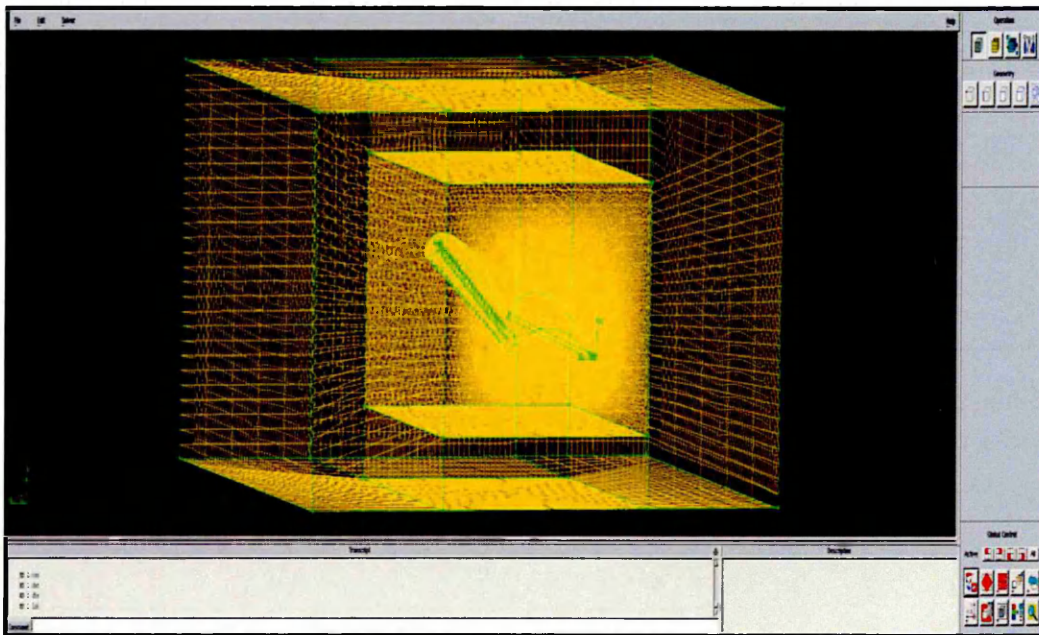


Figure (6-12) Multi block technique at meshing whole flow simulation box with blade model and holes film cooling

#### 6.4.2 Mesh independent solution

Acceptable numerical results are a key objective of any CFD simulation using available computer power. The use of larger number of cells in a model provides a better representation of the physical domain and achieves greater accuracy. A mesh-independent solution is a way to assure the accuracy and efficiency in all CFD computations [Chung (2002)]. As mentioned earlier, the multi-block method technique

has been used in this thesis. Thus, TGrid was used to complete the volumetric mesh. An unstructured mesh is employed for meshing the blade model, film cooling and nearest block volume due to the gas turbine blade complex design (sectional area from hub to shroud *changes* owing to the skewness degree, and film cooling holes geometry is also present). While the other block volumes (flow simulation box volumes) were meshed by a structured scheme. Therefore, there are many methods which can be implemented to satisfy unstructured adaptive meshes (the accuracy of numerical solution for an unstructured mesh could be achieved by adaptive method). These methods include:

1. Mesh refinement methods (h-methods)
2. Mesh movement methods (r-methods)
3. Mesh enrichment methods (p-methods)
4. Combined mesh refinements and movements (hr-methods)
5. Combined mesh refinements and enrichments (hp-methods)

The h-method is a refinement method which modifies the elements (cells) in which a *posteriori error indicator* is measured based on solution gradients which is larger than the preset criterion. The solution gradient variables are density, pressure, velocity and temperature. The mesh enrichment (p-methods) is assigned with a fixed mesh and the solutions are expected to improve by running higher polynomial or higher order functions. In the present thesis, unstructured grid methods (hp method) were employed. The meshing strategy was refined for three volumes (blade model, film cooling holes and simulation box) from 3,039,577 to 6,837,942 cells (elements). Since the value of  $y^+ \leq 140$  for the blade walls, further refinement was performed by increasing the number of cells near the blade walls to 8,935,794 which reduces the value of  $y^+$  to fall in the range  $y^+ \leq 65$ . Typically, when the first grid point is located away from the wall at  $50 < y^+ < 200$  this allows the standard wall function to work in the solution. However, refinement grid independence (h-method) was applied by increasing the number of elements from 8,935,794 to 10,141,446 and subsequently to 11,480,886. These increments in mesh density are obtained by employing the *size function tool* from the edges of the blade to the nearest flow simulation block, and the surrounding flow simulation block volumes. The temperature, pressure and velocity are the parameters of the solution gradient variable. Clearly, numerical results obtained with 10,141,446 elements achieve relatively good accuracy and a lower temperature error (about 0.70%) between the blade temperature and blade shadow temperature compared with smaller numbers of mesh

elements. Figure (6-13) shows the mesh refinement solution strategy for temperature, pressure and velocity along the blade surface as gradient variables.

Higher polynomial or higher order functions (p-methods) have also been employed in this thesis, for the fully turbulent channel flow and NACA 0012 airfoil benchmark simulations (discussed earlier). This has been achieved through increasing discretization from first order to third order and the numerical solutions have shown that second order discretization provides the best solution results. After performing the mesh independent computations for the 35° injection angle, the average skewness of all volumes has been shown to be approximately 0.91 (caused by the complex blade geometry). However, mesh independent method (hp methods) were also utilized for blade simulations with cooling holes injection angles of 45° and 60°.

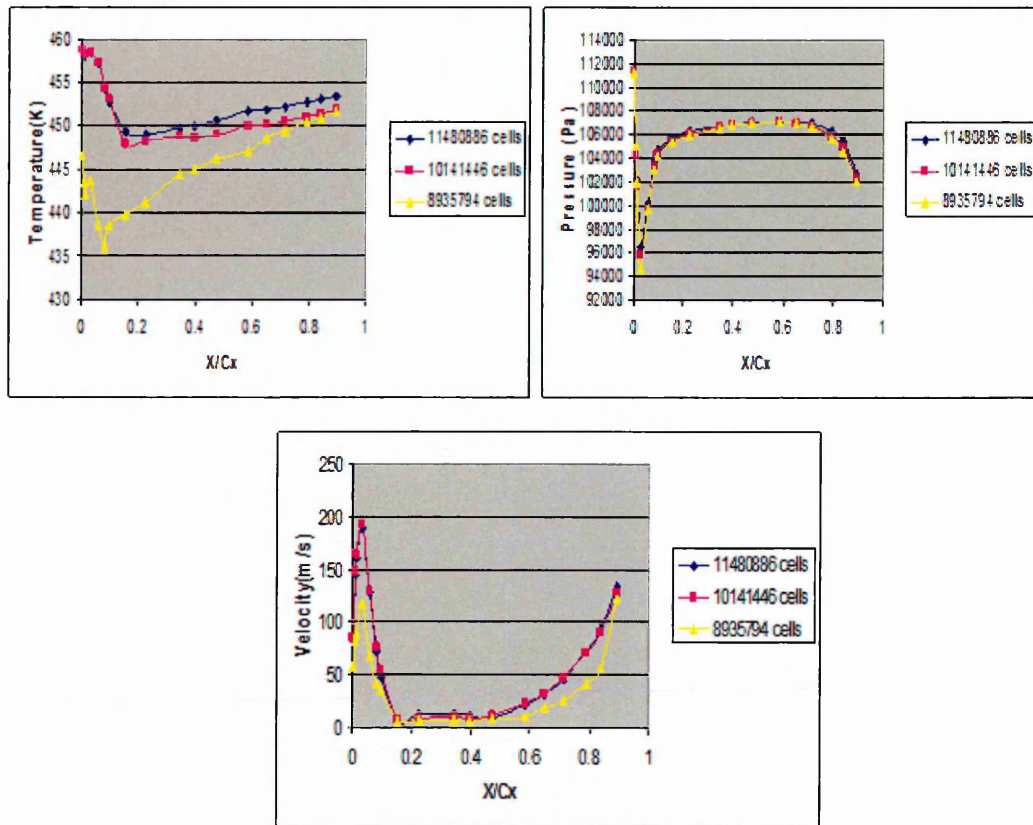


Figure (6-13) Mesh refinement solution strategy for temperature, pressure and velocity along the blade surface as gradient variables.

## 6.5 Boundary conditions

A key aspect of any CFD simulation is defining and applying physically realistic boundary conditions. In this study, a variety of boundary conditions have been applied through defining two fluid volumes. Namely, the main flow and the coolant fluid, in

addition to signifying the gas turbine blade as a solid volume. A wall boundary condition was used to define the flow boundaries in each region. As shown in Figure (6-14), the inlet and outlet wall of the flow simulation box were defined as the main inlet velocity flow field and the main outlet pressure flow field. Also the *cooling holes volume* which is represented by the holes surfaces and inlet coolant fluid were defined as the wall and inlet velocity. Finally, gas turbine blade walls were identified by hub, mid, shroud blade surface and trailing surface.

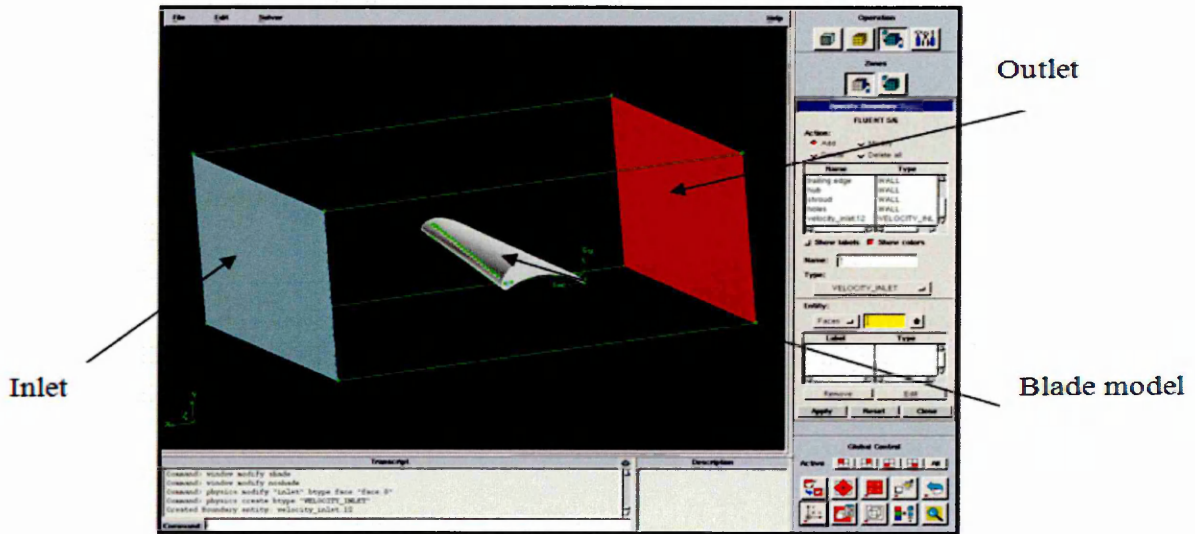


Figure (6-14) Boundary condition operations for blade, holes and simulation box volumes in GAMBIT

The initial boundary conditions details used in the Fluent software numerical simulation set up are given in Table 6-1. The boundary conditions in this research have been adopted from previous published papers [Garg and Abhari (1997)], [Burdet and Abhari (2007)].

**Table 6-1: Application of boundary conditions**

Boundary conditions	Values obtained from [Garg and Abhari (1997)], [Burdet and Abhari (2007)]
Hot air inlet velocity	163.4 m/sec
Hot air inlet temperature	460 K
Blowing ratio	M=1, M=1.5
Cooled air inlet temperature	287.5 K
Outlet temperature of channel	459.88 K

In the numerical calculations, the physical properties of the hot gas (fluid), cooled air (fluid) and blade model materials (carbon steel, solid) have been defined as illustrated in Table 6-2 and Table 5-1 respectively.

**Table 6-2: Inlet hot gas and cooled air applied to FLUENT software**

<b>Fluid Property</b>	<b>Values at temperature=287.5 K</b>	<b>Values at temperature= 460 K</b>
Density	1.2292 [kg/m <sup>3</sup> ]	0.76745[kg/m <sup>3</sup> ]
Specific heat	1005[J/kg-K]	1023.4[J/kg-K]
Thermal conductivity	0.025315[W/m-K]	0.03769[W/m-K]
Viscosity	1.79614*10 <sup>-5</sup> [kg/m-s]	2.5409*10 <sup>-5</sup> [kg/m-s]

## 6.6 Selecting solver, equation and solution convergence

Computational Fluid Dynamics (CFD) can successfully simulate turbulent internal and external aerodynamic flow, heat and mass transfer and also highly nonlinear, transient, multi-physical problems. This requires specification and solution of the governing conservation equations which describe the flow physics. In FLUENT these comprise:

1. Continuity equation
2. Momentum conservation equation.
3. Navier-Stokes equation.
4. Energy equation
5. Kinetic and epsilon transport (turbulence model) equations.

Currently, the Reynolds Averaged Navier-Stokes (RANS) equations are considered to be the accurate approximations which can be applied to perform CFD calculations for realistic simulation. Unfortunately, it is currently not viable to perform a Direct Numerical Simulation (DNS) for the Navier-Stokes equations for engineering problems; (DNS) is most accurate method, solving all turbulent scale, required very fine mesh and applied for simple geometry due to the lack of sufficient computer power. Therefore, before any CFD calculation can be performed, it is necessary to simplify the Navier-Stokes equations. It is up to the user to select the level of simplification. Simplification yields faster computations; but the results are of course less accurate [Lucas (2005)].

Flow in gas turbine blade passages are described as turbulent flows and because of the effects of freestream turbulence in gas turbine aerodynamics is one of the most important control parameters in assessing film cooling performance, since the source of this main turbulence is the combustor which is located upstream of the turbine blades. The turbulence levels and size of turbulent eddies will also vary depending on whether the turbine is designed for aerospace or power generation applications [Bogard and Thole, (2006)].

Numerous methods are used to describe turbulent flows in the FLUENT software. These include hydraulic diameter, turbulence length, turbulence ratio and turbulence intensity. In this study, both turbulent intensity and hydraulic diameter were defined in the numerical simulation. Turbulent intensity can be calculated from:

$$Tu = 0.16 * Re^{(-1/8)} \quad (6-1)$$

Where,

Tu is turbulence intensity

The inlet velocity of the hot air channel is the same as the values published by [Garg and Abhari (1997)], [Burdet and Abhari (2007)] as shown Table 6-1 which gives Tu=3.37%.

For the inlet cooled air through lateral holes, based on a blowing ratio (BR=1) a turbulent intensity was calculated, Tu = 4.45%.

The hydraulic diameter can be calculated from [Schlichting (1968)].

$$D_h = \frac{4 * \text{inlet area}}{\text{wetted perimeter}} \quad (6-2)$$

For the hot air channel: the inlet area<sub>(hot air channel)</sub> = 200\*110 = 22000 mm<sup>2</sup>

The wetted perimeter<sub>(hot air channel)</sub> = 2\*(200+110) = 620 mm

$$\text{so: } D_h = \frac{4 * 22000}{620} = 141.935 \text{ mm} \approx 0.142 \text{ m}$$

For the cooled air lateral hole  $D_h = \text{Diameter} = 4 \text{ mm} = 0.004 \text{ m}$

To obtain acceptable accuracy in any CFD modeling, it is necessary to satisfy certain requirements in the numerical scheme (solver). These requirements are defined as [Hirsch (1988)]:

1. Consistency
2. Stability

A finite-difference representation of a Partial Differential Equation (PDE). So, the Finite Difference Equation (FDE) is *consistent* if the difference between the PDE and its difference representation vanishes as the mesh is refined.

$$\lim_{\Delta x, \Delta t \rightarrow 0} (PDE - FDE) = \lim_{\Delta x, \Delta t \rightarrow 0} (\tau_n) = 0 \quad (6-3)$$

Hence, a scheme is consistent if the truncation error tends to zero for  $\Delta t, \Delta x$  [Mason, (1997)]. This condition leads to a determination of the order of accuracy of the scheme and its truncation error.

Stability depends on the numerical scheme used for the solution (implicit and explicit scheme). *An FDE is stable if the error is bounded* (in unstable solvers, the error can cause wild oscillation or divergence of the solution so the error grows, whereas for stable schemes the error decays).

The conditions of consistency and stability are prerequisites for convergence and are related to each other [Hirsch (1988)]. Hence, the solution of the FDE's should approach the solution of the PDE as the mesh is refined. All FLUENT simulations were executed until the solution convergence factor  $1 \times 10^{-7}$  were satisfied for the energy equation. The solution has been controlled by selecting the **SIMPLE** algorithm to solve velocity-pressure coupling with an implicit procedure, such that more than 3500 iterations are sustained to convergence (solution stability).

## 6.7 Gas turbine results

### 6.7.1 Effect of blowing ratio

Figure (6-15A), (6-15B) and (6-15C) illustrates the distribution of the static temperature of the solid blade from the hub to the shroud regions and from the blade leading edge to the trailing edge. Consequently, temperature distributions and amount of heat transfer results for the blade presents Conjugate Heat Transfer (CHT) and it is more realistic. Because of simultaneous calculations between aerodynamic and heat transfer in the external hot gas and internal cooling passages as conduction and convection heat transfer with solid body [Luo and Razinsky (2007)]. The effects of Blowing Ratio (BR) on the distribution of blade temperature ( $T_w$ ) through injecting coolant fluid into main hot gas are clear. Blowing Ratio (BR) in this research can be calculated by equation (5-3). Figure (6-15) depicts contour temperature distributions for blowing ratio BR=1, 1.5

and 2, respectively. The temperature colour map is graduated from low to high temperature (leading edge to trailing edge area). Consequently, with increasing of mass flux ratio (BR) the blade surface temperature will be reduced on both the pressure side and the suction side and also from the hub to the shroud. Thereby, the protected area of the blade from incoming hot gas will be increased with increasing blowing ratio. In this study, film cooling technology will be studied firstly- convection cooling through blowing coolant fluid in to the lateral hole from hub to shroud (internal cooling). Secondly, coolant fluid is injected for both the pressure and suction side as a secondary fluid to create a blanket above the blade surface (external cooling).

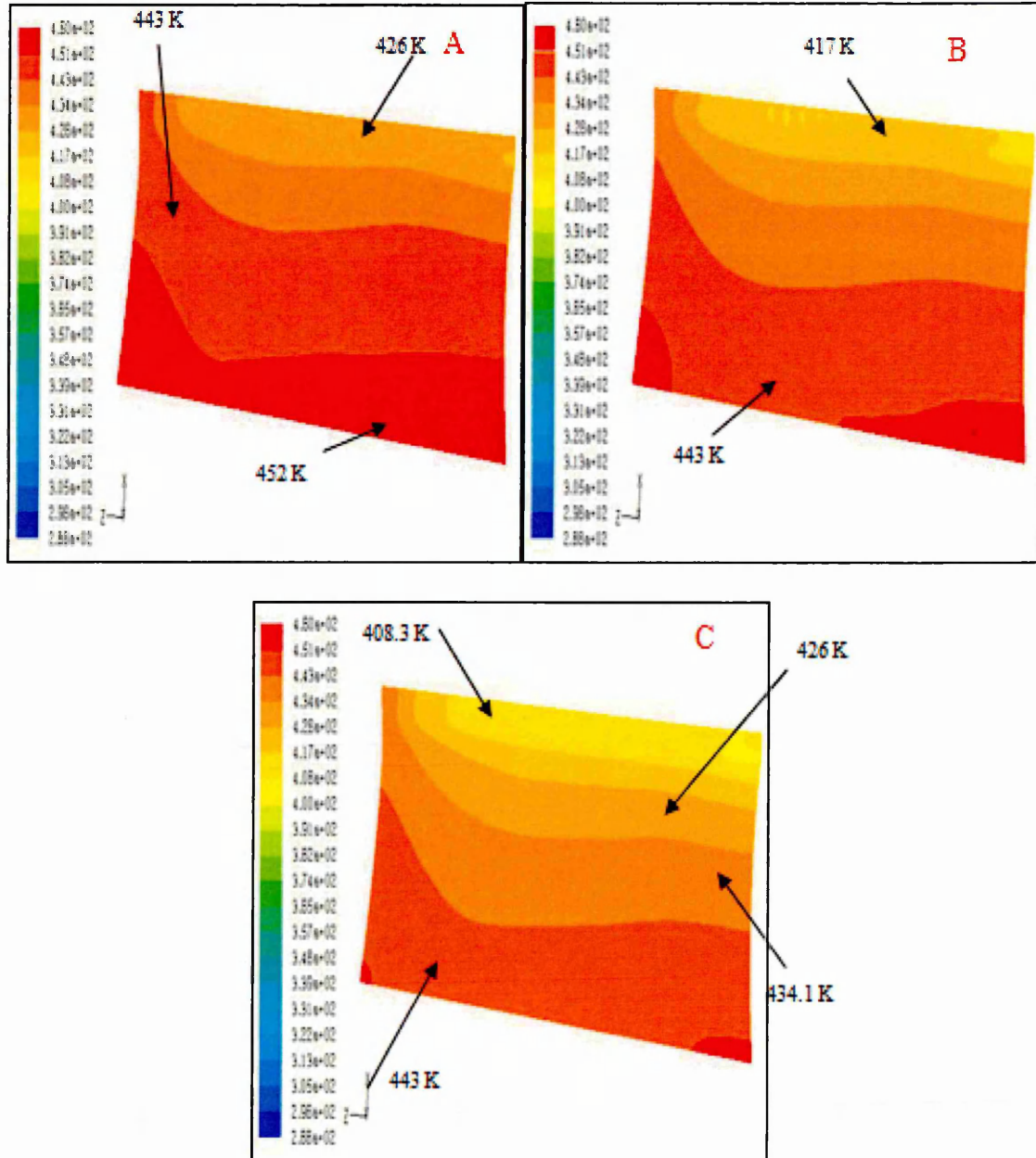


Figure (6-15) Predicted counter temperatures of the blade model at different blowing ratio A) BR=1, B) BR=1.5, C) BR=2 [Daud *et al.* (2011C)]

According to Figure (6-15) the drop in predicted blade temperature with increasing the of BR indicates that the cooling effectiveness will be enhanced from the hub to the shroud and from the leading to trailing edge, a result which correlates well with the computations of Kadja and Bergeles (1997).

This study is novel as it demonstrates the effect of cooling on the blade modeled as a solid body. Figure (6-16) presents the trajectory of temperature and cooling effectiveness distribution for both pressure side and suction side on the solid body blade (always the effectiveness will be reversed trajectory compares with temperature trajectory). In addition, the hub, mid and shroud area temperatures at blowing ratio  $BR=2$  are also illustrated. The temperature along the span of the blade can be detected from the distribution of the temperature at the hub area to mid and from the mid to shroud area. Invariably, the hub area temperatures will be lower than the mid and shroud area temperatures at the leading edge region. This is a result of the coolant fluid being blown (injected) from the blade base (hub area). In the midspan section the predicted temperatures curve descends much more than the hub temperature profile at  $X/Cx > 0.25$  on the pressure surface and at  $X/Cx < -0.02$  on the suction side Figure (6-16). This pattern is affected by the blade geometry. Namely, the camber of the blade and the angle of the twist-the blade cross section with the span and axial cord at each section changes from hub to shroud (blade design shape).

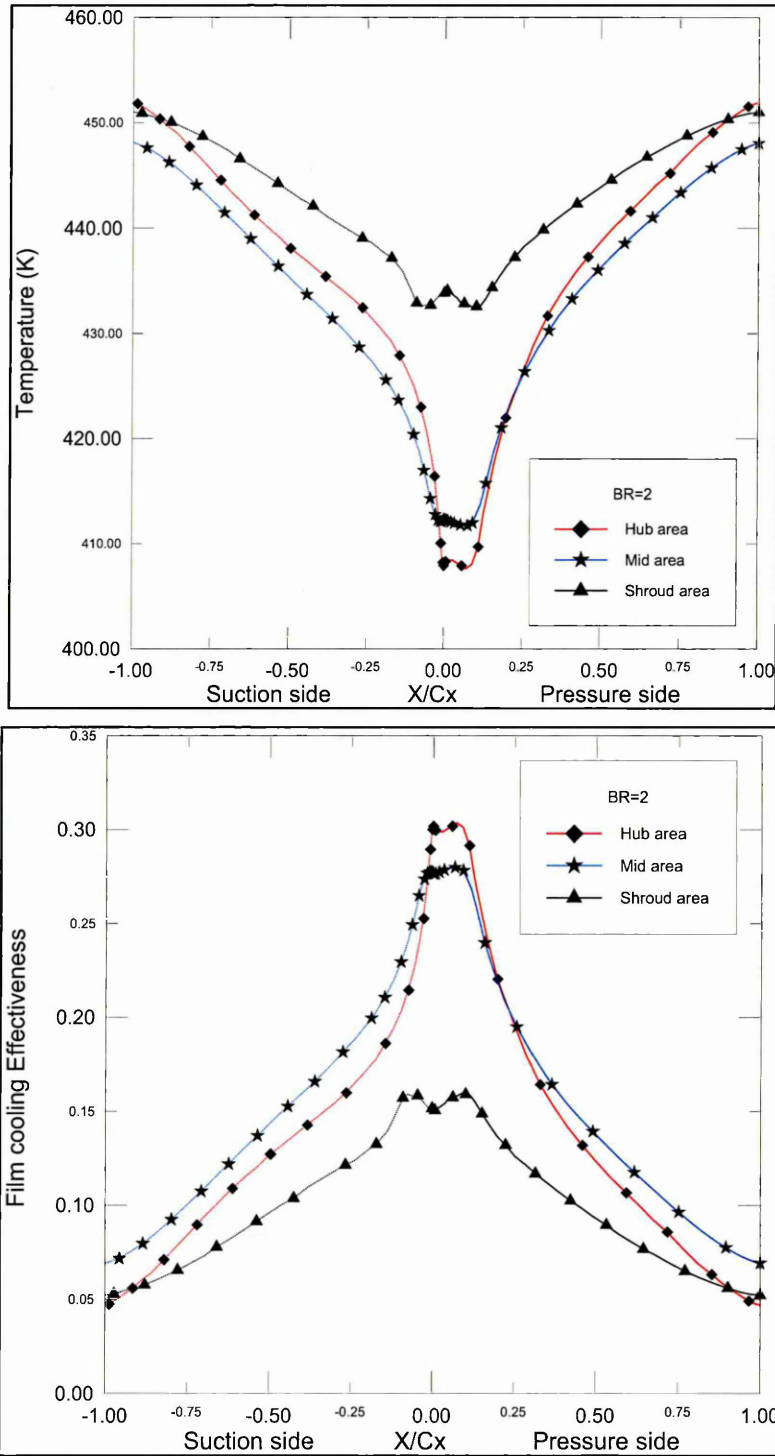


Figure (6-16) Temperature and the Effectiveness cooling distributions difference in hub, mid and shroud area on the blade model by injecting coolant air at BR=2 [Daud *et al.* (2011C)]

Figure (6-17) shows the cooling effectiveness ( $\eta$ ) in three regions (hub, midspan and shroud), for different blowing ratios, BR=1, 1.5 and 2. Figure (6-17A) displays the effects of increasing Blowing Ratio (BR) from 1 to 2 at the hub area. Significantly,

when increasing blowing ratio from BR=1 to 1.5, the cooling effectiveness will be increased by about 20.1% and 15.2% through respective increases in BR to 1.5 and 2 (near the leading edge of blade). The pressure side cooling effectiveness is higher than suction side at this region. Certainly, the thermal boundary layer is thicker on the pressure side due to the lower freestream velocity so, high BR enhanced film cooling on pressure side which a trend in agreement with Burdet and Abhari (2007), and Tao *et al.*(2008) attributable to the similar angle of injection ( $35^{\circ}$ ) and lateral holes inclined ( $9.13^{\circ}$ ) design. In addition to, Heidmann *et al.* (2003) found out, film holes on the pressure side provides better cooling performances.

The cooling effectiveness in the midspan area is illustrated in Figure (6-17B) and it also increases corresponding to the blowing ratio by about 21.3% and 13.6% through BR=1 to 1.5 and from BR=1.5 to 2. At a blowing ratio BR=1, the cooling effectiveness near the injection zone (leading edge zone) is higher on the suction side than that on the pressure side. But with increasing BR, the film cooling effectiveness on the pressure side will gradually increase compared with the suction side.

Figure (6-17C) shows the variation in cooling effectiveness with blowing ratio in the shroud region. The trajectory of the pressure and suction side is nearly analogous (matched). About 18.3% and 12.7% film cooling effectiveness will be enhanced with increasing blowing ratio from BR=1 to 1.5 and from BR=1.5 to 2 respectively. The film cooling effectiveness contours for the pressure and suction side on the blade model at blowing ratio BR = 2 is shown in Figure (6-18).

A good correlation has been found agree with previous studies illustrated by Kadja and Bergeles (1997) and Guangchao *et al.* (2008) and other published results on film cooling effectiveness utilizing cylindrical hole shapes. When the values of BR increases, the blade surface temperature drops and the cooling effectiveness is enhanced. BR is proportional to temperature difference ( $\Delta T$ ) and inversely proportional to cooling effectiveness ( $\eta$ ). Ou and Rivir (2001A) confirmed that the film cooling effectiveness enhanced for higher values of BR=1, 2 and 2.5. The effect of increasing the blowing ratio provides highest film cooling but also the highest Frössling number and the optimum blowing ratio was obtained at BR=2.

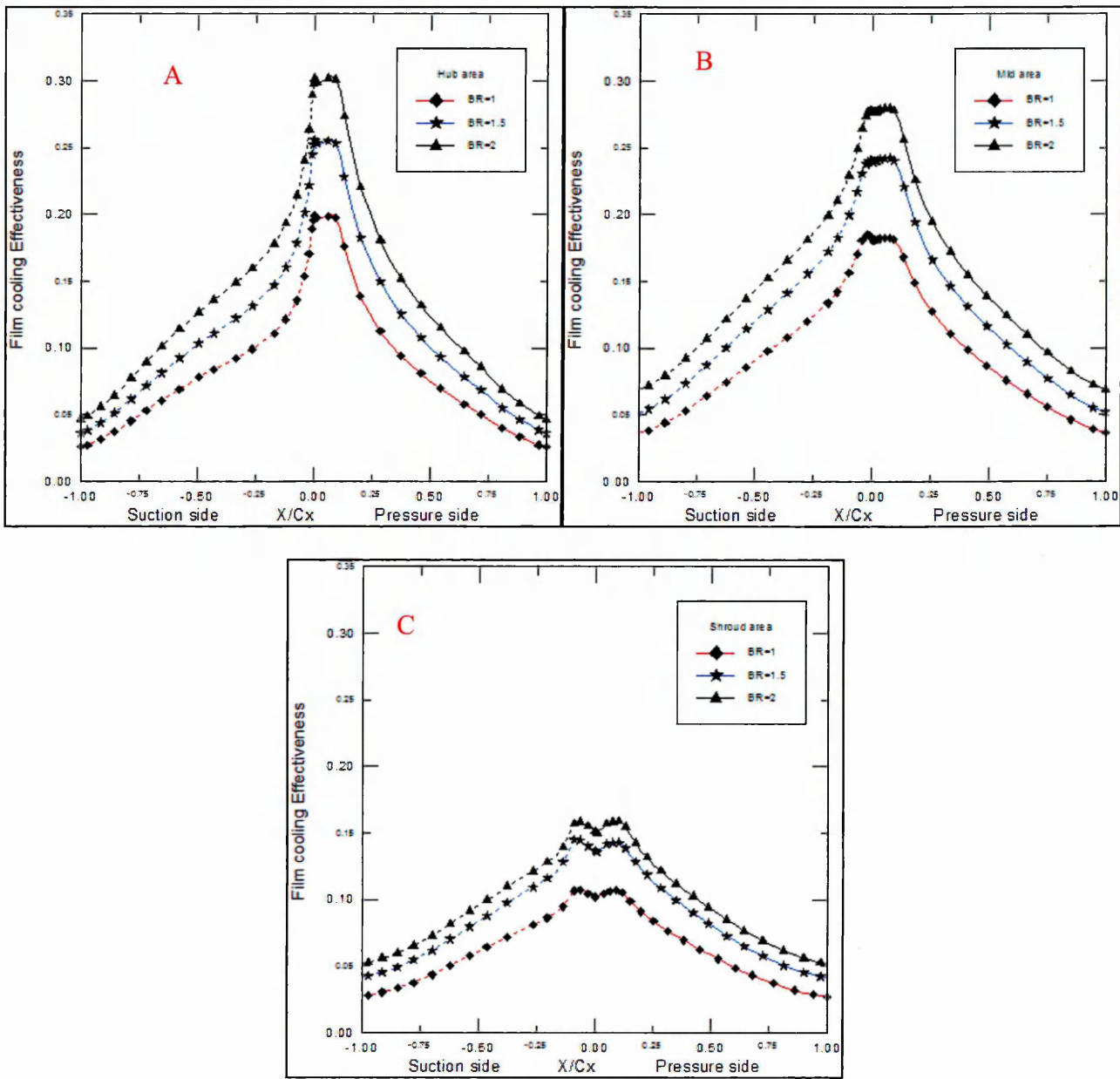


Figure (6-17) Effects of blowing ratio (BR) on the blade effectiveness cooling- A) hub, B) mid and C) shroud [Daud *et al.* (2011C)]

The values of cooling effectiveness change gradually from the leading edge to trailing edge (colder to hottest place). When the values of Blowing Ratio (BR) are reduced, the hottest area will be increased on both sides and the blade will be exposed to incoming hot gas.

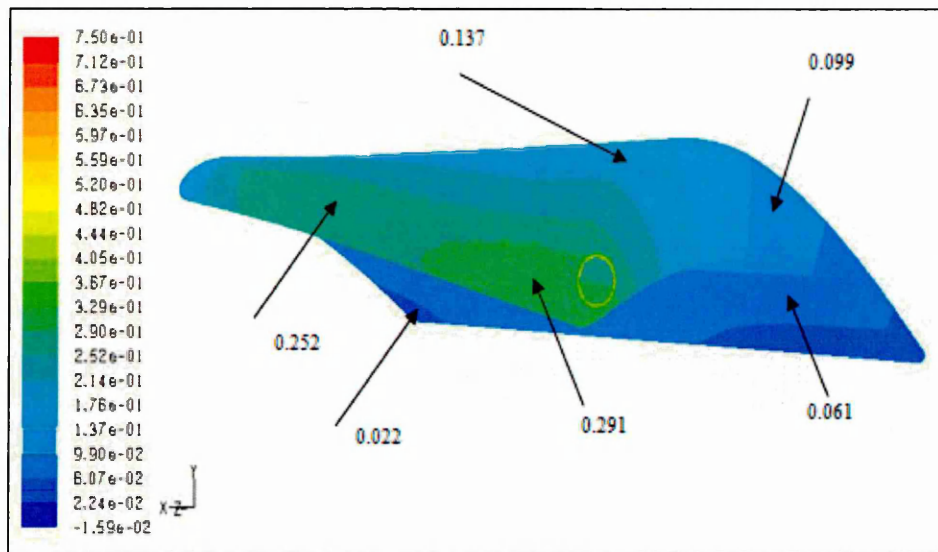


Figure (6-18) Film cooling effectiveness contour at blowing ratio  $BR=2$  on the blade model [Daud *et al.* (2011C)]

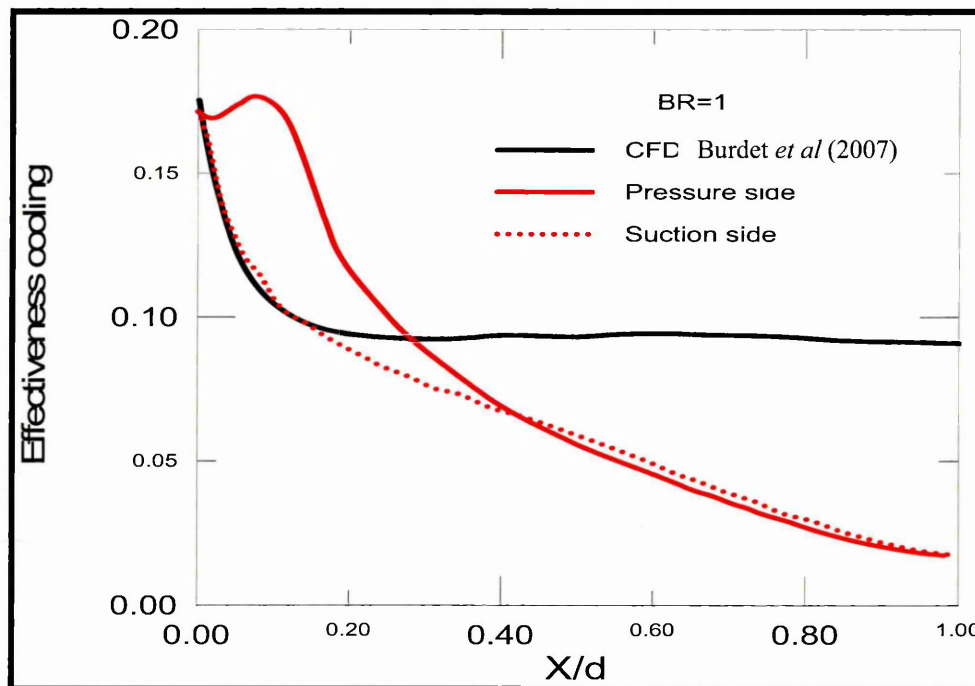


Figure (6-19) Distributions of film cooling effectiveness at blowing ratio  $BR=1$  at angle of injection  $35^\circ$ : comparison between CFD results of Burdet *et al.* (2007), the blade model calculation [Daud *et al.* (2011C)]

Figure (6-19) shows the comparison between the CFD prediction of Burdet *et al.* (2007) and the computed film cooling effectiveness ( $\eta$ ) on the blade model near hub position for  $BR=1$  at angle of injection  $35^\circ$ . The values of cooling effectiveness ( $\eta$ ) at  $X/d < 0.3$

on the pressure side are significantly higher than Burdet *et al.* (2007), which is beneficial. On the suction side at  $X/d < 0.18$  the values of  $(\eta)$  seems to coincide with Burdet *et al.* (2007) while, the profile of the cooling effectiveness  $(\eta)$  descend after this region. The drop in values of cooling effectiveness for both sides is attributed to the blade being modeled as a solid body which is more realistic than the previous studies (where blades were analyzed as a shell) and also the effects of blade design, holes diameter and number of holes along the span which are different from previous investigations.

Figure (6-20) shows the predicted profiles of Nusselt number ( $Nu$ ) via equation (5-4) based on the axial chord  $C_x$  at the mid span for BR=1, 1.5 and 2.

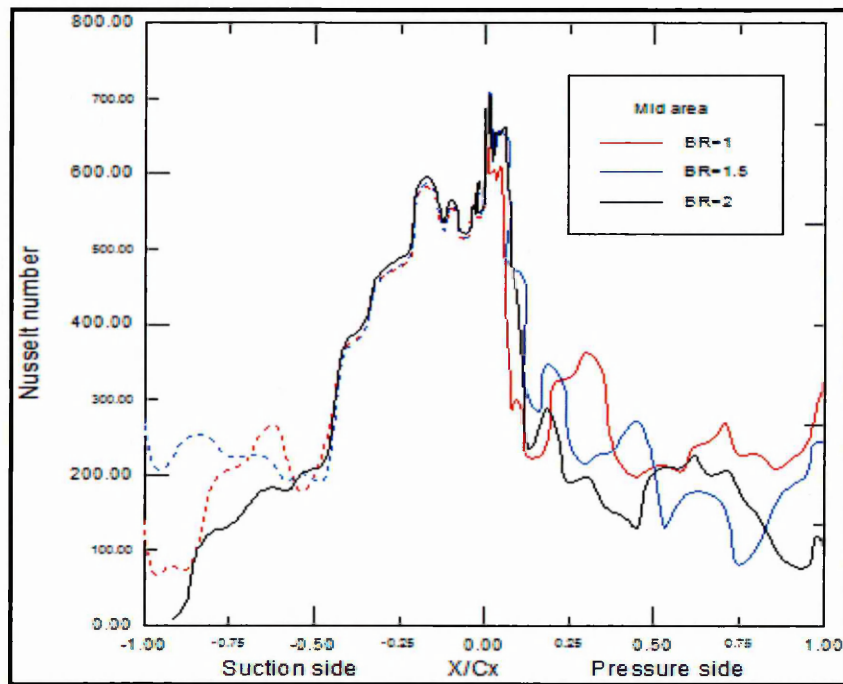


Figure (6-20) Predicted profile of Nusselt number ( $Nu$ ) at midspan for BR=1, 1.5, 2 [Daud *et al.* (2011C)]

Near the leading edge along the span (from hub to shroud) the heat transfer attains the maximum level which is where the boundary layer is thinnest and this is in good agreement with the results of Burdet and Abhari (2007), Garg and Abhari (1997) and Burdet *et al.*(2007). Actually leading edge section of a gas turbine blade is the first blade surface area exposed to incoming hot gas flow. Therefore the amount of heat transfer from the hot gas to the blade will be concentrated in this area and this produces

the maximum value in the heat convection to the heat conduction ratio (Nusselt number,  $Nu$ ).

On the pressure side ( $N_{\nu}$ ) suddenly drops after the leading edge. Certainly, the effects of film cooling are manifested through the creation of a layer of protection from the incoming hot gas on this side. At  $X/C_x > 0.15$ , the BR influence is observed as reducing ( $N_{\nu}$ ) – again this trend is in agreement with the studies of Kadja and Bergeles (1997) and Guangchao *et al.* (2008). On the suction side, the Nusselt number ( $N_{\nu}$ ) suddenly falls after the leading edge and in the region  $X/C_x = -0.25$  the values of ( $N_{\nu}$ ) slightly increase owing to the effects of turbulence and the camber of the blade and gradually falls. Better protection of the blade from the hot gas is achieved through increasing the cooling effectiveness,  $\eta$  and reducing the blade's Nusselt number ( $N_{\nu}$ ).

Figure (6-21) shows Nusselt number contours at the leading edge and the film cooling regions at  $BR=2$ . The maximum value of Nusselt number ( $N_{\nu}$ ) is determined at the leading edge along the blade span. This implies heat transfer from the hot gas in the direction of the blade. Near the holes, heat transfer to the blade is absent due to coolant fluid injection. Thus, the Nusselt number ( $N_{\nu}$ ) drops to negative values (heat transfer will be in the opposite direction).

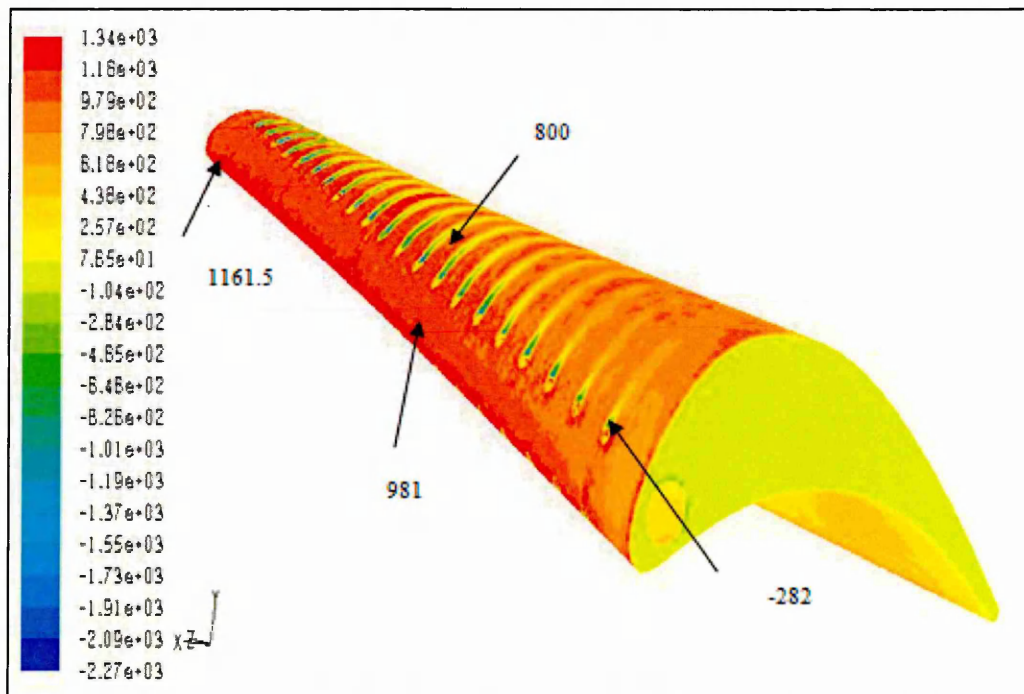


Figure (6-21) Nusselt number ( $Nu$ ) contours on the blade model for  $BR=2$  [Daud *et al.* (2011C)]

### 6.7.2 Effect of coolant temperature

This section of the numerical study is to investigate the effects of coolant temperature to provide good gas turbine blades protection from high turbine entry temperature. Figure (6-22) illustrates the effects of coolant fluid temperature on the distribution of film cooling effectiveness for the pressure side and suction side at the midspan location with BR=1, 1.5. In this study, two different coolant fluids (air at  $T_C=287.5$  and  $T_C=153$  K) have been injected to enhance blade protection. High cooling effectiveness was obtained through injected air as a coolant fluid at temperature of 287.5K. Evidently, from equation (5-1)  $\eta$  depends on  $T_\infty$ ,  $T_w$  and  $T_C$ . A decrease in  $T_C$ , does not necessarily produce an increase in cooling effectiveness ( $\eta$ ) since the blowing ratio (BR) will be also affected by the temperature property as indicated by equation (5-3).

Figure (6-23) depicts the effects of coolant temperature on static temperature contours especially on the pressure side of gas turbine blade with blowing ratio BR=1.5 with constant angle of injection  $35^\circ$ . Despite of drop in temperature distribution on surface of gas turbine cooled by coolant fluid at  $T_C=153$  K, the performance seems better in comparison with the gas turbine surface cooled by  $T_C=287.5$  K. But the investigation carried out in this research indicates that using a coolant fluid with  $T_C=287.5$  K gives better cooling performance. For example, at BR=1 and 1.5 about 7% and 13% value of film cooling effectiveness was enhanced via using coolant fluid at  $T_C=287.5$  K on the pressure side compared with coolant fluid at  $T_C=153$  K. As the coolant fluid is extracted from the compressor, resulting in losses in engine overall efficiency due to the loss of work producing capacity. In addition to thermodynamic and aerodynamic losses due to the ducting of the coolant to the blade surface and mixing of coolant air with hot mainstream flow [Sargison (2001)].

Two different coolant fluids (air at  $T_C=287.5$  and  $T_C=153$  K) have been used in this study. For both fluid cases the boundary conditions were extracted from the previous published papers. The first case was based on recommendations in [Garg and Abhari (1997), Burdet and Abhari (2007), (describing work conducted at NASA, USA) in which the coolant fluid was injected at temperature of 287.5K see Table 6-1. The second case was based on data obtained from ref. Lakehal *et.al* (2001), in which the coolant fluid was injected at  $T_C=153$  K. The justification for this lower temperature has been given by Lakehal et al. (2001) and is infact a benchmark for gas turbine film cooling studies. They infer in that paper that applied lower temperature are practical ( $T_C=153$  K) when aero-engines are operating at higher altitudes.

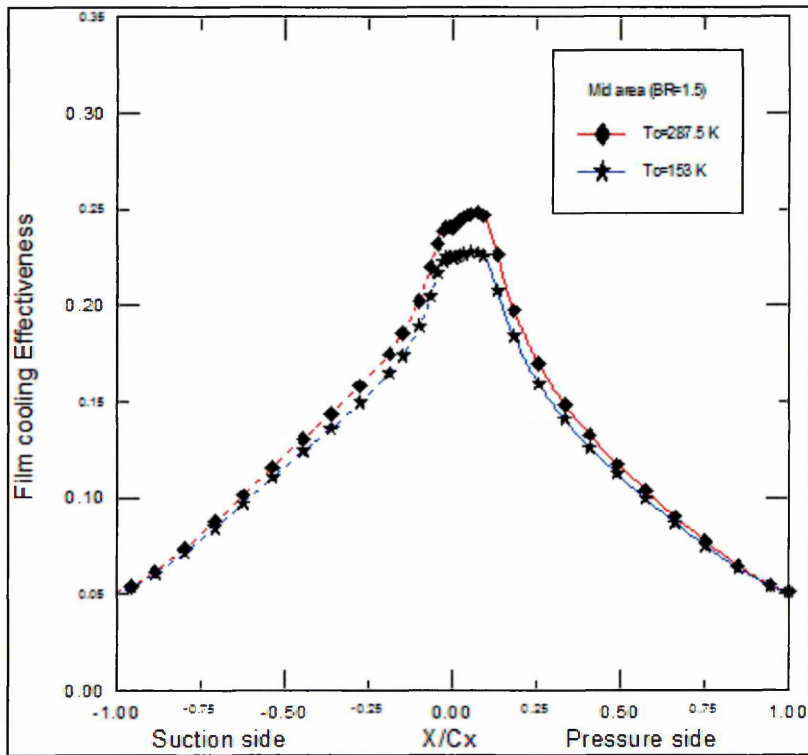
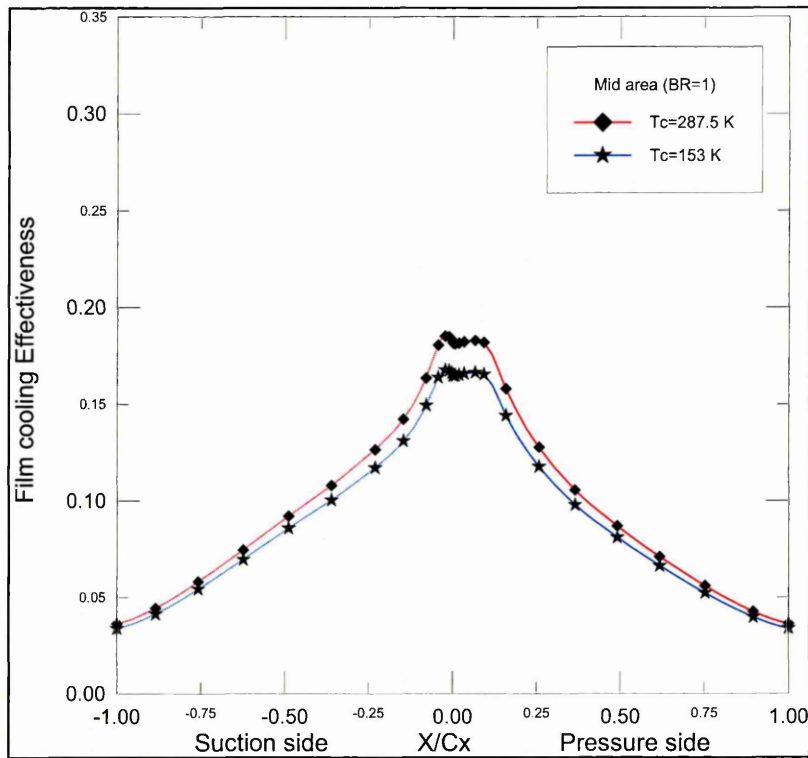


Figure (6-22) Effect of coolant fluid temperature on the film cooling effectiveness at BR=1, 1.5

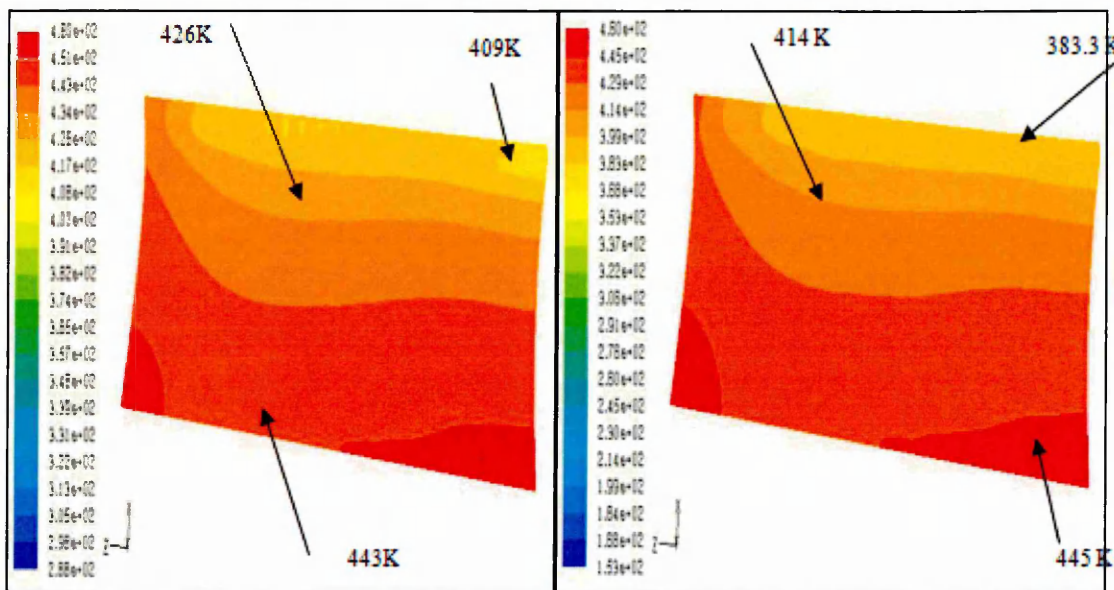


Figure (6-23) Effect of coolant fluid temperature on the temperature distribution BR=1.5 at 35 angle of injection

### 6.7.3 Effect of injection angle

Figure (6-24) depicts the effects of angle of injection at mid area with different (BR) on the blade cooling effectiveness. The mid area in gas turbine is exposed to hot gas from the combustor, thus it is considered as higher temperature degradation area than hub and shroud because of the combustor nozzle spray angle. Figure (6-24) shows that film cooling effectiveness when the angle of holes injection is  $45^{\circ}$  degree is better than  $35^{\circ}$  and  $60^{\circ}$  degree. In particular, near to the leading edge. For example, the value of film cooling effectiveness is enhanced by about 1.3% and 9.6% when the coolant fluid is injected at  $45^{\circ}$  compared with  $35^{\circ}$  and  $60^{\circ}$  respectively at BR=2, While, about 1% and 10% at BR=1.5. For flat plate cases, [Yuen and Martinz-Botas (2005)] discovered that the maximum cooling effectiveness was achieved at angle of injection of  $30^{\circ}$  in comparison with  $60^{\circ}$  and  $90^{\circ}$  degree. Consequently, it is evident that a better film hole configuration can provide better protection with less amount of coolant [Ahn *et al.* (2007)].

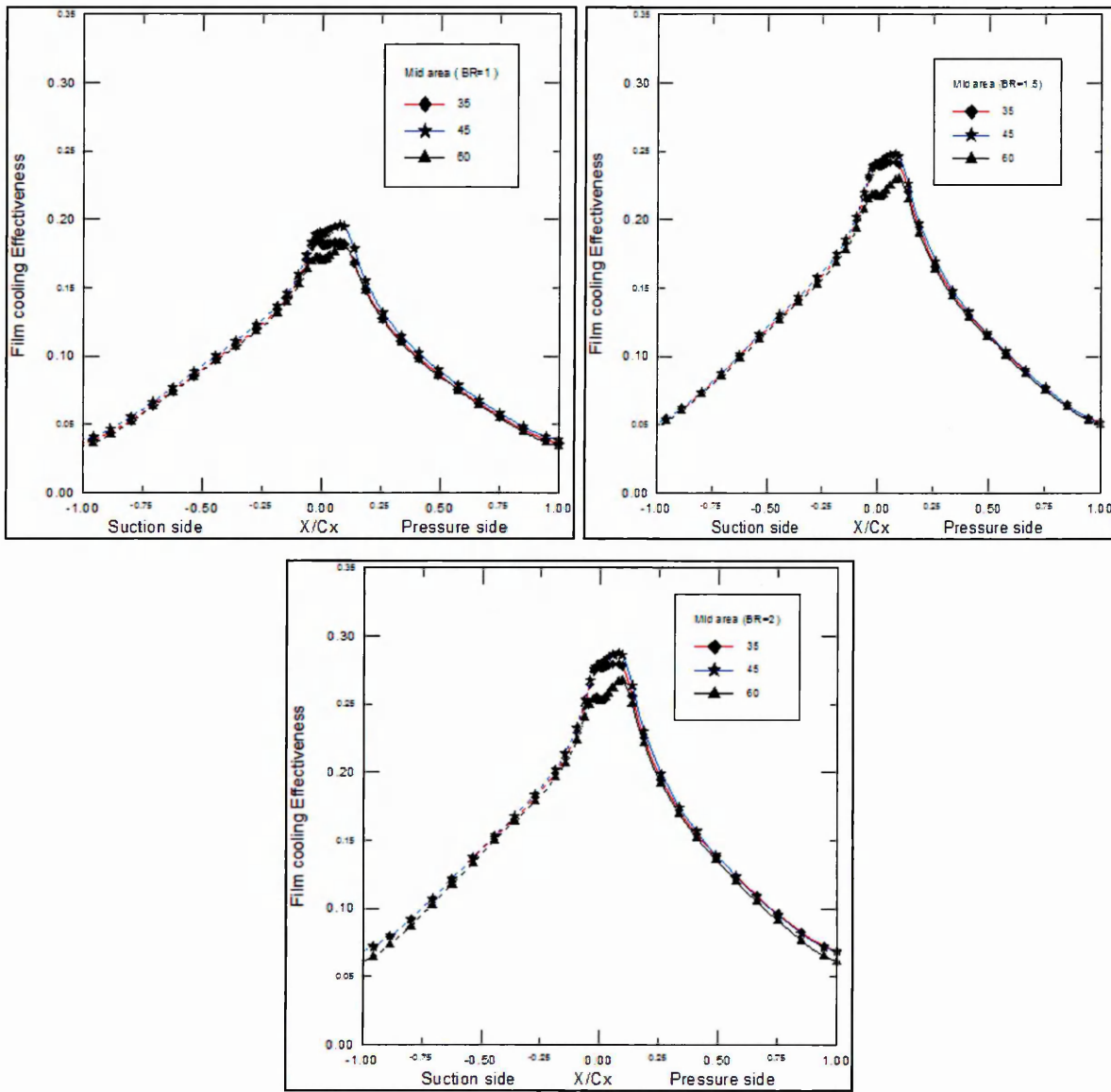


Figure (6-24) Effect angle of injection at mid area with different (BR) on the blade effectiveness cooling

Figure (6-25) presents pressure surface static temperature contours at BR=1 for angles of injection of  $35^{\circ}$ ,  $45^{\circ}$  and  $60^{\circ}$ . The effects of angles of injection ( $35^{\circ}$ ,  $45^{\circ}$  and  $60^{\circ}$ ) on blade temperature appear to be similar, but these effects clearly appear near the leading edge at the hub area. But injecting coolant fluid at angle  $45^{\circ}$  provides better protection for the blade because the mass flow of coolant is constant and the hot surface temperature is reduced. Figure (6-25) also illustrates that the hottest area is receding at the trailing edge for all angles of injection and that this hot area is the smallest with an angle of injection of  $45^{\circ}$ .

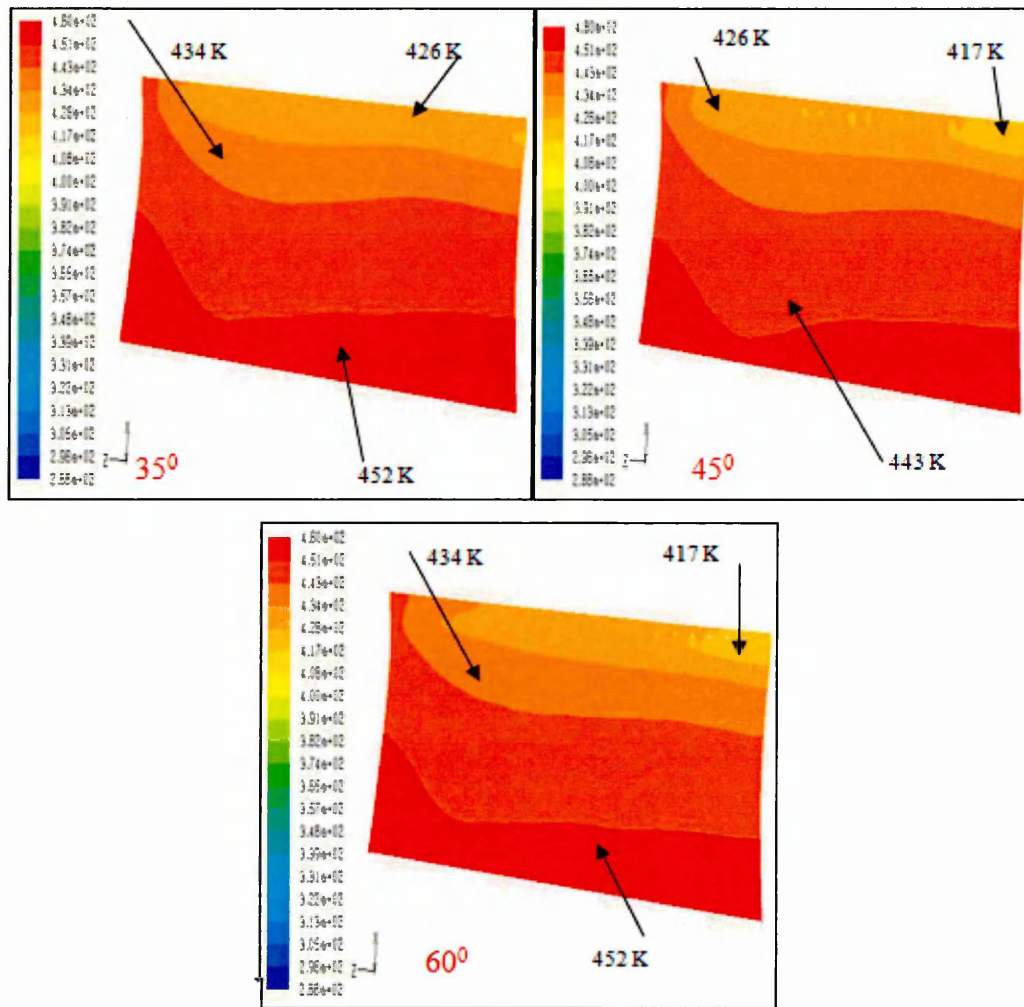


Figure (6-25) Effect of injection angle on gas turbine temperature distribution at blowing ratio BR=1

#### 6.7.4 Effect of hole numbers

This study numerically shows the effect of numbers of holes by reducing the holes from 42 to 32 and concentrate these holes near to the mid area. Figure (6-26) illustrates the cooling effectiveness trajectory in pressure and suction side at the hub, mid and shroud region. Obviously, with reducing the numbers of holes, a very small improvement in film cooling effectiveness trajectory is obtained at  $X/C_x > 0.3$  and  $X/C_x < -0.25$  (downstream) for hub area at the pressure and the suction side. While about a 7.5% drop appears in the leading edge due to the lack of cooling holes in this area.

Noticeably at mid area, the value of cooling effectiveness trajectory curve for 32 holes has been enhanced by about 2.7% at the leading edge and 12.5% at the trailing edge compared with the trajectory curve for 42 holes. Certainly, injected coolant fluid will be

accelerating when the number of holes is reduced as the coolant mass flow is constant. Therefore, cooling effectiveness is improved at the mid area as well at the second half of blade at the hub area (trailing edge) is enhanced due to skewness effects and blade geometry.

Despite of, some improvement in film cooling effectiveness located on the hub and mid area with reduction in number of holes, but shroud area is exposed to incoming hot gas as shown in Figure (6-26). Consequently, cooling effectiveness strongly drops down to about 75%.

Figure (6-27) depicts the static temperature contour at  $BR=1.5$  for two different blade geometry. The first blade is designed with 42 holes while the second blade is designed with 32 holes. Thus, Figure (6-27) confirms that reducing the number of holes has a minimal effect on the cooling process and the influence of the film cooling performance is low. Especially at the shroud region which is exposed to incoming hot gas temperature, noting that the durability of a gas turbine drastically depends on its components temperature, so thermal stress will increase on the blade.

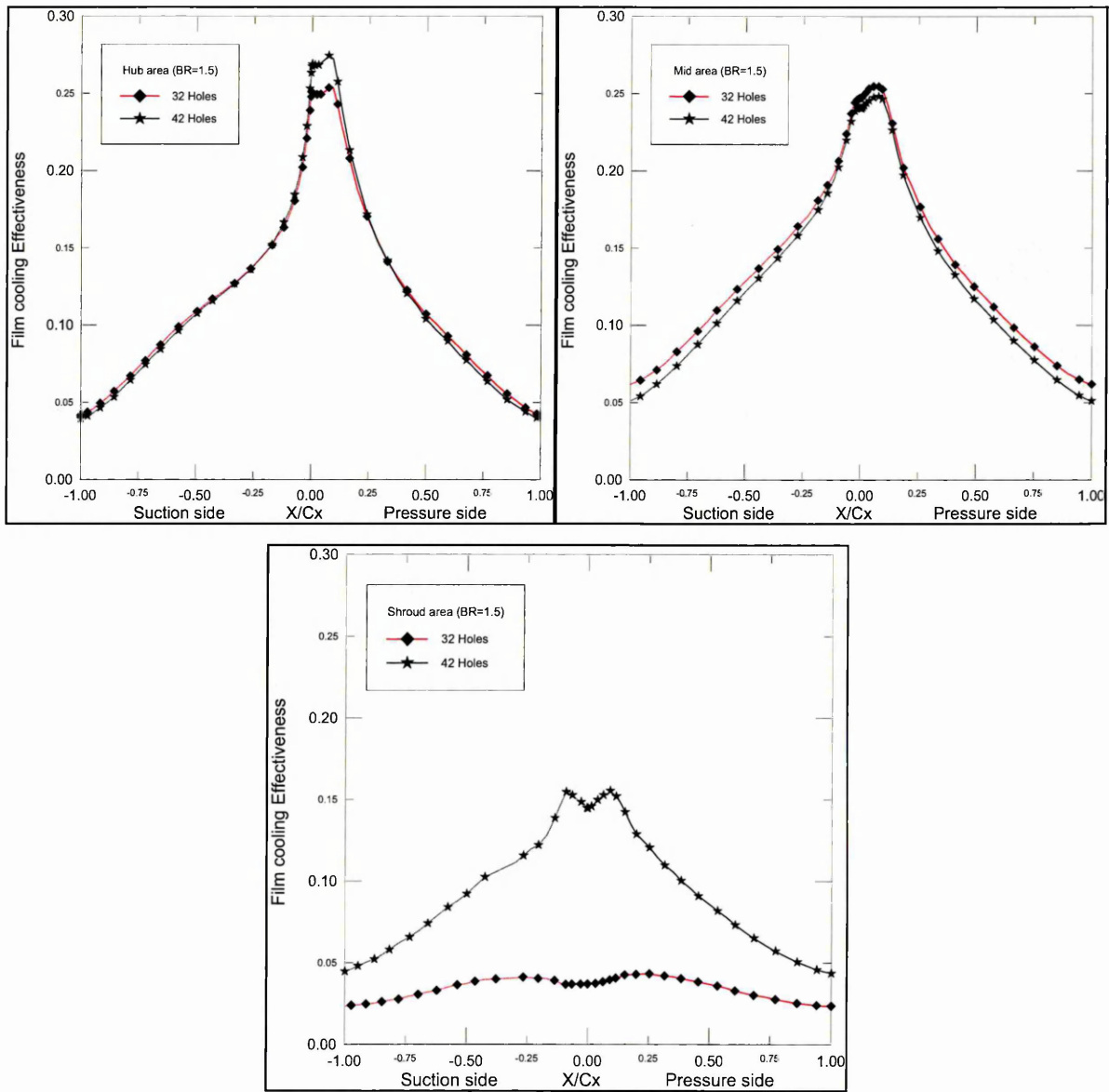


Figure (6-26) Cooling effectiveness trajectory at B R=1.5 for hub, mid and shroud area effected by number of holes.

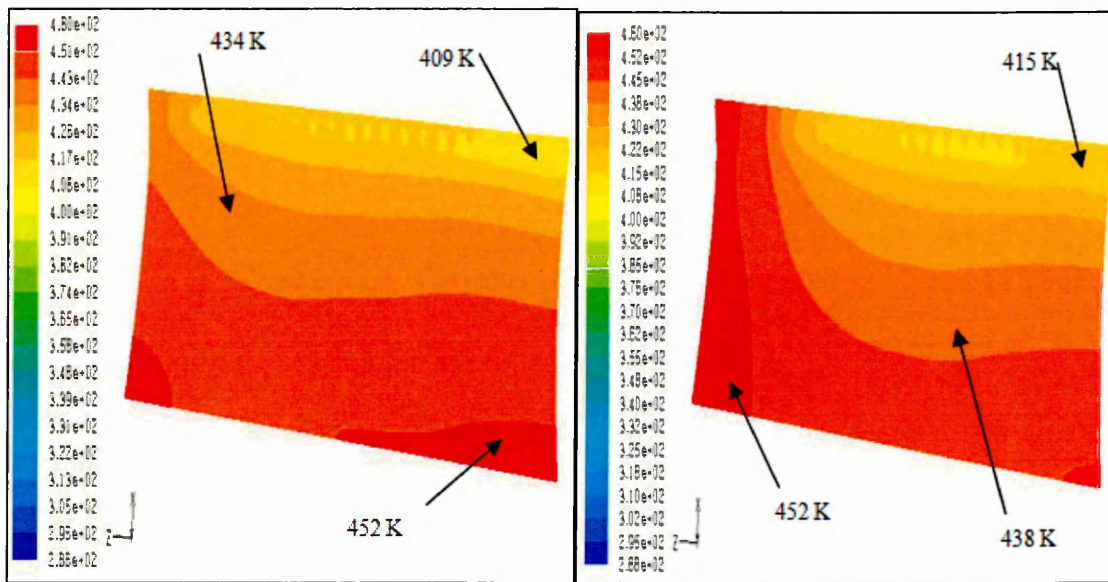


Figure (6-27) Effect of holes number on gas turbine temperature distribution at blowing ratio  $BR=1.5$  with angle of injection  $45^\circ$

### 6.7.5 Effect of hole diameter

In this section, the effect of the holes diameter on the gas turbine blade film effectiveness is presented. Figure (6-28) illustrates the blade film cooling effectiveness trajectory at hub, mid and shroud area related to varying the holes diameter from 1 mm to 0.5 mm with an angle of injection of  $45^\circ$  at  $BR=2$ . Consequently, film cooling effectiveness is reduced to about 31.5%, 39.4%, and 36.3% at the leading edge region with reduced holes diameter for hub mid and shroud respectively. Thus, it is not wise to reduce cooling holes diameter because coolant fluid will fare away from the blade surface due to the process of the penetration of a hot gas layer. While, film cooling effectiveness has been enhanced near to the trailing edge to about 54.8%, 29.5% and 21.1% for hub, mid and shroud area respectively due to spread of cooling fluid near the trailing edge.

The shape of film cooling holes is an important parameter influencing the value of heat transfer coefficient and overall film cooling performance. Hence, overall film cooling performance is significantly enhanced with expanded exits holes. In addition to, reduced amount of heat transfer coefficient at elevated blowing ratios as compared between cylindrical, fan shaped, and laidback fan shaped film cooling holes geometries. [Gritsch *et al.* (2000) and Yu *et al.* (2002)].

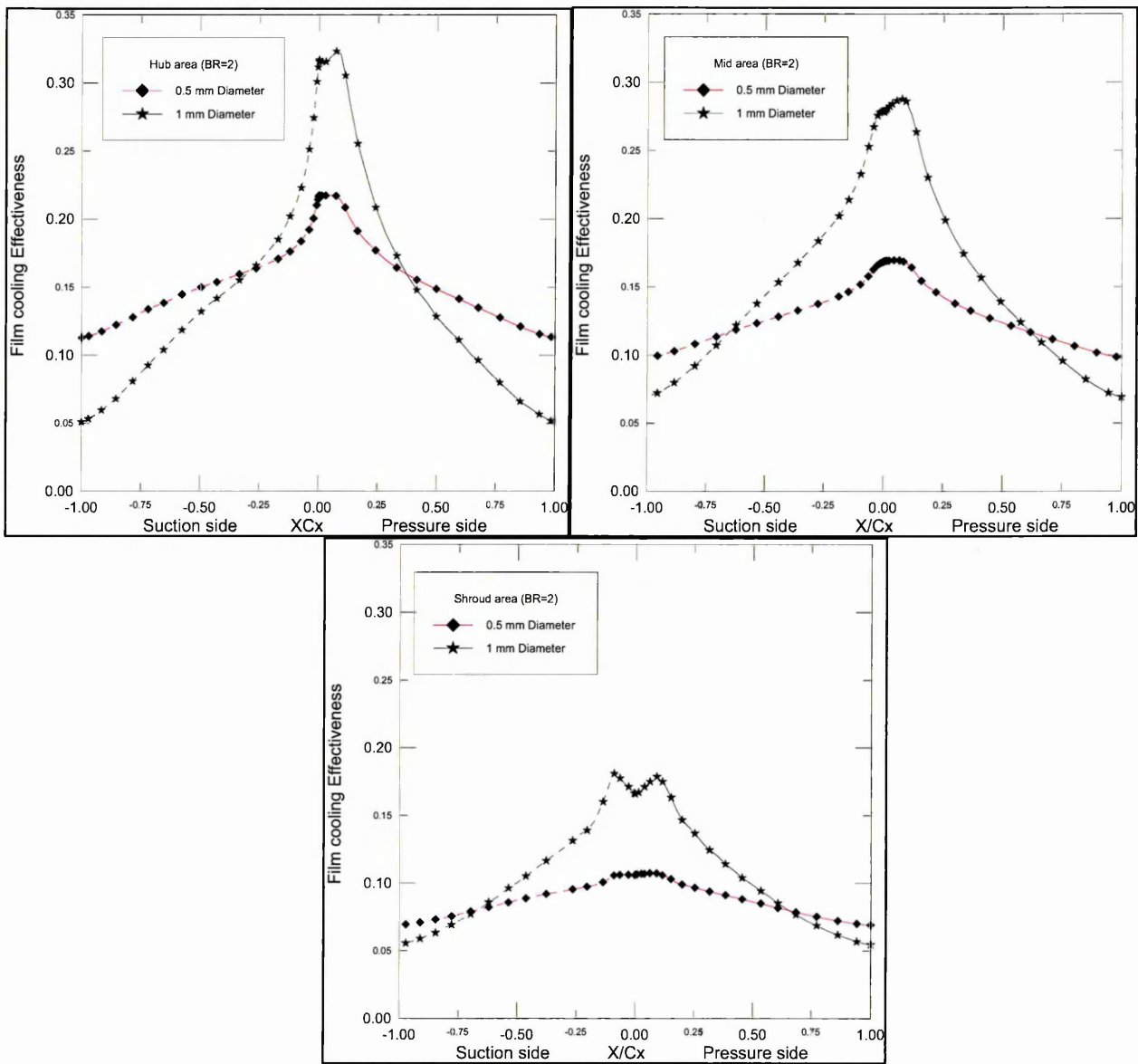


Figure (6-28) Cooling effectiveness trajectory at B R=2 for hub, mid and shroud area effected by holes diameter.

Figure (6-29) shows blade surface (pressure side) static temperature contours distribution at angle of injection of  $45^{\circ}$  with BR=2. Basic fluid flow information deals with the continuity equation and the velocity of the fluid flow increases with an increasing flow discharge or a reduction in cross section area. In this study, effects of film cooling holes diameter indicates that reducing holes diameter to 0.5 mm, the coolant fluid penetrated the main hot gas. Therefore, mixed fluid was located far away from the surface in comparison with cooling holes diameter of 1 mm. Thus, surface temperature distribution at 1 mm is lower extending in lateral direction along the blade

which confirms better protection was obtained through creating an attached blanket of cooled air covering the blade.

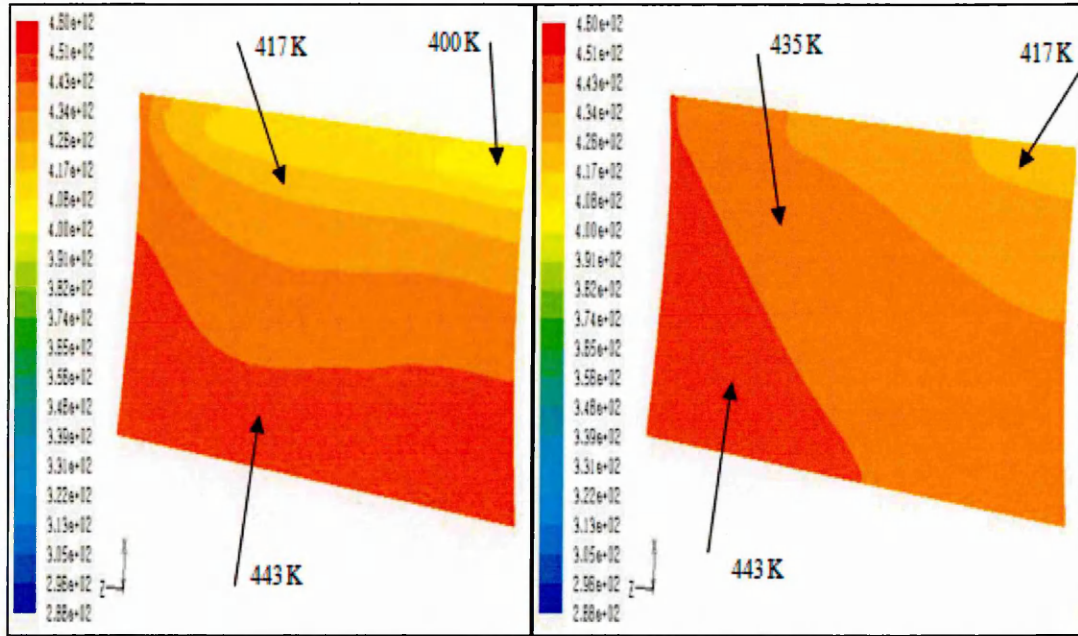


Figure (6-29) Effect of holes diameter on gas turbine temperature distribution at blowing ratio  $BR=2$  with angle of injection  $45^{\circ}$

## 6.8 Pressure coefficient and velocity vector for 3-D skewed blade

The film cooling performance in a realistic 3-D skewed gas turbine blade model through comparative numerical studies has been reviewed. The best case study has been selected as being where the film cooling holes have the following characteristics: with  $45^{\circ}$  angle of injection,  $BR=2$ ,  $D=1$  mm and 42 holes. Figure (6-30) show the static pressure coefficient distribution (CP) which is related to static pressure, according to equation (4-7). The trajectory of pressure coefficient on the pressure side and suction side does not show any critical location on the blade surface mode since the flow is incompressible.

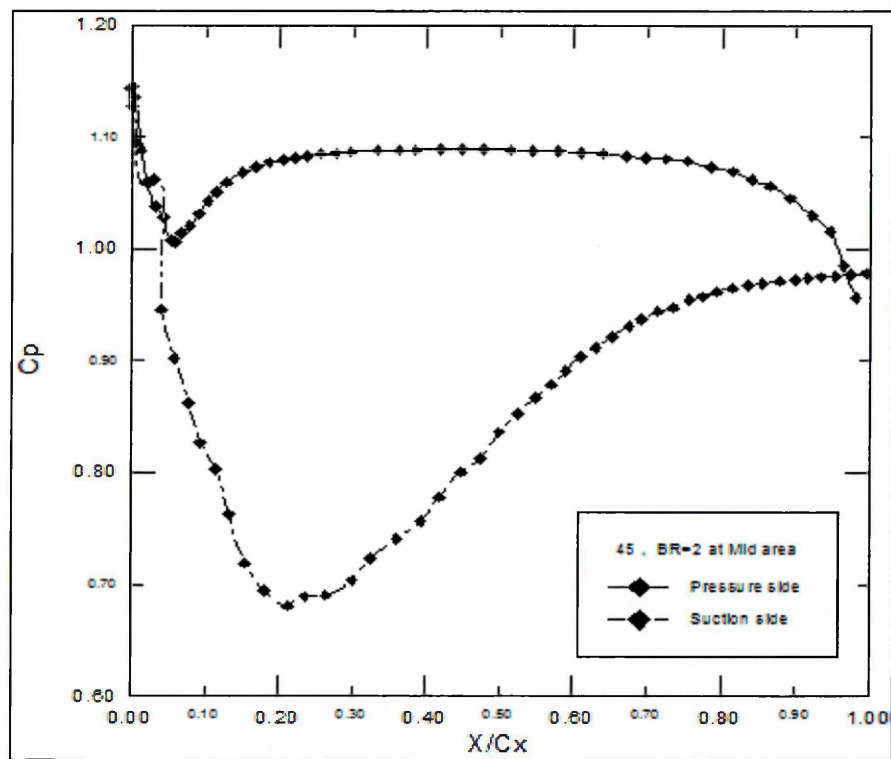


Figure (6-30) pressure coefficient distribution for gas turbine blade with  $45^{\circ}$  angle of injection at  $BR^0=2$ .

Moreover, the velocity vector for the best film cooling performance case has been demonstrated in Figure (6-31) at the hub, mid and shroud areas. In all cases, high value velocity vectors appear on the suction side and low velocity vectors are located on pressure side of the gas turbine blade. The value of the velocity vectors varies due to the effects blade cross-section area.

Clearly, flow separation appears in two locations. Firstly it arises at the trailing edge on the suction side for the hub area, due to blade camber. Secondly it arises on the pressure side after the leading edge due to the concave shape of the blade, as shown in Figure (6-31A) while the maximum velocity appears due to the blade camber.

Figure (6-31B) shows the velocity vector above the blade and in the film cooling holes for the mid-area. The velocity flow patterns are significantly affected by the blade but there is no separation in flow on the pressure side compared with the hub-section.

On the suction side the highest velocity is located near and above the blade camber while flow separation placed near trailing edge.

Figure (6-31C) illustrates the velocity vector on the shroud area. No separation appears near the trailing edge on the suction side or near the leading edge on the pressure side

compared with mid- and hub- areas, respectively. This variation in velocity vector values is related to the effects of 3-D skewed blade geometry design.

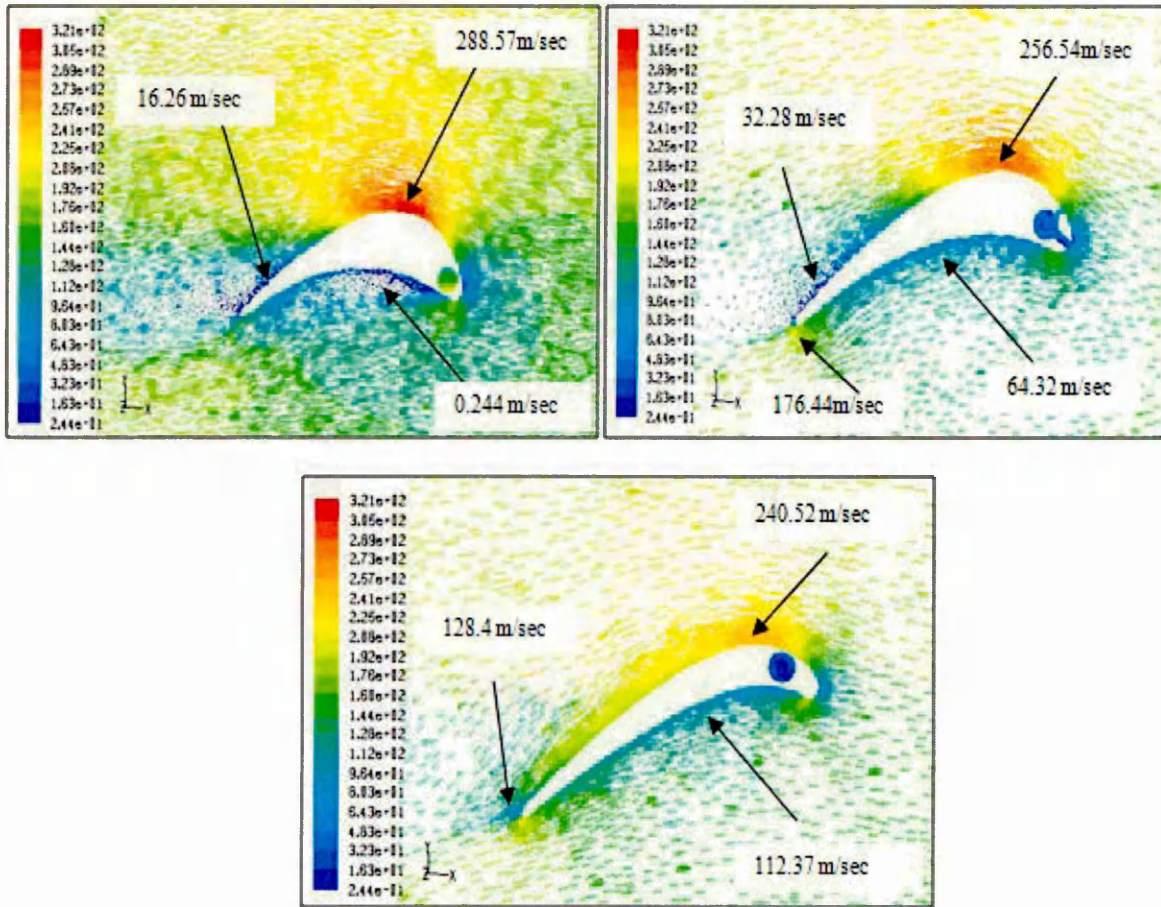


Figure (6-31) velocity vector for gas turbine blade with 45° angle of injection at  $BR^0=2$  for A) Hub B) Mid C) Shroud

## 6.9 Summary

In this chapter, the description of the process to acquire the gas turbine blade solid body is given in details. Various processes intrinsic to *pre-processing* (mesh generation) and selecting solution strategies (*processing*) have been discussed. These have included the generation of the physical domain (utilizing CMM measurements). The chapter also describes the steps followed to generate the computational domain design (volume meshing) and the methods used to assess its accuracy through utilization of the mesh-independent method.

Finally, jet-crossflow performance has been simulated in a realistic 3-D skewed gas turbine blade model in order to attain optimum film cooling design through comparative numerical studies. The acquired results demonstrated the effects of blowing ratio, coolant fluid temperature, angle of injection, number of holes and holes diameter on film cooling effectiveness and blade surface temperature as well as heat load of the blade as the Nusselt number varies. These have been summarized in Table 6-3 to provide a concise evaluation of different cases studied and aid in the selection of the optimum case. So, the average film cooling effectiveness values at the mid area on pressure side gas turbine blade. So, numerical study in this chapter established good film cooling performance accomplished via ejected coolant fluid during 42 cooling holes at  $D=1$  mm with  $BR=2$  and  $T_c=287.5$  K, for angle of injection of  $45^\circ$ . In addition to the Table 6-4 illustrate computational time with number of cells for 3 D skewed gas turbine blade simulations at different angle of injection  $35^\circ$ ,  $45^\circ$  and  $60^\circ$  respectively.

**Table 6-3: The average film cooling effectiveness values at the mid area on pressure side gas turbine blade**

Effect of BR at	BR=1	BR=1.5	BR=2	Reason and justification
angle of injection 35°	0.132	0.174	0.204	Best effectiveness was obtained for BR=2 due to more protection was achieved
Effect of coolant fluid temperature at 35°, BR=1.5	T <sub>C</sub> =287.5 K	T <sub>C</sub> =153 K		Coolant fluid ejected with T <sub>C</sub> =287.5 K provided good film cooling performance. So, there is no sense from reducing coolant fluid temperature due to equation (5-1) and (5-3).
	0.174	0.165		
Effect of angle of injection at BR=2	35°	45°	60°	Injecting coolant fluid at angle 45° presented better protection for the blade because the mass flow of coolant is constant and hot surface temperature is reduced.
	0.204	0.207	0.193	
Effect of holes number at 45°, BR=1.5	32 holes		42 holes	
	0.184		0.177	
Effect of holes diameter at 45° BR=2	D=1 mm		D=0.5 mm	
	0.207		0.144	

**Table 6-4 Computational time with number of cells for 3 D skewed gas turbine blade simulations at different angle of injection 35<sup>0</sup>, 45<sup>0</sup> and 60<sup>0</sup> respectively.**

<b>Case</b>	<b>Number of cell</b>	<b>Computational time</b>
Film cooling holes in gas turbine with angle of injection 35 <sup>0</sup>	10141446	240 hours
Film cooling holes in gas turbine with angle of injection 45 <sup>0</sup>	10408014	240 hours
Film cooling holes in gas turbine with angle of injection 60 <sup>0</sup>	10385045	240 hours

## *Chapter Seven*

### *Experimental Modeling, Preparation & Results*

## 7.1 Introduction

The modeling, design and manufacturing process of the gas turbine blade test specimen is described in this chapter. The main objective of this chapter is to experimentally investigate the effect of changing the blowing ratio and angle of injection of a real gas turbine blade specimen using thermal paint and a thermal wind tunnel. Therefore, the synthesis of the blade specimens was conducted in two stages:

Firstly, the geometric modeling of the gas turbine blade has been achieved with pro-engineer wildfire software which generates the blade turbine cross section (Hub, Mid and Shroud), film cooling holes and a fixing base. Consequently, three specimens were fabricated via laser sintering technology using direct metal 20 powder (material composition is a bronze based mixture containing Ni).

Secondly, a Thermal Wind Tunnel (TWT) was designed and built. Experimental apparatus is described in detail this chapter with operating principles where appropriate.

Finally, the experimental strategy is explained for extracting pertinent analytical data for subsequent evaluation of temperature distributions along the turbine blade specimen, as obtained with thermal paint technology and thermocouples sensors. This chapter also elaborates the interpretation of experimental data.

## 7.2 Gas turbine blade geometry

As mentioned previously (chapter 6) the geometric model has been used to create the fabricated blade. The blade Cartesian coordinate geometry model ( $x, y, z$ ) was measured using a Computer Aided Measuring Machine (CMM) and inserted in a CAD package (Pro/ Engineer Wildfire) to be assemble as a solid volume and as a smooth surface.

As illustrated in Figure (7-1), each specimen utilized a series of cooling holes. On each specimens leading edge a column of 21 holes each of 0.5 mm is placed—at the base of the specimen, five access holes were created to embedded the K-type thermocouples.

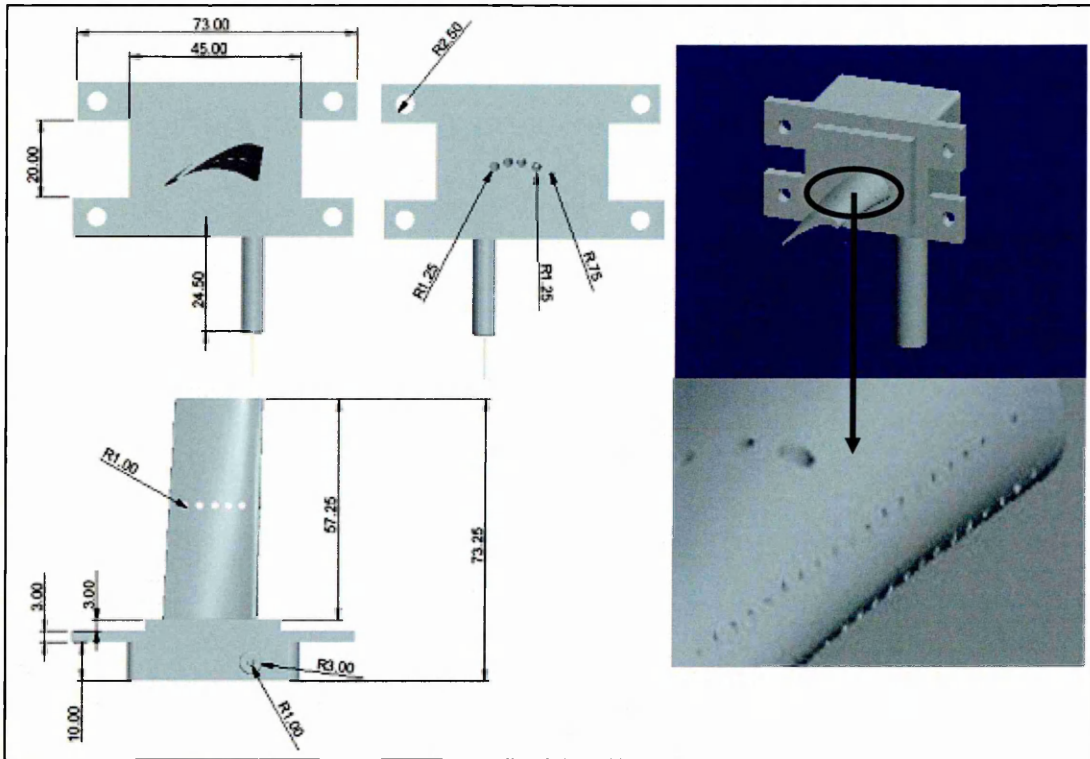


Figure (7-1) Gas turbine blade specimen model dimension and cooling holes position with projection side views

The application of film cooling holes provides an excellent and robust method of protection against the hot gas on a blade surface in the spanwise direction. After reviewing the previous published studies, such as (Yuen and Martinz-Botas(2005)) and (Lakehal *et.al* (2001)), it was established that these researchers employed lateral spacing (holes pitch)  $P=6D$  &  $3D$  and  $P=5D$  respectively. Therefore in the thesis, this approach was followed and the film cooling holes were distributed on the gas turbine blade model as one lateral hole in leading edge with 21 holes on each side with lateral spacing  $P=5D$ . For experimental testing, all gas turbine blade specimens were manufactured at half scale in order to reduce the cost of the metal powder (Direct Metal 20), reduce the cost of the wind tunnel test section and to achieve steady and uniform free stream mass flow. Three models were manufactured for experimental testing, as documented below:

1. Coolant air injected with angle  $35^{\circ}$
2. Coolant air injected with angle  $45^{\circ}$
3. Coolant air injected with angle  $60^{\circ}$

## 7.3 Gas turbine blade specimen manufacturing process

### 7.3.1 Laser sintering technology

Rapid Prototyping (RP) technology was developed in the 1980s and allows engineers in gas turbine technology to design and build very complex geometries to accurately simulate gas flow phenomena in complicated parts with high accuracy. RP avoids the traditional process in manufacturing and therefore there is no preheating.

The advantages of RP technology include significant shortening of the design-manufacturing cycle time, reducing the cost of product and also increasing competitiveness. RP systems available commercially are of several types and include Selective Laser Sintering (SLS) and three-dimensional printing (3DP). Type and materials properties as well as size of the prototype are however a great limitation of RP systems [Gibson and Shi (1997)]

The test blade specimen's fabrication was carried out with a EOSINT M 250 machine as shown in Figure (7-2). The machine includes a laser unit, a control computer, a build chamber, a powder dispenser, a wiper blade and a build cylinder. Specification of this machine can vary depending on the power of the laser beam and wavelength spot size. For example a typical specification may be: 200 W CO<sub>2</sub> laser, 10.6 μm and 0.3 mm. [Khaing et al. (2001)].

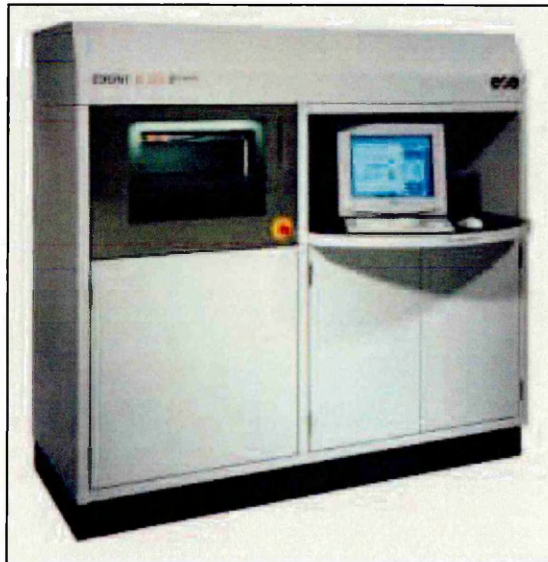


Figure (7-2) EOSINT M 280 direct metal laser sintering machine [BMT, (2011)]

### 7.3.2 Process of direct metal laser sintering (DMLS)

The manufacturing process using laser sintering technique starts with computer aided design (CAD), Pro-engineer and Solid works. Often 3D design involves very complex shapes and small features. These 3D solid models were exported as an STL file in order to import in EOSINT M 250. Figure (7-3) shows a schematic diagram of the EOS Machine [Custompartnet, (2011)]

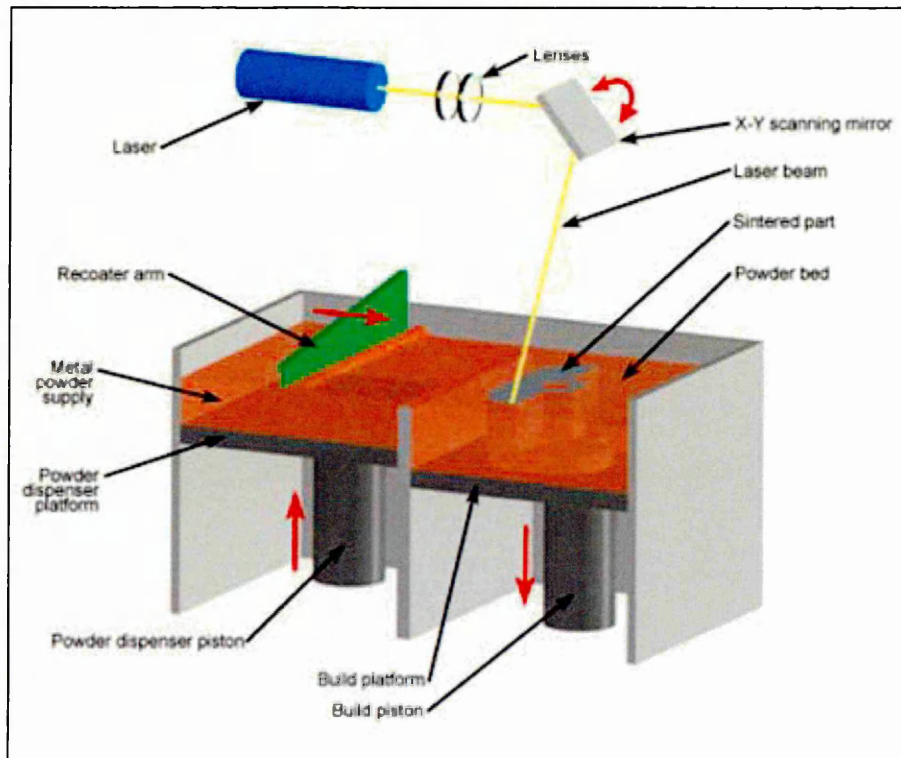


Figure (7-3) A schematic diagram of the EOS machine [Custompartnet, (2011)]

The first step in the fabrication process starts when the laser beam is scanned on the base without any powder deposit on it. Consequently the coated bronze melt is bonded very well to the mild steel base plate; subsequently the powder is deposited on the first layer, [Khaing et al(2001)]. The parts are built up layer-by-layer from a fine metal powder using a laser beam and the thickness of these layers for each step could be controlled for example as  $20\ \mu\text{m}$ . A heat sink should always be available in the fabrication process. Therefore, even extremely complex geometries may be compactly created with the laser sintering technique as individual parts and then be assembled later. Different materials powders are used in laser sintering technique namely, direct metal 20, direct steel 20 and direct steel H20

### 7.3.3 Direct metal 20 description, application

The three specimens were carried out using the Direct Metal 20, therefore Direct Metal 20 is a bronze-based metal powder with very fine grain structure and product parts therefore achieve excellent mechanical properties combined with good surface quality. The surfaces can be easily post-processed by shot-peening and few efforts required in finalized (surface polishing). Also powder mixtures include different components which expand during the laser-sintering process, partially compensating for the natural sintering shrinkage; hence a very high accuracy is achieved. This material is ideal for most prototype injection molding tool applications and for many functional metal prototype applications. Consequently, direct metal 20 presents a very broad window of usable process parameters for example, a wide range of achievable mechanical properties and speed of building the layer by layer. Table 7-1 demonstrates standard parameters properties of direct metal 20 [EOS (2004)]. Figure (7-4) shows blades specimens fabricated by direct metal laser sintering technology utilizing EOSINT M 250 X tended systems.

**Table 7-1: Material property of direct metal 20[EOS (2004)].**

<b>Material Properties</b>	<b>Direct Metal 20</b>
Minimum recommended layer thickness ( $\mu\text{m}$ )	20
Typical achievable part accuracy ( $\mu\text{m}$ )	$\pm 50$
Minimum wall thickness (mm)	0.6
Density in skin area ( $\text{g}/\text{cm}^3$ )	7.6
Density in core area ( $\text{g}/\text{cm}^3$ )	6.3
Remaining porosity (min. %)	8
Tensile strength(MPa, MPIF10)	Up to 400
Yield strength (MPa)	200
Young's Modulus (GPa)	80
Transverse rupture strength (MPa, MPIF 41)	700
Coefficient of thermal expansion ( $10^{-6}/\text{K}$ )	18
Thermal conductivity (W/Mk)	30
Maximum operating temperature ( $^{\circ}\text{C}$ )	400

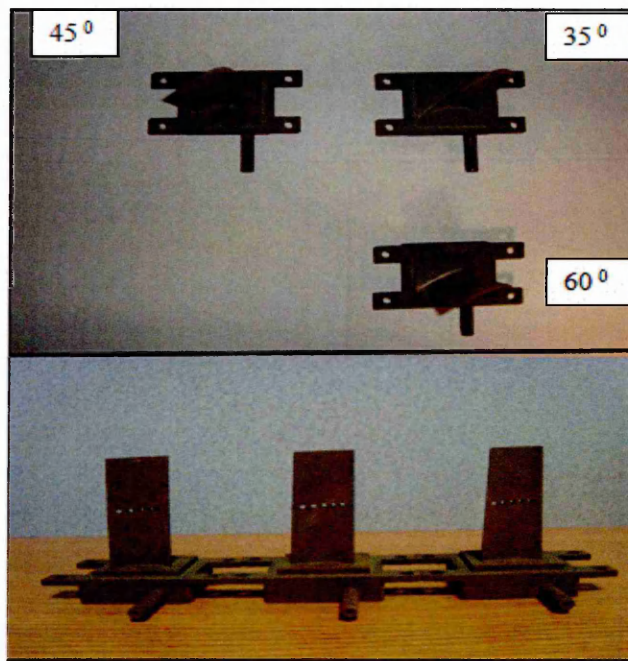


Figure (7-4) Gas turbine specimen fabricated in EOSINT M 250 X tended systems

To achieve experimental testing successfully an *additional part* appeared on the blade specimen just for fixing blade in the thermal wind tunnel and avoiding any movements. This extra part was external in fact to the proper test section. It was found to have little effect on the results.

## 7.4 Experimental equipment

To complete experimental test accurately and to quantify film cooling effectiveness, it was required to provide, hot gas at high temperature as the mainstream gas and secondly, cooled fluid as the coolant air. Therefore, instrumentation and equipment is used to control, maintain and measure the flow conditions inside thermal wind tunnel to record suitable experimental data. The relevant Instrumentation and equipment are listed below:

1. K-type thermocouples
2. Pico USB TC-08 temperature data logger
3. Computer (PC)
4. Thermal paint temperature technology (TPTT)
5. Air compressor for cold air

6. Gas turbine unit to supply hot air
7. Flow visualization and measurement system
  - a. LDA to measure the air velocity
  - b. Air flow meter to measure cold air

#### 7.4.1 K-type thermocouples

A series of K-type thermocouples were used to gather surface temperature of the gas turbine blade during experimental test. So, thermocouple is a sensor commonly used for measuring temperature. It usually consists of two *dissimilar* metals, joined together at one end. Figure (7-5) shows the thermocouple operation principle, normally when the junction of the two metals is heated or cooled a voltage difference is produced. Therefore, voltage difference will be converted into temperature; consequently voltage difference is directly proportional to the temperature value. [Omega, thermocouple (2011)].

The relationship between the temperature difference and output voltage of the thermocouples is *non-linear* and can be calculated from the following equation:

$$T = aV^2 + bV \quad (7-1)$$

where  $V$  is voltage, and the coefficients  $a$ ,  $b$  are found from calibration.

The measurements value of thermocouples must be compared with a cold junction and most junctions are merged with the circuit of the thermocouple connection to increase the accuracy. This method is known as cold junction compensation. [Sim (2008)].

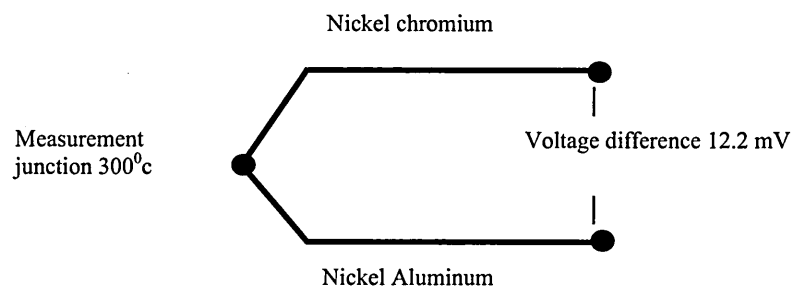


Figure (7-5) K-type thermocouples operation principle [Pico, thermocouple, (2011)]

Generally, thermocouples are available in different combinations of metals. Hence, thermocouples could be divided in to four common categories, for example;  $J$ ,  $K$ ,  $T$  and  $E$ . Each calibration has a different temperature range, although the maximum

temperature varies with the diameter of the wire used in the thermocouple. Very thin thermocouples may not reach the highest temperature range. Table 7-2 shows the international codes for thermocouple, temperature range and limits of error. [Omega, thermocouple, (2011)].

**Table 7-2: Common thermocouple temperature ranges [Omega, thermocouple, (2011)].**

Thermocouple type	Temperature Ranges
J	0 C <sup>0</sup> to 750 C <sup>0</sup>
K	-200 C <sup>0</sup> to 1250 C <sup>0</sup>
E	-200 C <sup>0</sup> to 900 C <sup>0</sup>
T	-250 C <sup>0</sup> to 350 C <sup>0</sup>

- **Thermocouple junction types**

The tip of the thermocouple probe is available in three different styles. Figure (7-6) illustrates these three cases- grounded, ungrounded and exposed junctions probe.

**A). Grounded junction**

In this type of thermocouple the wire is connected from inside of the probe wall using a Tungsten Inert Gas (TIG) welding machine and a completely sealed integral junction, also known as the sheath material. Thus, this probe provides a good temperature transfer with good response but requires time.

**B). Ungrounded junction**

In this type of thermocouple the wire is detached from the probe wall, while the wires themselves are connected but have insulation keeping them from the probe. Greater electrical isolation is offered for these thermocouples although they require longer times to achieve response.

**C). Exposed junctions**

In this type of thermocouple the wires extend out of the tip of the sheath so that the junction will be uncovered. These kinds of thermocouples have the fastest response times but cannot handle temperatures as high as those which can be accommodated by the grounded and ungrounded types. Also it is not recommended to utilize these systems in acidic fluids or atmospheres. [Ehow, thermocouple (2011)]

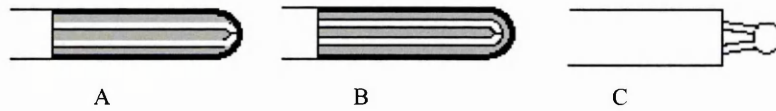


Figure (7-6) Thermocouple probe junction types, (A) grounded, (B) ungrounded and (C) exposed [Eutechinst, thermocouple (2011)]

In the present research, the K-type ungrounded thermocouples as shown in Figure (7-7) have been utilized to measure temperature at the mid area of the five points on the blade for each side (pressure and suction side). The thermocouple is a steel probe with 0.5 mm diameter and 250 mm length.

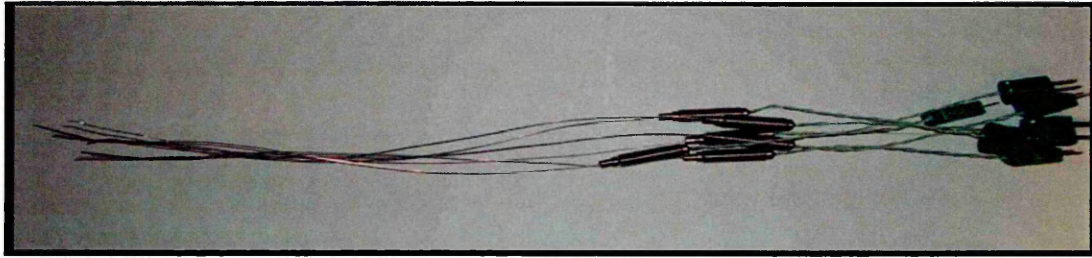


Figure (7-7) K-type stainless steel thermocouple probe at 0.5 mm diameter with miniature plug

#### 7.4.2 Pico USB TC-08 temperature data logger

A data logger was used to collect the temperature value and save it on the PC, thus data logger is an electronic device that is utilized to record measurements over time. Basically, Pico data loggers can measure temperature, pressure, relative humidity, light, resistance, current, power, speed and vibration by connecting suitable sensors. Typically, temperature measurement ranges from -270 to +1820 °C and 8 channels are available in the data logger when plugged into a PC as a USB port. [Pico data logger, (2011)]. This research utilized a Pico TC-08 data logger to record all the temperature values with time from the experimental measurement test, Figure (7-8) shows a Pico TC-08 data logger device. However, TC-08 data logger is designed to record a wide range of the temperature and can be made both fast and accurate using any thermocouple which has a miniature connector. Table 7-3 lists the specification of the TC-08 data logger. The supplied software displays the measured data in listed tables or graph charts. All recorded values are saved as Microsoft Excel sheets or other spreadsheet software.

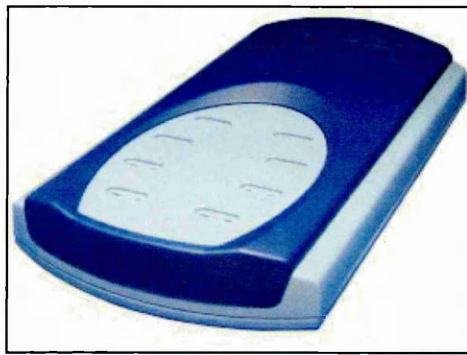


Figure (7-8) Pico TC-08 data logger device

**Table 7-3: Lists the specification of the TC-08 data logger [Pico data logger, (2011)].**

<b>USB TC-08 Specifications</b>	
Number of channels	8
Conversion time	100 ms (thermocouple and cold junction compensation)
Temperature accuracy	Sum of $\pm 0.2\%$ of reading and $\pm 0.5\text{ }^{\circ}\text{C}$
Voltage accuracy	Sum of $\pm 0.2\%$ of reading and $\pm 10\text{ }\mu\text{V}$
Overload protection	$\pm 30\text{ V}$
Maximum common mode voltage	$\pm 7.5\text{ V}$
Input impedance	$2\text{ M}\Omega$
Input range (voltage)	$\pm 70\text{ mV}$
Resolution	20 bits
Noise free resolution	16.25 bits
Thermocouple types supported	B, E, J, K, N, R, S, T
Input connectors	Miniature thermocouple
Output connector	USB — cable supplied
PC connection	USB 1.1
Power supply	From USB port
Dimensions	201 x 104 x 34 mm (7.91 x 4.09 x 1.34 in)
Supplied software	Pico Log Software Development Kit Linux drivers

### 7.4.3 Thermal paint temperature technology (TPTT)

All three specimens were fully coated by Thermal paint and the performance of film cooling; amount of heat transfer in the gas turbine has been investigated experimentally by many researchers using different methods including the Liquid Crystal Technique (LCT), Pressure Sensitive Paint (PSP) technique, Infrared Thermography Method (IR) and Thermal Paint Temperature Technology (TPTT). However, most previous studies by ([Tao *et al.* (2009)], [Tao *et al.* (2008)], [Hung *et al.* (2009)], [Yuen *et al.* (2005)], [Ou and Rivir (2001)], [Ou and Rivir (2001)], [Ekkad and Han (2000)]) have used the liquid crystal technique to complete film cooling experimental measurements on flat plates or gas turbine blades.

The Pressure Sensitive Paint (PSP) technique is widely used to measure local pressure distributions on the surface in order to, measure the film cooling effectiveness on the blade [Ahn *et al* (2005)]. Therefore, the pressure difference on the coated surface with PSP reveals the cooling effectiveness. Hence, the calibration should be obtained for the required important images for example, reference image (with illumination, no mainstream flow), air image and nitrogen image (with illumination, mainstream flow and air or nitrogen coolant fluid) and the black image (no illumination and no mainstream flow no coolant fluid). Several studies have used the PSP technique ([Takeishi *et al.* (2010)], [Gao *et al.* (2008)], [Ahn *et al.* (2007)], [Ahn *et al* (2005)]). Finally, IR is less abundant compared with the previous two types through study film cooling effectiveness since it is a relatively more expensive system than LCT processing system. Despite this, the IR technique is utilized to take measurements in high temperature range which enhances the accuracy of heat transfer coefficient and film cooling effectiveness. Actually, there are two types of IR system, scanning and staring system, so surface radiation measure point by point in scanning system, while in staring system used infrared sensor arrays(focal plane arrays) [ Schulz (2000)]. Also this technique has the ability to measure the entire initial model distribution and is not sensitive to the angle of illumination compared with LCT. Therefore, IR requires less intensive calibration than liquid crystal techniques and has the ability to attain information using a single transient test [Ekkad *et al.* (2004)] as a result, (IR) was used by ([Lu, *et al.* (2007)], [Ekkad *et al* (2004)], [S.V.Ekkad *et al.* (2000)] and [ Schulz (2000)]).

In this study temperature distribution of gas turbine blade specimens was measured experimentally using thermal paint temperature technology (TPTT). The test and analysis time can be reduced using thermal paint by a factor of 3 compared to a

traditional test. As a result of this, thermal paint reduced the cost of developing gas turbines. The process of coating involves painting the required area of a component with a very thin layer of selected paint. Thermal paint is like the liquid crystals in that it changes color at specific temperatures. However, unlike liquid crystals, thermal paint reaction is irreversible so that the paint retains the color corresponding to the highest temperature it has experienced, making it a permanent record [TPTT]. Moreover, the procedure of painting starts on the parts before the gas turbine engine is assembled. Thus, painted parts can be stored in dry conditions for an indefinite period without any resulting deterioration in performance. After the gas turbine engine is run for a limited period of time, the painted parts are removed and the temperatures distribution of is recorded as surface color contours. The paint is used to show the surface temperature variation for metallic, ceramic and plastic materials, with applications in a range of areas such as:

- Temperature distribution on axial flow compressor case exteriors, combustion liners, combustion chamber inner/outer-casings and fuel injectors, glow plugs, turbine stator vanes-all stages, turbine rotor blades-all stages, turbine rotor wheels, turbine vane cases and engine exhaust cones.
- Heat treatment processes.

- **Types of thermal paint**

There are two types of thermal paint; single change and multi change. Currently single-change market provides 12 types while the multi-change market provides 13 types illustrated in Table 7-4 and 7-5, respectively. Therefore, multi-change thermal paints can have 2 to 15 color changes with regard to temperature range.

In this experimental work, KN 5 has been used to paint the gas turbine blade surface specimen, and this type has 15 temperature change points (140-1250 °C).

**Table 7-4: Single change paints sorts [TPTT].**

Paint Name	Color Change Temp (C <sup>0</sup> ). After 10 Minutes of Heating	Initial Paint Color	Final Color After 10 Minutes Heating
CJKN 1	48	Pink	Lavender Blue
CJKN 2*	80	Pink	Lavender
CJKN 3	155	Blue	Dark Green
CJKN 5**	210	Yellow	Black/Brown
CJKN 6	240	Yellow	Red/Brown
CJKN 7	275	Blue/Grey	Lavender
CJKN 8	367	Mauve/Red	Grey
CJKN 9	400	Mauve	White
CJKN 10	447	Green	Salmon Pink
CJKN 11	458	Green	White
CJKN 12	550	Orange	Yellow
CJKN 13	630	Red	White

**Table 7-5: Multi-change paints sorts [TPTT].**

Paint Name	Temperature range (C <sup>0</sup> )
KN 1	160-250
KN 3A	430-1255
KN 4	90-220
KN 5	140-1250
KN 6	158-1380
KN 7	333-1280
KN 8	350-1050
KN 9	224-277
KN 11	120-300
KN 12	150-300
KN 13	510-1290
KN 14	390-1070
KN 15	240-1255

- **Thermal paint temperature calibration**

TPTT has conducted extensive calibrations for paints over 2, 5, 15, 30 and 60 minute time periods [TPTT]. In this study the sensitivity of thermal paint was checked also through painted a part of cooper pipe by thermal paint and inserted in a furnace after reaching a temperature 360 C<sup>0</sup> and keeps it for 5 minutes inside the furnace. Figure (7-9) shows the calibration process for cooper pipe with furnace and KN 5 coupon calibration.

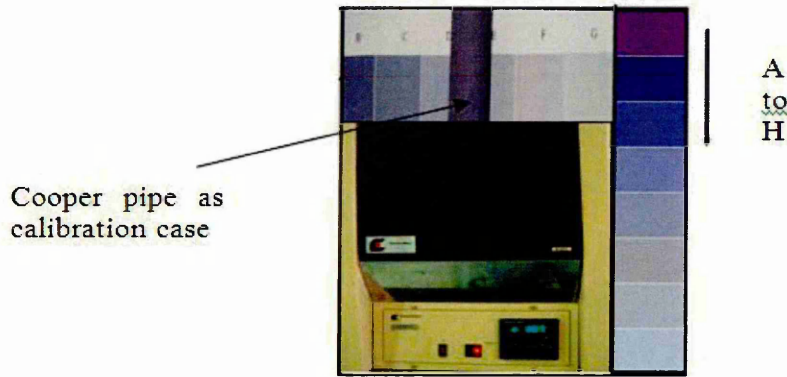


Figure (7-9) Calibration process for cooper pipe with furnace and KN 5 coupon calibration

As result of the high temperatures the thermal paint responds through changing PLUM colour (original colour) as A type to the GRAY colour as E type and fixed to be permanent colour due to change in thermal paint density. Table 7-6 shows temperature and colour density for each color transition. (C = Cyan; M = Magenta; V = Violet; Y= Yellow)

**Table 7-6: Temperature and colour density for each color transition. [TPTT].**

		A	B	C	D	E	F	G	H
<b>2min</b>	C <sup>0</sup>	<170	170	250	310	370	520	614	670
	Density	1.17M	1.43C	1.01C	0.73C	0.65M	0.54V	0.49V	0.47C
<b>5min</b>	C <sup>0</sup>	<160	160	244	300	360	500	597	650
	Density	1.20M	1.40C	0.97C	0.72C	0.65M	0.55V	0.47V	0.44C
<b>15min</b>	C <sup>0</sup>	<150	150	237	280	340	480	545	620
	Density	1.17M	1.35C	1.22C	0.75C	0.66M	0.52V	0.48V	0.43C
<b>30min</b>	C <sup>0</sup>	<145	145	235	260	320	468	527	600
	Density	1.2M	1.4C	0.99C	0.8C	0.67M	0.53V	0.45V	0.41C
<b>60min</b>	C <sup>0</sup>	<140	140	230	258	310	452	512	570
	Density	1.16M	1.32C	1.19C	0.75C	0.65M	0.53V	0.44V	0.42C

#### 7.4.4 Air compressor

Coolant fluid was supplied to the blade cooling holes system from air compressor tank. Therefore, a reciprocating air compressor has been used to pressurize air in storage at a certain pressure and temperature ( $T_c = 294.55 \text{ K}^0$ ) as a coolant fluid. Any air compressor requires an automatic control system. Namely, if there is any reduction in air quantity in the storage at discharging process through cooling process in testing time the compressor will be powered. Figure (7-10) shows the air compressor which has been selected in experimental works due to easy operation and movement with high safety, low noise and light weight.



Figure (7-10) Air compressor device

#### 7.4.5 Gas turbine unit

To obtain a continuous hot gas, the exhaust of gas turbine unit was utilized to be a supplier of hot gas to the thermal wind tunnel. Hence, the twin-shaft gas turbine is a basic experimental turbine engine unit services utilized for studying purposes (thermodynamic principles and turbine engine performance and characteristics). It is available in almost any university thermodynamics laboratory. The starting and running system initiates when the fan rotates with 12000 to 20000 rpm thus, the air passes from the compressor to the combustion chamber. After a few seconds fuel (Kerosene) is sprayed through special nozzle in to the combustion chamber (which keeps throttle valve opened between 2.5 to 3 full turns). A high energy spark ignition takes place between the mixture (air and Kerosene fuel) and flows into the gas generator turbine which will be self-sustaining. Hot gas passes from the gas generator turbine through a short duct to the power turbine and then the exhaust gas is discharged to the outlet. At the same time the fan will be automatically shut down; therefore the controlling system in the apparatus unit will operate regularly. In addition the technician or students can

adjust the throttle and loading system to keep the power turbine working between 5000 and 40000 rpm. [TecQuipment, (2011), TQ education (2004)]. Figure (7-11) shows the panel board for the gas turbine unit.

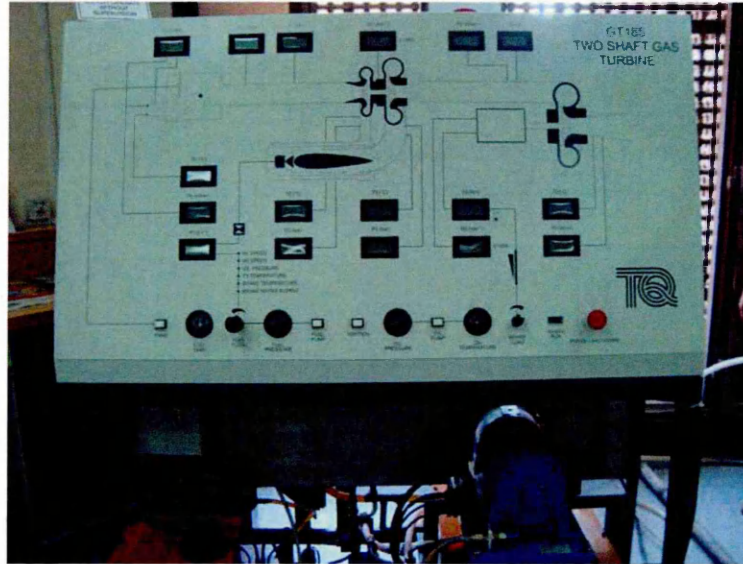


Figure (7-11) Panel board for gas turbine unit

Exhaust gas from the gas turbine unit has been used as the upstream hot gas in the thermal wind tunnel. While, compressed air has been supplied from the compressor and is utilized as coolant fluid.

#### 7.4.6 Flow visualization and measurement system

- **Laser Doppler Anemometer (LDA)**

Numerous previous experimental studies have quantified gas flow field velocity utilization Laser Doppler Anemometry (LDA) or Particle Image Velocimetry (PIV). In this research the LDA technique has been employed to measure inlet test section velocity through a point of intersection of two laser beams. Actually, LDA is now the usual fluid measurement technique in gas turbine aerodynamics [Campbell *et al.* (2000)], due to no calibration is required with easiness application to measure the reversing flow, chemical reaction, rotating machinery and high temperature media [Dantec, manual].

Figure (7-12) shows the LDA system principle. The process starts when the laser beam is split into two beams with equal intensities and then probe optics will receive them through optical fibers. Thus, the size and intersection point position of the two beams are determined by the focal length of the probe front lens. Normally, optics is used to

guide the two laser beams in to the measurement point (intersection of two beams). Therefore, interference fringes are formed from beams crossing through generated planes with high intensity and low intensity between these planes. The space between the planes (fringe distance) is calculated as an optical parameter, specifically from the angle between beams and light wavelength. Once, fluid flow passes through the interference fringes (beams intersection region) then the flow seeded particles produces scattered light. Therefore, the fluctuation intensity of scattered light is collected by a receiver lens and focused on a photo detector called Doppler frequency. Flow velocity measurements are calculated regarding to fringe distance (traveled distance) and spent time of Doppler frequency [Dantec, LDA, (2011)].

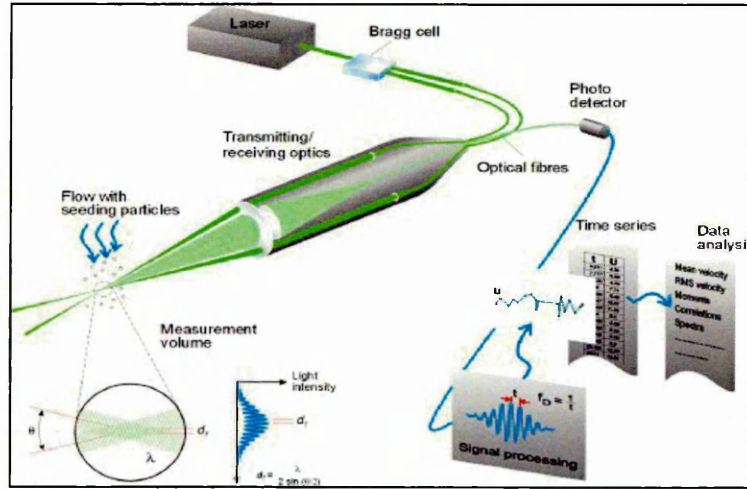


Figure (7-12) Laser Doppler Anemometer (LDA) system principle [Dantec, LDA,(2011)]

- **Air flow meter**

In this experimental study, the quantity of cold air has been controlled by a Rotameter instrument to achieve blowing ratio. Figure (7-13) depicts the air flow meter which is used to measure and control air quantity as a mechanical instrument.

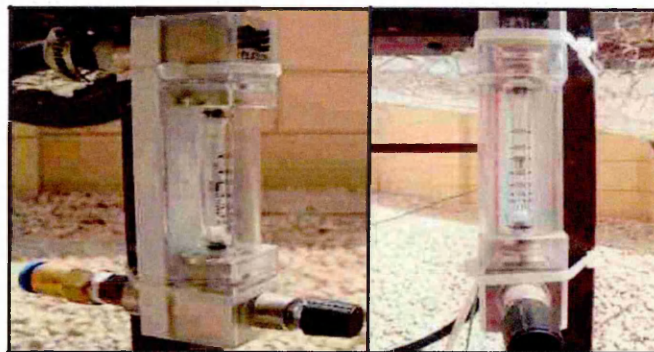


Figure (7-13) Rotameter airflow meter type

Moreover, airflow meter instrument is a tapered tube and a float. Therefore it is widely utilized in experimental investigations due to low cost, simplicity, low pressure drop and widely range ability. [Omega, flow meter, (2011)].

## **7.5 Thermal wind tunnel design**

The wind tunnel is an experimental research tool, designed to study aerodynamic and thermal flow fields over or around solid bodies. Many different types of wind tunnels exist and there are several different ways to classify wind tunnels, for example via speed of gas flow in the test section and also via tunnel geometry.

### **7.5.1 Speed region classification**

Generally the classification of the wind tunnel correlates with the velocity of air in the test section relative to the speed of sound and this ratio is called the Mach number (M).

1. Subsonic,  $M < 0.8$  the compressibility effect is neglected
2. Transonic,  $0.8 > M > 1.2$  the compressibility effect is considered
3. Supersonic,  $1.2 > M > 5$  the compressibility effect is considered
4. Hypersonic,  $M > 5$  the compressibility effect is considered with chemical state of gas

### **7.5.2 Tunnel geometry classification**

The second classification is recognized as the geometry for example. Open wind tunnel and closed wind tunnels. The gas flows through an open circuit tunnel in straight path, hence the direction of flow starts from the entrance through a contraction (nozzle) to test section followed by the diffuser to the exhaust of air during fan section. Such wind tunnels are often also designed as “open loop”. In closed wind tunnels, the gas recirculates inside the wind tunnel and there is no exchange of gas with the exterior, hence the term “closed loop” [Barlow *et al.* (1999)].

The Thermal Wind Tunnel (TWT) facility in this study was designed in the pro/Engineer Wildfire (CAE) package and constructed as one stationary gas blade model. Therefore, three parts constitute the wind tunnel- the nozzle, test section and diffuser. All appropriate dimensions are provided in Figure (7-14).

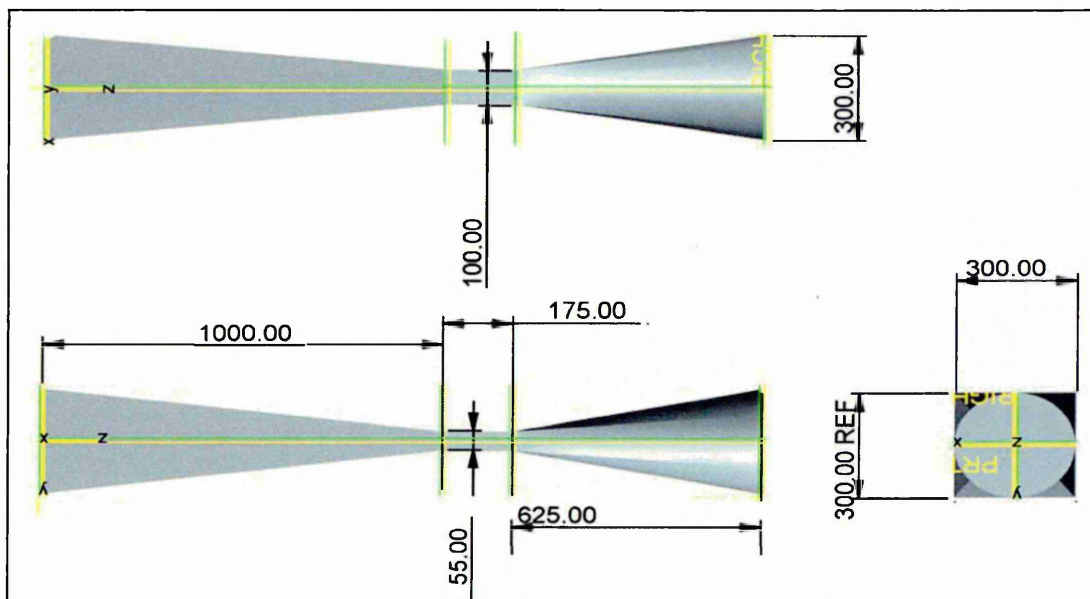


Figure (7-14) Thermal wind turbine (TWT) designed in pro/Engineer Wildfire (CAE) package

### 7.5.3 Thermal wind tunnel (TWT) CFD optimization

A commercial CFD code was used to achieve optimized design for the TWT, based on the initial calculation. The meshing process of the TWT geometry was executed using the Gambit pre-processor (version 2.0) and processing was conducted using the CFD code, FLUENT (version 6.3). The main objective of the design is to enhance the flow quantity at the test section before any fabrication process. Figure (7-15) illustrates pressure and velocity contours at the middle plane of the additional parts of TWT.

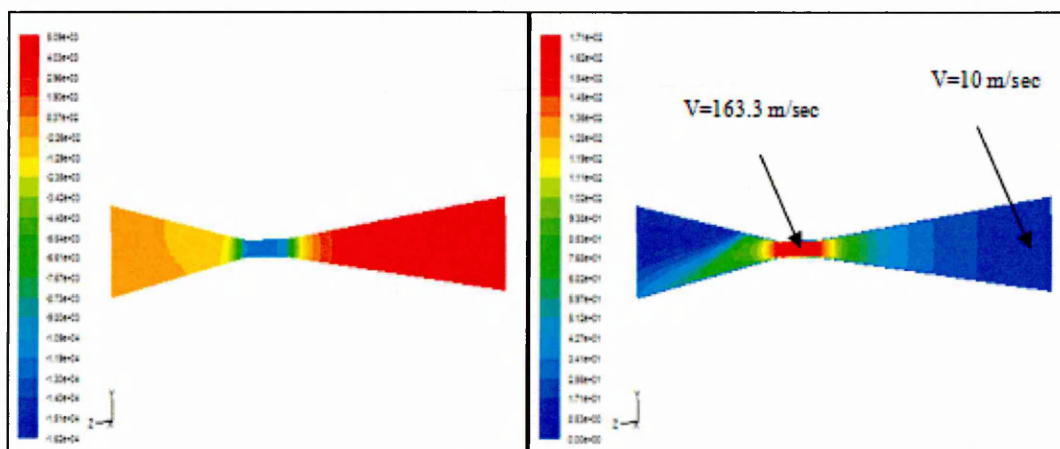


Figure (7-15) Pressure and velocity contour for additional parts of TWT

#### 7.5.4 Uniformity of test section air velocity

The coefficient of uniformity is used to determine the quantity of air velocity distribution at the TWT test section. This parameter can be defined as follows:

$$C_u = (V_{\max} - V_{\min}) / V_{\text{avg}} \quad (7-2)$$

where,  $V_{\max}$  is the maximum air velocity,  $V_{\min}$  is the minimum air velocity and  $V_{\text{avg}}$  is the average air velocity at the inlet of the test section.

By applying velocity value in equation (7-2)

$$C_u = (165.98 - 142.96) / 163.323 = 0.1409$$

The closer the value to zero the more uniform the air flow distribution. The design objective is to minimize the value of  $C_u$  to be the lowest value possible. In this study the coefficient of uniformity calculated at the test section is  $C_u = 0.14$ . Therefore, Figure (7-16) represented full Thermal Wind Tunnel (TWT) manufactured design.



Figure (7-16) Full Thermal wind Tunnel (TWT) manufactured design.

### 7.6 Preparation and Experimental test rig setup

The present investigation is carried out in a continuous flow thermal wind tunnel. This section describes the preparation process and the experimental test procedure with boundary conditions. The preparation processes includes two steps. Firstly, the

fabrication process of thermal wind tunnel (TWT) via metal plate with 3 mm thickness is correlated with geometrical design - see Figure (7-14). Therefore a series of manual steps is required to achieve TWT experimental tests. TWT frame was achieved by cutting three rectangular holes at the middle of the test section. One of these holes was arranged for the specimen and the others for thermal glass using traditional tools. The dimensions of these glasses are (75\*135\*5) mm and (35\*135\*5) mm which are successfully cut with water jet technology. Figure (7-17) illustrates the preparation process steps to finalize TWT.



Figure (7-17) Preparation process steps to finalize TWT.

Thermal glass has been fixed into suitable holes locations by using Superwool. Superwool is very sticky and adheres well to dense and also light weight materials and is therefore suitable for operations up to 1000<sup>0</sup> C when dry [RS Component].

Secondly, specimen preparation for experimental test is achieved by inserting a number of thermocouples inside the gas turbine blade specimen across five lateral holes, in order to measure temperature points at the mid area of the blade surface (pressure and suction side). The tip of the temperature sensors has been bent to be in contact with the surface and insulates the thermocouple probes from the specimen body by using superwool mastic (fixing these thermocouples, insulates the thermocouples from each

other and prevents any leaks). Figure (7-18) shows thermocouples (K type) concealed in the gas turbine and fixed by superwool.

As mentioned in section 7.4.3 the coating process involves painting the necessary area of a component with a very thin layer of selected paint. Thermal paint (KN5) has been used to visualize temperature distributions for both sides and for all gas turbine specimens. Figure (7-19) illustrates the gas turbine blade coated by thermal paint (KN5) and thermal paint on the vibrator machine.

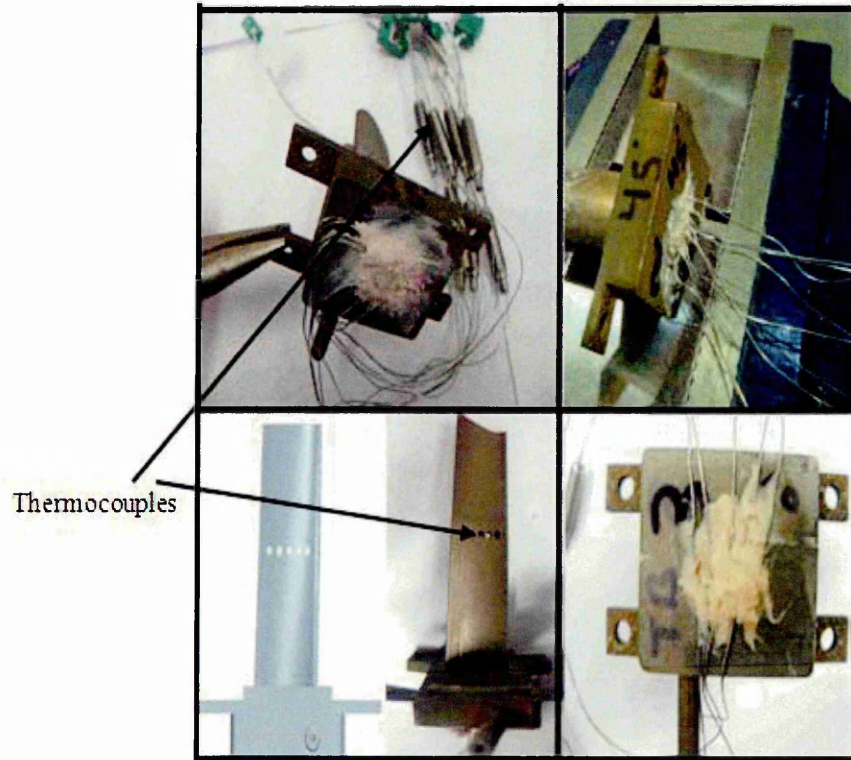


Figure (7-18) Thermocouples (K type) concealed in gas turbine blade



Figure (7-19) Illustrates gas turbine blade coated by thermal paint (KN5) and thermal paint on vibrator machine

Actually, vibrator machine was used to keep the thermal paint homogenous in the container and in process of coating blade specimen layer by the brush. Special care was taken in order to make sure that all the cooling holes were free of paint by inserting a pin on each hole.

Experiments require a complete system setup to fix the gas turbine blade specimen in the proper place at the test section using a holder which calibrates levels of thermal wind tunnel to be horizontal(a spirit level). It is also necessary to connect the air compressor to the film cooling holes through an air flow meter to control quantity of coolant fluid ( $V^0$ ). Moreover, main flow (hot gas) for all experimental tests has been extracted from the gas turbine unit (**GT 1 85 Two Shaft Gas Turbine**), by connecting the exhaust gas pipe to the inlet hot supplier of the thermal wind tunnel.

Temperature data logger software has been installed on a laptop to record temperature measurement data after connecting the second end of thermocouples to the computer through temperature data logger device. Figure (7-20) depicts setup process through the fixed gas turbine specimen in a test section using the holder with number of thermocouples and a hose of coolant supplier. This also calibrates levels of thermal wind tunnel to be horizontal.



Figure (7-20) Setup process of thermal wind tunnel, fixed gas turbine specimen in test section, inserting thermocouples, coolant air supplier, and calibrates levels to be horizontal.

### 7.7 Experimental test procedure

To ensure the repeatability of the experimental test procedure and to achieve good comparison between experimental results for the same test specimen, the same sequence was used for each experiment. Figure (7-21) presents a schematic of the film cooling test rig and data acquisition system.

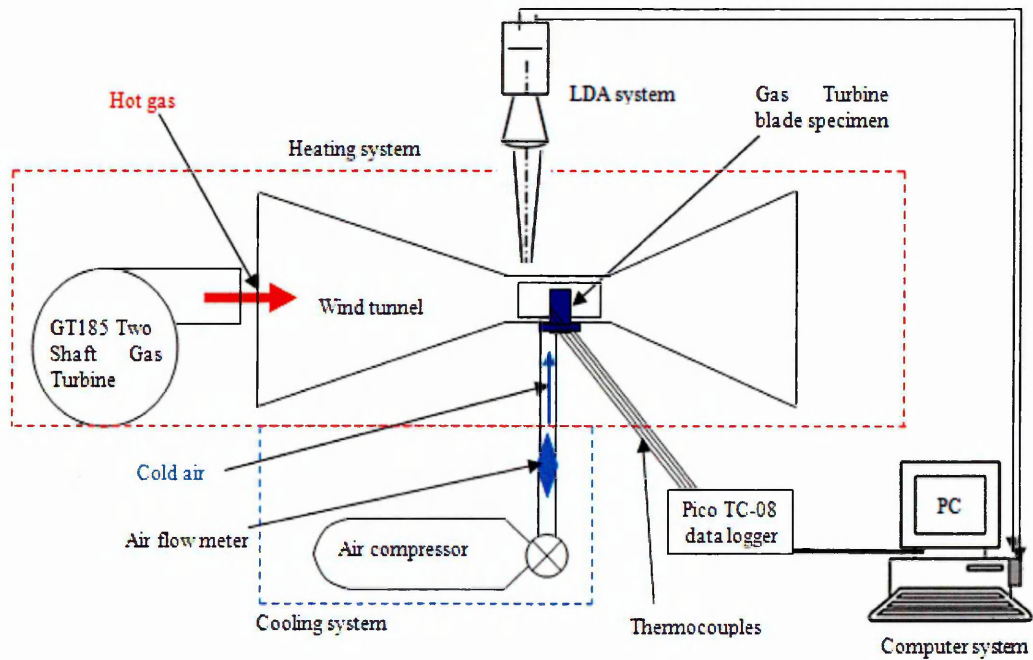


Figure (7-21) Schematic of film cooling test rig and data acquisition system.

The experimental steps are detailed as below:

- Running GT185 two shaft gas turbine unit steadily with speed 31800 rpm to keep exhaust gas temperature maintained at 893.15 K.
- As the maximum operating temperature of gas turbine blade specimen is 673.15 K. Therefore, the thermocouple temperature measurement has to start when the main gas flow temperature reaches 633.15 K. The duration of the test was the same for each experiment and set as 5 minutes (see **KN5 Table7-4 and 7-5 of Temperature and Color Density for Each Color Transition**). Thermal paint is used as a qualitative way to present the performance of film cooling holes on the blade.
- Mainstream velocity at the inlet of the test section was taken using Laser Doppler Anemometry (LDA). Thus, mean velocity of the hot gas was  $V_{\infty}=9.35$  m/sec. Figure (7-22) depicted experimental velocity measurements utilizing LDA with velocity component values.
- The amount of the coolant fluid has been controlled by Rotameter to accomplish the desired blowing ratio ( $V^0=600$  cm<sup>3</sup>/min). Continually, the cooled air was injected at a temperature of  $T_C = 294.55$  K from the compressor tank. A blade specimen with 45° holes injection was fixed in the test section and is the first experimental test case.
- During test time (5 minutes) the temperature data logger recorded temperature measurements in the mid area of the blade specimen across thermocouples. Thermal paint is used to record and retain colour temperature distribution above the blade specimen. A high resolution camera was utilized to document surface temperature (pressure and suction side) for the test case which is permanent irreversible (corresponding to the highest temperature).
- To achieve repeatable experimental tests for the same blade specimen to the second and third blowing ratio value  $V^0=800$  and 1000 cm<sup>3</sup>/min respectively, scaling of permanent thermal paint on the specimen surface is required. Therefore, Chloroform solvent (CHCl<sub>3</sub>) and Nitric acid (HNO<sub>3</sub>) with 30% concentration was utilized to removed the thermal paint through submerged the blade specimen in Chloroform. Following a waiting period of one minute the specimen is brushed with Nitric acid several times. As result of the chemical reaction, removing the thermal paint is achieved. Figure (7-23) illustrates the process of removing thermal paint from blade specimens.

- Repainting was carried out for blade specimens with film cooling holes injected at angle  $45^{\circ}$  using thermal paint to prepare for a new test case ( $V^0=800$  and  $1000 \text{ cm}^3/\text{min}$ ). The measurement data results with surface temperature distribution photographs were documented for each case. While blade specimens with film cooling holes injected at angle  $35^{\circ}$  and  $60^{\circ}$  was coated by thermal paint and attained just for  $V^0=1000 \text{ cm}^3/\text{min}$ .
- In this study, the effect of a blowing ratio ( $V^0=1000, 800$  and  $600 \text{ cm}^3/\text{min}$ ) has been carried out for a blade specimen with film cooling holes injected at an angle of  $45^{\circ}$ . Also, the angle of injection effect was examined experimentally for  $35^{\circ}, 45^{\circ}$  and  $60^{\circ}$  blade specimen. Table 7-7 shows boundary conditions of the experimental test.

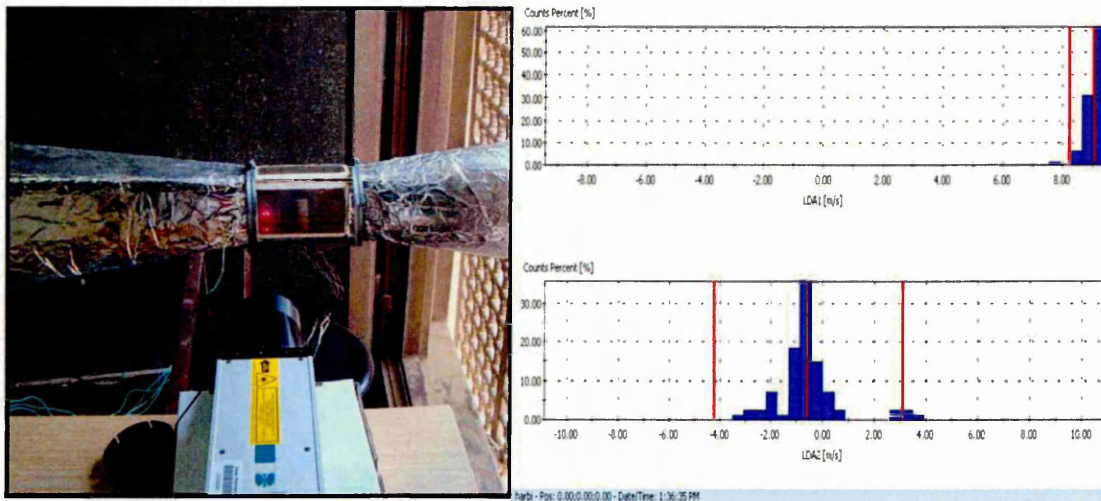


Figure (7-22) Experimental measurement of mainstream velocity at the inlet of test section utilizing LDA.

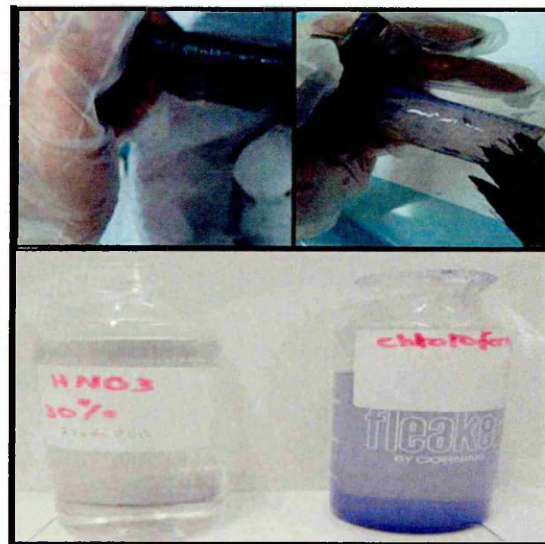


Figure (7-23) Process of scaling thermal paint from blade specimen using Chloroform solvent and 30% of Nitric acid.

**Table 7-7: Experimental test boundary conditions**

Test section boundary conditions	
TWT Hot Temperature	Above 633.15 K
TWT Hot air Velocity	9.35 m/sec
Coolant Fluid Temperature	294.55 K
Coolant Fluid Flow rate	1000, 800 and 600 (cm <sup>3</sup> /min)

### 7.8 Accuracy of instrument and equipment

Experimental measurement accuracy drastically depends on type the instrument and equipment certainty which used to acquire suitable data. Consequently, percentage error of measurement equipment are listed in Table (7-8) and all equipments were calibrated before used in this study.

**Table 7-8: Percentage error of measurement equipment**

Equipment	Accuracy
EOSINT M 270 direct metal laser sintering machine	50 (μm)
K-type thermocouples	0.75%
Pico TC-08 data logger	0.2 %
Laser Doppler Anemometer (LDA)	0.1%
Rotameter airflow meter	3% for full scale
Thermal paint colour isotherms accuracy	(±8 °C)
Total percentage error	4.05%

Total percentage error was equal to 4.05% for all experimental study cases. So, Figure (7-24) presented a variation of temperature (K) as Y axis against the testing time (sec) for blade specimen cooled at  $V^0=1000$  (cm<sup>3</sup>/min) with an angle of injection of 45°. Error bar shows ranges of experimental error at measured points for the inlet and outlet of the test section. In addition to, measurements point at the thermocouple (1) near the leading edge. Actually, the error bar of the experiment study was illustrated just for one case at three positions to keep figures more apparent.

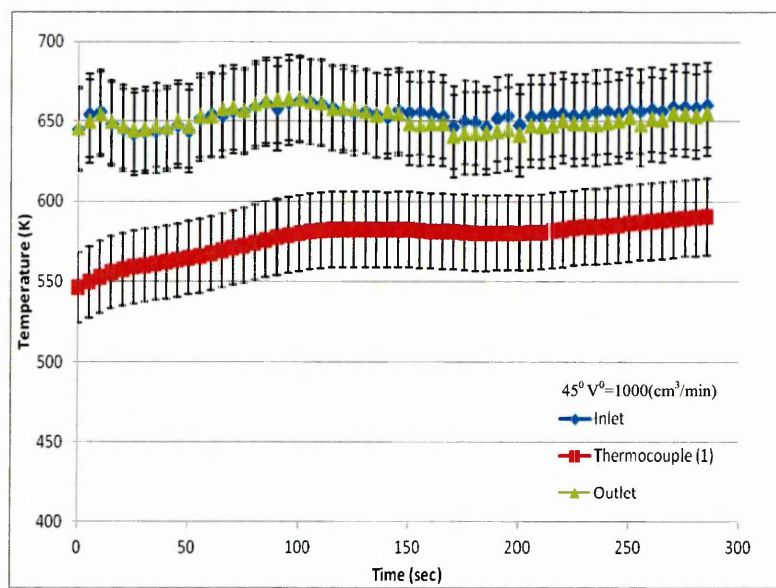


Figure (7-24) Percentage error bar for inlet and outlet test section temperature measurements point at thermocouple (1) against time

## 7.9 Experimental Results Analysis

### 7.9.1 Coolant fluid injected at 45<sup>0</sup> degree

Figure (7-25) illustrates the variation of temperature (K) as Y axis against the testing time (sec) as X axis for inlet and outlet test sections in addition to, five measurement points located at the mid area of the gas turbine specimen. Three different blowing ratios were examined, hence Figure (7-25A), Figure (7-25B) and Figure (7-254C) shows the variation of temperature with  $V^0=1000, 800$  and  $600$  ( $\text{cm}^3/\text{min}$ ) respectively. Transient temperature has been measured with five thermocouples (K type) concealed in the middle of the blade along the span as shown in Figure (7-18).

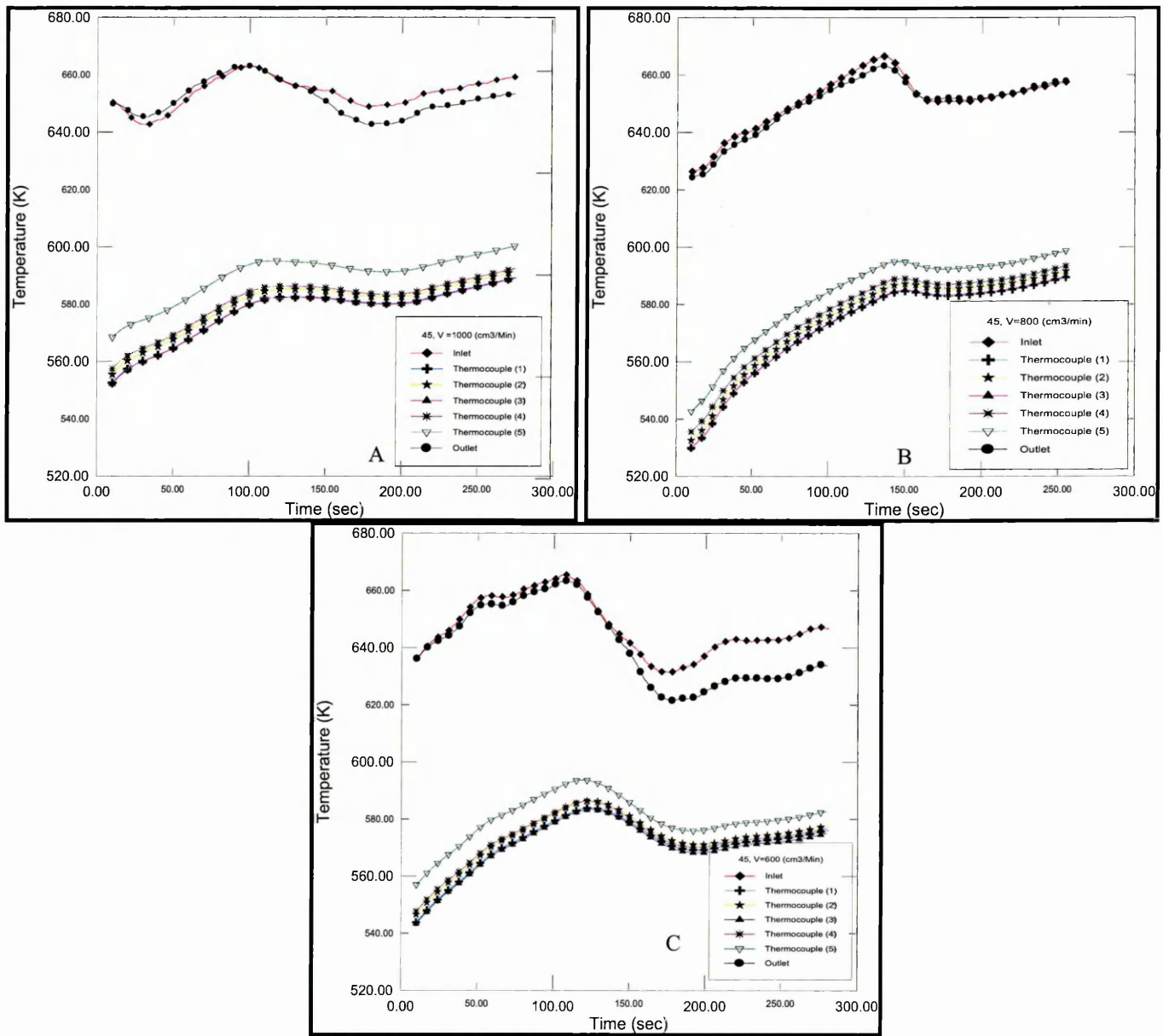


Figure (7-25) Inlet and outlet test section temperature with five core blade temperature against time

In all test cases, the thermocouples were arranged to be; thermocouple (1) records temperature values near the leading edge and so on to thermocouple (5) presents temperature values near the trailing edge for  $V^0 = 1000, 800$  and  $600$  ( $\text{cm}^3/\text{min}$ ). Actually, running average option has been applied in Grapher software to plot and demonstrate temperature measurement trajectory against time to keep the curves smooth.

Clearly, the distributions of blade temperature in Figure (7-25) were arranged from the lowest to the highest value. Hence, temperature values measured by thermocouples (1) and (3) were the lowest data against time. The interpretations of lowest temperature are

certainly due to location of the thermocouple at point (1), very close to the film cooling holes. While, the effect of recirculation on the gas flow and coolant fluid on the pressure side due to blade design geometry (blade twist design), is demonstrated with temperature of the thermocouple at point (3) and the coolant fluid directly impacts on this measured area at the suction side due to blade camber.

The measured temperatures by thermocouples (2), (4) and (5) were shown increase in temperature values along the blade due to the progressively decreasing influence of the coolant fluid (far away from film cooling holes) downstream.

Table 7-9 shows average temperature (K) values during the testing time for the inlet, five measurement points and outlet of the test section. In addition to, temperature difference values ( $\Delta T$ ) related to the main inlet temperature. The positive effect on the performance of using a single row of film cooling holes is clearly apparent through reduced blade temperature when compared with incoming hot gas. For example; at  $V^0=1000$  ( $\text{cm}^3/\text{min}$ ) the first and last temperature values were reduced to 578.6 K and 591.7 K from the main inlet temperature of 655.1 K.

Certainly, the maximum temperature difference between the hot main gas flow and measured points in the blade specimen provides better gas turbine blade protection. For example; at  $V^0=800$   $\text{cm}^3/\text{min}$  the temperature difference of first and fourth point with the main flow was 75.24 and 72.7 K.

**Table 7-9: Average temperature values and difference**

$V^0$	Inlet (K)	Measurement points in blade specimen(K)					Outlet (K)
		(1)	(2)	(3)	(4)	(5)	
1000	655.1	578.6	580	578.38	583.10	591.70	652.37
$\Delta T$	N/A	76.50	75.1	76.72	72	63.4	2.72
800	652.35	577.11	577.51	576.31	579.65	585.56	651.25
$\Delta T$	N/A	75.24	74.84	76.04	72.7	66.79	1.1
600	648.85	574.9	576.95	574.2	576.58	583.18	642.71
$\Delta T$	N/A	73.95	71.9	74.65	72.27	65.67	6.14

Figure (7-26) demonstrates the variation of film cooling effectiveness as the Y axis against time as the X axis through study effect of increasing  $V^0$  ( $V^0=1000, 800$  and  $600$  ( $\text{cm}^3/\text{min}$ )) for measurement point (1) near to the leading edge and point (5) near to the trailing edge. To compare the effect of increasing  $V^0$  on film cooling effectiveness, a selected measurement temperature had been used to plot the efficiency of cooling holes

(these selected point had the same inlet boundary condition at the test section) during the same testing time reveals at 150 to 200 second for each blowing ratio. Therefore, Figure (7-26A) illustrates film effectiveness trajectory at measured point (1) with blowing ratio 1000, 800 and 600 ( $\text{cm}^3/\text{min}$ ) against interval time. Obviously, the film cooling effectiveness was enhanced with increased  $V^0$ . Hence, more protection occurs near leading edge from incoming hot gas.

Moreover, the calculated average value of film effectiveness during 150 to 200 second was 0.196, 0.190 and 0.179 for  $V^0=1000, 800$  and  $600$  ( $\text{cm}^3/\text{min}$ ) respectively. So, highest effectiveness was obtained for  $V^0=1000$  ( $\text{cm}^3/\text{min}$ ).

Figure (7-26B) shows film effectiveness trajectory at a measured point (5) near the trailing edge with a blowing ratio 1000, 800 and 600 ( $\text{cm}^3/\text{min}$ ) against interval time. Clearly, the film effectiveness was enhanced with increased  $V^0$  as well, and the calculated average value of film effectiveness during 150 to 200 second was 0.165, 0.164 and 0.161 for  $V^0=1000, 800$  and  $600$  ( $\text{cm}^3/\text{min}$ ) respectively.

As a result, the effect of increasing  $V^0$  shows that better film effectiveness was acquired for  $V^0=1000(\text{cm}^3/\text{min})$  near the leading and trailing edge in addition to, film cooling effectiveness at leading edge was higher than trailing edge. Certainly, due to cooling holes position and the effect of cold air reduced gradually in downstream direction.

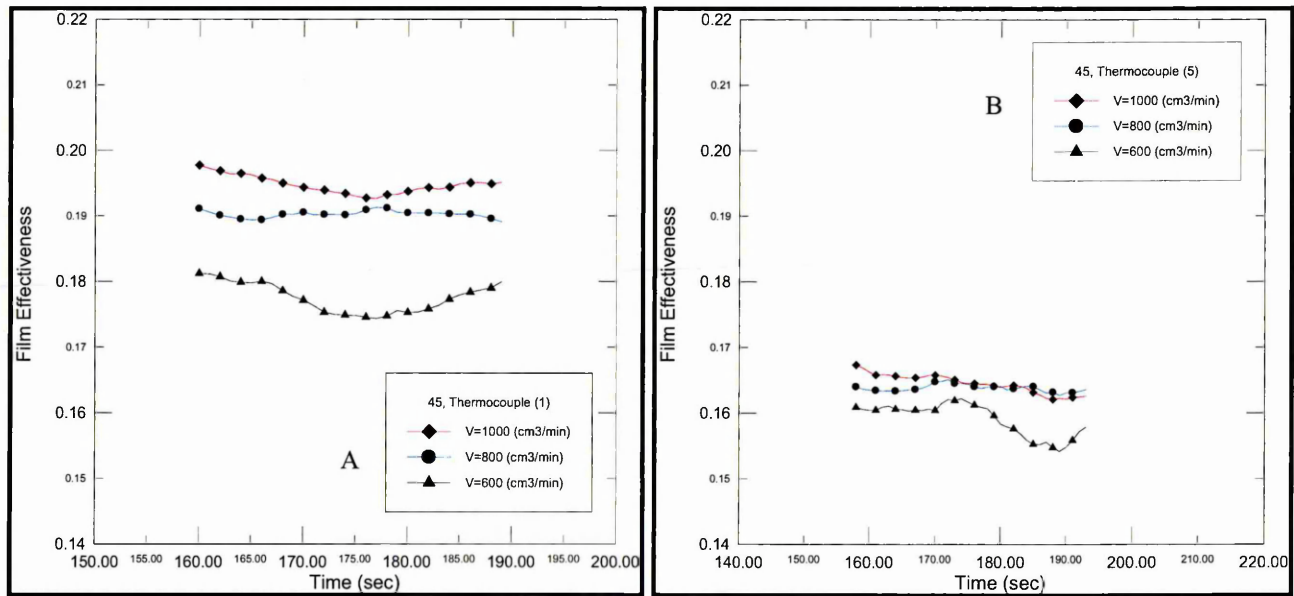


Figure (7-26) Effects of  $V^0$  on film cooling effectiveness at A) measurement point (1) and B) measurement point (5)

Experimental measurement presents result is clarified-a blanket of cold air surrounds the blade surface and achieves a decrease in temperatures at the blade surface through

an increase amount of coolant fluid ratio. Coolant fluid interacts with the hot main gas flow to accomplish an efficient mixing process (jet-crossflow).

Figure (7-27) shows the variation of average film cooling effectiveness as Y axis against  $X/C_X$  ratio as X axis. Where X is the position of measurement points and  $C_X$  is the blade axial chord.

Average film cooling effectiveness values in Figure (7-27) were calculated from the average value of the last 30 measurement temperature at each of the measurement point. So, Figure (7-27A), Figure (7-27B) and Figure (7-27C) show the average film effectiveness for  $V^0=1000, 800, 600$  ( $\text{cm}^3/\text{min}$ ) respectively.

Clearly, trajectory curves of film cooling effectiveness for all  $V^0$  seem to follow the same pattern, so the highest values of film effectiveness were located at measurement (1) and (3) recorded as 0.186 and 0.185 for  $V^0=1000$  ( $\text{cm}^3/\text{min}$ ). This is certainly due to the closer proximity of measurement point (1) to the film cooling holes. Whereas, the effect of blade design geometry (blade twist design from hub to shroud) and blade camber causes, the coolant fluid to directly impact on this measured area at the suction side which appeared on effectiveness value at point (3).

However, the value of film cooling drops down progressively in a downstream direction for measured points (4) and (5). Hence, Table 7-11 demonstrates the average value of effectiveness at last 30<sup>th</sup> measured point in mid area in all measured location along the blade for each  $V^0$ .

From Table 7-10, there are some discrepancy in calculated value of film cooling through increased  $V^0$  for example, at measured point (1) the average value of film cooling effectiveness was 0.186, 0.188 and 0.193 for  $V^0 =1000, 800$  and  $600$  ( $\text{cm}^3/\text{min}$ ) respectively, therefore the maximum value was obtained for  $V^0 =600$  ( $\text{cm}^3/\text{min}$ ). Hence, this discrepancy occurred due to, gas flow temperature in the experimental test was transient condition and the values of film cooling were calculated for the last 30<sup>th</sup> measurement points.

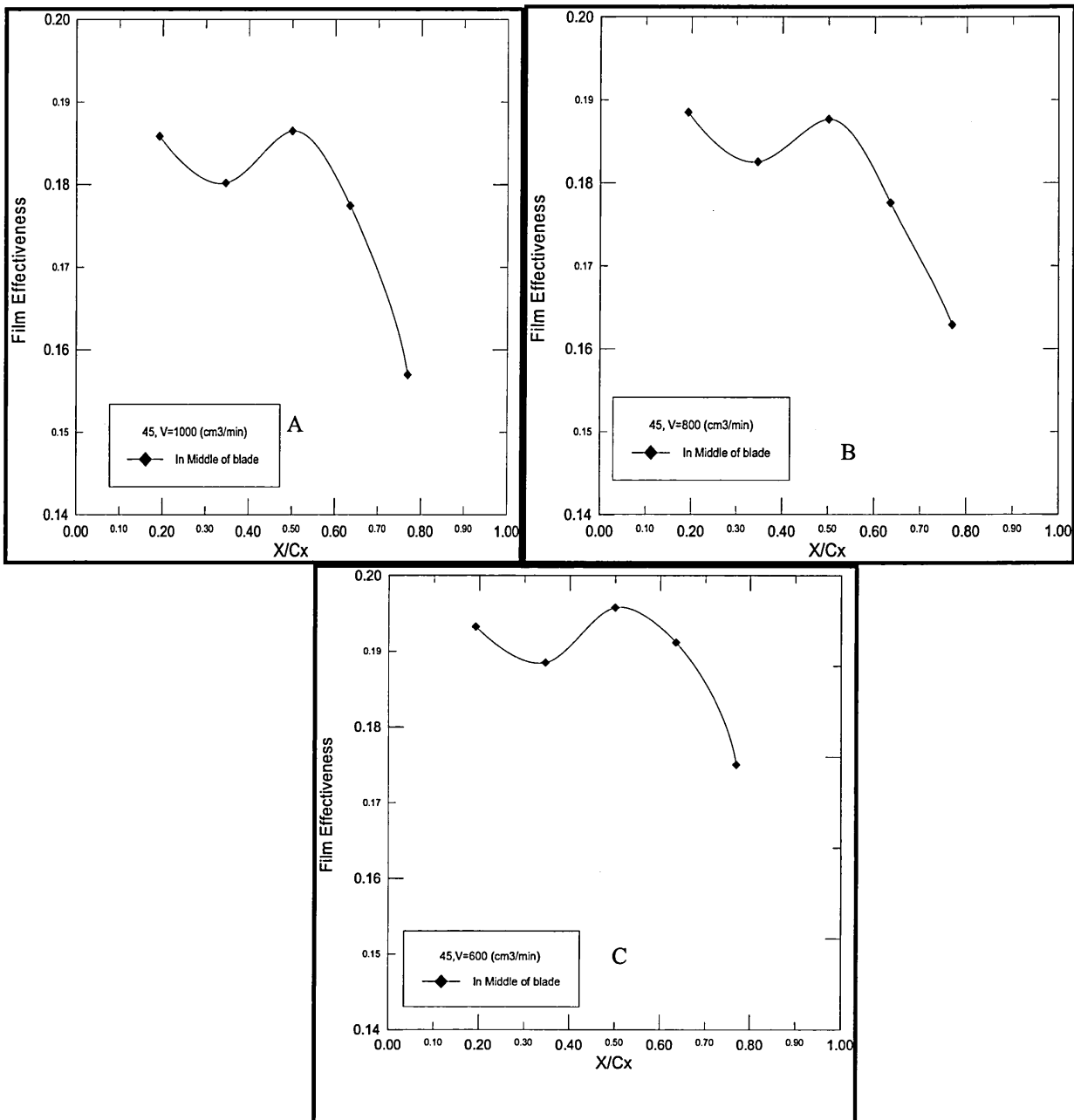


Figure (7-27) Average of film cooling effectiveness for the last 30<sup>th</sup> point of measured temperature for each location at holes angle of injection  $45^\circ$  for A)  $V^0=1000$ , B)  $V^0=800$  and C)  $V^0=600$  (cm<sup>3</sup>/min)

**Table 7-10: Film cooling effectiveness values for each  $V^0$  at the last 30<sup>th</sup> points.**

$V^0$	Inlet	Thermocouples K-type					outlet
		(1)	(2)	(3)	(4)	(5)	
1000	N/A	0.186	0.180	0.185	0.177	0.157	N/A
800	N/A	0.188	0.182	0.187	0.177	0.163	N/A
600	N/A	0.193	0.189	0.195	0.191	0.175	N/A

Figure (7-28) illustrates the detailed of temperature distributions for each of the tested blowing ratio. Thermal paint images clearly show blade temperature on the pressure side during 5 minute tests so, horizontal axis represents the blade spanwise ( $C_z$ ) and vertical axis represents the blade axial chord ( $C_x$ ).

As the value of  $V^0$  increases, the lateral force of the jet becomes stronger and the low temperature region travels to the top of the holes location in the route of holes exit (gas turbine blades surface become more protected from the hot gas and extends the cooled area). Normally, the jet effect begins to decrease downstream due to mixing process.

The effect of varying  $V^0$  has been explored on the blade surface and compared with KN5 guide calibration see Figure (7-9). For example, on the pressure side changes in steps of temperature patterns was depicted in Figure (7-28A), Figure (7-28B) and Figure (7-28C) for  $V^0=1000$ , 800 and 600 ( $\text{cm}^3/\text{min}$ ) respectively. Hence, good temperature colour difference was depicted during increased  $V^0$  values from 600 to 1000 ( $\text{cm}^3/\text{min}$ ). As a result, effect of increasing  $V^0$  shows that better protection from the hot gas was acquired for  $V^0=1000(\text{cm}^3/\text{min})$  near the leading and trailing edge which extended from the hub to the shroud area see Figure (7-28).

In this research, five colour legends steps has been selected to work with, due to the blade specimen melting temperature (673.15 K). Hence, the Thermal Paint Temperature Technology (TPTT) shows blade surface temperature pattern and the difference from one legend step to other is above than 50 K see Table7-6. Anyway, good correlation has been obtained between the blade pressure side surface temperature image and KN5 guide calibration so, hub area is more protected than mid and shroud area, certainly coolant fluid absorbed heat via the blade along the lateral hole through heading from the hub to the shroud. Therefore, internal and external was cooling completely achieved.

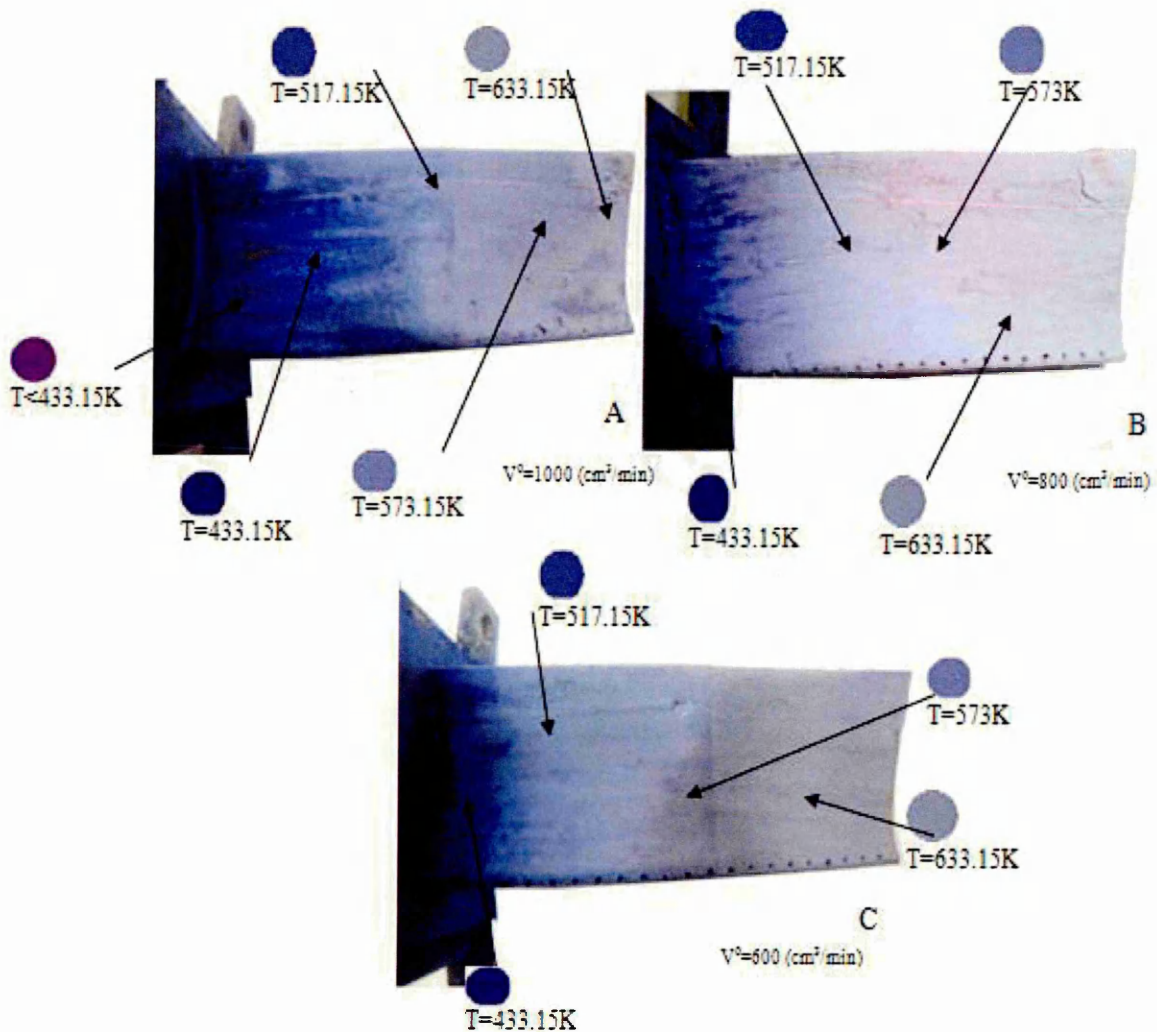


Figure (7-28) Blade surface temperature distribution patterns represented by thermal paint for A)  $V^0 = 1000$ , B)  $V^0 = 800$ , C)  $V^0 = 600 \text{ (cm}^3/\text{min)}$

### 7.9.2 Coolant fluid injected at $60^\circ$ degree

The second experimental measurements test case was accomplished through blowing cooled air at angle of injection  $60^\circ$ . In this measurements test case the number of thermocouples had been increased to speculate the temperature variation on both blade sides (pressure and suction side). Undoubtedly, the mode of fixing these thermocouples on the blade surface required some attention since the blade was fabricated in half scale. As the trailing edge is thin, one thermocouple was deemed enough to gather the temperature on each side. So, 9<sup>th</sup> measurement points had been used to cover the blade specimen.

Figure (7-29A) illustrates the variation of experimental temperatures (K) as Y axis against testing time (sec) as X axis for inlet and outlet test section. In addition to, 9 measurement points were located at the mid area of the gas turbine specimen for pressure and suction side at  $V^0=1000 \text{ cm}^3/\text{min}$ . Experimental measurements of transient temperature for pressure and suction side demonstrated difference in temperature between each side. However, film cooling performance was obtained through achieving acceptable temperature difference between incoming hot gas at the inlet of test section and blade surface measurements values.

Variation of measured surface temperature between pressure and suction side was depicted in Figure (7-29B) near the leading edge (point (1)) against tested time. Namely, average temperature difference between blade surface was obtained due to, attribute of holes injection angle, blade design (twist) and cross section variation from hub to shroud for example, about 1.47 K the difference among blade surface side near the leading edge for  $V^0=1000 \text{ cm}^3/\text{min}$ .

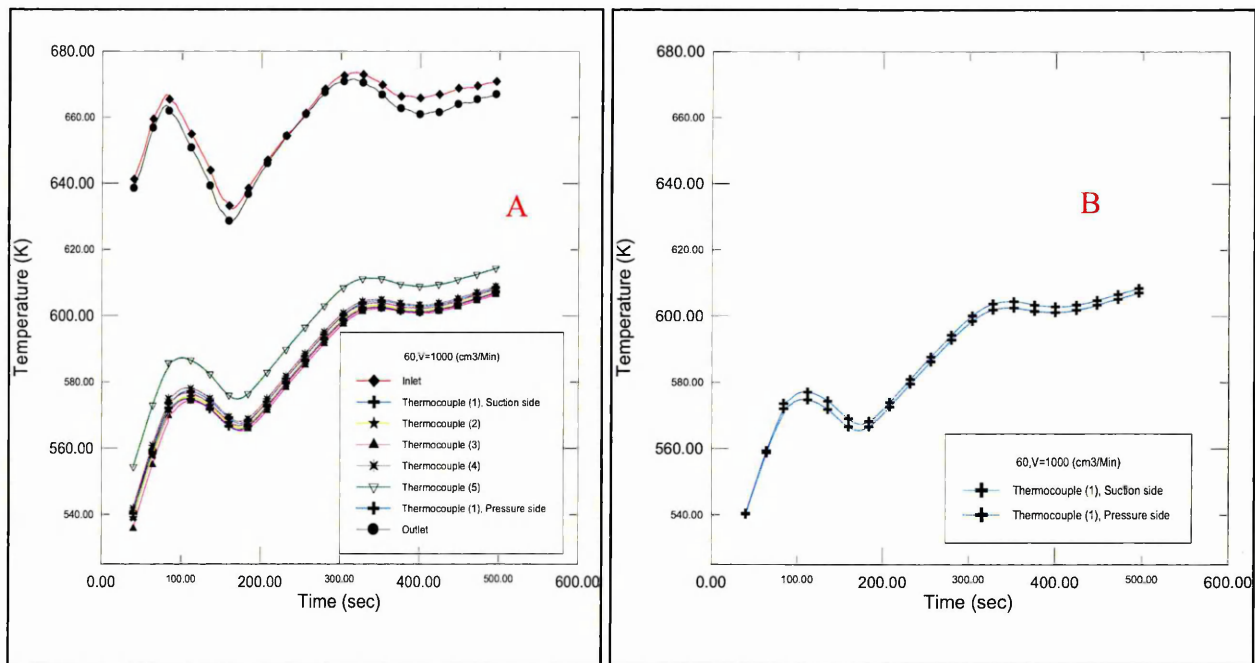


Figure (7-29) A) Transient temperature thermocouple measurements at  $V^0=1000 \text{ cm}^3/\text{min}$ , B) Temperature difference between pressure side and suction side

Table 7-11 demonstrates the average temperature value at  $V^0=1000, 800, 600$  ( $\text{cm}^3/\text{min}$ ) for Pressure Side (PS) and Suction Side (SS). In some thermocouples measurement points, the temperature difference between both sides shows small variation, for example at  $V^0=800$  ( $\text{cm}^3/\text{min}$ ) was change in steps between zero to 3.36.

Reasonable temperature difference was acquired between blade surface and inlet test section due to the impact of film cooling holes, for example about 73.63 K variation among measured point (1) on suction side and inlet of the hot gas. In addition to, about 8.41K between the leading edge and trailing edge of blade for the suction side at  $V^0=1000$   $\text{cm}^3/\text{min}$ .

**Table 7-11: Average thermocouple temperature for all  $V^0$ . and both sides**

$V^0$	Inlet (K)		Temperature of thermocouples K-type (K)					Outlet (K)
			(1)	(2)	(3)	(4)	(5)	
1000	658.52	SS	584.89	583.36	582.11	585.63	593.30	655.46
		PS	583.42	583.53	583.05	584.68	593.30	
800	658.81	SS	591.59	590.24	588.47	592.07	599.47	652.68
		PS	590.42	590.60	591.83	591.99	599.47	
600	658.00	SS	588.37	587.01	584.95	588.51	596.17	651.63
		PS	586.68	586.80	588.54	588.03	596.17	

Figure (7-30A) shows the effect of varying  $V^0$  on film cooling effectiveness located on measurement point (1) as Y axis against the testing time (sec) as X axis. Although, inlet temperature boundary condition was transient, the nearest inlet test section temperature trajectory between  $V^0=1000, 800$  and  $600$  ( $\text{cm}^3/\text{min}$ ) reveals at 360 to 420 seconds. Hence, in Figure (7-30A) the film effectiveness curve at  $V^0=1000$  ( $\text{cm}^3/\text{min}$ ) provides better job to protect blade from the hot gas. Moreover, the average film effectiveness value during the above duration for measured point (1) was 0.174, 0.155 and 0.148 for  $V^0=1000, 800$  and  $600$  ( $\text{cm}^3/\text{min}$ ) respectively.

Figure (7-30B) illustrates the variation of average film cooling effectiveness as Y axis for both sides against  $X/C_x$  ratio as X axis, where X is the location of measurement points and  $C_x$  is the blade axial chord at  $V^0=1000$  ( $\text{cm}^3/\text{min}$ ).

The average values of cooling effectiveness were calculated from the last 30<sup>th</sup> recorded measurements during testing time for each point. Therefore, the efficiency of cooling holes emerged clearly at 1 and 4 measurements point on the pressure side is higher than

suction side by about 2.17% and 1.3% respectively. However, the cooling effectiveness at the 3<sup>rd</sup> measurement point on the suction side is slightly better about 0.68% due to the blade camber design. The equivalent value of the film cooling effectiveness is located at 2 and 5 measurements points.

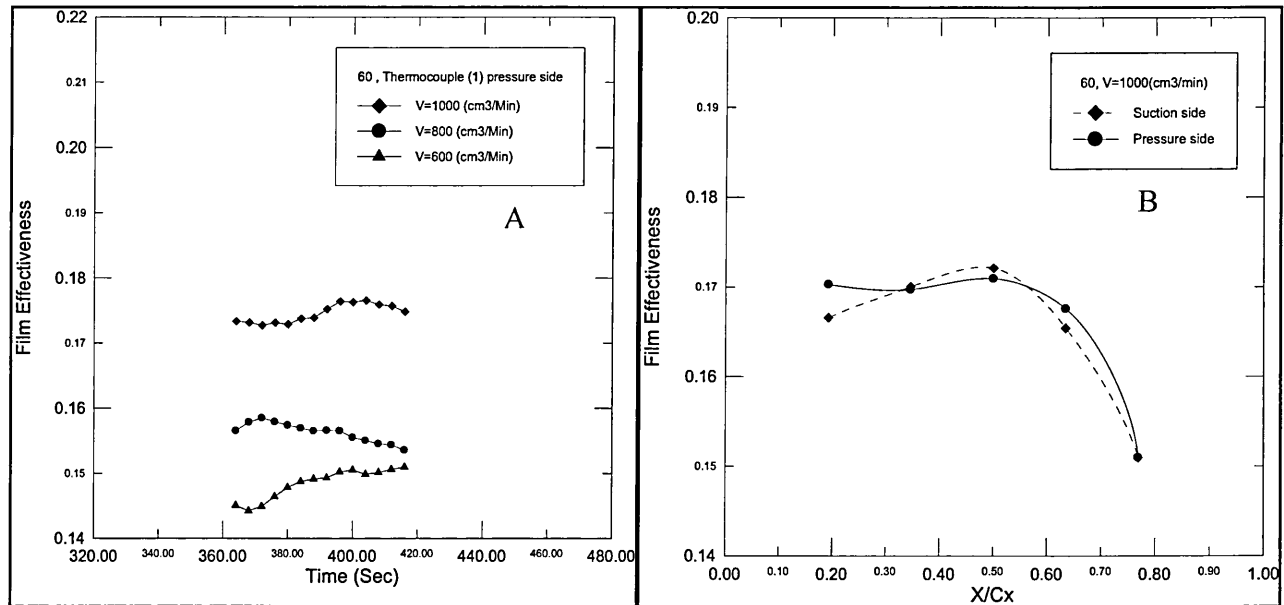


Figure (7-30) A) Effect of varying  $V^0$  on film cooling effectiveness against time for holes angle of injection  $60^\circ$  B) Average film cooling effectiveness measurements along the blade at the mid region  $V^0=1000 \text{ cm}^3/\text{min}$ .

### 7.9.3 Coolant fluid injected at $35^\circ$ degree

The final experimental test case was examined for injected coolant fluid with an angle of  $35^\circ$  degree. In this test case, 9 thermocouples were embedded in the blade specimen to measure blade surface temperature on both sides.

The variation for experimental measurements of transient temperature (K) for both side (pressure and suction side) as Y axis against testing time (sec) as X axis at  $V^0=1000 \text{ cm}^3/\text{min}$  is demonstrated in Figure (7-31A). Effect of film cooling holes is clearly presented in the temperature difference between hot inlet temperature and blade surface temperature. For example, near the trailing edge the temperature difference among measured point (5) and inlet test section was about 70.46 K.

Figure (7-31B) shows transient temperature for pressure and suction side (K) as Y axis at measured point (1) against time (sec) as X axis. Clearly, temperature on the suction side is higher than pressure side so, the average temperature difference between both sides about 3.56K at this measured point.

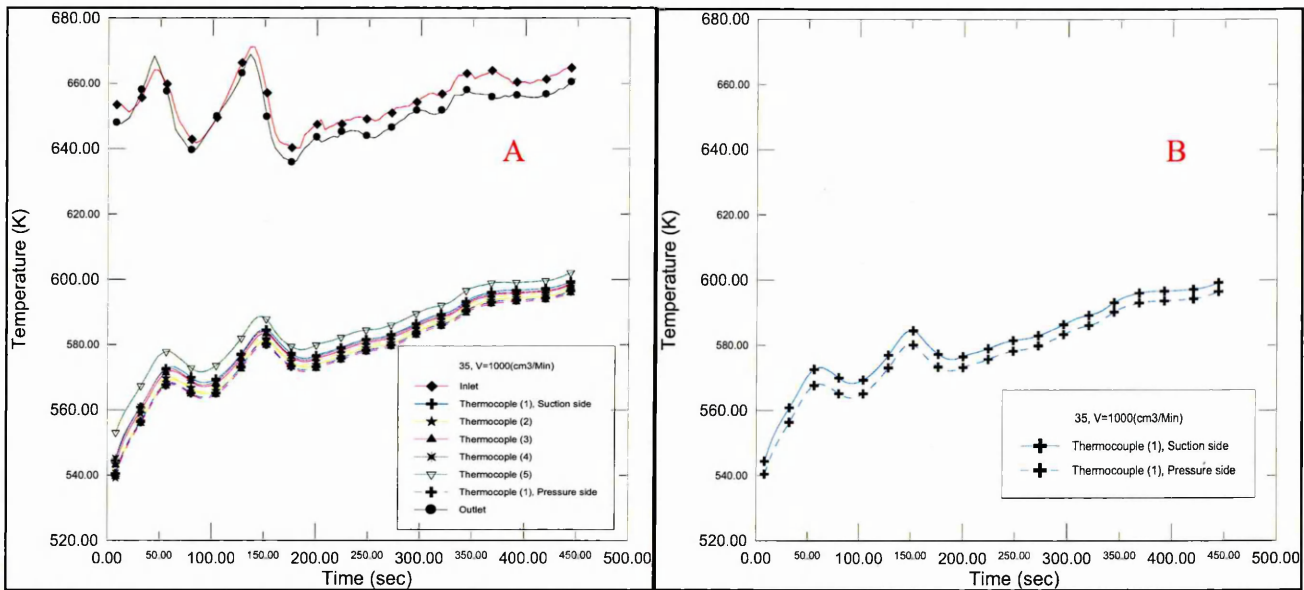


Figure (7-31) A) Transient temperature measurements at  $V^0=1000 \text{ cm}^3/\text{min}$ , B) Temperature measurements for pressure side and suction side.

Average temperature value for all volumetric flow rate ( $V^0=1000, 800, 600 \text{ cm}^3/\text{min}$ ) are presented in Table 7-12 for pressure side and section side. In some thermocouple measurement points, the temperature difference between both sides shows that the temperature on the PS seems lower in most of thermocouple measurements point due to the effect of film cooling holes.

Also, there is a small change in steps temperature difference between the leading edge and trailing edge temperature for example, about 3.6 and 7.16 K at  $V^0=1000 \text{ (cm}^3/\text{min)}$  on the suction and pressure side respectively.

**Table 7-12: Average thermocouple temperature difference for all  $V^0$  and both sides**

$V^0$	Inlet (K)		Temperature of thermocouples K-type (K)					Outlet (K)
			(1)	(2)	(3)	(4)	(5)	
1000	655.08	SS	581.02	577.94	579.96	580.57	584.62	651.27
		PS	577.46	576.91	579.12	577.43	584.62	
800	651.09	SS	589.65	587.41	588.69	589.86	592.67	648
		PS	587.46	586.19	589.33	586.89	592.67	
600	659.06	SS	595.58	593.26	594.76	596.06	599.44	657.05
		PS	581.02	577.94	579.96	580.57	584.62	

Figure (7-32) illustrates blade surface film cooling effectiveness as Y axis for both side (pressure and suction side) at angle of injection  $35^\circ$  at  $V^0=1000 \text{ cm}^3/\text{min}$  against  $X/C_x$  ratio. Film cooling value was calculated from average temperature values at last 30<sup>th</sup> recorded measurements during the testing time for each point. However, the majority of average film cooling effectiveness measurement points on the pressure side is higher than measurements point on the suction side, except for the 2 thermocouple point. Consequently, film effectiveness points on the pressure side are better than suction side by about 4.23%, 3.64% and 3.47% for 1, 3 and 4 thermocouples respectively. While, suction side film cooling is highest just at 2 thermocouples about 1.43% of this is due to location of this thermocouple near the blade camber.

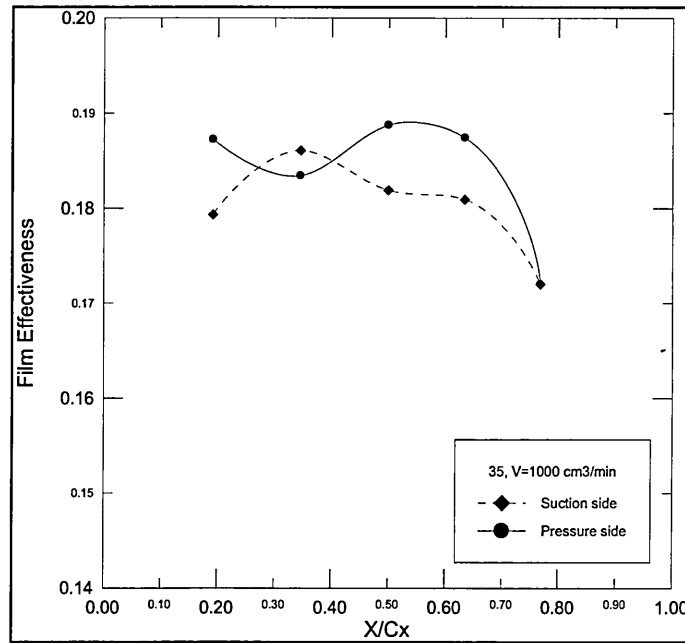


Figure (7-32) Average film cooling effectiveness measurements along the blade for holes angle of injection  $35^\circ$  at the mid region  $V^0=1000 \text{ cm}^3/\text{min}$ .

#### 7.9.4 Thermal paint sensitivity for different angles of injection

Thermal paint has been used to depict blade surface temperature distribution for different hole injections at  $45^\circ$ ,  $35^\circ$  and  $60^\circ$  at the same blowing ratio ( $V^0=1000 \text{ cm}^3/\text{min}$ ). The pressure side temperature during the 5 minute tests is illustrated in Figure (7-33), therefore the horizontal axis represents blade spanwise ( $C_z$ ) and the vertical axis represents blade axial chord ( $C_x$ ).

Flow field in modern gas turbine compose a complex flow phenomena with high turbulence levels. Additional complications are generated via applied film cooling holes

nearby the leading edge of the blade due to the resulting interference between the mainstream and ejected coolant fluid. As result, the effect of angle of injection drastically embodies key parameter on the performance of film cooling.

Pressure surface temperature pattern for blade specimen cooled by air ejected at angle  $45^\circ$ ,  $35^\circ$  and  $60^\circ$  was depicted in Figure (7-33A), Figure (7-33B), and Figure (7-33C) respectively. Clearly, blade specimen cooled by air ejected at angle  $45^\circ$  provides more blade surface protection from incoming high temperature through extending the purple colour of from hub to shroud in streamwise direction see Figure (7-33).

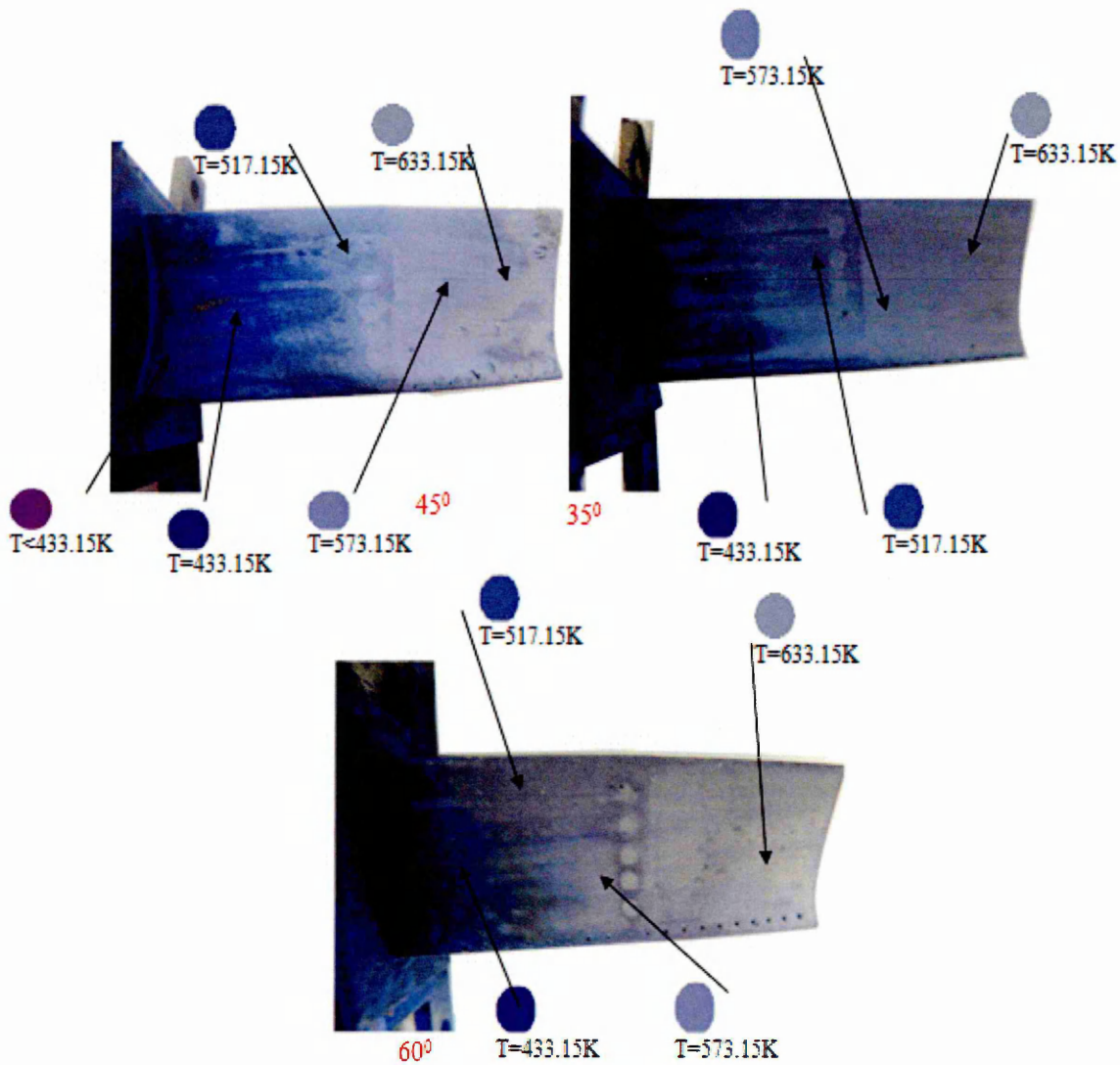


Figure (7-33) Blade surface temperature distribution patterns coloured by thermal paint for holes injection at  $45^\circ$ ,  $35^\circ$  and  $60^\circ$  at  $V^0 = 1000(\text{cm}^3/\text{min})$

Certainly, better film cooling performance was obtained when the coolant fluid covering blade surface with lower turbulence level this occurs as the interference between jet-flow and mainstream take place nearby the blade surface. Accordingly, the effect of holes injection and the blade geometry demonstrates the key of protection with blowing ratio and others parameters studied numerically in chapter six in this research.

Basically, thermal paint KN5 shows qualitative blade surface temperature distribution so the variation of temperature from hub to shroud and from leading edge to trailing edge (along blade) was completely identified. Blade surface temperature pattern was evaluated with KN5 guide and factory temperature colour range Tabled 7-6. Therefore, some temperature values are indicated on the blade as shown in Figure (7-33).

## 7.10 Experimental and numerical validation

To validate numerical results a comparison case has been included. The experimental boundary conditions (blade specimen material model as direct metal 20, hot gas and coolant fluid properties) which are acquired from TWT are implemented in the Fluent software as shown in Tables (7-1) and (7-7) respectively. One representative case has been utilized with two different volumetric flow rates,  $V^0=1000, 800$  (cm<sup>3</sup>/min) for the coolant air injected at an angle of 45<sup>0</sup>.

Figure (7-34) illustrates the variation of the temperature distribution ( $K$ ) at the blade mid-section (plotted on the  $Y$ -axis) for both numerical and average experimental data against  $X/C_X$  ratio (plotted on the  $X$ -axis), where  $X$  is the position of measurement points and  $C_X$  is the blade axial chord.

The experimental average temperatures for the five measured points were recorded during the test time. Therefore, the experimental average temperatures have been presented in Table (7-9). These average temperatures have been plotted to achieve comparison with Fluent numerical calculations on the pressure side along the blade.

Figure (7-34A) shows temperature trajectories for the numerical and experimental data for  $V^0=1000$  (cm<sup>3</sup>/min). The results show some slight variation; the temperature difference between the measurement point (1) for the experimental data and Fluent data at the same location is 32.28 (K). The total percentage error is found to be (4.05%) (see Table (7-8)). It is important to note that human error which is unavoidable from fixing thermocouples in the specimen during testing time (5min) contributes significantly to

this error. Effectively the percentage error between numerical and experimental temperature is a maximum of about 5.58% see equation (5-2). The correlation overall between numerical FLUENT and experimental results is therefore very good.

Figure (7-34B) shows temperature trajectories for the numerical and experimental data for  $V^0=800$  ( $\text{cm}^3/\text{min}$ ). The temperature difference between the measurement point (1) for the experimental data and Fluent data at the same location is 35.26 (K).

The numerical calculations of the temperature for 3-D skewed gas turbine blade are sufficiently accurate since this percentage error is 5.58% and 6.11% for  $V^0=1000, 800$  ( $\text{cm}^3/\text{min}$ ) and these constitute very low errors.

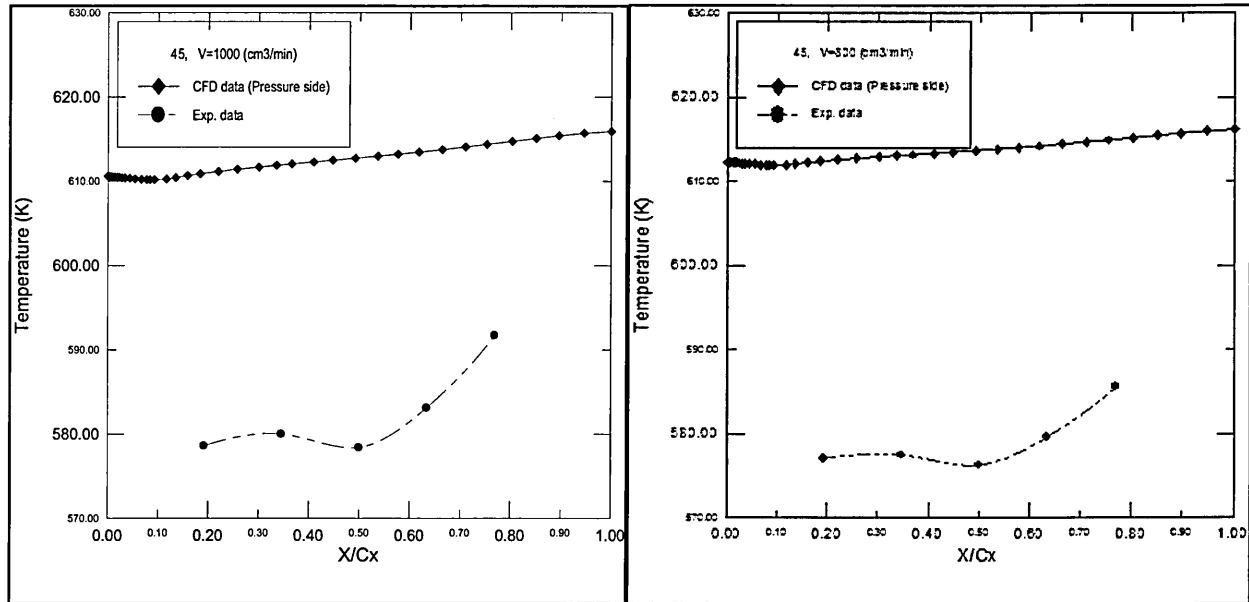


Figure (7-34) Temperature comparison between numerical and experimental data for holes angle of injection  $45^0$  along the blade with A)  $V^0=1000$  ( $\text{cm}^3/\text{min}$ ) B)  $V^0=800$  ( $\text{cm}^3/\text{min}$ ).

## 7.11 Summary

This chapter presented the process of experimental and fabrication for gas turbine blade specimens using laser sintering technology and Thermal Wind Tunnel (TWT). Three specimens were produced with different film cooling holes angle ( $45^0$ ,  $35^0$  and  $60^0$ ) and a thermal wind tunnel (TWT) was fabricated. Experimental equipment specification and accuracy has been explained, also the preparation and experimental procedure test and duration steps of each case, have been described.

Measurement results of the experimental investigation were presented in plots and tables as temperature distribution at the mid area along the blade for five thermocouples points, used to indicate temperature on pressure and suction side. In order to illustrate film cooling effectiveness thermal paint technology was utilized as a qualitative way through studying the effect of increase blowing ratio ( $V^0 = 1000, 800$  and  $600 \text{ cm}^3/\text{min}$ ) as well as, effect of angle of holes injection ( $35^\circ, 45^\circ$  and  $60^\circ$ ). Generally a good accuracy has been achieved, which generally corroborates the CFD simulations discussed in earlier chapters.

## 8.1 Conclusions

The cooling performance of gas flow in a gas turbine blade was numerically and experimentally investigated to examine the influence of different film cooling holes parameters on cooling effectiveness. In this study, a modern gas turbine blade geometry was used as a solid body with the blade cross section from hub to shroud with a varying with a degree of skewness. Four distinctive stages were planned to achieve the aim of this research through numerical and experimental methods. The conclusions of this research are summarized relating to each of these stages as follows:

1. Numerical simulation of fully developed two-dimensional channel flow and turbulent aerodynamic flow on a NACA 0012 airfoil as modeled in chapter 4. The following conclusions are derived:
  - To achieve good numerical results, it is recommended to employ a Boundary Layer (BL) mesh with high mesh density and quantity of cells in the vicinity of the wall and a coarse mesh far away from the wall.
  - The triangular mesh type attains acceptable numerical results for the NACA0012 airfoil in comparison with the experimental data of Sagrado (2007). Therefore, for more complex geometries it is preferable, cheaper and faster to use a hybrid B.L plus triangular mesh type.
  - By adding a boundary layer mesh, the effects of mesh type for Quad and Triangular elements seem similar. However, the solution for a Quad mesh yields slightly better results.
  - The value of friction Reynolds number( $Re_\tau = 590$  and  $2320$ ) near to the wall attains a maximum value due to the shear force and velocity gradients, fluid property ( $\mu$ ) and type of wall (no slipping). Therefore,  $Re_\tau$  is strongly proportional to the velocity gradients.
  - Enhancement Wall Treatment (EWT) achieves a better correlation with the logarithmic law than the Standard Wall Function (SWF) as is demonstrated by the velocity profiles for all turbulence models employed in the FLUENT simulations.
  - The RNG turbulence model achieves better accuracy in comparison with other turbulence models (S-A,  $k-\epsilon$ , and (SST)  $k-\omega$ ).The RNG model achieves good correlation with the experimental results of Sagrado (2007).

- The present CFD study suggests that for wall bounded turbulence, the first grid point away from the wall should be located at  $y^+ \sim 12$ , when employing the RNG turbulence model with EWT.
  - With the k- $\epsilon$  turbulence model with SWT, it is found that the CFD results are inadequate when  $50 < y^+ < 200$ . This indicates that the RANS method is still expensive for engineering problems.
2. Numerical simulations of the heat transfer and the performance of film cooling for a single hole, two rows of holes and holes arrangement was modeled in chapter 5. Different solid plate material properties with two blowing ratios were investigated for both solid and shell plate cases, utilizing the FLUENT code. The main findings of this stage of the research are as follows:
- The FLUENT computations demonstrate sufficient accuracy and very good agreement with earlier numerical studies of flat plate film turbulent cooling (see Liu *et al.*(2008) and Sinha (1999)) for X/D=1, 3, 6 and 10.
  - The highest cooling effectiveness corresponds to the lowest thermal conductivity (the heat absorbing capability of materials dictates the rate at which heat is drawn from the hot gas flow and this varies considerably from one material to another).
  - Film cooling effectiveness is greatly influenced by the material thermal properties (coolant fluid absorbing heat from the solid plate through lateral direction flow up to the jet in cross-flow). The best material is shown to be steel, especially near film cooling holes.
  - There is no enhancement in film cooling effectiveness on the plate with increasing BR from 0.5 to 1 since the jet flow penetrates the mainstream flow and this disturbs the film cooling layer; the coolant fluid is therefore blown too far from the wall.
  - This study recommends the use of a low blowing ratio to maintain the presence of coolant near the wall. Additionally, it is recommend to use high blowing ratios when the injection holes are positioned opposite to the mainstream flow (the coolant fluids will overcome the hot gas).
3. The film cooling performance for a complex gas turbine blade at the leading edge was thoroughly investigated. The effect of utilizing three blowing ratios (BR=1, 1.5

and 2), varying coolant fluid temperatures ( $T_C=287.5$  K and  $T_C=153$  K), three angles of injection ( $35^\circ$ ,  $45^\circ$  and  $60^\circ$ ), increased number of cooling holes (32 and 42 holes) and varying cooling holes diameter ( $D=0.5$  mm and 1mm) were numerically studied. The main findings of this stage of the research are as follows:

- Film cooling effectiveness near the leading edge significantly increases with blowing ratio ( $\eta$  is proportional with BR). The influence of increasing BR on the film cooling effectiveness appeared on the pressure and suction side; the pressure side effectiveness cooling is much more enhanced than the suction side (high BR enhanced film cooling on pressure side). Furthermore the response of film cooling effectiveness along the span from the hub to the shroud section is enhanced with an increase in the blowing ratio.
  - There is no benefit in the injection of coolant fluid at a low temperature to enhance blade cooling at a constant BR (see equation 5-1 and 5-3).
  - The heat load on the blade represented by Nusselt number ( $N_u$ ) is strongly influenced by increasing BR (BR=1, 1.5 and 2).
  - The effect of the angle of injection ( $35^\circ$ ,  $45^\circ$  and  $60^\circ$ ) is a significant parameter in accomplishing better gas turbine blade protection from overheating. The FLUENT computations show that with injecting coolant fluid at an angle of  $45^\circ$  improved protection is achieved for the blade since the mass flow of coolant is constant and the hot surface temperature is reduced (coolant fluid extracted from compressor). Moreover, with increased number of holes in the spanwise direction, the blade surface degradation near shroud area is comprehensively reduced.
    - Film cooling performance is significantly enhanced with bigger diameter exit holes. Blades with large cooling hole diameter ( $D=1$  mm) provided better cooling performance due to reduced jet penetration.
4. Thermal Paint Temperature Technology (TPTT) was used in conjunction with a high-resolution photographic imaging system and a Thermal Wind Tunnel (TWT) to study the effect of blowing ratio and angle of holes injection on the film cooling effectiveness for a 3-dimensional skewed gas turbine blade specimen. The results have shown that:
- Lower temperatures are achieved near the leading edge and the blade surface is successfully protected with the increasing of the blowing ratio (film cooling effectiveness,  $\eta$ , is proportional to BR).

- The influence of increasing  $V^0$  ( $V^0 = 600, 800$  and  $1000 \text{ cm}^3/\text{min}$ ) on the film cooling effectiveness is examined for both the pressure and suction sides of the blade- the pressure side effectiveness cooling is found to be more enhanced than the suction side at higher BR.
- As the BR is increased, the lateral jet force is elevated and the low temperature region migrates to the top of the holes location. The gas turbine blades surface is therefore better protected from the hot gas and the cooled region on the blade is extended. Generally, the film cooling effectiveness along the span from the hub to the shroud section is enhanced with the increasing blowing ratio and the jet effect begins to decrease downstream.
- Thermal Paint Temperature Technology (TPTT) provides a reliable method for quantifying the effect of BR and the angle of cooling holes on blade surface temperature distributions in a real gas turbine blade with complex geometry (skewed). The technology is relatively simple and it is an effective flow visualization technique.

This study is presented as novel for the following reasons

1. The study utilized different cross section blade geometry (from hub to shroud) with angle of twist (blade skewness).
2. The study considered the main flow (hot gas) and coolant system (cooled fluid) differing in temperature and pressure.
3. The study considered a modern realistic blade as a solid body (other researchers have considered the blade as only an empty shell or surface). Consequently, the blade material thermal properties effects were simulated properly.
4. The experimental investigation qualitatively captured the blade surface temperature using Thermal Paint Technology (TPT) during high temperature boundary condition through permanent photographic imaging.

## 8.2 Future Work

This research is characterized into two distinctive parts. Firstly, the investigation of FLUENT code numerical accuracy, sensitivity and performance and its associated solver and turbulence models to predict the aerodynamic flow and heat transfer quantities and qualities. through Three different benchmarks were utilized. Namely, *turbulent channel flow*, *NACA 0012airfoil* and *film cooling for flat plate surface*.

Secondly, numerical and experimental methods were used to characterize factors that directly influence the performance of gas turbine cooling. An extensive investigation was carried out to identify critical design parameters that affect optimum film cooling.

As future work and to further build on this study, it is recommended to extend both numerical and experimental investigation as follows:

- Investigate the effect of multiple (not single) gas turbine blades rotation on film cooling effectiveness.
- Carry out numerical and experimental investigation of the effect of unsteady flow *e.g. pulsing* on film cooling of gas turbines.
- Use plasma actuator technology to improve the performance of film cooling in gas turbine (a novel method which has been applied at Florida University, USA). This mechanism entails pushing or pulling *cold fluid* which remains attached to the surface and sustains a higher degree of cooling effectiveness for the entire blade geometry.

## References

AHN, J. MHETRAS, S. and HAN, J.C. (2005). Film cooling effectiveness on a gas turbine blade tip using pressure sensitive paint. *Transaction of the ASME*, 127, 521-530.

AHN, J. SCHOBELI, M.T. HAN, J. C. and MOON, H. K. (2007). Effect of rotation on leading edge region film cooling of a gas turbine blade with three row of film cooling holes. *Heat and Mass Transfer*, 50, 15-25.

AMERI, A. A. (2001). Heat Transfer and Flow on the Blade Tip of a Gas Turbine Equipped with a Mean-Camberline Strip. *NASA/CR-2001-210764- GT-0156*, Prepared under contract NAS3-00180, 12.

AMES, F. E. JOHNSON, J. D. and FIALA, N. J. (2006). The influence of aero-derivative combustor turbulence and Reynolds number on vane aerodynamics losses, secondary flow and wake growth. *ASME Turbo Expo*, Proceedings GT-90168.

ANDERSON, J.D. (1995). *Computational Fluid Dynamics" the basic with applications*, Chapter 2, New York, United States of America, McGraw-Hill Book.

ANDERSON, J.D. TANNEHILL, J.C. and PLETCHER (1984). *Computational Fluid Dynamics and Heat Transfer, series in computational methods in mechanics and thermal sciences*, Chapter 5. New York, United States of America, McGraw-Hill Book.

ANDERSON, W.K. (1992). Grid generation and flow solution method foe Euler Equations on Unstressed Grids. *NASA Langley Research center, Hampton, VA23665-5225*.

ANTHONY G. (2006). *Gas Turbine, Handbook*, Third Edition <http://www.scribd.com/doc/4565510>.

AZZI A. and LACHEHAL D. (2002). Perspectives in modeling film cooling of turbine blades by transcending conventional two-equation turbulence models. *Turbomachinery, Transactions of the ASME*, 124, 472-484.

AZZI A. and JUBRAN B.A. (2004). Influence of leading edge lateral injection angles on the film cooling effectiveness of a gas turbine blade. *Heat and Mass Transfer*, 40, 501-508.

BARLOW J.B. RAE W.H. and POPE J.A. (1999). *Low speed wind tunnel testing* Canada, John Wiley and Sons Inc.

BATHIE W.W. (1995). *Fundamentals of gas turbines, Second Edition*, United States of America, John Wiley and Sons.

BLAZEK J. (2005). Computational fluid dynamics. *Principles and Applications*. 2nd ed. Amsterdam; San Diego Elsevier Science & Technology.

BMT, Betta Machine Tool, metal laser-sintering (2011) [online]. Last accessed on -1-December -2011 at: <http://www.bettamachinetools.com.au/EOSINT-M-280-pdf.html>

BOGARD D.G. and THOLE K. A. (2006). Gas turbine film cooling. *propulsion and power*, 22 (2), 249-270.

BOYCE M. P. (2002). *Gas Turbine Engineering, Handbook, Chapter: 9 Axial-flow turbines*, Elsevier Gulf.

BRADSHAW P. CEBECI T. and WHITELAW J.H. (1981). *Engineering calculation methods for turbulent flow*, New York, Academic press Inc.

BREDBERG J. (2002). Turbulence modelling for internal cooling of gas-turbine blades. *Thermo and Fluid Dynamics*. Goteborg, Sweden, Chalmers University of Technology.

BROOKS F.J. (2008). GE Gas Turbine performance characteristics. *GE Power Systems*,  
*Last updated 10/12/2008*,  
[http://www.gepower.com/prod\\_serv/products/tech\\_docs/en/downloads/ger3567h.pdf](http://www.gepower.com/prod_serv/products/tech_docs/en/downloads/ger3567h.pdf),  
20.

BURD S. and SIMON T.W. (2000). Effects of hole length, supply plenum geometry, and freestream turbulence on film cooling performance. *NASA, CR-2103360*.

BURDET A. ABHARI R.S. and ROSE M.G. (2007). Modeling of film cooling part 2 model for use in three dimensional computational fluid dynamics. *Turbomachinery, Transactions of the ASME*, 129, 221-231.

BURDET A. and ABHARI R.S. (2007). Three dimensional flow prediction and Improvement of Holes Arrangement of a Film- Cooled Turbine Blade Using Feature Based Jet Model. *Turbomachinery, Transactions of the ASME*, 129, 258-268.

CAMPBELL M. COSGROVE J.A. GREATED C.A. JACK S. and ROCKLIFF D. (2000). Review of LDA and PIV applied to the measurement of sound and acoustic streaming *Optics and Laser Technology* 32, 629-639.

CARULLO J.S. NASIR S. CRESS R.D. NG W.F. THOLE K.A. ZHANG L.J. and MOON H.K. (2011). The effects of freestream turbulence, turbulence length scale and exit Reynolds number on turbine blade heat transfer in a transonic cascade. *Turbomachinery, Transactions of the ASME*, 133, 1-11.

CELIK I. (1993). Numerical uncertainty in fluid flow calculation needs for future research. *Transaction of the ASME*, 115, 194-195.

CHEN H.C. and PATEL V.C. (1988). Near -wall turbulence models for complex flows including separation, *AIAA Journal* 26 part 6 641-648.

CHMOTINE L.N. AVGOUSTINONVITCH V.G. and EGOROV M.I. (1997). Numerical study of unsteady flow in high pressure turbine of aircraft engine. *33rd AIAA/ASME/SAE/ASEE Join Propulsion Conference & Exhibit, July6-9. Seattle,*

CHUNG T.J. (2002). *Computational fluid dynamic, (Structured Grid Generation)*, Cambridge, United Kingdom, Cambridge university press.

COULTHARD S.M. (2005). Effects of pulsing on film cooling of gas turbine airfoils. IN TRIDENT SCHOLAR PROJECT REPORT NO. 333 (Ed. United States Naval Academy, Annapolis, Maryland.

Custompartnet, metal laser-sintering (2011). [online]. Last accessed on -20-August - 2011 at: <http://www.custompartnet.com/wu/direct-metal-laser-sintering>

Dantec, Dantec Dynamics manuel, Laser Optical Measurement System and Sensors Publication No.: 239-v4.

Dantec (2011). Dantec Dynamics [online], Laser Doppler Anemometry - measurement principles, Last accessed on 1- October -2011 at: <http://www.dantecdynamics.com/Default.aspx?ID=822>

DAUD H.A. LI Q. BEG O.A. and ABDULGHANI S.A.A. (2011A). Numerical investigations of wall-bounded turbulence. *IMechE, Mechanical Engineering Science*, 225(C), 1163-1174

DAUD H.A. LI Q. BEG O.A. and ABDULGHANI S.A.A. (2011B). Numerical study of flat plate film cooling effectiveness with different material properties and hole arrangements. *The Twelfth UK National Heat Transfer Conference*. 30/31st August & 1st September 2011 at UK, the University of Leeds.

DAUD H.A. LI Q. BEG O.A. and ABDULGHANI S.A.A. (2011C). Numerical simulation of blowing ratio effects on film cooling on a gas turbine blade. *Computational Methods and Experimental Measurements XV*. New Forest, UK.

DAUD H.A. LI Q. BEG O.A. and ABDULGHANI S.A.A. (2012) Numerical Investigation of Film Cooling Effectiveness and Heat Transfer along a Flat Plate, in press *Int. J. of Appl. Math and Mech.* 8(17):p. 17-33.

DJAVARESHKIAN M.H. and REZA-ZADEH S. (2006). Application of normalized flux in pressure - based algorithm. *Computers and Fluids*, available online at [www.ScienceDirect.com](http://www.ScienceDirect.com)., 36, 1224-1234.

DJOUMAA S. MESSAOUDI L. and GIEL P.W. (2007). Transonic turbine blade loading calculation using different turbulence models -effects of reflecting and non reflecting boundary conditions. *Applied thermal Engineering*, 27, 779-787.

EGHLIMI A. KOUZOUBOV A. and FLETCHER C.A.J. (1997). A new RNG-based two equation model for predicting turbulent gas particles flow. *Int. Conference on CFD in Mineral and Metal Processing and Power Generation CSIRO*. Sydney Australia.

Ehow, eHow thermocouples junction type (2011)[online]. Last accessed on 15- January -2011 at:[http://www.ehow.com/list\\_7598326\\_thermocouple-junction-types.html](http://www.ehow.com/list_7598326_thermocouple-junction-types.html)

EKKAD S.V. OU S. and RIVIR R.B. (2006). Effect of jet pulsation and duty cycle on film cooling from a single jet on a leading edge model. *Transaction of the ASME*, 128, 564-571.

EKKAD S.V. OU S. and RIVIR R.B. (2004) A transient infrared thermography method for simultaneous film cooling effectiveness and heat transfer coefficient measurements from a single test. *Transaction of the ASME*, 126, 597-603.

EKKAD S.V. and HAN C. (2000). A transient liquid crystal thermography technique for gas turbine heat transfer measurements. *Measurement Science Technology*, 11, 957-968.

EL-SAYED A.F. (2008). *Aircraft propulsion and gas turbine engines*, Boca Raton, United States of America, Taylor and Francis Group.

EOS GmbH (2004). Electro Optical System, Robert-Stirling-Ring 1, MaterialData\_M\_en.doc 6 / 6 D-82152 Krailling / München, [www.eso.info](http://www.eso.info). 2004.

Eutechinst , Eutechinst. Instruments, thermocouples (2011) [online]. Last accessed on 14- January -2011 at: <http://www.eutechinst.com/techtips/tech-tips33.htm>

FLUENT (2006A). Gambit 2.0, user manual [Computer program].Adobe.

FLUENT (2006B). Fluent user manual 6.3[Computer program].Adobe.

FOREST A.E. WHITE A.J. LAI C.C. GUO S.M. OLDFIELD M.L.G. and LOCK G.D. (2004). Experimentally aided development of a turbine heat transfer prediction method. *Heat Transfer and Fluid Flow*, 25, 606-617.

GAO Z. NARZARY D.P. and HAN J.C. (2008). Film cooling on a gas turbine blade pressure side or suction side with axial shaped holes. *Heat and Mass Transfer*, available online at [www.ScienceDirect.com](http://www.ScienceDirect.com). , 51, 2139-2152.

GARG V.K. (2002). Heat transfer research on gas turbine aerofoils at NASA Glenn Research Centre. *Int. J. Heat and Fluid Flow*, 23 (2), 109-136.

GARG V.K. and ABHARI R.S. (1997). Comparison of predicted and experimental Nusselt number for a film cooled rotating blade. *Heat and Fluid Flow*, 18, 452-460.

GARG V.K. and GAUGLER R.E. (1997). Effect of cooling temperature and mass flow on film cooling of turbine blades. *Heat Mass Transfer*, 40(2), 435-445.

GERENDAS M. and FISTER R.P. (2000). Development of Very Small Aero -Engine. *ASME International*, GT no.536.

GHORAB M.G. (2010). Experimental investigation of advanced film cooling schemes for a gas turbine blade. *Mechanical and Industrial engineering* Montreal, Quebec, Canada, Concordia University.

GIAMPAOLO T. (2006). *Gas Turbine Handbook:Principles and Practices*, United States of America, Florida, The Fairmont Press, Inc.

GIBSON I. and SHI D. (1997). Material properties and fabrication parameters in selective laser sintering process. *Journal of Rapid prototyping* 3 NO.4, , 129-136, .

GORD M. F. (2007). Heat transfer over rotor surface in a pre-swirl rotating disc system. *International Journal of Dynamic of Fluids*, 3(1), 81-94.

GORD-FARZANEH (2007). Heat transfer over rotor surface in a pre-swirl rotating disc system. *Dynamic of Fluids*, 253 (1), 81-94.

GRITSCH M. SCHULZ A. and WITTIG S. (2000). Film cooling holes with expanded exits: near-hole heat transfer coefficients. *Heat and Fluid Flow*, 21, 146-155.

GUANGCHAO L. HUIREN Z. and HUIMING F. (2008). Influences of Hole Shape on Film Cooling Characteristics with CO<sub>2</sub> Injection. *Chinese journal of Aeronautics*, available online at [www.ScienceDirect.com](http://www.ScienceDirect.com)., 393-401.

HASLINGER W. and HENNECKE D.K. (1997). High resolved distribution of adiabatic film cooling effectiveness for turbine leading edge film cooling. *International Air Breathing Engines, 13 th, ISABE*. Chattanooga.

HEIDMANN J.D. (1995). A numerical study of the effect of wake passing on Turbine Blade Film cooling. *NASA Technical Memorandum*, AIAA-3044.

HEIDMANN J.D. KASSAB A.J. and STEINTHORSSON E. (2003). Conjugate heat transfer effects on a realistic film cooling turbine vane. *ASME Turbo Expo, (GT2003-38553)*, 1-11.

HIRSCH C. (1988). *Numerical computation of internal and external flows, Fundamentals of numerical discretization*., Great Britain, John Wiley and Sons.

HOWELL R.J. (1999). Wake Separation bubble Interaction in low Reynolds number turbomachinery. *Degree of Doctor of Philosophy in Mechanical Engineering*. Gonville and Caius College, Cambridge.

HOWELL R.J. HODSON H.P. and SCHULTE V. (2001). Boundary layer development in the BR710 and BR 715LP turbines, the implementation of high lift and ultra life concepts. *ASME Turbo Expo*, GT-0441, 1-8.

HUNG M.S. DING P.P. and CHEN P.H. (2009). Effect of injection angle orientation on concave and convex surface film cooling. *Experimental Thermal and Fluid Science*, 33, 292-305.

- IWAMOTO K. KASAGI N. and SUZUKI Y. (2005). Direct numerical simulation of turbulent channel flow at  $Re_{\tau}=2320$ . *16th Symposium on Smart Control of Turbulence, March 6-9, Tokyo.*
- JIA R. SUNDEN B. MIRON P. and LEGER B. (2005). A Numerical and Experimental Investigation of the Slot Film Cooling Jet With Various Angles. *Turbomachinery, Transactions of the ASME*, 127, 635-645.
- JOVANOVIC M.B. DE LANGE H.C. and VAN STEENHOVEN A.A. (2006). influence of hole imperfection on jet cross flow interaction *Heat and Fluid Flow*, 27, 42-53.
- KADER B. (1993). Temperature and concentration profiles in fully turbulent boundary layer. *Int. J. Heat Mass Transfer* 24 part 9, 1541-1544.
- KADJA M. and BERGELES G. (1997) Computational study of turbine blade cooling by slot- injection of a gas. *Applied Thermal Engineering*, 17(12), 1141-1149.
- KAMAKOTI R. (2004). Computational Aeroelasticity using Pressure - Based Solver. *Mechanical and Aerospace Engineering*. Florida, United States of America, Florida.
- KANE M. and YAVUZKURT S. (2009). Calculation of gas turbine blade temperatures using an iterative conjugate heat transfer approach. *Int. Symp. on Heat Transfer in Gas Turbine Systems*. 9-14-August, Antalya, Turkey,.
- KASSIM M S. YOOSIF A.H. and AL-KHISHALI K.J.M. (2007). Investigation into flow interaction between jet and cross mainstream flows. *Mechanical Engineering*. Baghdad, Iraq Technology.
- KHAING M.W. FUH J.Y.H. and LU L. (2001). Direct metal laser sintering for rapid tooling processing and characterization of EOS parts. *J. of Material Processing Technology* 113, 269-272.

KIM J. MOIN P. and MOSER R.D. (1987). Turbulence statistics in fully developed channel flow at low Reynolds number. *Fluid Mechanics*, 177, 133-166.

KIM Y.W. DOWN J.P. SOECHTING F.O. ABDEL -MESSEH W. STEUBER G.D. and TANRIKUT S. (1995). A Summary of the Cooled Turbine Blade Tip Heat Transfer and Film Effectiveness Investigations (Performed by Dr D. E. Metzger). *Turbomachinery, Transactions of the ASME*, 117, 1-11.

KIM Y. W. AND. METZGER D. E. (1995 ) Heat transfer and effectiveness on film cooled turbine blade tip models. *Turbomachinery, Transactions of the ASME*, 117, 10.

KRAVCHENKO A. G. MOIN P. AND. MOSER R. (1996) Zonal embedded grids for numerical simulations of wall-bounded turbulent flows. *Journal of Computational Physics* 127, 412–423.

LAKEHAL D. (2002). Near wall modeling of turbulent convective heat transport in film cooling of turbine blades with the aid of direct numerical simulation data. *Turbomachinery, Transactions of the ASME*, 124, 485-498.

LAKEHAL D. THEODORIDIS G. S. and RODI W. (2001). Three dimensional flow and heat transfer calculations of film cooling at the leading edge of a symmetrical turbine blade model. *Heat and Fluid Flow*, 22, 113-122.

LAUNDER B.E and SPALDING D.B. (1972). *Mathematical models of turbulence* London, UK.

LEE S. J. and JANG Y.G. (2005). Control of flow around a NACA0012 airfoil with a micro-riblet film. *fluid and structures, available online [www.elsevier.com/locate/jfs](http://www.elsevier.com/locate/jfs)*., 20, 659-672.

LIU C.L. ZHU H. R. and BAI J.T. (2008). Effect of turbulent Prandtl number on the computation of film-cooling effectiveness. *heat and mass transfer*, 51, 6208-6218.

LU Y. (2007). Effect of holes configurations on film cooling from cylindrical inclined holes for the application to gas turbine blades. *Degree of Doctor of Philosophy in*

*Agricultural and Mechanical College. United States of America, Louisiana State University.*

LU Y. ALLSON D. and EKKAD S.V. (2007). Turbine blade showerhead film cooling influence of hole angle and shaping. *Heat and Fluid Flow*, 28, 922-931.

LUCAS P. (2005). Computationally efficient solution based mesh adaptation. *Degree of Doctor of Philosophy in Aerospace Engineering Delft, Nederland, Technical University Delft.*

LUO J. and RAZINSKY E.H. (2007). Conjugate heat transfer analysis of a cooled turbine vane using the V2F turbulence model. *Turbomachinery, Transactions of the ASME*, 129, 773-781.

MARTINI P. SCHULZ A. WHITNEY C.F. and LUTUM E. (2003). Experimental and Numerical investigation of trailing edge film cooling down stream of a slot with internal rib arrays. *proceedings of the institution of mechanical engineers, Power and energy*, 217(A), 393-401.

MASON W.H. (1997). *Applied computational aerodynamics*. Last accessed on 8-December-2011 at: <http://www.scribd.com/doc/6818944/Mason-Applied-Computational-Aerodynamics>

MATHUR S.R. and MURTHY J.Y. (1997). A Pressure -based method fore unstructurad meshes. *Numerical heat transfer*, 31(2), 195-215.

MEI Y. and GUHA A. (2005). Implicit numerical simulation of transonic flow through turbine cascades on unstructured grids. *IMEchE, Power and Energy*, 209,(A).

MICHELASSI V. RODI W. and GIE P.A. (1998). Experimental and numerical investigation of boundary layer and wake development in a transonic turbine cascade. *Aerospace Science and Technology*, 3, 191-204.

MOSER R. D. KIM J. and MANSOUR N.N. (1999). Direct numerical simulation of turbulent channel flow up to  $Re=590$ . *Physics of Fluids A*, 11,(4), 943-946.

NASIR H. (2008). Turbine blade tip cooling and heat transfer. *Degree of Doctor of Philosophy in Agricultural and Mechanical College*. United States of America, Louisiana state university.

NEMDILI F. AZZI A. and JUBRAN B.A. (2011). Numerical investigation of the influence of a hole imperfection on film cooling effectiveness. *Numerical Method for Heat & Fluid Flow*, 21 No.1, 46-59.

NIX A.C. (2003). Effects of high intensity, large- scale freestream combustor turbulence on heat transfer in transonic turbine blades. *Degree of Doctor of Philosophy in Mechanical Engineering*. USA, Virginia Polytechnic Institute and State University.

NORMAN C.A. and ZIMMERMAN R.H. (1948). *Introduction to gas turbine and jet propulsion Design*, New York, United States of America, Harper, and Brothers.

OBBERG E. and JONES F.D. (1917) *Machinery's encyclopedia, Gas turbine with 1925 Supplement*, New York, The Industrial Press - Technology & Engineering.

Omega, OMEGA Engineering Technical Reference, Thermocouples (2011). [online]. Last accessed on - 15-August-2011 at: <http://www.omega.com/prodinfo/thermocouples.html>

Omega (2011). Omega Engineering Technical Reference [online], Flow meter. Last accessed on 12-December-2011 at: <http://www.omega.com/prodinfo/flowmeters.html>

OU S. and RIVIR R. (2001A). Leading edge film cooling heat transfer with high free stream turbulence using a transient liquid crystal image method. *Heat and Fluid Flow*, 22, 614-623.

OU S. and RIVIR R. (2001B). 90skew leading edge film cooling effectiveness heat transfer and discharge coefficients for cylindrical film holes at high free stream turbulence. *RTO AVT Symposium on advanced flow management part B- Heat transfer and cooling in propulsion and power systems*. hold in Loen, Norway.

PALMER E. MISHRA R. and FIELDHOUSE J. (2008). A computational fluid dynamic analysis on the effect of front row pin geometry on the aerothermodynamic property of a pin-vented brake disc. *IMechE, Mechanical Engineering Science*, 222(D), 1231-1245.

PAPADAKIS G. and BERGELES G. (1995). A locally modified second order upwind scheme for convection terms discretization *International Journal Numerical Mathematic Heat Fluid Flow* 5, 49-62.

PATANKAR S.V. (1980). *Numerical heat transfer and fluid flow, Chapter 2*, United States of America, Hemisphere Publishing Corporation, McGraw-Hill Book.

PENG W.W. (2007). *Fundamentals of Turbomachinery*, Hoboken, New Jersey, United States of America, John Wiley and Sons.

PEYRET R. (2000). *Handbook of Computational Fluid Mechanics*, Academic Press.

Pico, Pico Technology, thermocouples data logger (2011).[online]. Last accessed on 20-Novamember-2011 at: <http://www.picotech.com/thermocouple.html>

Pico, Pico Technology, Thermocouples (2010) [online]. Last accessed on 14-sptember 2010 at: <http://www.picotech.com/applications/thermocouple.html>

PRITCHARD L.J. (1985). An eleven parameter axial turbine airfoil geometry model. *The Gas Turbine Conference and Exhibit*. Houston, Texas, March 18<sup>th</sup> to 21<sup>st</sup> Williams International, 85-GT-219, ASME.

RENZE P. SCHRODER W. and MEINKE M. (2008). Large- eddy simulation of film cooling flow at density gradients. *Heat Fluid Flow*, 29, 18-34.

ROLLS ROYCE (2008). [Online] Turbojet at Boeing, Everett, Washington, Last updated 14/2/2008. [http://www.wingweb.co.uk/Images/-Rolls-Royce\\_Avon\\_Boeing.jpg](http://www.wingweb.co.uk/Images/-Rolls-Royce_Avon_Boeing.jpg).

RS Component (2011). Superwool 612 fibre mastic cartridge,\_RS Stock No.417-6785. Last accessed on 16-sptember -2011 at: <http://uk.rs->

[online.com/web/p/products/4176785/?searchTerm=417-6785&relevancy-data=636F3D3126696E3D4931384E525353746F636B4E756D626572266C753D656E266D6D3D6D61746368616C6C26706D3D5E5C647B337D5B5C732D2F255C2E5D5C647B332C347D2426706F3D3126736E3D592673743D52535F53544F434B5F4E554D424552267573743D3431372D363738352677633D4E4F4E4526](http://online.com/web/p/products/4176785/?searchTerm=417-6785&relevancy-data=636F3D3126696E3D4931384E525353746F636B4E756D626572266C753D656E266D6D3D6D61746368616C6C26706D3D5E5C647B337D5B5C732D2F255C2E5D5C647B332C347D2426706F3D3126736E3D592673743D52535F53544F434B5F4E554D424552267573743D3431372D363738352677633D4E4F4E4526)

SAGRADO A.G. (2007). Boundary layer and trailing edge noise sources. *Degree of Doctor of Philosophy in Mechanical Engineering*. Cambridge, (UK).

SALIM S.M. and CHEAH S.C. (2009). Wall  $y^+$  strategy for dealing with wall-bounded turbulent flows. *International MultiConference of Engineers and Computer Scientists, IMECS*. Hong Kong.

SARGISON J.E. (2001). Development of a novel film cooling hole geometry. *Degree of Doctor of Philosophy in Department of Engineering Science*. Hilary Term, Jesus College, University of Oxford.

SAUMWEBER C. SCHULZ A. and WITTIG S. (2003). Free-stream turbulence effects on film cooling with shaped holes. *Turbomachinery, Transactions of the ASME*, 125, 65-73.

SCHLICHTING H. (1968). *Boundary layer theory*, United States of America, McGraw Hill.

SCHLICHTING H. and GERSTEN K. (2003). *Boundary layer theory*, Springer-Verlag Berlin McGraw Hill.

SCHULZ A. (2000). Infrared thermography as applied to film cooling of gas turbine components. *Measurement Science Technology*, 11, 948-956.

SIM L. F. (2007). Numerical and experimental optimization of a high performance heat exchanger. *Mechanical Eng. Dept, SHU*. Sheffield, UK, Sheffield Hallam.

SINHA A.K. BOGARD D.G. and CRAWFORD M.E. (1999). Film cooling effectiveness downstream of a single row of holes with variable density ratio. *ASME J. Turbomachinery*, 113, 442-449.

TAKEISHI K. ODA Y. EGAWA Y. and KITAMURA T. (2010). Film cooling with swirling cooling flow. *11th international conference on advanced computational methods and experimental measurements in Heat transfer, WIT Transactions on Engineering Sciences*. Estonia, 189-200.

TAO Z. YANG X. DING S. XU G. WU H. DENG H. and LUO X. (2008). Experimental Study of Rotation effect on Film Cooling over the Flat wall with a Single Hole. *Experimental Thermal and Fluid Science*, available online at [www.ScienceDirect.com](http://www.ScienceDirect.com)., 32, 1081-1089.

TAO Z. ZHAO Z. DING S. XU G. YANG B. and WU H. (2009). Heat transfer coefficients of film cooling on a rotating turbine blade model- part I: effect of blowing ratio. *Turbomachinery, Transactions of the ASME*, available online at [www.ScienceDirect.com](http://www.ScienceDirect.com) 131, 041005-1 to 0410015-12.

TecEquipment (2011). Technical Teaching Equipment for Engineering, thermodynamics, Ltd, Bonsall Street, Long Eaton, Nottingham NG10 2AN, UK, [online]. Last accessed on 6- December - 2011 at: <http://www.tecequipment.com/Thermodynamics/Gas-Turbines/GT185.aspx>

THE FREE LIBRARY (1989). Searching for the small-shop CMM. Last accessed 5th August 2011 at <http://www.thefreelibrary.com/Searching+for+the+small-shop+CMM%3f-a07739701>, Nelson.

THEODORIDIS G.S. LAKEHAL D. and RODI W. (2001). Three dimensional calculation of the flow field around a turbine Blade with film cooling injection near the leading edge. *Flow, Turbulence and Combustion*, 66, 57-83.

THORPE S.J. YOSHINO S. AINSWORTH R.W. and HARVEY N.W. (2004). An investigation of the heat transfer and Static pressure on the over - tip casing wall of an

axial turbine operating at engine representative flow conditions (I) Time mean result  
*Heat and Fluid Flow*, 25, 933-944.

TQ education (2004). GT 185 Twin shaft gas turbine manual, TQ education and training  
Ltd, CH/PE/dlb/0504

TU J. YEOH G.H. and LIU C. (2008). *Computational fluid dynamics: a practical  
approach*, USA, Elsevier Inc.

VOGEL G. and GRAF A.B.A. (2003). A novel transient heater-foil technique for  
Liquid Crystal experiments on film-cooled surfaces,. *Transactions of the ASME*, 125,  
529-537.

WOLFSTEIN M. (1969). The velocity and temperature distribution of one-dimensional  
flow with turbulence augmentation and pressure gradient, . *Int. J. Heat Mass Transfer*  
12, 301-318.

YAKHOT V. ORSZAG S.A. THANGAM S. GATSKI T.B. and SPEZIALE C.G.  
(1992). Development of turbulence models for shear flows by a double expansion  
technique. *Phys. Fluids A*, 4, 1510-1520.

YOUNG J.B. and HORLOCK J.H. (2006). Defining the efficiency of a cooled turbine.  
*Transactions of the ASME*, 128.

YU Y. YEN C.H. SHIH T.I.P. CHYU M.K. and GOGINENI S. (2002). Film cooling  
effectiveness and heat transfer coefficient distributions around diffusion shaped holes.  
*Transaction of the ASME*, 124, 820-827.

YUAN F. ZHU X.-C. and DU ZHAO H. (2007). Experimental measurement and  
numerical simulation for flow filed and film cooling effectiveness in film cooled  
turbine. *Hydrodynamics*, available online at [www.ScienceDirect.com](http://www.ScienceDirect.com)., 19(4), 459-466.

YUEN C.H.N. and MARTINEZ-BOTAS R.F. (2005). Film cooling characteristics of a  
single round hole at various streamwise angles in a crossflow: Part I effectiveness,. *Heat  
Mass Transfer*, 48, 4995-5016.

YUEN C.H.N. and MARTINEZ-BOTAS R.F. (2003). Film cooling characteristics of a single round hole at various streamwise angles in a crossflow Part II: heat transfer coefficients. *Heat and mass transfer*, 46 237-249.

ZHANG Y. and ORSZAG S.A. (1998). Two-equation RNG transport modeling of high Reynolds number pipe flow. *Scientific Computing*, 13, 471-483.

## *Appendix A*

*Continuity equation, momentum equation  
and energy equation derivatives*

### Continuity equation

Figure (A-1) illustrate details of the flow model as an infinitesimally small element fixed in space, with the fluid moving through it. Note, the velocity and the density are the function of  $(x, y, z)$  and time  $t$ . There is mass flow through this element, considering the left and right faces of the element which are perpendicular to the  $x$  axis and the area of these faces is  $dydz$ . Hence, the mass flow through the left face is  $(\rho u)dydz$  and the mass flow across the right face is expressed as [Anderson (1995)].

$$\{\rho u + [\partial(\rho u) / \partial x]dydz\} \quad (A-1)$$

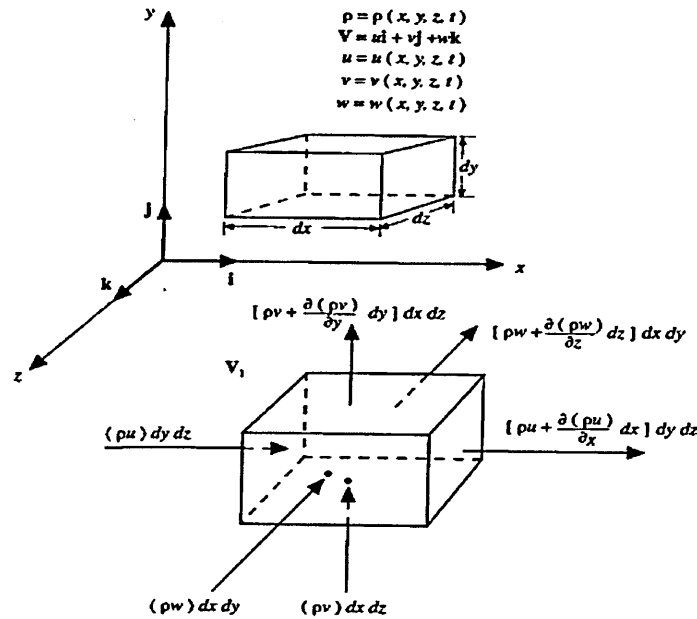


Figure (A-1) Model of infinitesimally small element fixed in space and a diagram of the mass fluxes through the various faces of the element for a derivation of the continuity equation [Anderson (1995)].

$$\text{Net outflow in x direction: } [\rho u + \frac{\partial(\rho u)}{\partial x} dx]dydz - (\rho u)dydz = \frac{\partial(\rho u)}{\partial x} dx dy dz$$

$$\text{Net outflow in y direction: } [\rho v + \frac{\partial(\rho v)}{\partial y} dy]dx dz - (\rho v)dx dz = \frac{\partial(\rho v)}{\partial y} dx dy dz$$

$$\text{Net outflow in z direction: } [\rho w + \frac{\partial(\rho w)}{\partial z} dz]dx dy - (\rho w)dx dy = \frac{\partial(\rho w)}{\partial z} dx dy dz$$

$$(A-2)$$

So, the net mass flow out of the element is given by

$$\text{Net mass flow} = \left[ \frac{\partial(\rho u)}{\partial x} + \frac{\partial(\rho v)}{\partial y} + \frac{\partial(\rho w)}{\partial z} \right] dx dy dz \quad (\text{A-2})$$

The total mass of fluid in the infinitesimally small element is  $\rho(dx dy dz)$ ; hence the time rate of increase of mass inside the element is given by

$$\text{Time rate of mass increase} = \frac{\partial \rho}{\partial t} (dx dy dz) \quad (\text{A-3})$$

The physical principle that mass is conserved and can be expressed finally as the net mass flow out of the element must be equal the time rate of decrease of mass inside the element, in terms of equation (A-2) & (A-3) as

$$\frac{\partial \rho}{\partial t} + \left[ \frac{\partial(\rho u)}{\partial x} + \frac{\partial(\rho v)}{\partial y} + \frac{\partial(\rho w)}{\partial z} \right] = 0 \quad (\text{A-4})$$

The partial differential equation form of the continuity equation can be written as:

$$\frac{\partial \rho}{\partial t} + \nabla \cdot (\rho V) = 0 \quad (\text{A-5})$$

Equation (A-5) is the continuity equation is also known as the mass conservation equation.

### Momentum equation

Newton's second law states that (the rate of change of momentum of a fluid particle equals to the sum of the forces on the particle). There are two sources of force:

1. Body force: gravity force, centrifugal force, electromagnetic force.
2. Surface force: pressure force, viscous force, shear and normal force.

The body force per unit mass acting on the fluid element is  $f$ , with  $f_x$  as its x component and the volume element is  $(dx dy dz)$ , so

$$\text{Body force on fluid element acting in x direction} = \rho f_x dx dy dz \quad (\text{A-6})$$

Net surface force in x direction =

$$\begin{aligned} & \left[ p - \left( p + \frac{\partial p}{\partial x} dx \right) \right] dy dz + \left[ \left( \tau_{xx} + \frac{\partial \tau_{xx}}{\partial x} dx \right) - \tau_{xx} \right] dy dz + \\ & \left[ \left( \tau_{yx} + \frac{\partial \tau_{yx}}{\partial y} dy \right) - \tau_{yx} \right] dx dz + \left[ \left( \tau_{zx} + \frac{\partial \tau_{zx}}{\partial z} dz \right) - \tau_{zx} \right] dx dy \end{aligned} \quad (\text{A-7})$$

So, the total force in the x direction  $F_x$  is given by the sum Eqs. (A-6) and (A-7)

$$F_x = \left[ -\frac{\partial p}{\partial x} + \frac{\partial \tau_{xx}}{\partial x} + \frac{\partial \tau_{yx}}{\partial y} + \frac{\partial \tau_{zx}}{\partial z} \right] dx dy dz + \rho f_x dx dy dz \quad (\text{A-8})$$

Referring to Newton's second law ( $F=ma$ ), eqs. (A-8) represent left hand, also the right hand is ( $m$ ) mass of the fluid element and ( $a_x$ ) is the acceleration component in x direction thus:

$$m = \rho dx dy dz \quad (\text{A-9})$$

$$a_x = \frac{Du}{Dt} \quad (\text{A-10})$$

By combining eqs. (A-8), (A-9) and (A-10), we obtain

$$\rho \frac{Du}{Dt} = -\frac{\partial p}{\partial x} + \frac{\partial \tau_{xx}}{\partial x} + \frac{\partial \tau_{yx}}{\partial y} + \frac{\partial \tau_{zx}}{\partial z} + \rho f_x \quad (\text{A-11a})$$

$$\rho \frac{Dv}{Dt} = -\frac{\partial p}{\partial y} + \frac{\partial \tau_{xy}}{\partial x} + \frac{\partial \tau_{yy}}{\partial y} + \frac{\partial \tau_{zy}}{\partial z} + \rho f_y \quad (\text{A-11b})$$

$$\rho \frac{Dw}{Dt} = -\frac{\partial p}{\partial z} + \frac{\partial \tau_{xz}}{\partial x} + \frac{\partial \tau_{yz}}{\partial y} + \frac{\partial \tau_{zz}}{\partial z} + \rho f_z \quad (\text{A-11c})$$

Equations (A-11) are the momentum equations for x, y, z components respectively. The Navier-Stokes equation can be obtained by conservation on left hand of eqs. (A-11) and substituting eq (A-5) which is the continuity equation giving:

$$\rho \frac{Du}{Dt} = \frac{\partial(\rho u)}{\partial t} + \nabla \cdot (\rho u V) \quad (\text{A-12})$$

By substituting eq. (A-12) to eq. (A-11a) for x component

$$\frac{\partial(\rho u)}{\partial t} + \nabla \cdot (\rho u V) = -\frac{\partial p}{\partial x} + \frac{\partial \tau_{xx}}{\partial x} + \frac{\partial \tau_{yx}}{\partial y} + \frac{\partial \tau_{zx}}{\partial z} + \rho f_x \quad (\text{A-13a})$$

Similarly for Eqs. (A-11b), (A-11c)

$$\frac{\partial(\rho v)}{\partial t} + \nabla \cdot (\rho v V) = -\frac{\partial p}{\partial y} + \frac{\partial \tau_{xy}}{\partial x} + \frac{\partial \tau_{yy}}{\partial y} + \frac{\partial \tau_{zy}}{\partial z} + \rho f_y \quad (\text{A-13b})$$

$$\frac{\partial(\rho w)}{\partial t} + \nabla \cdot (\rho w V) = -\frac{\partial p}{\partial z} + \frac{\partial \tau_{xz}}{\partial x} + \frac{\partial \tau_{yz}}{\partial y} + \frac{\partial \tau_{zz}}{\partial z} + \rho f_z \quad (\text{A-13c})$$

Eq. (A-13a), (A-13b) and (A-13c) represent conservation form of the **Navier-Stokes** equations. In Newtonian fluid the shear stress ( $\tau$ ) is proportional to the time rate strain (velocity gradients) so:

$$\begin{aligned}
\tau_{xx} &= \lambda(\nabla \cdot V) + 2\mu \frac{\partial u}{\partial x} & , \tau_{xy} = \tau_{yx} &= \mu \left[ \frac{\partial v}{\partial x} + \frac{\partial u}{\partial y} \right] \\
\tau_{yy} &= \lambda(\nabla \cdot V) + 2\mu \frac{\partial v}{\partial y} & , \tau_{xz} = \tau_{zx} &= \mu \left[ \frac{\partial w}{\partial x} + \frac{\partial u}{\partial z} \right] \\
\tau_{zz} &= \lambda(\nabla \cdot V) + 2\mu \frac{\partial w}{\partial z} & , \tau_{yz} = \tau_{zy} &= \mu \left[ \frac{\partial w}{\partial y} + \frac{\partial v}{\partial z} \right]
\end{aligned} \tag{A-14}$$

Through substituting eq(A-14) in eqs. (A-13a), (A-13b), (A-13c) we get the complete form of the Navier-Stokes equations:

$$\begin{aligned}
\frac{\partial(\rho u)}{\partial t} + \frac{\partial(\rho u^2)}{\partial x} + \frac{\partial(\rho uv)}{\partial y} + \frac{\partial(\rho uw)}{\partial z} &= -\frac{\partial p}{\partial x} + \frac{\partial}{\partial x} \left( \lambda \nabla \cdot V + 2\mu \frac{\partial u}{\partial x} \right) + \\
&\frac{\partial}{\partial y} \left[ \mu \left( \frac{\partial v}{\partial x} + \frac{\partial u}{\partial y} \right) \right] + \frac{\partial}{\partial z} \left[ \mu \left( \frac{\partial u}{\partial z} + \frac{\partial w}{\partial x} \right) \right] + \rho f_x
\end{aligned} \tag{A-15a}$$

$$\begin{aligned}
\frac{\partial(\rho v)}{\partial t} + \frac{\partial(\rho uv)}{\partial x} + \frac{\partial(\rho v^2)}{\partial y} + \frac{\partial(\rho vw)}{\partial z} &= -\frac{\partial p}{\partial y} + \frac{\partial}{\partial x} \left[ \mu \left( \frac{\partial v}{\partial x} + \frac{\partial u}{\partial y} \right) \right] + \\
&\frac{\partial}{\partial y} \left( \lambda \nabla \cdot V + 2\mu \frac{\partial v}{\partial y} \right) + \frac{\partial}{\partial z} \left[ \mu \left( \frac{\partial w}{\partial y} + \frac{\partial v}{\partial z} \right) \right] + \rho f_y
\end{aligned} \tag{A-15b}$$

$$\begin{aligned}
\frac{\partial(\rho w)}{\partial t} + \frac{\partial(\rho uw)}{\partial x} + \frac{\partial(\rho vw)}{\partial y} + \frac{\partial(\rho w^2)}{\partial z} &= -\frac{\partial p}{\partial z} + \frac{\partial}{\partial x} \left[ \mu \left( \frac{\partial u}{\partial z} + \frac{\partial w}{\partial x} \right) \right] + \\
&\frac{\partial}{\partial y} \left[ \mu \left( \frac{\partial w}{\partial y} + \frac{\partial v}{\partial z} \right) \right] + \frac{\partial}{\partial z} \left( \lambda \nabla \cdot V + 2\mu \frac{\partial w}{\partial z} \right) + \rho f_z
\end{aligned} \tag{A-15c}$$

Where  $\lambda$  is the second viscosity coefficient and equal to  $-\frac{2}{3}\mu$ . [Anderson (1995)]

### Energy equation

The first law of thermodynamic is a statement of the energy conservation equation. The first law states that [Anderson (1995)]:

$$\begin{array}{lclcl}
\text{Rate of change of} & & \text{Net flux of heat} & & \text{Rate of work done on} \\
\text{energy inside the} & = & \text{into element} & + & \text{element due to body and} \\
\text{fluid element} & & & & \text{surface force}
\end{array}$$

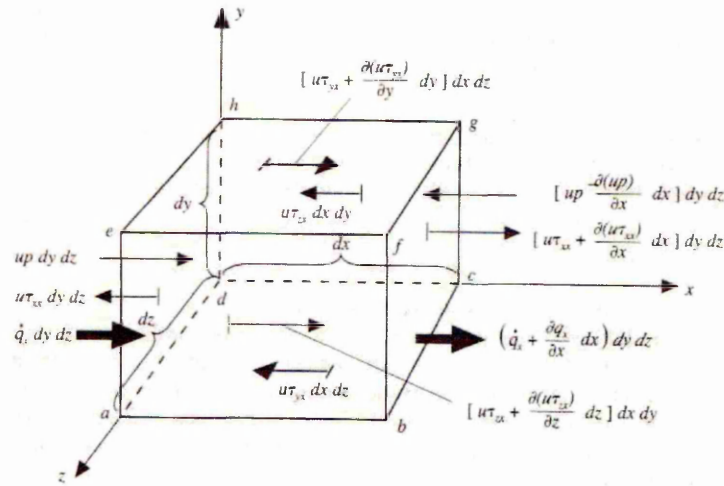


Figure (A-2) Model used for the derivation of energy equation with only fluxes in x direction [Anderson (1995)]

Figure (A-2) demonstrate the moving fluid element, so we now explain briefly the energy equation derivation.

- Rate of work done on element due to body and surface force is represented through this equation:

$$\begin{aligned}
 = - & \left[ \left( \frac{\partial(up)}{\partial x} + \frac{\partial(vp)}{\partial y} + \frac{\partial(wp)}{\partial z} \right) + \frac{\partial(u\tau_{xx})}{\partial x} + \frac{\partial(u\tau_{yx})}{\partial y} + \right. \\
 & \left. \frac{\partial(u\tau_{zx})}{\partial z} + \frac{\partial(v\tau_{xy})}{\partial x} + \frac{\partial(v\tau_{yy})}{\partial y} + \frac{\partial(v\tau_{zy})}{\partial z} + \frac{\partial(w\tau_{xz})}{\partial x} + \right. \\
 & \left. \frac{\partial(w\tau_{yz})}{\partial y} + \frac{\partial(w\tau_{zz})}{\partial z} \right] dx dy dz + \rho f \cdot V dx dy dz
 \end{aligned} \quad (A-16)$$

- Net flux of heat into element = heating of the fluid element+ volumetric heating of element :

$$= [\rho q^* + \frac{\partial}{\partial x} (k \frac{\partial T}{\partial x}) + \frac{\partial}{\partial y} (k \frac{\partial T}{\partial y}) + \frac{\partial}{\partial z} (k \frac{\partial T}{\partial z})] dx dy dz \quad (A-17)$$

Where  $q^*$  is the rate of volumetric heat generation.

- Rate of change of energy inside the fluid element where  $e$  is internal energy and  $\frac{V^2}{2}$  is kinetic energy ( total energy):

$$= \rho \frac{D}{Dt} \left( e + \frac{V^2}{2} \right) dx dy dz \quad (A-18)$$

For conservation form:

$$\rho \frac{D}{Dt} \left( e + \frac{V^2}{2} \right) dx dy dz = \frac{\partial}{\partial t} \left[ \rho \left( e + \frac{V^2}{2} \right) \right] + \nabla \cdot \left[ \rho \left( e + \frac{V^2}{2} \right) V \right] dx dy dz \quad (\text{A-19})$$

By manipulating eqs. (A-16), (A-17) and (A-19) as a first law of thermodynamics we obtain the final form of energy equation:

$$\begin{aligned} \frac{\partial}{\partial t} \left[ \rho \left( e + \frac{V^2}{2} \right) \right] + \nabla \cdot \left[ \rho \left( e + \frac{V^2}{2} \right) V \right] = \rho q \cdot + \frac{\partial}{\partial x} \left( k \frac{\partial T}{\partial x} \right) + \frac{\partial}{\partial y} \left( k \frac{\partial T}{\partial y} \right) + \\ \frac{\partial}{\partial z} \left( k \frac{\partial T}{\partial z} \right) - \frac{\partial (up)}{\partial x} - \frac{\partial (vp)}{\partial y} - \frac{\partial (wp)}{\partial z} + \frac{\partial (u\tau_{xx})}{\partial x} + \frac{\partial (u\tau_{yx})}{\partial y} + \\ \frac{\partial (u\tau_{zx})}{\partial z} + \frac{\partial (v\tau_{xy})}{\partial x} + \frac{\partial (v\tau_{yy})}{\partial y} + \frac{\partial (v\tau_{zy})}{\partial z} + \frac{\partial (w\tau_{xz})}{\partial x} + \\ \frac{\partial (w\tau_{yz})}{\partial y} + \frac{\partial (w\tau_{zz})}{\partial z} ] dx dy dz + \rho f \cdot V \end{aligned} \quad (\text{A-20})$$

## *Appendix B*

### *Gas turbine geometric program*